A multiphysics model for improving the ultrasonic assessment of large arteries.

Een multifysisch model voor verbeterde ultrasone beeldvorming van slagaders.

Abigail Swillens

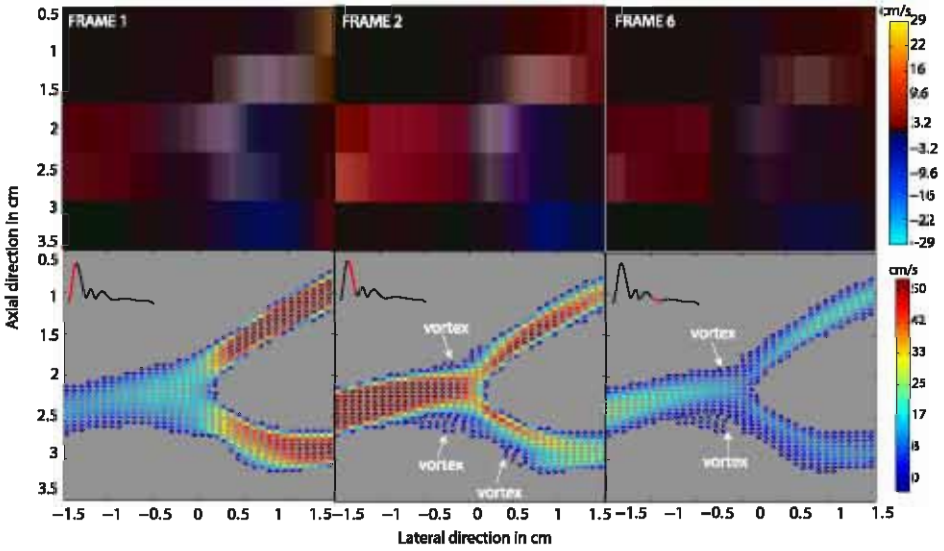

Promotoren: Prof.dr.ir. P. Segers, dr.ir. L. Lovstakken, Prof.dr. ir. J. Vierendeels
Proefschrift ingediend tot het behalen van de graad van
Doctor in de Ingenieurswetenschappen: Biomedische Ingenieurstechnieken

Vakgroep Civiele Techniek
Voorzitter: Prof.dr.ir. J. De Rouck
Faculteit Ingenieurswetenschappen
Academiejaar 2009-2010

UNIVERSITEIT GENT

Supervisors:

Prof.dr.ir. Patrick Segers
Dr.ir. Lasse Lovstakken
Prof.dr. ir. Jan Vierendeels

Research lab:

Institute Biomedical Technology
Biofluid, Tissue and Solid Mechanics for Medical Applications
Ghent University
De Pintelaan 185 - Blok B
B–9000 Gent
Belgium

Members of the exam committee:

Chairman:	
Prof. dr. ir. Ronny Verhoeven	Faculty of Engineering, UGent
Secretary:	
Dr. Ewout Vansteenkiste	Faculty of Sciences, UGent
Reading committee:	
Prof. dr. ir. Leif Rune Hellevik	Norwegian Institute of Science and Technology, Norway
Prof. dr. Jan D'hooge	Faculty of Medicine, KUL, Belgium
Prof. dr. ir. Jorgen Arendt Jensen	Technical University of Denmark, Denmark
Dr. ir. Lasse Lovstakken	Norwegian Institute of Science and Technology, Norway
Prof. dr.ir. Patrick Segers	Faculty of Engineering, UGent
Prof. dr. ir. David Steinman	University of Toronto, Canada
Prof. dr. ir. Hans Torp	Norwegian Institute of Science and Technology, Norway
Prof. dr.ir. Pascal Verdonck	Faculty of Engineering, UGent
Prof. dr. ir. Jan Vierendeels	Faculty of Engineering, UGent

This research was funded by a grant of the Special Fund for Scientific Research of the Ghent University (BOF).

Preface

Five years ago, I was confronted with the difficult choice of finding an interesting subject for my master thesis which would keep me passionate and motivated for an entire year. However, as a student in physical engineering, most thesis projects which presented themselves were quite theoretical, while I was longing to get back in touch with the *applied* sciences. As I was getting quite desperate to find subjects which would fit my interests, my now husband Wim gave me a golden tip to check out the thesis subjects of a certain professor Segers. And yes indeed, before I knew it, I had started a thesis on aneurysms in the department of prof. Verdonck and prof. Segers. Everything went quite smoothly, and attracted by the pleasant and interesting working environment, I started a PhD the next year.

While the aims of my master thesis were pretty well defined, I was hired on a huge project intended for three PhD-students, with as a final goal almost every research topic performed nowadays at our department. In this jungle of biomedical research subjects, I quite quickly decided to go for ultrasound imaging and go back to my roots, since the fundamental physics behind this technique felt close to my background as an engineer in physics. At the same time, prof. Segers (or by that time already Patrick), had the magnificent insight that combining two such different scientific disciplines like ultrasound imaging and computational fluid dynamics (CFD) might help improving the current ultrasonic imaging methods.

Although an extensive knowledge on fluid dynamics is present in our lab and that of prof. Jan Vierendeels (my co-supervisor), I felt a bit lost in the complex world of ultrasound imaging. However, again Patrick came up with the right plan at the right moment, and proposed to seek collaboration with the ultrasound department of prof. Hans Torp at the NTNU in Trondheim (Norway). A plan which certainly appealed

to me, both at a professional and a personal level. The ultrasound research at the NTNU has world renown and furthermore, it had also been one of my dreams to once study abroad. And so my Norwegian adventure was planned... After surviving the harsh fall and winter season of 2007 in Trondheim, I came back to Gent knowing the Belgian climate is not that bad after all, but more importantly with lots of ultrasound knowledge under my belt which really launched my PhD! Due to the intense and successful Norwegian collaboration and two more stays in Trondheim (now strategically chosen during spring), I got the opportunity to go for a joint PhD with the NTNU.

It is thus obvious that both my innovative research project combining ultrasound and CFD, as well as the opportunity I got to collaborate with Norway are the milestones of this PhD-book. The people responsible for these opportunities need an extensive *thank you* from me. To start with, thank you Patrick, for being the inspiration behind this research, which resulted for me in a highly rewarding PhD-project, and at the same time gave me a goldmine of interesting research projects for the future. Also my Norwegian (research) adventure would not have been possible if you had not given me the freedom to do this. I also thank you for the opportunity and support given to present my work at international conferences, which allowed me to build an international network. Further, I feel that our collaboration has always been very fruitful, with you getting me back from my ultrasound or CFD/FSI-planet on time by asking the right critical questions. I would also like to thank you for your *open door*, which gave me the chance to chat or discuss anything when needed. Also the emotional support and pat on the shoulder a PhD-student needs from time to time was highly appreciated.

My next thank you goes to Norway, first of all with Hans Torp giving me the chance to stay at his department for several months. Of course, I would also like to pay my gratitude to Lasse, who put from the very beginning a lot of his time into teaching me about ultrasound simulations and signal processing. I appreciate it a lot that without knowing me (or Patrick) at all, he was prepared to invest in my project. He also gave the right directions to my research at the right time, and suggested the most interesting research topics to investigate with our simulation environment. Besides the fact you gave me a thorough introduction into the world of ultrasound, it was also really nice to be introduced

into other fruitful projects in Trondheim like the pig coronary experiment (thank you Havard), and I hope more will come of this in the future. Finally, thank you also Lasse, not only for the scientific guidance, but also for giving me a second home in Trondheim, making sure I also had a nice time outside the lab.

Another important part of my PhD-project consisted of fluid-structure interaction simulations of blood vessels, and I thank Jan Vierendeels and Joris Degroote a lot for their contributions in this matter. Thanks a lot Joris, for helping me out with the FSI-modeling of a blood vessel, I hope we will have a further fruitful collaboration in the future. In this respect, I also thank my ex-colleague Lieve Lanoye for teaching me the first steps in FSI, and my ex-colleague Guy Mareels for introducing me to CFD.

This brings me to thanking all my other colleagues at the lab. First and foremost, prof. Pascal Verdonck to have made it possible to do research in biomedical engineering at Ghent University, by building out a lab which has gained an international reputation over the years. I would also like to thank prof. Verhegghe for his support and maintenance of the cluster and computational infrastructure. Further I would like to thank my officemates Bram, Seba (thank you for the nice lay-out of this book) and Charlotte and ex-officemates Tom, Thomas, Guy and Lieve for the pleasant atmosphere. Thanks also to Peter and Matthieu if some explanation on the Abaqus-front was needed. I would of course also like to thank all my other nice colleagues: Koen, Jan, Gianluca, Luis, Dieter, Frédéric, Benjamin, Sofie, Tomas, Francesco, Michele and Daniel. And of course also a thank you to my colleagues in Trondheim for giving me a nice time, with a special thanks to Svein-Erik, Sigrid, Jochen, Martijn and Paul-Roger for spending some of their precious spare time with me outside the lab. Also the administrative and technical staff I would like to thank: Ayfer, Saskia and Jurgen.

Further, I thank the jury for taking their time to read through this immense book: Jan D'hooge (thank you also for helping with my first steps in simulating ultrasound), Leif Rune Hellevik, Jorgen Arendt Jensen, David Steinman, Hans Torp, Ewout Vansteenkiste, Pascal Verdonck and Ronny Verhoeven.

Finally, I would like to end with a personal note. Thanks to all my

friends, who were interested how my research was progressing and who stayed patient when once more I was absorbed by my work or off to Norway again. I would also like to pay my gratitude to my parents, mama en papa, thanks a lot for just *always* being there, for being a listening ear on the ups and downs during my PhD-career and supporting me when abroad in Norway. My final thank you goes to my husband and soulmate Wim, for all the cheering and support along my PhD-path, even if that meant dropping me off at the airport, not to see each other for the next three months. Thanks for your belief in me as a PhD-student, and of course your eternal love and support. You're simply the best husband in the world and I'm sure this is just the beginning of an incredible journey together.

Abigail Swillens
14th May Gent, 2010

Samenvatting
Summary

Samenvatting

Inleiding

Hart- en vaatziekten vormen nog steeds de grootste doodsoorzaak in de westerse wereld. Tijdige diagnose en identificatie van risicopatiënten is dan ook cruciaal om de dodentol en de kosten in de gezondheidszorg te beperken. Ultrageluid is een standaard medische beeldvormingstechniek in de cardiovasculaire sector, gezien het wijd beschikbaar en relatief goedkoop is, maar ook omwille van zijn niet-invasieve en schadeloze aard, en klinisch bewezen waarde. Hoewel cardiale beeldvorming steeds een belangrijk onderzoeks- en toepassingsgebied van medisch ultrageluid geweest is, blijven de vasculaire applicaties wat achterop hinken. In de zoektocht naar efficiënte detectie van cardiovasculaire ziektes, is nochtans een groot potentieel weggelegd voor vasculaire beeldvorming. Daarom richt deze doctoraatsthesis zich op de ontwikkeling van ultrasone beeldvormingsmodaliteiten voor vasculaire toepassingen, en wordt daarbij voornamelijk gefocust op visualisatie van de bloedstroming en in mindere mate op het begroten van de vaatwandmechanica.

In-vitro en in-vivo validatie van nieuwe beeldvormingstechnieken is vaak onvoldoende gezien de in beeld gebrachte hemodynamica en arteriële mechanica niet gekend is. Daarom hebben we een computationele simulatie-omgeving ontwikkeld om de werking van nieuwe modaliteiten te testen en te optimaliseren. Een multidisciplinaire aanpak is hierbij noodzakelijk om tot een geavanceerd model te komen, zowel op het gebied van ultrasone beeldvorming als numerieke modellering van hemodynamica en arteriële mechanica. Gezien de multidisciplinaire aard van dit werk, geeft het eerste deel van dit manuscript de nodige achtergrond omtrent de verschillende wetenschapsdomeinen betrokken in deze simulatie-omgeving. De fysische principes en technologie waarop het ultrasone beeldvormingsproces steunt, worden belicht in hoofdstuk 1. Gezien dit onderzoek zich voornamelijk richt op

de ontwikkeling van stromingsvisualisatie met ultrageluid, geeft hoofdstuk 2 een gedetailleerd overzicht van frequent gebruikte methodes om de stromingssnelheid te schatten. Achtergrond rond het simuleren van medisch ultrageluid wordt verstrekt in hoofdstuk 3, waarbij voornamelijk wordt gefocust op de software aangewend in deze doctoraatsthesis (Field II). We bespreken zowel theoretische aspecten van Field II als voorgaand onderzoek gerelateerd aan dit werk. De behandeling van de achtergrond van onze simulatietool wordt afgerond met een hoofdstuk over numerieke modellering van bloedvaten. We geven een introductie tot algoritmes gebruikt in computationele stromings- en structuurdynamica. Verder komen technieken aan bod om vloeistof-structuur interactie te simuleren.

De volgende delen van dit manuscript bespreken de feitelijke resultaten van dit doctoraatsonderzoek en zijn gebaseerd op artikels die gepubliceerd of ingediend zijn in tijdschriften met *peer-review*. Deel II beschrijft de eerste stap in het ontwikkelen van onze multidisciplinaire simulatie-omgeving: koppeling van computationele stromingsdynamica (CFD) en Field II. Onze methodologie wordt uitgebreid beschreven en gevalideerd, en vergeleken met eenvoudigere simulatie technieken van stromingsvisualisatie met ultrageluid. In deel III worden experimentele methodes voor het in beeld brengen van stroming bestudeerd met onze simulatietool. In een eerste hoofdstuk, worden twee technieken voor 2D stromingsvisualisatie onderzocht: *speckle tracking* (ST) en *vector Doppler*. In een volgend hoofdstuk stellen we een nieuwe aanpak voor die voorgaande snelheidsschatters combineert: (i) *speckle tracking* om de laterale (loodrecht met de scanlijn) snelheid te meten, en (ii) de autocorrelatiemethode, zoals gebruikt in *color flow imaging* (CFI), om de axiale (evenwijdig met de scanlijn) snelheid te bekomen. Deel IV handelt over de volgende stap in de ontwikkeling van onze simulatie-omgeving: de integratie van vloeistof-structuur interactie en ultrageluidsimulaties. Onze simulatie-aanpak wordt geïllustreerd met twee applicaties waar vloeistof-structuur interactie van belang is. Eén is gerelateerd aan de hemodynamica en de andere aan de arteriële wandmechanica: meting van wandschuifspanning en arteriële distensie.

Deel I - Achtergrond

Hoofdstuk 1 - Fundamenten van medisch ultrageluid

Dit hoofdstuk beschrijft de fysische principes en technologie betrokken in het ultrasone beeldvormingsproces. Ultrasone golfpropagatie en verstrooiing in zacht weefsel vormen de fundamentele processen die deel uitmaken van medisch ultrageluid. Hierbij exciteert een *transducer* met behulp van bijvoorbeeld het piëzo-elektrisch effect ultrasone golven, die worden verstrooid wanneer een verandering in akoestische impedantie van het onderzochte medium optreedt. De verstrooide golven worden terug ontvangen door een transducer, en worden dan verwerkt om het weefsel te visualiseren en/of te karakteriseren. We lichten het ontwerp van *transducers* en ultrasone bundelvorming kort toe en geven meer aandacht aan beeldvormingstechnieken gebruikt in *lineaire array transducers* voor vasculaire toepassingen. Dit type transducer bouwt het beeld sequentieel op door de gepaste elementen van de transducer te activeren. Voor elke uitgezonden en ontvangen ultrasone bundel zijn focusserings- en apodisatietechnieken noodzakelijk om een optimale beeldkwaliteit te garanderen.

Het vervolg van dit hoofdstuk behandelt mogelijke scansequenties, een belangrijke aspect bij het valideren en ontwikkelen van nieuwe technieken, aangezien de frame rate en het bereik van meetbare snelheden hiervan afhangt. In het bijzonder worden scansequenties voor ultrasone stromingsvisualisatie toegelicht. Finaal wordt een overzicht gegeven van frequent gebruikte medische beeldvormingsmodaliteiten (*B-mode-*, *speckle-* en Doppler-beeldvorming), maar we geven ook een korte aanzet tot meer geavanceerde technieken zoals harmonische beeldvorming en *shear-wave imaging*.

Hoofdstuk 2 - Ultrasone beeldvorming van snelheden

Gezien onze simulatie-omgeving zich vooral richt op het verbeteren van ultrasone beeldvorming van bloedstroming, geven we een gedetailleerde beschrijving van frequent gebruikte technieken voor stromingsvisualisatie. We bespreken zowel continue als gepulse excitatie van ultrasone golven. Continue golfexcitatie is de basis van de oudste methodes om bloedsnelheden te detecteren, maar is niet in staat om een onderscheid in diepte te maken. Men heeft dan ook gepulse systemen ontworpen om deze limitatie te overwinnen. Zowel de continue als gepulste systemen die heden ten dage worden aangewend in

de klinische praktijk, kunnen slechts in één dimensie snelheid meten, namelijk in de richting van de scanlijn. Daarom geven we eerst een overzicht van deze meer gekende 1D-snelheidsschatters, vooraleer de eerder experimentele 2D-visualisatietechnieken te behandelen.

Allereerst komt het Doppler-effect aan bod, de basis van de oudste systemen die de stroming in beeld brengen. Sommige hedendaagse applicaties steunen nog steeds op het Doppler-effect, en de nodige achtergrond met betrekking tot Doppler-signaalverwerking wordt verstrekt. Vervolgens bespreken we uitgebreid een andere belangrijke klasse van snelheidsschatters, die het mogelijk maakt om stroming te visualiseren in een volledige 2D-regio. De autocorrelatiemethode is de meest gevestigde techniek, en vormt de basis van de meeste *color flow imaging* (CFI) systemen. Deze techniek wordt vaak benoemd als een Dopplermethode, maar in feite detecteert ze de faseverschuiving in het ontvangen signaal door de beweging van de verstrooiers (rode bloedcellen), eerder dan de echte Doppler-frequentieverschuiving. Meer bepaald wordt de stromingssnelheid gemeten aan de hand van geschatte faseverschuivingen tussen opeenvolgend ontvangen ultrageluidsignalen (*phase-shift estimation* = *PE*). Een andere CFI-techniek schat de tijdsverschuiving tussen opeenvolgend ontvangen ultrasone golven om de stromingssnelheid te bekomen (*time-shift estimation* = *TE*).

Een belangrijk artefact bij stromingsvisualisatie in het algemeen is de aanwezigheid van signaal afkomstig van het omringend weefsel. Daarom geven we een introductie tot filtertechnieken (*clutter filtering*) om de invloed van het weefselsignaal op de snelheidsschatting te minimaliseren. We besluiten dit hoofdstuk met een studie van 2D stromingsvisualisatietechnieken: *speckle tracking* en *vector Doppler*. De eerste techniek correleert opeenvolgend ontvangen specklebeelden om een 2D-snelheidsvector af te schatten. Vector Doppler is een 2D uitbreiding van de meer gekende 1D-autocorrelatietechniek, zoals gebruikt in CFI. Ultrageluidsignalen worden ontvangen via twee verschillende richtingen om alzo een 2D-snelheidsschatting te bekomen.

Hoofdstuk 3 - Ultrageluidsimulaties

In dit werk gebruiken we de open source Field II-software om het ultrasoon beeldvormingsproces te simuleren. Deze simulatietool is gebaseerd op fysische modellen voor ultrasone golfpropagatie en verstrooiing. Arbitraire transducers, bundelvorming en scansequenties

kunnen gemodelleerd worden met een grote flexibiliteit, dankzij een numerieke benadering van de spatiale impulsrespons van de transducer. Weefsel wordt gemodelleerd als een verzameling van random puntverstrooiers waarop de ultrasone golven reflecteren. Verdere theoretische details omtrent deze simulatie-aanpak worden gegeven in dit hoofdstuk.

Het Field II-programma heeft een Matlab-interface, waarmee de probe, de scansequentie en de simulatieparameters kunnen worden gedefinieerd. We geven dan ook verdere details hoe Field II in praktijk kan worden gebruikt. We besluiten dit hoofdstuk met een literatuurstudie van onderzoek gerelateerd aan dit doctoraatswerk, en meer in het bijzonder worden studies besproken die eveneens computationele stromings- en structuurdynamica koppelen aan ultrageluidsimulaties.

Hoofdstuk 4 - Numerieke modellering van bloedvaten

Gezien dit doctoraatswerk twee verschillende vakgebieden verenigt, namelijk ultrasone beeldvorming en numerieke modellering van bloedvaten, is ook een achtergrondkennis van computationele stromings- en vaatwandmechanica vereist. In computationele stromingsdynamica (CFD) staan de Navier-Stokes vergelijkingen centraal, die het behoud van massa en momentum van een fluïdum uitdrukken. In complexe vloeistofdomeinen, zoals het geval in het cardiovasculair system, kan deze set van niet-lineaire partiële differentiaalvergelijkingen echter niet analytisch opgelost worden en bijgevolg zijn numerieke technieken noodzakelijk. Wij gebruiken hiertoe het commerciële CFD-pakket Fluent, dat gebaseerd is op een eindige-volume-methode om de Navier-Stokes vergelijkingen te discretiseren in tijd en ruimte. We geven ook een korte beschrijving van enkele pijnpunten bij het aanpakken van een CFD-probleem in de praktijk, zoals de generatie van een computationeel grid en de keuze van de randvoorwaarden.

Vervolgens wordt kort computationele structuurdynamica (CSD) behandeld. Het commerciële pakket Abaqus wordt hiervoor aangewend. Dit pakket is gebaseerd op een eindige-elementen-methode om het behoud van momentum op te lossen. Dit in tegenstelling met de eindige-volume-methode waarop CFD gebaseerd is. Een ander belangrijk verschil met CFD is de gridformulering. CFD gebruikt een Euleriaanse gridformulering, waarbij het computationeel grid gefixeerd is in de

ruimte. De Lagrangiaanse formulering is de meest intuïtieve methode voor structuurmechanische problemen, waarbij het grid zich verplaatst met de materiaalvervorming. Net zoals voor het CFD-gedeelte, bespreken we kort enkele praktische problemen in het geval van CSD, zoals de keuze van het element en de randvoorwaarden.

Het laatste deel van dit hoofdstuk handelt over de simulatie van vloeistof-structuur interactie (FSI). Wanneer men het volledige gedrag van de bloedvaten wil modelleren, heeft men inderdaad te maken met een gekoppeld probleem van het vloeistof- en structuurgedeelte. De bloedstroming beïnvloedt de verplaatsing van de wand, en omgekeerd beïnvloedt de wandmechanica de hemodynamica. De belangrijkste simulatietechnieken gebruikt in FSI-modellering worden besproken. Een belangrijk onderscheid kan gemaakt worden tussen monolitische en gepartitioneerde FSI-simulaties. Bij de monolitische methode worden de vergelijkingen die het vloeistof- en structuurdomein bepalen gelijktijdig opgelost als één grote set vergelijkingen. Deze methode is in het bijzonder geschikt voor eenvoudigere FSI-problemen. In dit werk gebruiken we echter een gepartitioneerde aanpak, wat betekent dat we een commercieel pakket voor CFD (Fluent) en CSD (Abaqus) met elkaar koppelen. Dit heeft als nadeel dat er geen directe toegang is tot de numerieke berekeningen gebruikt in beide pakketten, wat het koppelingsalgoritme compliceert. Aan de andere kant is er het voordeel dat methodes specifiek ontwikkeld en geoptimaliseerd voor stromings- en structuurberekeningen kunnen aangewend worden tijdens de koppelingsprocedure.

Een gepartitioneerde FSI-simulatie van bloedvaten vereist een sterke koppeling van het fluïdum- en structuurdomein, wat inhoudt dat een evenwicht tussen vloeistof en structuur moet worden opgelegd aan de *interface*. Bijgevolg is een iteratieve procedure noodzakelijk om tot een geconvergeerde oplossing te komen. In deze context leggen we de verschillen uit tussen sterk en zwak gekoppelde FSI-simulaties en de mogelijke iteratieprocedures voor sterk gekoppelde modellen. We besluiten dit hoofdstuk met meer details over de sterk gekoppelde aanpak gebruikt in deze thesis, namelijk de *IBQN-LS (interface block quasi-Newton least-squares)* methode.

Deel II - Integratie van computationele stromingsdynamica en ultrageluidsimulaties

Hoofdstuk 5 - Koppeling van ultrageluid en CFD simulaties

In dit hoofdstuk presenteren we de eerste stap in de ontwikkeling van onze simulatie-omgeving: de integratie van CFD met Field II ultrageluidsimulaties. Ondanks de afwezigheid van de vaatwand in deze fase van het werk, tonen we aan dat onze CFD-Field II simulaties een groot potentieel hebben in het valideren en ontwikkelen van nieuwe beeldvormingsmodaliteiten voor de bloedstroming. In eerste instantie geven we een uitgebreide beschrijving van onze ultrageluidsimulaties, en demonstreren we dat we zeer realistische vasculaire probes kunnen simuleren. Verder focussen we op de koppeling van CFD met Field II. Field II modelleert weefsel als een verzameling van puntverstrooiers, waarvan de positie kan aangepast worden tijdens de gesimuleerde scansequentie. We bepalen de snelheid van de verstrooiers op basis van de bekomen CFD-snelheidsvelden, wat toelaat ultrasone beelden van complexe stromingsvelden te simuleren. Temporele en spatiale interpolatie van de CFD-stromingsvelden is hiervoor noodzakelijk omdat (i) de tijdstap in ultrageluidsimulaties veel kleiner is dan in CFD-simulaties, (ii) de snelheden van de CFD-gridknopen moeten geïnterpoleerd worden naar de random verstrooierposities.

We valideren onze methodologie in een 3D rechte buis met Poiseuille stroming (parabolisch), waar we perfect inzicht in en controle hebben over het in beeld te brengen stromingsveld. Gezien dit een eerste fase is in de ontwikkeling van onze simulatie-omgeving, onderzoeken we eerst reeds gevestigde beeldmodaliteiten voor de stroming, en met name *color flow imaging* gebaseerd op de autocorrelatiemethode. De resultaten in de buis zijn in lijn met voorgaand onderzoek rond deze beeldvormingstechniek, waarbij we ons baseren op (i) bias en standaarddeviatie bekomen met een statistische analyse van 40 schattingen van het parabolisch stromingsprofiel, en (ii) contourplots die het axiaal stromingsveld van CFI vergelijken met het CFD-referentieveld.

Vervolgens onderzoeken we de meer realistische en complexe stromingscondities in een halsslagader (carotis arterie). Zowel *color flow imaging* als *pulsed wave Doppler* worden gesimuleerd en vertonen een goede overeenkomst met de CFD-referentie. We tonen verder nog aan dat CFI niet in staat is complexe stromingsvelden in beeld te brengen. We

besluiten dat we een veelzijdige tool hebben ter ondersteuning van de ontwikkeling van stromingsbeeldvorming met ultrageluid, waarbij we flexibele controle hebben over zowel de stromings- als beeldvormingsparameters.

Hoofdstuk 6 - CFI-simulaties gebaseerd op een in-vitro stromingsmodel van de halsslagader

In het voorgaande hoofdstuk stelden we een redelijk complexe aanpak voor om ultrasone beelden van bloedstroming te simuleren. Daarom onderzoeken we in dit hoofdstuk eenvoudigere simulatietechnieken om synthetische *color flow beelden* te bekomen. Een gebruikelijke methode is om eenvoudigweg het CFD-stromingsveld te projecteren op de richting van de scanlijn, verder benoemd als *kleurcodering van de CFD-simulaties*. We bestuderen zowel instantane als dynamische kleurcodering, naargelang de scantijd om één beeld te produceren in rekening wordt gebracht of niet. We vergelijken deze eerste orde simulatiemethodes met de eerder voorgestelde tweede orde benadering die CFD en Field II koppelt.

Aangezien we ook willen nagaan in hoeverre de gesimuleerde beelden waarheidsgetrouw zijn, is deze studie gebaseerd op een in-vitro stromingsmodel van een halsslagader. De referentie voor de gesimuleerde ultrasone beelden zijn dan ook *color flow beelden* gemeten tijdens de in-vitro experimenten. CFD-berekeningen van het in-vitro model zijn mogelijk door het siliconen model in te scannen en de nodige randvoorwaarden te meten tijdens het experiment. Vervolgens kan een computationeel fantoom voor Field II-simulaties geconstrueerd worden op basis van deze CFD-simulaties, wat toelaat ultrasone beelden te simuleren van het in-vitro stromingsmodel. De beelden opgenomen tijdens het experiment worden dan vergeleken met de eerste en tweede orde simulatiemethodes, om de getrouwheid van de simulatie-omgeving na te gaan. We besluiten dat het koppelen van CFD-simulaties met een simulatiemodel voor ultrasone beeldvorming noodzakelijk is om de dynamische aspecten als ook de statistische eigenschappen van de beeldvorming mee in rekening te brengen.

Deel III - Analyse van 2D-stromingsvisualisatie met ultrageluid gebruik makend van CFD-gebaseerde ultrageluidsimulaties en in-vivo data

Hoofdstuk 7 - 2D-visualisatie van de bloedstroming met ultrageluid: een vergelijkende studie van speckle tracking en vector Doppler op basis van CFD-simulaties in een halsslagader

In het vakgebied van medisch ultrageluid is multidimensionale stromingsvisualisatie reeds vaak onderzocht, maar desondanks is er nog steeds geen robuuste methode die de klinische praktijk bereikt heeft. Daarom onderzoeken wij met behulp van onze CFD-gebaseerde ultrageluidsimulaties de performantie van twee frequent bestudeerde technieken, namelijk *speckle tracking* (ST) en *vector Doppler* (VD). Speckle tracking schat 2D-snelheidsvectoren door het correleren van opeenvolgend bekomen specklebeelden met gepaste *tracking* algoritmes. Een grote uitdaging hier is de decorrelatie van specklepatronen door temporele en spatiale stromingsgradiënten. Verder is een scanacquisitie noodzakelijk die voldoende hoge framesnelheid biedt om hoge bloedsnelheden, zoals aanwezig in het arterieel systeem, te detecteren. Vector Doppler is de uitbreiding van 1D snelheidsmeting op basis van de autocorrelatiemethode. De gereflecteerde golven worden ontvangen via twee verschillende richtingen door de transducer op te splitsen in een centrale transmissie-apertuur, geflankeerd door twee receptieaperturen. De snelheidsschattingen van beide richtingen worden gecombineerd om een 2D-snelheidsvector te vormen. Zoals voor de traditionele 1D-Dopplermethodes, wordt deze techniek geplaagd door aliasingartefacten.

Om meer inzicht te verkrijgen in de performantie van *speckle tracking* en *vector Doppler* in de aanwezigheid van complexe stromingscondities, bestuderen we eerst deze technieken in een 3D rechte buis met parabolische snelheidsprofielen. Dit vereenvoudigd model laat toe om factoren te bestuderen die de werking van deze snelheidsschatters eventueel belemmeren, zoals verschillende ruisniveaus en posities van het bloedvat. De statistische eigenschappen (bias en standaarddeviatie) van ST en VD worden berekend op basis van een ensemble van 80 schattingen van het snelheidsprofiel.

Vervolgens worden pulsatiele stromingscondities in een model van een halsslagader onderzocht, op basis van de CFD-simulaties bekomen in

hoofdstuk 5. We simuleren 2x4 cm scans van de carotisbifurcatie voor een volledige hartcyclus. Dezelfde scansequentie wordt gebruikt voor beide methodes, wat toelaat ST en VD direct met elkaar te vergelijken in de tijd. We simuleren een *beam interleaved* scanacquisitie, vaak gebruikt in CFI om de framesnelheid te verhogen. Deze acquisitietechniek verhoogt de frequentie waarmee ultrasone bundels worden uitgestuurd door de scan op te splitsen in laterale subregio's, ook *interleave-regio's* genaamd. In onze simulaties variëren we de snelheid waarmee ultrasone bundels worden uitgestuurd (*puls-repetitie-frequentie = PRF*), gezien deze parameter de werking van beide snelheidsschatters sterk beïnvloedt (PRF's van 2 en 4 kHz worden bestudeerd). De keuze van PRF is gerelateerd aan aliasingartifacten in *vector Doppler*, maar beïnvloedt ook *speckle tracking* gezien deze parameter de breedte van de *interleave-regio* en de snelheidsresolutie mee bepaalt. Verder worden de beeldvormingsparameters van beide technieken apart geoptimaliseerd gezien de aard van beide meettechnieken sterk verschillend is.

Clutter filtering is een belangrijk en tegelijk uitdagend aspect van 2D stromingsvisualisatie, gezien zowel de grootte als de hoek van de geschatte snelheidsvector beïnvloed wordt door het filteringsproces. Ondanks het feit dat de vaatwand niet gesimuleerd wordt in deze fase van ons werk, incorporeren we toch het effect van *clutter filtering* op de geschatte stromingssnelheden, in de veronderstelling dat het signaal van het omliggend weefsel volledig geattenueerd is door de filter. Hetzelfde type filter wordt toegepast voor ST en VD.

Om een intuïtief overzicht te verschaffen van de performantie van ST en VD, maken we vectorplots van het geschatte snelheidsveld en vergelijken we deze met de CFD-referentie. De resultaten worden verder onderzocht met behulp van een lineaire regressie-analyse, die de geschatte snelheden voor elk frame en elk gesampled punt in de ruimte plot versus de overeenkomstige CFD-snelheid. Met een temporele analyse van de gemiddelde absolute afwijking tussen geschatte en referentiesnelheid, demonstreren we de accuraatheid van de methodes in functie van de fase in de hartcyclus. Op basis van de studie in de buis en het carotismodel besluiten we dat ST de betere laterale snelheidsschatter is en VD de betere axiale snelheidsschatter, waarbij ST gevoeliger is aan de positie van het bloedvat en VD robuuster in de aanwezigheid van hoge ruisniveaus. Zowel ST en VD zijn in staat complexe stromingspatronen in beeld te brengen, maar gezien praktische limitaties van VD

op het vlak van aliasingartifacten en scanacquisitie, lijkt ST een praktischere aanpak.

Hoofdstuk 8 - Studie van 2D-stromingsvisualisatie van de carotis met een techniek die speckle tracking en een schatting van de faseverschuiving combineert: ultrageluidsimulaties en in-vivo data

Het voorgaande hoofdstuk toonde aan dat ST de betere laterale snelheidsschatter is en VD de betere axiale snelheidsschatter. Een logisch vervolg van deze studie is om een nieuwe techniek voor te stellen die het beste van beiden combineert: ST om de laterale snelheid (v_x) te meten en de autocorrelatiemethode (*phase-shift estimation = PE*) om de axiale snelheid (v_z) te detecteren. ST en PE combineren in één snelheidsschatter is echter niet evident omdat de principes achter beide meettechnieken sterk verschillend zijn. Een gemeenschappelijke scanacquisitie vinden is uitdagend gezien men streeft naar een optimale trackingsetup en tegelijk aliasingartifacten moet vermijden.

Eerst wordt de combinatie van beide technieken geanalyseerd met behulp van CFD-gebaseerde ultrageluidsimulaties en drie verschillende combinaties worden hierbij onderzocht: (i) v_x van ST en v_z van PE, (ii) v_x van ST en v_z van PE maar gecorrigeerd voor aliasing met behulp van v_z van ST, (iii) vereenvoudiging van ST op basis van v_z van PE, opdat enkel laterale tracking nodig is. Deze laatste aanpak wordt verder benoemd als *vereenvoudigde ST* en is minder rekenintensief dan volledige ST. De prestatie van deze combinatietechnieken wordt vergeleken met pure ST voor twee verschillende setups (variatie van de PRF zoals uitgelegd in hoofdstuk 7).

Voor twee belangrijke fases in de hartcyclus (systole en diastole) vergelijken we de drie combinatietechnieken en ST met de CFD-referentie op basis van vectorplots. In het bijzonder zoomen we in op klinisch relevante stromingspatronen, zoals vortices en de hoge snelheden in de externe carotis. Met een lineaire regressie-analyse tonen we aan dat 2D-stromingsbeeldvorming robuuster wordt wanneer PE gebruikt wordt om de axiale snelheidscomponent te schatten. In de aanwezigheid van hoge ruisniveaus wordt dit effect nog duidelijker. De *vereenvoudigde ST* vertoont licht verminderde performantie vergeleken met de andere combinatietechnieken, maar heeft potentieel om *real-time* implementatie van 2D-stromingsvisualisatie mogelijk te maken dankzij de relatief lage rekenintensiteit.

Zoals het geval was voor ST en VD op zich is de prestatie van de gecombineerde technieken sterk afhankelijk van de fase in de hartcyclus. Dit tonen we aan met een temporele analyse van de gemiddelde absolute afwijking tussen de geschatte snelheid en de CFD-referentie. Hierbij focussen we op twee belangrijke zones, de carotis communis en externa. Verder ondersteunen we onze simulatieresultaten met in-vivo data afkomstig van een halsslagader van een gezonde vrijwilliger. In eerste instantie beoordelen we de haalbaarheid van de bestudeerde technieken door superpositie van de vectorplots op de *color flow beelden.* We bekomen aanvaardbare resultaten, in lijn met stromingspatronen die men verwacht in een gezonde carotis. Verder leggen we een link tussen de resultaten van de simulaties en de in-vivo analyse door de technieken onderling te vergelijken. Daarvoor maken we een statistische analyse van de hoek van de geschatte stromingsvectoren, in zones waar men verwacht dat de stroming gealigneerd is met de as van het bloedvat. We concluderen dat in-vivo applicatie van ST en de combinatietechnieken haalbaar is op basis van de geanalyseerde dataset.

DEEL IV - INTEGRATIE VAN VLOEISTOF-STRUCTUUR INTERACTIE EN ULTRAGELUIDSIMULATIES

Hoofdstuk 9 - Een simulatie-omgeving om ultrasone visualisatie van de bloedstroming en vaatwand te valideren op basis van FSI-simulaties: ultrasone meting van arteriële distensie en wandschuifspanning

In dit hoofdstuk presenteren we de meest geavanceerde ontwikkeling in onze multidisciplinaire simulatie-omgeving, die toelaat synthetische ultrageluidbeelden van zowel de bloedstroming als de vaatwand te simuleren. Om realistische beelden van zowel de hemodynamica als vaatwandmechanica te bekomen, worden vloeistof-structuur interactie (FSI) simulaties geïntegreerd met Field II. De FSI-simulaties worden uitgevoerd met een code ontwikkeld aan de UGent (departement prof. Vierendeels), die de commerciële pakketten Fluent en Abaqus sterk met elkaar koppelt aan de hand van een i*nterface quasi-Newton techniek.*

De FSI-resultaten integreren met het Field II-model is echter geen eenvoudige uitbreiding van de voorgaande CFD-Field II koppeling. Het vloeistofdomein wijzigt nu gedurende de ultrageluidsimulaties en een

continue beweging van de verstrooiers tijdens de gesimuleerde scanprocedure moet verzekerd worden. We voorzien dan ook een uitgebreide beschrijving en illustratie van onze methodologie om computationele Field II-fantomen voor de stroming te construeren. Ook het creëren van Field II-fantomen voor de structuur vereist een complexe aanpak, die verstrooiers genereert per computationele gridcel om zo wijzigingen in mechanische eigenschappen en dus ook in ultrasone verstrooiing in rekening te kunnen brengen.

Gezien de koppeling van FSI met Field II complex is, illustreren we onze methodologie aan de hand van een redelijk eenvoudige vasculaire configuratie, met name een 3D rechte buis representatief voor de carotis communis. Aan de inlaat van de buis leggen we een massadebiet op, gebaseerd op stroming gemeten in een gezond individu. Aan de uitlaat van de buis leggen we een niet-invasief gemeten drukprofiel op, waarvan de amplitude wordt gewijzigd om verschillende graden van distensie te simuleren. In deze configuratie zijn de resulterende hemodynamica en vaatwandmechanica relatief eenvoudig om te interpreteren, wat de validatie van onze simulatie-omgeving vergemakkelijkt.

De RF-data van de FSI-Field II koppeling worden dan verder verwerkt om twee klinisch relevante applicaties van arteriële functie te onderzoeken, gerelateerd aan zowel de vervorming van de vaatwand als de arteriële hemodynamica: arteriële distensie (gerelateerd aan arteriële stijfheid) en wandschuifspanning (een stimulus van endotheelfunctie en gerelateerd aan de ontwikkeling van atherosclerose). We schatten arteriële distensie met behulp van een reeds ontwikkeld algoritme om de vaatwand te tracken. Stromingsprofielen en wandschuifspanningen worden bekomen langsheen een scanlijn aan de hand van de autocorrelatiemethode.

De distensie-applicatie blijkt zeer gevoelig aan de meetlocatie, zoals reeds eerder aangetoond met in-vivo data. Verder tonen we aan dat sterke speculaire reflecties bij de overgang tussen verschillende weefseltypes de accuraatheid van de meting benadeelt.

De studie van de meting van de wandschuifspanning toont dat met ultrageluid de maximale afschuifsnelheid bekomen wordt op een zekere afstand van de wand. Dit is enigszins verwacht gezien ultrageluid moei-

lijk snelheden nabij de wand kan meten. De geschatte afschuifsnelheden correleren echter wel goed met de FSI-referentie, wat suggereert dat correctie van de onderschatting door ultrageluid mogelijk is in de gesimuleerde stromingscondities.

DEEL V - CONCLUSIES

Hoodstuk 10 - Conclusies

In hoofdstuk 10 formuleren we algemene besluiten evenals perspectieven voor toekomstig onderzoek. We besluiten dat we een flexibele tool ontwikkeld hebben om ultrasone diagnose van de bloedvaten te valideren en te verbeteren. Mogelijkheden voor verder onderzoek situeren zich voornamelijk op het gebied van vasculair onderzoek in muizen en cardiale beeldvorming, maar ook op het vlak van geavanceerdere technieken zoals *contrast-enhanced imaging*, *harmonic imaging* en *intravasculair ultrageluid*. Een andere belangrijke focus voor de toekomst is klinische validatie van de onderzochte beeldvormingsmodaliteiten.

Summary

Introduction

Cardiovascular diseases are considered as one of the largest epidemics of the 21^{st} century, and hence early diagnosis and identification of subjects at risk are essential in decreasing its death toll and health care expenses. As ultrasound is a widely available, non-invasive, harmless and low-cost medical imaging technique and further has proven clinical value, it is one of the preferred screening tools of the cardiologist. While the field of cardiac imaging has received much attention over the years, with advanced 3D imaging tools as the latest novelty, vascular imaging has been lagging behind. However, when screening patients for cardiovascular disease, a large clinical potential for vascular imaging exists. Therefore, this dissertation focuses on the improvement of vascular ultrasound imaging, mainly investigating blood flow visualization, but to a lesser extent also the assessment of arterial wall mechanics.

With this focus in mind, we developed a computer simulation environment to validate and develop vascular imaging modalities, as in-vitro and in-vivo testing often provide insufficient validation because the imaged vascular behaviour is unknown. A multidisciplinary approach was employed resulting in an advanced simulation model, both at the level of ultrasound imaging as well as the numerical modeling of hemodynamics and vascular wall mechanics. Given the multidisciplinary nature of this work, the first part provides the necessary background on the different scientific domains covered by our simulation approach. Chapter 1 explains the physics and technology involved in the ultrasonic image formation process. As our simulations are mostly applied to investigate blood flow visualization, chapter 2 gives a detailed overview on the most commonly applied ultrasonic velocity estimators. A final chapter (chapter 3) on ultrasonic imaging was written to give more insight in simulating medical ultrasound, and more

particularly in the software applied in this work, i.e. Field II. We provide a background on the simulation approach of Field II, as well as a short overview of previous research related to the presented dissertation. The last chapter of the background part concerns the numerical modeling of blood vessels. An introduction to the algorithms in computational fluid dynamics and structure mechanics is given, as well as to the more complex modeling of fluid-structure interaction (FSI).

The subsequent parts of the manuscript present the results of the research performed during this PhD and are based on papers published and submitted to peer-reviewed journals. Part II describes the first step in the development of our simulation environment: coupling computational fluid dynamics (CFD) with the Field II ultrasound simulation software. Our methodology is elaborately described and validated, and further compared to simpler simulation approaches of ultrasonic blood flow imaging. In part III, the developed simulation tool is applied to experimental flow estimators. In a first chapter, two common 2D flow visualization approaches are compared: speckle tracking and vector Doppler. In a next chapter, a new flow estimator is proposed and investigated, combining (i) speckle tracking to image lateral (perpendicular to scanline) flow velocity and (ii) the autocorrelation approach, as used in color flow imaging, to visualize axial (parallel to scanline) flow velocity. Part IV deals with the integration of fluid-structure interaction simulations with the Field II ultrasound simulation model. Our simulation approach is illustrated with two applications where fluid-structure intraction is relevant, one related to the blood flow, and one to the moving wall: wall shear rate and arterial distension imaging.

PART I - BACKGROUND

Chapter 1 - Fundamentals of medical ultrasound imaging

This chapter describes the physics and technology involved in the ultrasonic image formation process. Ultrasonic wave propagation and scattering in soft tissue form the fundamental processes involved in medical ultrasound imaging. Ultrasound waves are excited by a transducer through the piezo-electric effect, and are scattered when changes in acoustic impedance of the imaged medium are met. The backscattered ultrasound signals are received by a transducer and further processed to image and characterize the tissue. In this context, transducer design and ultrasonic beam formation are briefly described, and we

especially give attention to image formation techniques used in linear array probes for vascular applications. This transducer type sequentially builds up an image, by activating the appropriate transducer elements. For each emitted and received ultrasonic beam, appropriate focusing and apodization techniques are required, to enhance image quality. Further, as a large part of this manuscript deals with blood flow visualization, we discuss the scan sequencing setups used in blood velocity imaging, as they play an important role when validating and developing new techniques. Indeed, the applied scan sequencing greatly influences the frame rate and range of measurable velocities. Finally, an overview is given of nowadays commonly used imaging modalities (gray-scale imaging, speckle imaging and Doppler flow imaging), but we also give a short introduction to more advanced techniques, like harmonic and shear-wave imaging.

Chapter 2 - Velocity imaging with ultrasound

As we mainly apply our simulation environment to study ultrasonic flow visualization, we give a detailed description of currently applied and investigated flow imaging methods. Distinction is made between continuous and pulsed excitation of the ultrasonic waves. The earliest systems used continuous wave excitation, but were unable to detect the depth from which the backscattered signal originated. Pulsed wave systems were developed to overcome this limitation. Both the pulsed and continuous wave systems used in today's clinical practice measure velocities in one dimension, i.e. along the scanline. Hence, we first give an overview of the commonly applied 1D flow estimators, before shortly discussing the more experimental 2D flow estimators, which are further investigated in this thesis.

The basis of the earliest flow imaging methods is explained, i.e. the Doppler effect. Doppler flow imaging is still used in today's ultrasound scanners, and the necessary signal processing techniques to detect the Doppler frequency shift of the backscattered ultrasound signal are clarified. Next, another important class of velocity estimators is discussed, which provides the necessary frame rate to create flow images of larger 2D regions of interest. The autocorrelation method is an established approach in this matter, and is most often used in color flow imaging (CFI). Although it is often referred to as a Doppler method, it measures the phase shift in the received signal due to the movement of the red blood cells (scatterers) rather than the real Doppler frequency shift.

Another type of velocity estimation, also used in CFI, is time-shift estimation, which correlates subsequently received ultrasound signals to find an estimate of the flow velocity. Further, it should be noted that flow estimation in general is hampered by artifacts such as the presence of strong tissue signal in the vessel lumen, due to ultrasound beam side lobes and reverberations. Therefore, we also give an introduction to different filtering techniques to remove this clutter signal. We conclude this chapter with two techniques under study for 2D flow estimation: speckle tracking and vector Doppler. The first technique tracks blood movement by correlating subsequently acquired speckle images. The latter is the extension of the commonly applied 1D autocorrelation method, as used in CFI, and simultaneously receives signal along two different scan directions to obtain a 2D velocity vector estimate.

Chapter 3 - Ultrasound simulations

The Field II simulation software was used in this dissertation to mimick the ultrasonic imaging process. This software is based on physical models for the ultrasonic wave propagation and scattering process. Arbitrary transducer geometries, beamformation and scan sequences can be simulated with great flexibility, by numerical approximation of the spatial impulse response of the transducer. Tissue is modeled as a collection of random point scatterers on which the ultrasound waves reflect. Further details on this simulation approach are provided in this chapter. The Field II-program can be accessed through a set of Matlab-routines, which define the probe, scansequencing and simulation setup, and we give a summary on how to use Field II in practice. We conclude this chapter with an overview of previous research which is closely related to ours. More specifically, we will present studies which also integrate computational fluid and wall mechanics with ultrasound simulation models.

Chapter 4 - Numerical modeling of the blood vessel

As our research merges the field of ultrasonic imaging with the domain of computational blood vessel modeling, a background on computational fluid and wall mechanics is required. The field of computational fluid dynamics (CFD) is introduced with the Navier-Stokes equations, which express the conservation of mass and momentum of a fluid flow. However, this set of coupled non-linear partial differential equations can not be solved analytically for complex fluid domains, and hence

numerical techniques are required. We used the commercial CFD-software Fluent, which uses a finite volume method to discretize these equations in time and space. We also give a short description on some practical issues involved in setting up a CFD-problem, like the creation of a computational mesh and the choice of boundary conditions.

Next, numerical modeling of (tissue) mechanical problems will be tackled. In this work, we used the commercial software package Abaqus for this purpose, which is based on a finite-element model to solve the conservation of momentum, as opposed to the finite volume technique used in CFD. Another difference between numerical modeling of fluid and tissue is the applied grid formulation. CFD uses an Eulerian grid formulation, meaning that the computational grid is fixed as the fluid flows. The Lagrangian formulation is typically used in structural mechanics, i.e. the grid moves according to the structural deformation. As was the case for the CFD-section, we briefly discuss practical issues involved in numerically solving a structural mechanical problem, e.g. the element choice, boundary conditions etc...

Finally, we advance to the simulation of fluid-structure interaction (FSI). Indeed, numerical modeling of the integral blood vessel behaviour is a coupled problem of the fluid and structural domain. The flow field influences the structural displacement, but on the other hand, the vessel wall mechanics also influences the hemodynamics. The main simulation approaches applied in FSI-simulations are discussed. An important distinction can be made between monolitic and partitioned solvers. The most straightforward way of simulating FSI is the monolitic approach, which means that the equations governing the fluid and solid domain are solved simultaneously as one big set of equations, and which is particularly suited for simpler FSI-problems. In this work, we use a partitioned approach, meaning that we couple a fluid and structural solver, i.e. Fluent and Abaqus. This has the disadvantage that the calculation procedures used in the commercial software packages can not be accessed, which complicates the coupling algorithms. However, it has the benefit that more advanced simulation models of the fluid flow and structural mechanics can be applied.

Using a partitioned technique for blood vessel modeling requires a strong coupling of the fluid and solid solver, i.e. an equilibrium between the fluid and solid domain should be imposed at the interface,

and hence an iterative approach is necessary to find a converged solution. In this context, we explain the differences between strong and weak coupling techniques and some possible iteration approaches for strongly coupled partitioned solvers. We conclude this chapter with more details on the strongly coupled partitioned solver we used, the interface block quasi-Newton least-squares model (IBQN-LS).

PART II - INTEGRATING COMPUTATIONAL FLUID DYNAMICS AND ULTRASOUND SIMULATIONS

Chapter 5 - Coupling ultrasound and CFD simulations

In this chapter, we present the first step in the development of the ultrasound simulation environment: the integration of CFD with Field II ultrasound simulations. Although in this stage the blood vessel is modeled as a rigid structure and only the fluid domain is simulated, we demonstrate that this CFD-Field II simulation tool has large potential in validating ultrasonic flow imaging modalities. In first instance, we provide an elaborate description on our ultrasound simulation setup, showing that we can model highly realistic ultrasound probes for vascular imaging purposes. The next part of our methods section focuses on coupling CFD with the Field II ultrasound simulation model. Field II models tissue as a random distribution of point scatterers, and their position can be updated during the simulated scan procedure. Therefore, we derive the scatterer velocity from the CFD-simulations, which then allows to simulate ultrasound images from complex flow velocity fields. For this purpose, temporal and spatial interpolation of the CFD velocity field is necessary because (i) the time step used in ultrasound simulations is much smaller than in CFD-calculations; (ii) the velocities at the CFD grid nodes should be interpolated to the random point scatterers.

We first validate our methodology in a 3D straight tube with parabolic flow, where we have perfect control over and insight in the imaged flow field. As this is the first phase in the development of our simulation tool, we investigate already established flow imaging methods, and more particularly color flow imaging based on the autocorrelation approach. The tube results indicate that we obtain results in line with previous research on the autocorrelation method for blood velocity estimation, based on (i) bias and standard deviation obtained from a statistical analysis of 40 estimations of the parabolic flow profile, and

(ii) contourplots comparing the axial velocity estimated by CFI and the axial velocity component calculated from the CFD flow field.

Once the validation in the straight tube is performed, we progress to the more complicated and realistic flow situation present in the carotid artery. Both color flow imaging and pulsed wave Doppler are simulated and show good comparison with the axial velocity component of the CFD flow field. Moreover, we confirm the inability of color flow imaging to portray complex 3D velocity fields. We conclude that we have a versatile tool to validate and develop flow imaging methods with flexible control over both the flow and imaging setup.

Chapter 6 - CFI-simulation based on an in-vitro carotid flow model

In the previous chapter, we introduced a quite complex approach in simulating ultrasonic flow images. Therefore, we investigate in this chapter simpler methods to obtain synthetic color flow images. A common approach is the simple projection of the CFD flow field on the ultrasonic scanline direction, also referred to as color-coding of the CFD-simulations. We study both an instantaneous and dynamic color-coding approach, depending whether the scan time to produce one color flow image is taken into account or not. We compare these first order approaches to our previously presented (second order) approach, coupling CFD and Field II.

Moreover, since we also want to assess the realism of the simulated ultrasound images, this study is based on an in-vitro carotid flow model. A reference to the simulated ultrasound images is obtained by recording color flow images during the experiments. CFD-calculations are performed by scanning the in-vitro model and reconstructing a computational mesh, and by measuring boundary conditions during the experiments. By constructing computational scatterer phantoms for the Field II-simulations, based on these CFD-results, ultrasound images of the in-vitro flow model are simulated. This then allows to compare the experimentally recorded images to the first and second order simulation approaches, and hence to assess the realism of our simulation environment. We conclude that a full coupling of CFD and ultrasound simulations is indispensable to capture the dynamics of the image formation as well as the statistical aspects of the estimated velocity field.

Part III - Analysis of 2D ultrasonic blood flow estimators using CFD-based ultrasound simulations and in-vivo data

Chapter 7 - 2D blood flow estimation: speckle tracking versus vector Doppler based on CFD-simulations in a carotid artery

For years, 2D blood flow visualization has been a hot research topic in the medical ultrasound community, but no clinically robust method has resulted yet. We assess the performance of two frequently studied 2D flow imaging methods, speckle tracking (ST) and vector Doppler (VD), using our CFD-based ultrasound simulations. Speckle tracking measures blood flow by correlating subsequently acquired speckle images with appropriate tracking algorithms. Major challenge here is the decorrelation of speckle patterns due to spatial and temporal flow gradients. Further, a scan acquisition scheme should be found, which provides sufficient frame rate to track the high flow velocities in the arterial system. The crossed-beam vector Doppler technique is the extension of the previously studied 1D color flow imaging based on the autocorrelation approach. Backscattered ultrasound waves are received along two different directions by splitting the transducer in a central transmit aperture and two receive apertures on the sides. The 2D velocity vector can then be constructed through triangulation of the autocorrelation velocity estimates obtained along the two receive directions. As for the classical 1D Doppler techniques, this method is mainly hampered by aliasing.

To better understand the performance of speckle tracking and vector Doppler in the presence of complex flow conditions, we first examine these techniques in a 3D straight tube with stationary parabolic flow. Such a simplified setup allows to study the sensitivity of these flow estimators to factors possibly degrading their performance, like different noise levels, vessel positions and angles. The statistical properties of ST and VD, i.e. bias and standard deviation, are assessed based on an ensemble of 80 flow velocity estimations.

Next, pulsatile flow conditions in a carotid artery model are considered, using the CFD flow fields obtained in chapter 5. For the complete cardiac cycle, we simulate 2x4 cm scans of the carotid bifurcation area, using the same scan sequencing setup for both imaging methods, which allows for a direct comparison of both techniques in time. We simulate a beam interleaved acquisition scheme, a technique commonly used in CFI to increase frame rate, and which minimizes the

time between firing beams by dividing the scanwidth in lateral subregions (interleave regions). We vary the speed with which ultrasound beams are fired (PRF = pulse repetition frequency), since this parameter greatly influences the performance of both flow estimators (PRF of 2 and 4 kHz is studied). The PRF-choice is related to aliasing artifacts present in Doppler-related techniques like VD, but also affects speckle tracking performance because this parameter is linked to the interleave region width and the achievable velocity resolution. The imaging setup is further optimized for each technique seperately due to their inherently different measurement nature.

Clutter filtering is an important aspect of 2D flow visualization, and can be particularly troublesome because both the magnitude and angle of the flow velocity vector estimate are influenced by the filtering. Although no vessel wall is present in this stage of the simulations, we incorporate the effect of clutter filtering on the flow estimates, assuming all clutter (surrounding tissue signal) is attenuated, and the same filter type is applied to both imaging methods.

To provide an intuitive overview of the flow estimator performance, we make vector plots of the estimated velocities and compare them to the CFD velocity vectors. The results of the carotid scans are further analyzed based on a linear regression analysis, plotting the estimated velocities from every frame and spatial sampling point versus their corresponding reference CFD velocity. With a temporal analysis of the mean absolute deviation between estimated and reference velocity, we demonstrate that the accuracy of the imaging method is related to the cardiac phase. We conclude that based on both the tube and carotid study, ST is the better lateral flow velocity estimator and VD the better axial flow velocity estimator, with ST more sensitive to vessel position and angle, and VD more robust in the presence of degraded signal-to-noise levels. Both ST and VD are able to resolve complex blood flow, but due to practical limitations for VD regarding aliasing and scanning flexibility, ST appears a more practical approach.

Chapter 8 - 2D flow imaging in the carotid bifurcation using a combined speckle tracking and phase-shift estimator based on ultrasound simulations and in-vivo analysis

The previous chapter demonstrated that ST is superior in measuring lateral flow velocity and VD better in detecting axial flow velocity, and

hence the natural result of this study is to propose a new flow velocity estimator combining the best of both worlds: ST for measuring lateral flow (v_x) and the autocorrelation technique (phase-shift estimator=PE) for measuring the axial flow velocity component (v_z). However, combining ST and PE flow estimation is not as straightforward as it seems due to their different measurement nature. A common acquisition scheme should be found ensuring good tracking results and at the same time avoiding aliasing, which is a challenging task.

First, the combined flow estimator is analyzed with CFD-based ultrasound simulations and three different combinations are investigated: (i) v_x from ST and v_z from PE, (ii) v_x from ST and v_z from PE but corrected for aliasing artifacts based on v_z from ST, and (iii) using v_z from PE to simplify the ST-algorithm so that it tracks lateral flow v_x only. This latter approach is further referred to as simplified ST, and is less computational expensive compared to full speckle tracking. The performance of these combined estimation approaches is compared to pure ST, for two imaging setups (varying PRF, as explained in the summary of chapter 7).

For two important cardiac phases (systole and diastole), the three combined estimator approaches and ST are compared to the CFD reference flow field using vectorplots. In particular, we zoom in on clinically relevant and imaging-wise challenging flow features, like swirling flow and the high flow velocities present in the external carotid artery. Based on a linear regression analysis, we show that the robustness of 2D flow imaging increases by using PE for measuring axial flow. This becomes clearer when analyzing simulations with decreased signal-to-noise levels. The simplified ST is slightly degraded compared to the other combination approaches, but shows potential for real-time implementation due to its reduced computational cost.

As for flow imaging with ST and VD, the mutual performance of the flow estimators is highly dependent on the cardiac phase, which we demonstrate with a temporal analysis of the mean absolute deviation between the estimated axial velocity and the CFD reference, focusing on two important imaging zones, i.e. the common and external carotid artery. Finally, we support our simulation results with in-vivo data recorded in the carotid artery of a healthy volunteer. In first instance, the feasibility of the proposed flow estimators is judged by superimposing vectorplots on the recorded color flow images. Reasonable results

are obtained, in line with expected flow patterns in healthy carotid bifurcations. Further, a link between the results from the simulations and the in-vivo analysis is made by comparing the imaging techniques with each other. For this purpose, the estimated flow angle is analyzed in parts of the carotid artery where flow is expected to be aligned with the axis of the vessel geometry. It can be concluded that in-vivo application of ST and the combined estimators is feasible for the recorded carotid dataset.

Part IV - Integrating fluid-structure interaction and ultrasound simulations

Chapter 9 - A simulation environment for validating ultrasonic blood flow and vessel wall imaging based on FSI-simulations: ultrasonic assessment of arterial distension and wall shear rate

In this chapter, we present the latest development in our multidisciplinary simulation environment, which allows to simulate not only synthetic ultrasound images of blood flow but also of the vessel wall. To obtain realistic images of both the hemodynamics and vessel wall mechanics, fluid-structure interaction (FSI) simulations are integrated with the Field II model. The FSI-simulations are performed with an in-house code (Tango), which strongly couples the flow solver Fluent and the structural solver Abaqus with an interface quasi-Newton technique.

Coupling the flow field and structural displacements from the FSI-results is not straightforward, and can not be considered as a simple extension of the CFD-Field II coupling. As the fluid volume is now changing during the ultrasound simulations, a continuous movement of the scatterer ensemble should be obtained during the simulated scan procedure. Therefore, we provide an elaborate methodology and illustration on creating fluid scatterer phantoms based on FSI. When coupling the FSI-results of the structural domain to the Field II model, a refined approach should be followed as well, which creates scatterers in each grid cell of the structural computation, so that changes in material properties, and hence ultrasonic scattering properties, can be accounted for. Again, we give extensive details on the creation of the structural scatterer phantom.

As the concept of coupling FSI with Field II ultrasound simulations is

complex in itself, we choose for a relatively simple vascular geometry to illustrate our methodology, i.e. a 3D straight tube representative of the common carotid artery. We apply a mass flow inlet boundary condition at the tube inlet, based on flow measured in a healthy subject. A downstream pressure condition, based on a non-invasively measured pressure waveform, is chosen and scaled to simulate three different degrees of arterial distension. The resulting hemodynamics and vessel wall mechanics in such a setup are still relatively straightforward to interpret, which enhances the validation of our simulation environment.

The RF-data resulting from the FSI-Field II coupling are further processed to investigate two clinically relevant imaging applications of arterial function related to both vessel wall deformation and arterial hemodynamics: arterial distension (related to arterial stiffness) and wall shear rate (a stimulus of endothelial function and associated with the development of atherosclerosis). Using an available wall tracking algorithm, arterial distensibility is assessed. Using an autocorrelation estimator, blood velocity and shear rate are obtained along a scanline.

In general, we obtain very good agreement between the flow and distension as obtained from the FSI-US model and the reference FSI values. The distension application reveals a high sensitivity of distension measurements to the measurement location, previously reported based on in-vivo data. We further demonstrate that strong reflections between tissue transitions can potentially cloud a correct measurement.

The shear rate study reveals that maximum shear rate assessed with ultrasound is underestimated for the given simulation setup. Moreover, maximal shear rate is obtained at a distance from the wall, as can be expected because of the difficulty ultrasound has in measuring near-wall velocities. However, we also demonstrate that ultrasound shear rates correlate well with the FSI ground truth for all distension degrees, which suggests that correction of the severe underestimation by ultrasound might be feasible in certain flow conditions.

PART V - CONCLUSIONS

Chapter 10 - Conclusions

In this chapter, some general conclusions are formulated. We conclude that we have developed a versatile tool for validation and improvement

of ultrasonic diagnosis of vascular disease. Perspectives for future research include expanding the simulation environment to vascular research in mice and cardiac imaging, and towards advanced imaging techniques like contrast-enhanced imaging, harmonic imaging or intravascular ultrasound. Another important focus for the future is clinical validation of the investigated imaging modalities.

Contents

List of Figures

List of Tables

Introduction

Introduction

Framework

Early detection of cardiovascular disease is essential in decreasing its death toll and health care expenses. The main cause of cardiovascular disease is *atherosclerosis*, a thickening and hardening of the arterial wall, due to an accumulation of fatty deposits in the vessel wall (e.g. lipids) and formation of a fibrous cap. Advanced atherosclerosis is associated with focal arterial lesions, which may lead to vessel-narrowing *plaques*. These frequently observed atherosclerotic manifestations are associated with a high morbidity and mortality because they may rupture, depending on the vulnerability of the lesion. Plaque rupture may block blood flow to vital organs, like the brain (stroke) or heart (cardiac infarction). To improve early detection, it is important to know how preliminary stages of atherosclerosis reveal themselves. Previous research has demonstrated that atherosclerosis is associated with changes of both the vessel wall mechanics and hemodynamics.

In the context of impaired vessel wall mechanics, increased arterial stiffness has been proven to be an early marker of cardiovascular disease [1]. Non-invasive estimation of arterial stiffness has drawn much research attention. A common method to assess arterial stiffness is by measurement of pulse wave velocity (PWV), i.e. the velocity with which the arterial pressure and flow waves travel through the cardiovascular system, and which is a global measure of arterial stiffness. Several techniques, like ultrasound [2], laser-Doppler [3] and tonometry [4], have tried to effectively measure PWV, but the techniques are still mainly applied for research purposes. Another useful manner to measure affected mechanical properties is via arterial wall distension. Ultrasonic techniques have been successfully developed to assess vessel diameter distension during the cardiac cycle by estimating the tissue velocity [5]. However, also this application has not found its way

yet to clinical practice. Furthermore, neither PWV, nor vessel wall distension, allow non-invasive measurement of the true mechanical properties of the vascular wall.

Atherosclerosis is also associated with certain hemodynamical aspects. For instance, low and oscillatory wall shear stress, i.e. the tangential force exerted by the blood flow on the endothelial cells of the vessel wall, has been shown to be an important mechanical stimulus of endothelial function and hence a potential contributor to a pro-atherogeneric environment [6]. Ultrasonic imaging methods of wall shear stress have been proposed [7, 8], but further research is required before clinical implementation. In addition, complex 3D flow patterns are present in the cardiovascular system, particularly in the vicinity of atherosclerotic lesions like stenotic plaques. However, clinical practice still relies on ultrasonic flow imaging techniques in one dimension, based on Doppler-related effects. Multidimensional flow visualization has been an important research topic for years in the ultrasound community, but no robust technique has resulted yet.

To visualize zones of disturbed blood flow and vessel wall deformation, ultrasonic echography is still an interesting and relevant tool, as the technique is:

- Non-invasive
- Radiation-free
- Low-cost compared to other imaging methods like CT and MRI
- Widely available to the cardiologist and vascular specialists

Ultrasound is commonly applied in clinical practice, with current cardiovascular imaging modalities allowing to visualize both structural and morphological information of the cardiovascular system, as well as to assess blood flow velocities and cardiac tissue velocities and strains. Ultrasound is a highly valuable technique in this context as it can achieve the high frame rates necessary to capture the dynamics of cardiovascular function. However, for economical reasons, ultrasonic imaging research has focused to a large extent on cardiac applications, and therefore, the vascular imaging tools are lagging behind. Hence, this manuscript should also be situated in this context, as many clinically relevant imaging applications for blood vessels have been insufficiently explored.

Given also the rapidly growing interest in arterial dysfunction as an early phenotype of atherosclerosis and prognostic marker, developing ultrasonic imaging tools for blood vessels becomes more and more a topic of interest.

Especially in the framework of early detection of cardiovascular disease, vascular imaging plays an important role, as some arterial locations, like the carotid artery, are prone to atherosclerosis. Consequently, this arterial site is of high importance when developing new vascular imaging methods, as it further has the advantage that it is easily accessible with ultrasound. Furthermore, it provides the brain of blood flow, and hence is also an essential location to screen for a potential risk of stroke. Finally, the carotid artery is a large elastic vessel of which the behaviour is thought to go hand in hand with the aorta. Therefore, the multidisciplinary ultrasound simulation environment developed in this dissertation will focus on imaging applications for the carotid artery. However, the applied methodology can be easily expanded to other arterial sites if desired.

Background of medical ultrasound imaging

Diagnostic ultrasound imaging is based on the *pulse-echo imaging* principle: pressure pulses are emitted with an ultrasonic frequency, i.e. above the audible range (> 20kHz), and reflect when changes in acoustic impedance of the imaged medium are met. Emission and reception of the pressure pulses is performed by a transducer made of piezoelectric material, which allows to convert electrical to acoustical energy and vice versa. The backscattered signal received by the transducer is then further processed to visualize and characterize the imaged tissue.

The roots of medical ultrasound are found in the world of *sonar* (sound navigation and ranging), a terminology grouping all the pulse-echo detection methods based on sound waves. The most common application of sonar is underwater detection, as used by submarines, and the technique was first explored after the sinking of the Titanic to find a method to detect icebergs (1913, [9]). However, the principle has existed over millions of years as several animals emit sounds to probe their surroundings. One of the most well known examples are dolphins, which locate their prey by emitting sounds, since the underwater environment they live in provides very poor visibility (cfr. fig. 1).

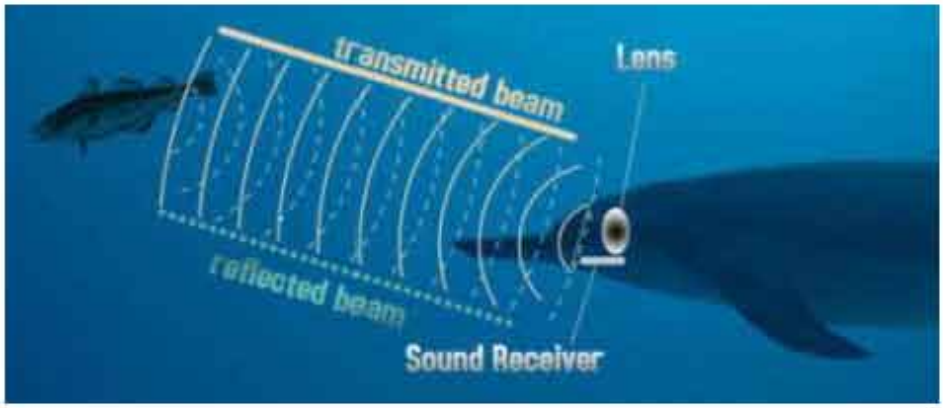

FIGURE 1: The pulse-echo imaging used in diagnostic ultrasound is related to the natural sonar performed by dolphins. To probe the underwater environment, acoustic waves are emitted which reflect on the surrounding objects. Source:www.scienceinthenews.org.uk

Another domain related to medical ultrasound is *radar* (radio detection and ranging), which performs pulse-echo imaging based on electromagnetic waves, and is used to locate aircrafts, ships, motor vehicles, etc... However, most people know radar as the technique used in speed cameras to detect speeding cars by registering the Doppler frequency shift of the reflected electromagnetic wave.

The developments in the sonar and radar technology in the first half of the 20^{th} century inspired scientists to apply the pulse-echo imaging principle in the human body. The first attempts to image the human body were made in the late 1940's [10]. But the feasibility of medical ultrasound was only established by Ludwig in 1950 [11], who discovered that real-time ultrasonic imaging of the human body is possible due to some fortunate properties of ultrasonic wave propagation in soft tissue. Ludwig demonstrated that the ultrasonic wavespeed in different types of soft tissue is very similar. This makes it possible to reliably reconstruct the imaged tissue geometry, as the arrival time of the echo can then be related to the depth location it originated from. Although the wave speed and impedances of different types of soft tissue are relatively similar, the reflection coefficient is sensitive to small variations in acoustic impedance. Hence, different types of tissue can indeed be recognized on an ultrasound image.

In the early 1960's, the first commercial scanners for static grayscale

imaging of tissues and organs became available. However, improvements in several scientific domains were necessary to come to the diagnostic ultrasound scanners known today. Progress at the level of acoustics, piezo-electric materials, transducer design, electronics and its miniaturization, digital technology and statistical signal processing has played a crucial role.

The main aim of diagnostic ultrasound was initially to characterize tissue, and detect abnormalities like tumors and cysts [12, 13]. In parallel, the possibilities of ultrasound in detecting the heart motion were also explored [14]. Satomura [15] was the first to report the ultrasonic detection of movement based on the Doppler shift (1957), which was the basis of continuous and pulsed wave ultrasound systems to detect blood flow, and later also tissue velocities. From the 1960's on, probably the most well known application of medical ultrasound was investigated, i.e. obstetrics and fetal medicine. Many other applications of ultrasound in medicine have been developed over the past decades, and we refer to [16] for a complete overview.

Improving ultrasonic imaging for cardiovascular applications

Multidisciplinary simulation approach

Although the diagnostic ultrasound scanners from today are the result of numerous advances in several research areas, still many of the imaging goals are not fully achieved. Of note, vascular imaging applications show several limitations. Only 1D blood flow measurements are performed in clinical practice, visualizing the velocity component along the scanline. Blood flow assessments are further hampered by the presence of strong tissue signals in the vessel lumen (called clutter) due to ultrasound beam side lobes and reverberations. As for vascular wall mechanical applications, assessment of the mechanical properties has only been investigated to a very limited extent, with the arterial distension estimation the most successful application so far, but which has the disadvantage that it measures vessel kinematics rather than true vessel mechanics. Hence, improved imaging and post-processing methods are needed.

When developing new techniques, testing and validation play an important role. Imaging development based on in-vitro and in-vivo experimental settings does not allow proper validation of the ultrasound

images, since the imaged flow field and/or vessel wall deformation is not known. For this purpose, other measurement techniques, also prone to errors, are necessary to reveal the hemodynamics and vessel wall mechanics behind the ultrasound image. A simulation environment which allows to create synthetic ultrasound images based on arbitrary but fully known hemodynamics and vessel wall mechanics would be highly useful. However, it should be noted that simulations can not include all the physical phenomena involved in the image formation process, as is the case for in-vitro and in-vivo testing. As such, simulations which provide a gold standard in the validation procedure have an important complimentary role compared to in-vitro/in-vivo testing.

An important tool in this context is the *Field II* ultrasound simulation software developed by Jensen et al [17, 18]. This ultrasound simulator allows to model any linear imaging setup with advanced transducer geometries, scan sequencing and beam formation. The backscattered radiofrequent (RF) signals are obtained by modeling the tissue as a distribution of point scatterers on which the ultrasound waves reflect. Hence, realistic ultrasonic images of arbitrary flow fields and wall deformations can be simulated, by moving the scatterers during the simulated scan procedure according to realistic and complex 3D blood velocities and structural displacements.

However, this approach is not as straightforward as it seems. Because of the complex arterial geometries and vascular material properties, the scatterer movement can not be obtained through an analytical solution of the equations governing the blood flow and vascular wall behaviour. Complex numerical techniques are required for this purpose. When solely studying the blood flow in a rigid vessel model, numerical techniques for solving complex fluid dynamical problems, often lumped in the terminology *computational fluid dynamics* (CFD), can be applied. If a model of the integral blood vessel behaviour is desired, a *fluid-structure interaction* (FSI) problem should be solved. Indeed, the blood flow field influences the vessel wall deformation and, the other way round, the structural behaviour influences the hemodynamics. Hence, the required numerical approach becomes even more complex, as an equilibrium solution to a coupled fluid-structure interaction problem should be found.

As can be deduced from the previous paragraph, an ultrasound simulation environment for improvement of cardiovascular imaging is in fact a *multiphysical simulation tool.* First of all, thorough knowledge on the ultrasound image formation and ultrasound simulation approaches should be acquired. For this purpose, the research presented in this dissertation was performed in close collaboration with the department of Circulation and Medical Imaging at the NTNU in Norway (Prof. Hans Torp and Dr. Lasse Lovstakken). Furthermore, know-how on the numerical modeling of blood vessels is required, both at the level of fluid dynamics and tissue mechanics, with both competences present within Ghent University (IBiTech-bioMMeda and research group of Prof. Jan Vierendeels).

Developing the simulation environment

Building on the acquired knowledge in the domains of ultrasonic imaging and numerical modeling of fluid and structural mechanics, the multiphysical simulation environment was developed. In a first stage, complex 3D velocity fields were simulated in a realistic patient-specific geometry of a carotid artery using computational fluid dynamics (CFD), which were subsequently coupled to Field II. This could be achieved by temporal and spatial interpolation of the CFD flow field. The resulting model is a versatile tool in validating and developing flow imaging modalities.

In a second phase, the ultrasound signal from the vessel wall was included by integrating fluid-structure interaction simulations with the ultrasound simulator. This, however, did not entail a straightforward expansion of the previously developed coupling between CFD and Field II. Both the scatterer phantom for the blood pool and vessel wall required a more advanced approach. The fluid scatterer phantom in particular was highly challenging as straightforward interpolation techniques were no longer applicable due to the changing fluid volume and FSI grid formulation.

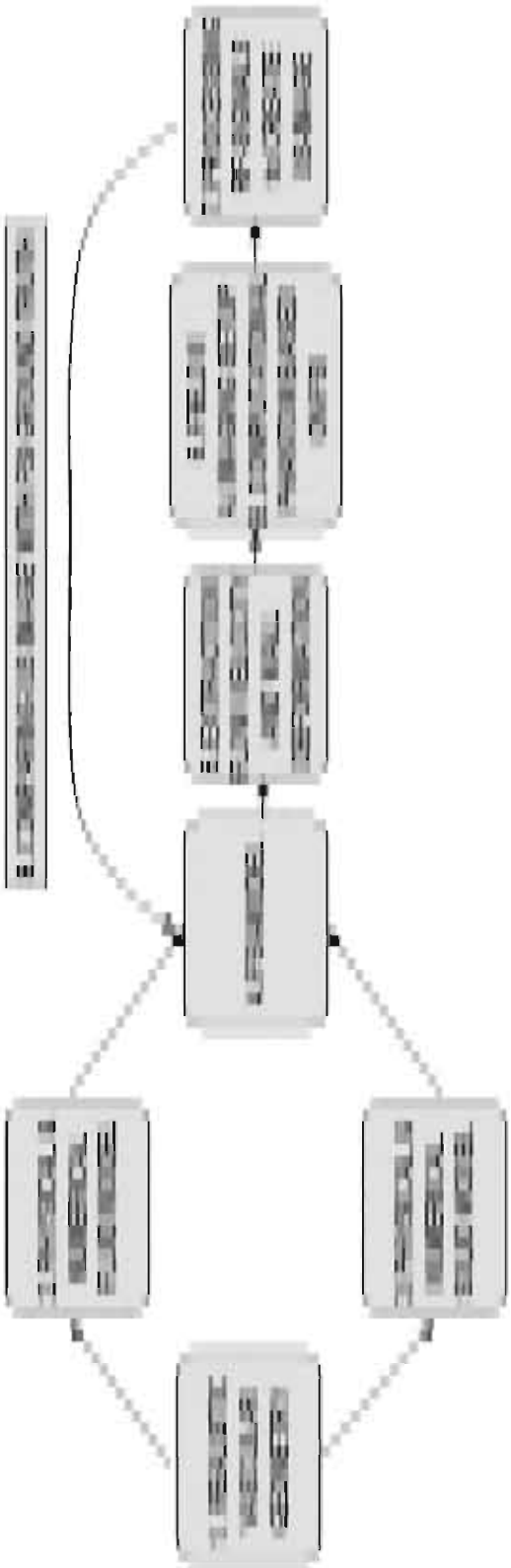

Figure 2: A flowchart illustrating the methodology of the ultrasound simulation environment.

The scatterers of the structural phantom were created for each computational grid cell seperately, to account for changes in material properties, and hence ultrasonic scattering properties. Further, specular reflections between tissue transitions are present in real ultrasound images, which were appropriately mimicked in Field II. Given the complexity of the methodology to couple FSI and ultrasound, it was first applied to a straight 3D tube representative of the common carotid artery.

Overview methodology

The flowchart in fig. 2 gives an overview of the multiphysics simulation approach, in the case of coupling FSI and ultrasound simulations:

1. A reliable vascular geometry and mesh are created, e.g. using 3D-reconstruction of medical scans.
2. A blood flow model is chosen, which entails determining the viscosity, density, etc... Further, the boundary conditions at the in- and outlets of the fluid domain should be correctly applied (e.g. a pressure signal, flow signal, impedance).
3. The vessel wall model is chosen, including, amongst others, material properties and boundary conditions at the extremes and outer boundary of the vessel wall.
4. Besides deciding on the physical models for the flow and structural domain, the parameters determining the numerical schemes for the flow, structural and FSI-calculation should be carefully chosen.
5. The desired imaging setup is defined/programmed in Matlab, which is the interface through which the Field II program can be accessed.
6. Based on the FSI-simulations, blood velocities and mechanical deformations are extracted, which are used as an input to the construction of the scatterer phantom. During the simulated scan procedure, the location and velocities of the scatterers in the computational phantom are updated according to the FSI-results.

7. The output of the ultrasound simulations, i.e. the backscattered RF-signals, are further processed according to the imaging technique of interest.

8. The synthetic ultrasound image can be directly compared to the true flow and arterial wall behaviour behind the image, as obtained from the FSI-simulations.

Imaging applications

Although an important part of this dissertation deals with developing the multidisciplinary methodology behind the simulation environment, probably the most interesting part of this work is the application to clinically relevant imaging techniques. Furthermore, comparison of simulated images with in-vitro and in-vivo data might further demonstrate the clinical relevance of our developed methodology, and serves to a certain extent as validation of the methodology.

In first instance, our CFD-Field II approach was illustrated through examples of commonly applied flow estimators: color flow imaging and pulsed wave Doppler. Simulated results were compared with the CFD ground truth, and the realism of the images was also assessed through comparison with data from an in-vitro carotid artery setup. Although the performance and usefulness of our simulation environment was demonstrated, the investigated flow estimators were still limited by the 1D nature of the measurement and aliasing.

In an attempt to overcome these limitations, multidimensional flow visualization was extensively investigated, studying two approaches currently examined in several ultrasound departments: *speckle tracking* and crossed-beam *vector Doppler*. The former tracks velocities in 2D by correlating subsequently acquired speckle images. The latter is the extension of the 1D Doppler techniques, by simultaneously receiving Doppler signals along two different directions. As our results indicated that speckle tracking is superior in measuring velocities *perpendicular* to the scanline, and vector Doppler performs better in estimating flow *parallel* to the scanline, we proposed and investigated a 2D flow estimator, which combines the best of both worlds. In this study, we also demonstrated the feasibility of 2D flow estimation in an in-vivo carotid setting.

In the final section of this dissertation, we used our full FSI-Field II model to assess two clinically relevant imaging applications, related to the blood flow and vessel wall: wall shear rate and arterial distension imaging. We chose these applications as they are particularly sensitive to and depending on fluid-structure interaction. The applications were investigated on a model configuration representative for the straight common carotid artery segment.

Structure

This manuscript is built up according to the previously discussed steps necessary to create and apply a multidisciplinary ultrasound simulation environment, and is therefore divided in four parts.

In a first part, a thorough background is offered on the multidisciplinary knowledge required to perform this work. The physics behind ultrasonic image formation are explained before going deeper into ultrasonic velocity estimators and ultrasonic simulation approaches. This background part is concluded with a chapter on numerical modeling of blood vessels, providing a brief overview on computational fluid and structure mechanics, as well as numerical algorithms applied in fluid-structure interaction simulations.

In the following parts, the actual research results of this dissertation are presented, based on accepted and submitted peer-reviewed papers (an overview is given in the next section). Part II provides a thorough overview of the methodology to couple CFD and Field II ultrasound simulations, and validation is provided through comparison of simulated color flow and pulsed wave Doppler images with the true flow field. In a next chapter, this quite advanced approach is compared to simpler simulation strategies, like projection of the CFD flow field along the scanline. Furthermore, results from our CFD-Field II simulation tool are compared to ultrasonic images acquired in an in-vitro carotid artery setup.

The third part of this manuscript deals with applications of the simulation environment for the validation and development of multidimensional flow visualization. Two important 2D flow estimators, speckle tracking and vector Doppler, are studied and compared to each other. Based on the obtained results, a 2D flow estimator combining the best

of both imaging techniques is proposed in a next chapter, and feasibility of the technique is demonstrated both through simulations and in-vivo data.

The final part elaborates on the complex and advanced simulation approach integrating fluid-structure interaction simulations and Field II. The potential of this new simulation strategy is exemplified with two clinically relevant imaging techniques requiring the presence of the moving vessel wall: wall shear rate and arterial distension imaging.

LIST OF PUBLICATIONS

First author peer-reviewed journals

- Abigail Swillens, Patrick Segers, Hans Torp, Lasse Lovstakken. Two-dimensional blood velocity estimation with ultrasound: speckle tracking versus crossed-beam vector Doppler based on flow simulations in a carotid bifurcation model. IEEE Transactions on Ultrasonics Ferroelectrics and Frequency Control. vol. 57, no. 2, p. 327-339, 2010

- Abigail Swillens, Thomas De Schryver, Lasse Lovstakken, Hans Torp, Patrick Segers. Assessment of Numerical Simulation Strategies for Ultrasonic Color Blood Flow Imaging, Based on a Computer and Experimental Model of the Carotid Artery. Annals of Biomedical Engineering. vol. 37, p. 2188-2199, 2009

- Abigail Swillens, Lasse Lovstakken, Jan Kips, Hans Torp, Patrick Segers. Ultrasound Simulation of Complex Flow Velocity Fields Based on Computational Fluid Dynamics. IEEE Transactions on Ultrasonics Ferroelectrics and Frequency Control. vol. 56, p. 546-556, 2009.

- Abigail Swillens, Lieve Lanoye, Julie De Backer, N Stergiopulos, Pascal Verdonck, Frank Vermassen, Patrick Segers. Effect of an abdominal aortic aneurysm on wave reflection in the aorta. IEEE Transactions on Biomedical Engineering. vol. 55, p. 1602-1611, 2008

Submitted for publication

- Abigail Swillens, Patrick Segers, Lasse Lovstakken. Two-dimensional flow imaging in the carotid bifurcation using a combined speckle tracking and phase-shift estimator: a study based on ultrasound simulations and in-vivo analysis. Ultrasound in Medicine and Biology

- Abigail Swillens, Joris Degroote, Jan Vierendeels, Lasse Lovstakken, Patrick Segers. A simulation environment for validating ultrasonic blood flow and vessel wall imaging based on fluid-structure interaction simulations: ultrasonic assessment of arterial distension and wall shear rate. Medical Physics

Co-author peer-reviewed journals

- Håvard Nordgaard, Abigail Swillens, Dag Nordhaug, Idar Kirkeby-Garstad, Denis Van Loo, Nicola Vitale, Patrick Segers, Rune Haaverstad, Lasse Løvstakken. Impact of competitive flow on wall shear stress in coronary surgery: Computational fluid dynamics of a LIMA-LAD anastomosis in a porcine model. Cardiovascular Research. In press.

- Joris Degroote, Abigail Swillens, Peter Bruggeman, Robby Haelterman, Patrick Segers, and Jan Vierendeels. Simulation of fluid-structure interaction with the interface artificial compressibility method. International journal for numerical methods in biomedical engineering, vol.26, no.3-4, p.276-289, 2010.

- Bram Trachet, Abigail Swillens, Denis Van Loo, Christophe Casteleyn, Anne De Paepe, Bart Loeys, Patrick Segers. The influence of aortic dimensions on calculated wall shear stress in the mouse aortic arch. Computer methods in Biomechanics and Biomedical Engineering, vol.12, no.5, p.491-499, 2009

- Julio Chirinos, Patrick Segers, A. Raina, H. Saif, Abigail Swillens, Amit Gupta, Raymond Townsend, A. Emmi, James Kirkpatrick, Martin Keane, Victor Ferrari, Susan Wiegers, Martin St John Sutton. Arterial pulsatile hemodynamic load induced by isometric exercise strongly predicts left ventricular mass in hypertension. Am J Physiol Heart Circ Physiol., vol. 298, no.2, H320-30, 2009

- Julio Chirinos, Patrick Segers, Amit Gupta, Abigail Swillens, Ernst Rietzschel, Marc De Buyzere, James Kirkpatrick, Thierry Gillebert, Yan Wang, Martin Keane, Raymond Townsend, Victor Ferrari, Susan Wiegers, Martin St John Sutton. Time-Varying Myocardial Stress and Systolic Pressure-Stress Relationship. Role in Myocardial-Arterial Coupling in Hypertension. Circulation. vol. 119, p. 2798-2807, 2009

- Bram Trachet, Philippe Reymond, Jan Kips, Abigail Swillens, Marc De Buyzere, Bert Suys, Nikos Stergiopulos, Patrick Segers. Numerical validation of a new method to assess aortic pulse wave velocity from a single brachial artery recording. Annals of Biomedical Engineering. DOI:10.1007/s10439-010-9945-1

One

Background

CHAPTER 1

Fundamentals of medical ultrasound imaging

1.1 Introduction

In this chapter, we will give an overview of the image formation process performed by conventional medical ultrasound scanners. Typically, the image formation is based on *pulse-echo imaging*. This means that an ultrasonic probe, also called a transducer, excites ultrasonic pulses, which travel through the imaged medium and reflect/scatter when changes in acoustic impedance are met. The backscattered signals are received by the transducer, and further processed to image and characterize the imaged medium.

This chapter deals step by step with the physics and technology involved to obtain high-quality ultrasound images. First, the physics of the ultrasound wave propagation will be explained. More particularly, we will discuss the scattering and reflection processes occuring in the imaged medium, which create the backscattered signal received by the transducer. Next, the technology responsible for the excitation and receive process of the ultrasound signals will be clarified. Transducer design and ultrasonic beam formation are the main focus here. Further, commonly applied scan acquisition schemes will be investigated, an

important part of the imaging setup, as they may greatly affect the accuracy of ultrasonic flow imaging methods, as discussed in part II and III of this dissertation. Finally, different types of ultrasonic imaging systems are discussed, i.e. conventional imaging methods like gray scale imaging and one-dimensional (1D) flow assessment. Also, more advanced techniques, like harmonic imaging and shear wave imaging, will be briefly discussed.

We would like to stress that the following text is inspired on several textbooks on ultrasound, and the most important sources are the *Doppler Ultrasound* book of *Evans and McDicken* [19], the *Foundations on Biomedical Ultrasound* of *Cobbold* [20], the *Diagnostic Ultrasound* book of *Shung* [21], the *Diagnostic Ultrasound Imaging book* of *Szabo*[22], *Estimation of blood velocities using ultrasound* of *Jensen* [23], and *Ultrasound Imaging: Waves, Signals, and Signal Processing* of *Angelsen*[24].

1.2 THE FUNDAMENTAL PHYSICS OF DIAGNOSTIC ULTRASOUND

1.2.1 Propagation of ultrasound waves

Ultrasonic waves are in general acoustic waves with a frequency above the audible range (> 20 kHz), which cause mechanical stresses and vibrations in matter. When a stress is applied normal to the material surface, a *longitudinal pressure wave* is excited, i.e. the oscillatory motion of the particles in the medium is parallel to the wave propagation direction. As shown in panel (a) of fig. 1.1, the passage of longitudinal waves creates zones of compression and rarefaction, propagating with a speed depending on the medium properties. In case of a solid medium, shear waves may also be supported, i.e. the oscillatory motion of the particles in the medium is perpendicular to the wave propagation direction. Panel (b) in fig. 1.1 demonstrates the concept of shear wave propagation, showing that in contrast to longitudinal waves, no density changes occur. The ultrasound imaging applications currently used in clinical practice are based on longitudinal waves because the shear waves at diagnostic imaging frequencies vanish very quickly.

The speed c with which the longitudinal waves propagate is related to the compressibility κ and density ρ of the medium:

$$c = \sqrt{\frac{1}{\rho\kappa}} = \sqrt{\frac{K}{\rho}} \tag{1.1}$$

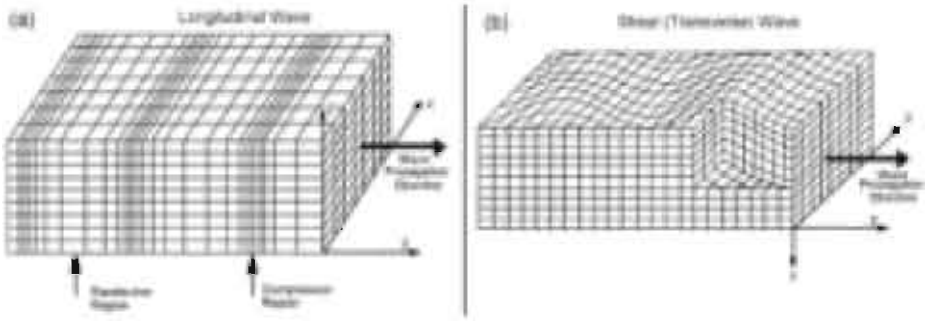

FIGURE 1.1: Panel (a) shows the propagation of longitudinal waves, giving rise to rarefaction and compression zones. Panel (b) shows the concept of shear wave propagation. This figure was adapted from [20].

This equation is often expressed as a function of the bulk modulus K, which is proportional to the inverse of the compressibility. Equation 1.1 shows that a less compressible medium has a higher wave speed. Most soft tissues in the human body have a wave speed clustered around 1540 m/s, and this value is assumed on most modern ultrasound scanners. In case of blood imaging, the density ρ is approximately 1055 kg/m^3 and the adiabatic compressibility κ is 0.38/GPa.

Image degradation may occur if the sound speed in certain regions is too much differing from 1540 m/s, with improper focusing of the ultrasound beam as a result (cfr. section 1.3.2.d), also called *phase aberration*. Bone is one of the structures which should be avoided in this sense, due to its very high wave speed of 3500 m/s. Frequency dependent changes in the wave speed (*dispersion*) can be neglected in the range of conventionally applied frequencies (1-20 MHz).

For shear waves, the wave speed is defined as:

$$c = \sqrt{\frac{\mu}{\rho}} \tag{1.2}$$

with μ the shear modulus, which relates the shear stress with the shear strain. Typically, the shear wave speed (a few meters per second) is much lower in soft tissues than the longitudinal wave speed.

1.2.1.a Non-linear acoustics

In case of non-linear propagation, the ultrasonic waves do not retain their shape as they pass through the material. As the wave speed is

dependent on the stiffness of the medium, and stiffness is usually dependent on pressure, the wave speed may change during the passage of an ultrasonic pressure wave. The wave speed is generally higher in the tissue portions affected by the positive parts of the pressure cycle, and is lower in the portions experiencing the negative pressures. For increasing depths in the tissue, the waveform is gradually more distorted, until a saw tooth shape (shock wave) is obtained in the case of a sinusoidal pressure wave (cfr. fig. 1.2). The high frequency components in the wave created by non-linear propagation are most persistent in non-attenuating media like water (cfr. section 1.2.3).

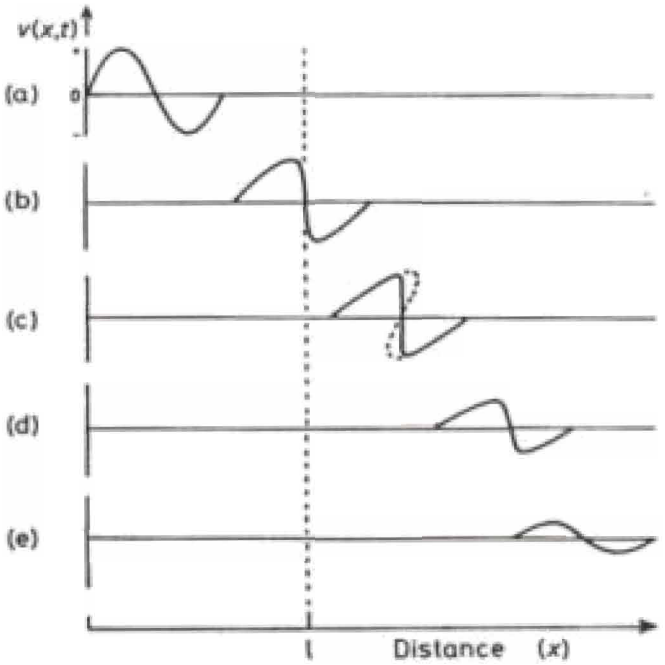

Figure 1.2: Because of non-linear effects, the waveform changes throughout depth. This figure was adapted from [19].

Most modern ultrasound scanners use an ultrasonic pressure *pulse* (cfr. section 1.3.1) excited by a *transducer* (cfr. section 1.3.2) to image the tissue. Increased power and higher frequencies of this ultrasonic excitation pulse favour non-linear propagation. Besides a pulsed excitation, some imaging applications are based on a continuous wave excitation, which implies that these devices are less susceptible to non-linear effects since they generally use pressure waves with a lower amplitude.

1.2.2 Scattering

The energy of the ultrasonic vibrations scatters with changes in acoustic impedance of the medium, or more specifically with changes in density or compressibility. The scattering process is crucial since it is the information contained in the backscattered waves, i.e. the amplitude, phase and frequency content, which is used during the imaging process.

Different kinds of scattering exist. *Specular reflections* occur when the dimensions of the reflecting object are much larger than the ultrasonic wavelength (typically a few 100 μm). Vessel walls and bones are common structures causing specular reflection. The pressure amplitudes of the reflected and transmitted wave can be described using reflection (R) and transmission (T) coefficients. These coefficients are written as a function of the impedances (Z) and angles (θ) of the incident (Z_i and θ_i) and transmitted waves (Z_t and θ_t). The acoustic impedance Z for a plane wave is the product of the medium density ρ and wave speed c: $Z = \rho c$.

$$R = \frac{Z_t cos(\theta_i) - Z_i cos(\theta_t)}{Z_t cos(\theta_i) + Z_i cos(\theta_t)} \tag{1.3}$$

$$T = \frac{2Z_t cos(\theta_i)}{Z_t cos(\theta_i) + Z_i cos(\theta_t)} \tag{1.4}$$

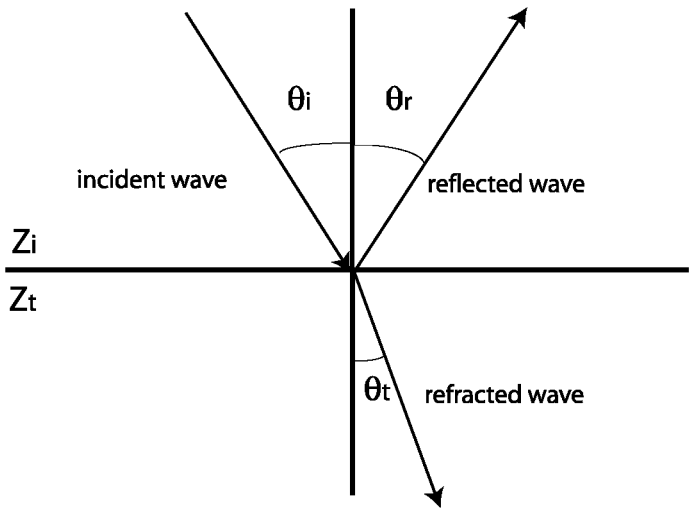

FIGURE 1.3: For objects much larger than the wavelength, specular reflection occurs and the beam further propagating is refracted.

This phenomenon is illustrated in fig. 1.3. In vascular flow imaging, these specular reflections are not desirable and mainly removed by clutter filtering (cfr. section 2.5).

A physical phenomenon related to the occurence of specular reflection is *refraction*. This is the deviation of a beam when it crosses a boundary between two media in which the sound speed is different. Blood vessels can often be imaged very clearly and refraction does not impose a severe problem. However, distortion of the ultrasonic beam can be expected to be significant for calcified vessel walls containing plaques. The intensity pattern is then disturbed and this adds to the velocity bias in case of ultrasonic flow measurements (cfr. chapter 2).

When an ultrasound wave is scattered by an inhomogeneity of dimensions smaller than the ultrasound wavelength, *diffusive scattering* occurs. The roughness features on the scattering object then fail to construct any significant interference pattern. This kind of scattering is the main contributor to a medical ultrasound image. The nature of the discontinuities in soft tissue is not known but is usually considered to be a random distribution of closely packed scattering centres.

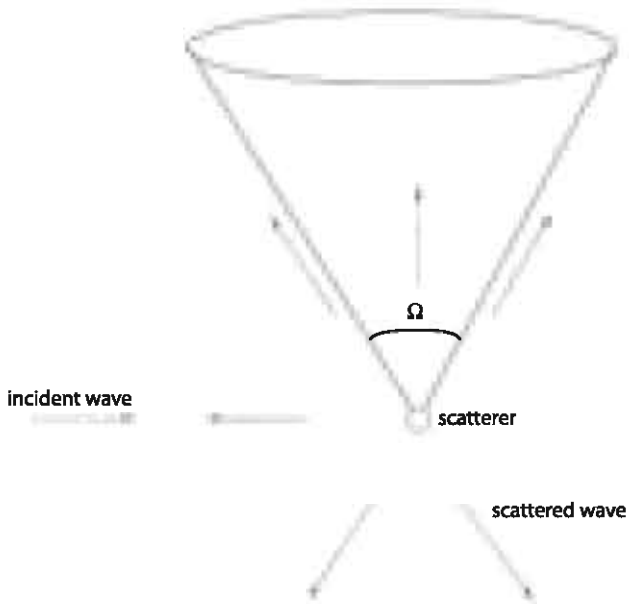

Figure 1.4: Illustration of the differential cross-section of a scatterer, which represents the power scattered into a steradian Ω. This figure was adapted from [21].

Diffusive scattering is generally described by a scattering cross-section, which is the ratio between the scattered power S and the incident intensity I. The differential cross-section is defined as:

$$\sigma(\Omega) = \frac{S(\Omega)}{I} \tag{1.5}$$

when one looks at the radiated power for a steradian (sr) Ω in a certain direction, and is expressed in cm^2/sr. This is illustrated in fig. 1.4. Particularly interesting is the backscatter cross-section, which is the differential cross-section at 180^o of the incident wave, and determines the intensity of the signal received by the transducer.

The last type of scattering is in between the first two categories, and is called *diffractive scattering*. The size of the scattering object is then comparable to the wavelength and ultrasound is scattered directionally.

1.2.2.a Scattering from blood

Blood consists of a plasma fluid containing red blood cells, white blood cells, and platelets. The red blood cells represent about 45 % of the blood volume in a healthy adult, while the white blood cells account for 0.8 % and the platelets for 0.2 %. Since the red blood cells are by far the most dominant particles in blood, the effect of the platelets and the white blood cells on the backscattering can be ignored. The red blood cells are biconcave discs with an approximate thickness of 2 μm and diameter of 7 μm. The frequencies used in diagnostic ultrasound range from 2-15 MHz for human applications. Hence, the wavelength (range 0.77-0.1 mm) is much larger than the dimensions of the red blood cells, causing diffusive scattering.

In particular, *Rayleigh scattering* occurs, which means that the scattered intensity has a fourth power dependence on frequency. Hence, using higher pulse frequencies for imaging, results in stronger reflections from blood compared to the surrounding tissue. Because of this frequency dependence, the centre frequency of the backscattered signal is higher than the emitted centre frequency, which could in principle cause an overestimation of the Doppler velocities (cfr. section 2.1.2), with augmenting impact for larger bandwidths of the emitted ultrasound pulse. This phenomenon is however mainly compensated by attenuation (see section 1.2.3).

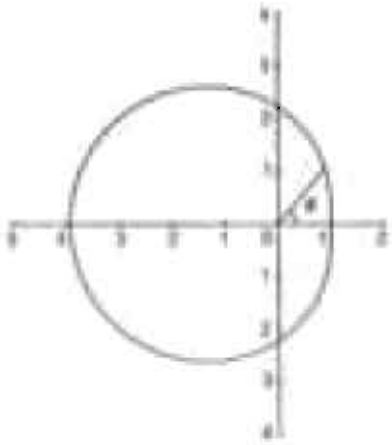

FIGURE 1.5: The angular scattering distribution of blood, represented by a polar diagram of the normalized scattered power (dB) as a function of the scattering angle ϕ. This figure was adapted from [19].

The angular distribution of scattering in blood is asymmetric, with the backscattered cross-section almost 6dB larger than at forward angles. Fig. 1.5 illustrates the normalized scattered power (dB) in a polar diagram, as a function of the scattering angle ϕ. It is visible that the scattered power is minimal for a forward scattering angle ϕ of zero degrees, and is maximal for a backscattered angle ϕ of 180 degrees. The scattering is weak and it is thus safe to neglect multiple scattering.

The signal received from blood can be considered as a Gaussian random process, due to the contribution of numerous independent particles. However, it should be noted that for realistic hematocrit values (45 %), the locations of the red blood cells are correlated, as the distance between two neighbouring red blood cells is only 10 % of their diameter. The flow situation may also give rise to correlated scattering. For slow flow and small shear rates, the red blood cells clot into stacks, called 'rouleaux', which influences the backscattering. Turbulence is another flow condition affecting the scattering process, causing an increase in ultrasound backscatter [25].

1.2.3 Attenuation

An ultrasonic wave propagating through a heterogeneous medium loses energy, or is attenuated as a function of depth z and frequency f:

$$p(z) = p(z = 0)exp(-\alpha f z) \tag{1.6}$$

P is the pressure of a plane monochromatic wave propagating in the Z-direction, and decreasing exponentially as a function of the distance z; α is the attenuation coefficient in dB/(MHz cm). The fact that the amplitude of the backscattered signal decreases with increasing depth can be compensated in the receiving amplifier of the ultrasound transducer (cfr. section 1.3.2), using time gain compensation or TGC.

The most important mechanism behind attenuation is probably *absorption*: the conversion of wave motion energy into heat. The absorption mechanisms in biological tissues are quite complex and are assumed to arise from (1) the viscosity of the medium and (2) most importantly relaxation phenomena. Relaxation refers to the time a particle needs to return to its original position after it has been pushed to a new position by the passage of a wave. Depending on the length of the relaxation time compared to the period of the wave, the stress imposed by the wave is relaxed by a flow of energy to internal molecular energy (thermal relaxation) or changed structural states. Both absorption phenomena depend on the frequency of the wave. Several other mechanisms also contribute to attenuation. The previously mentioned scattering, reflection and refraction are of importance, as well as nonlinear propagation and ultrasonic beam divergence.

The contribution of scattering to attenuation is most often reported to be below 10%, but this is dependent on the nature of the tissue and the frequency of the wave. Scattering increases with the percentage of fat and collagen, but decreases with the water content. The attenuation in blood is low, approximately 0.2 dB/(MHz cm).

Experimental results show a linear dependence of the attenuation coefficient α on frequency in biological tissues for transducer frequencies below 15 MHz. Consequently, the high frequency components of an ultrasonic pulse will be more reduced in amplitude compared to the low frequency components. As such, the centre frequency of the backscattered signal is decreased compared to the emitted centre frequency. This can lead to an underestimation of the Doppler signal (cfr. section 2.1.2), with increasing impact for depth, higher frequencies and bandwidth of the emitted waves.

The choice of the transducer frequency is influenced by attenuation because the attenuation coefficient is related to the maximal penetration depth of the signal. Superficial structures, like the carotid artery,

can be examined with 7-12 MHz probes while deeper structures like the heart require a lower frequency (2-5 MHz).

1.3 BASIC IMAGING PRINCIPLES

1.3.1 Pulse-echo imaging

Conventional diagnostic ultrasound uses pulse-echo imaging. A transducer (cfr. section 1.3.2) excites a pulsed ultrasonic pressure field, which propagates through the imaged medium, and reflects/scatters when changes in acoustic impedance are met (cfr. section 1.2.2). The signal backscattered to the receiving transducer is a radio-frequent signal (RF-signal), denoting its frequency information is in the frequency bands used for radio communication. With appropriate postprocessing of the RF-signal, imaging and characterization of the insonified tissue is possible. For this purpose, the RF-signal received at a time instance t should be related to the depth d from which the backscattered signal originated, through the following relation:

$$d = \frac{ct}{2} \tag{1.7}$$

with c the ultrasound wave speed, and the factor 2 refers to the fact that the pulse has to travel back and forth from the transducer. Because the ultrasound wave speed in tissue is high (1540 m/s), backscattered signals are received very quickly, which makes real time ultrasonic imaging feasible. The principle of pulse-echo imaging is illustrated in fig. 1.6.

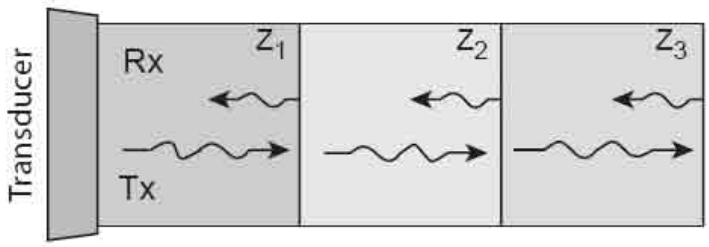

FIGURE 1.6: A transducer emits ultrasound pulses which are scattered when changes in acoustic impedance are met (Z_i). The backscattered signal is received by the transducer and its amplitude, frequency or phase content is used to form the image. This figure was adapted from [26].

1.3.2 Transducers

1.3.2.a *Piezo-electric effect*

Transducers are used for the excitation and reception of ultrasonic pressure waves. They are made of *piezo-electric* materials, which allow to convert electrical energy to acoustic energy, and vice versa. Piezo-electric materials produce an electrical signal when experiencing a vibration (direct effect), and on the other hand vibrate when a time-varying electrical field is applied (reverse effect). As the image formation consists of both transmission and reception of ultrasonic pressure signals, the reverse piezo-electric effect is used on transmit and the direct effect on receive. Initially, natural piezo-electric ceramics like quartz were used, but most modern transducers are made of ceramics like lead zirconate titanate (PZT).

The piezo-electric effect can be intuitively explained when considering the material to consist of electrical dipoles, i.e. a seperation of the positive and negative charge inside a molecule. When applying an electrical field, the dipoles are aligned in a preferential direction, changing the thickness of the material. The other way round, a stress causing deformation of the piezo-electric material rearranges the dipoles, inducing a net charge across the material. Therefore, each side of the piezo-electric slab in a transducer is coated with a thin metallic layer acting as an electrode.

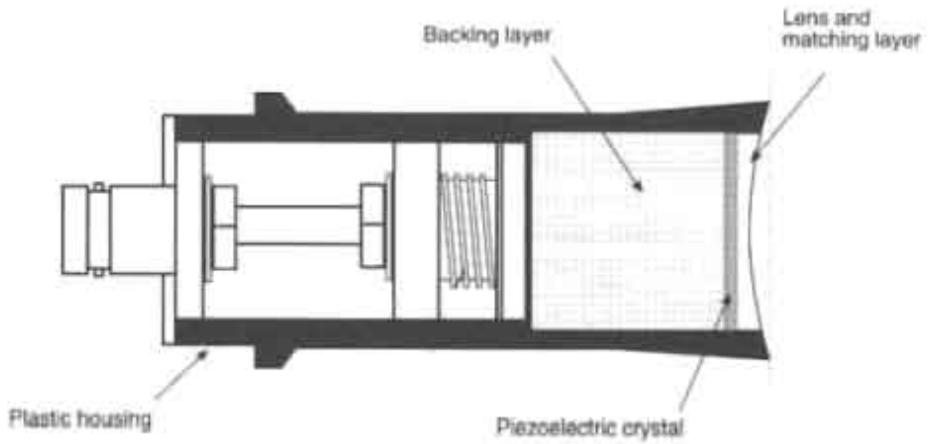

FIGURE 1.7: An ultrasound transducer consists of a piezo-electric slab to create the ultrasonic pressure field. Acoustic matching and backing layers are present to increase the energy transmission into the tissue. This figure was adapted from [23].

1.3.2.b *Transducer efficiency*

The transducer is designed in such a way that a maximal acoustic energy output is generated (cfr. fig. 1.7). Therefore, the mismatch in acoustic impedance between the transducer and tissue should be minimized. Although PZT demonstrates a very efficient conversion from electrical to mechanical energy, it has the disadvantage of having an acoustic impedance 20 times larger than tissue, meaning that about 80% of the energy is reflected back into the transducer. This causes internal reverberations inside the piezo-electric slab, continuing long after the electrical excitation has stopped, a phenomenon called *ringing*. For this reason, a *backing layer* is put behind the slab to absorb the ultrasound waves. However, for continuous wave excitation (cfr. section 2.1), no absorbing backing layer is necessary. To achieve sufficient imaging sensitivity, the degree of absorption of the backing layer should be limited. Otherwise, too much energy of the excitation signal and the waves backscattered from the tissue is converted into heat.

The acoustic mismatch between the transducer and tissue also limits the energy transmitted into the tissue. To solve this issue, acoustic matching layers are necessary at the front of the piezo-electric slab to increase the transmitted acoustic power. Typically, this is achieved with a *quarter wavelength plate* with impedance $\sqrt{Z_{PZT}Z_T}$ (Z_{PZT} and Z_T the impedance of respectively PZT and the tissue), in which the ultrasound waves reverberate. The waves successively transmitted by the plate constructively interfere, while the waves reflected back into the transducer destructively interfere.

The size of the piezo-electric slab also influences the efficiency of the energy transmission, since transducer resonance occurs at the frequency for which the slab thickness is half a wavelength ($\frac{\lambda}{2}$). The ultrasonic wave reflected by the front of the slab then constructively interferes with the orignal wave, increasing the energy output. Internal losses due to heating and unwanted vibration modes may further degrade the transducer efficiency.

The processes mentioned in the previous paragraphs all influence the energy transmission of the transducer, and their combined effect is reflected in the *transducer bandwidth*, representing the frequency range of ultrasonic excitations resulting in efficient energy transmission into the tissue. Large transducer bandwidths are desirable since imaging

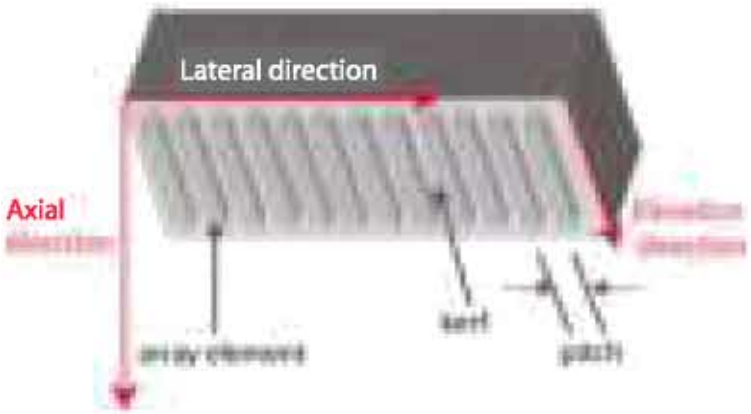

FIGURE 1.8: Nomenclature used for array transducers. This figure was adapted from [21].

resolution increases with short pulses, i.e. large pulse bandwidths (cfr. section 1.3.4.b). Pulse bandwidths larger than the transducer bandwidth can not be achieved. A wide transducer bandwidth is also necessary for some special imaging techniques, like harmonic imaging (section 1.5.1).

1.3.2.c *Transducer type*

Nowadays, transducers consist of an array of piezo-electric elements, which allows flexible electronical control of the beam formation and scanning procedure, both on transmit and receive. Common nomenclature for array transducers is presented in fig. 1.8. The gap in between array elements is called the *kerf*. This space between elements is acoustically isolated to avoid cross-talk between elements. The distance between the centre of the elements is called the *pitch*. The imaging axis perpendicular to the transducer surface is called the *axial direction*, and the axis parallel to the transducer surface is the *lateral direction*. This 2D plane defines the imaging plane which is visualized on a scanner. The direction perpendicular to the imaging plane is the *elevation direction*.

The most important types of multi-element transducers are the linear array and phased array transducer. A *linear array* sequentially scans parts of the tissue. The origin of the beam is moved in the lateral direction by changing the group of excited elements in the array (cfr. fig. 1.9), resulting in several *scanlines* with backscattered information. The

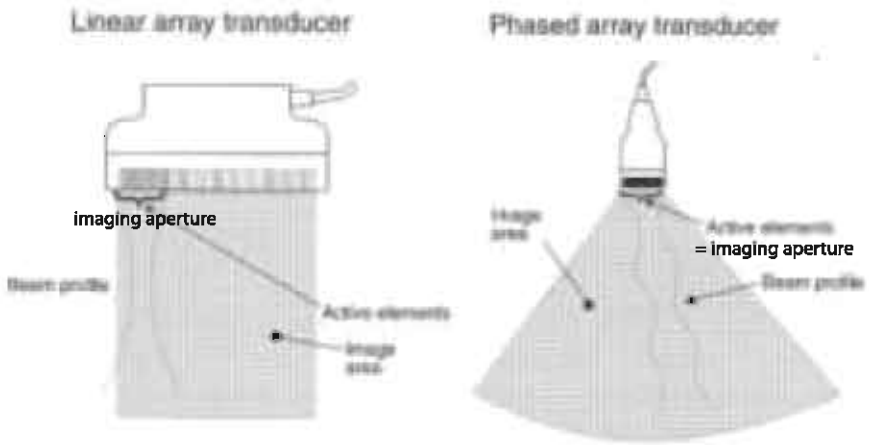

FIGURE 1.9: Illustration of a linear array and phased array transducer. This figure was adapted from [23].

group of activated elements is called the imaging *aperture*. In contrast to linear arrays, all the transducer elements of a *phased array* are simultaneously activated to steer the scanlines, resulting in a cone-shaped image, as can be seen in fig. 1.9.

1.3.2.d *Beam formation of array transducers*

The acoustic field generated by a transducer is determined by diffraction, i.e. the spreading out of a wave from its source. A diffraction pattern is created depending on the size/shape of the source compared

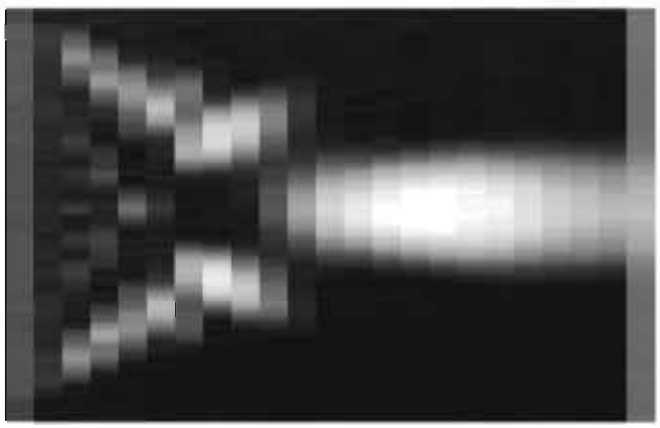

FIGURE 1.10: A diffraction field from a 40 wavelength wide line aperture positioned on the left of the image. This figure was adapted from chapter 6 in [22].

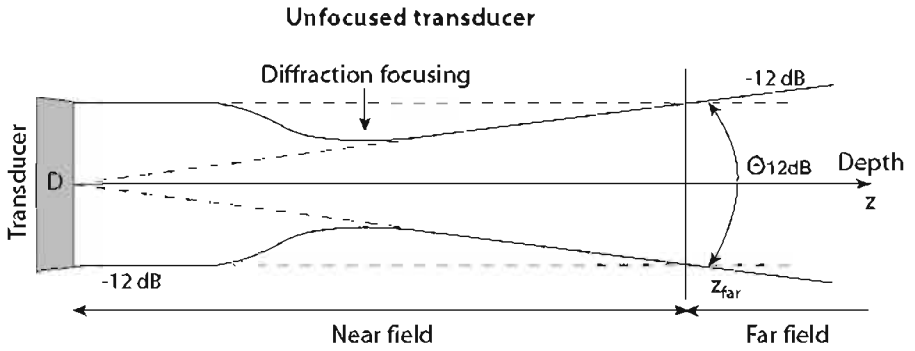

FIGURE 1.11: The beam of an unfocused transducer converges because of diffraction phenomena. The imaged depth can be divided into a near field and far field. This figure was adapted from [26].

to the wavelength. Fig. 1.10 shows the diffraction field from a 40 wavelength wide line aperture. For an array transducer, the ultrasound field can be derived by calculating the diffraction pattern from each individual element. The resulting beam shape is then determined by the overlap and interference effects of the individual diffraction patterns.

Because the transmitting aperture is typically large compared to the wavelength, a directional ultrasound beam arises, which converges due to a natural focusing process, called *diffraction focusing*, as illustrated in fig. 1.11. This effect causes a beam to converge, even for unfocused transducers, i.e. no external focusing processes (e.g. lens) are applied. Sharper beams are created for larger apertures or decreased wavelengths, because diffraction effects become more prominent as the size of the source decreases compared to the wavelength.

The propagation of an ultrasound beam arising from an unfocused transducer can be divided into specific zones depending on the imaging depth. Two distinct regions can be recognized, called the *near* field and *far* field, as can be seen in fig. 1.11. In the near field, diffraction effects are prominent, and in the *extreme* near field, the beam width is a close replica of the applied aperture. The far field is the region where the amplitude of the pressure wave decreases at a fixed rate.

When exciting the transducer with a single frequency wave, also called *continuous wave excitation*, the acoustic intensity on the imaging axis will be strongly varying in the near field (Fresnel zone) and will fall off

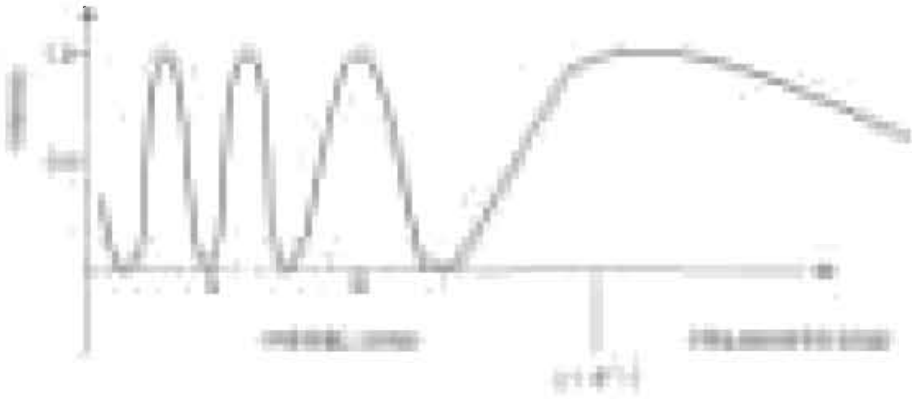

FIGURE 1.12: The acoustic intensity created by a continuous wave system strongly oscillates in the near field (Fresnel zone), and falls off at a fixed rate in the far field (Fraunhofer zone). The transition between both zones is $\frac{a^2}{\lambda}$ for a circular transducer, with a the radius of the transducer and λ the wavelength. This figure was adapted from [19].

at a fixed rate in the far field (Fraunhofer zone), as illustrated in fig. 1.12. For a circular transducer with radius a, the transition between Fresnel and Fraunhofer zone is $\frac{a^2}{\lambda}$. On the other hand, a pulsed excitation will demonstrate a much smoother field because the minima and maxima of the pressure distribution will occur at different locations for each frequency component in the pulse bandwidth, smoothing the resulting field.

Diffraction focusing is, however, not sufficient for medical imaging applications, since the diffraction focus typically occurs deep compared

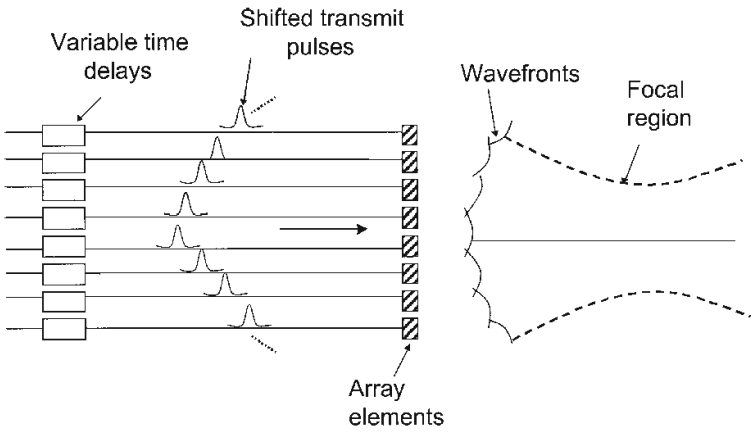

FIGURE 1.13: The concept of electronic focusing of an array transducer. This figure was adapted from chapter 7 of [22].

to the tissue regions we want to image. Therefore, transducers have the ability to flexibly control the focusing region by using a lens, a curved aperture, or by applying electronical delays between the different elements of the array. For this last focusing procedure, elements near the centre of the aperture experience a larger time delay, so that the spherical wavefronts from the individual elements add up to the desired focusing (illustrated in fig. 1.13). The resulting focus position is the combination of the natural diffraction focusing and the *geometric focusing* induced by one of the previously mentioned processes. When further mentioning the term *focusing*, we refer to the combined effect of natural and geometric focusing.

Using geometric focusing, a much more narrow beamwidth can be obtained at relevant imaging depths compared to diffraction focusing. This is because the geometric focusing process accelerates the depth dependent evolution of the unfocused beam cross-sections (*beamprofiles*). For an unfocused transducer, the beam evolution stretches from the near field to the extreme far field, but focusing compresses this into a smaller region equal to the geometric focal length. Indeed, geometric focusing allows to image an object in the far field, while with diffraction focusing relevant imaging depths are located in the near field. Except for this lateral compression and axial shift of the beamprofiles, the beamshapes are the same as for the unfocused transducer. An example of a 1D cross-section of an ultrasound beam is illustrated in fig. 1.14. This far-field beamprofile is the result from a continuous wave excitation of a rectangular transducer.

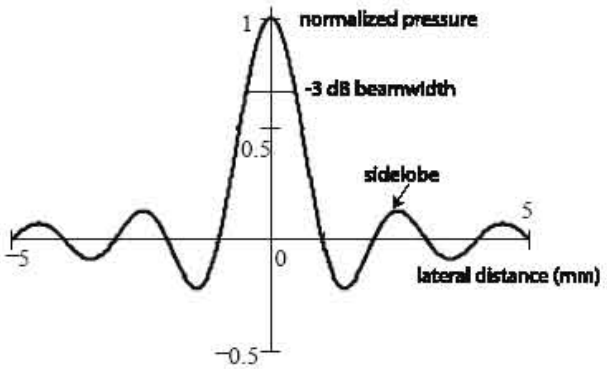

FIGURE 1.14: Far-field beamprofile from a rectangular transducer in continuous wave excitation. This figure was adapted from [20].

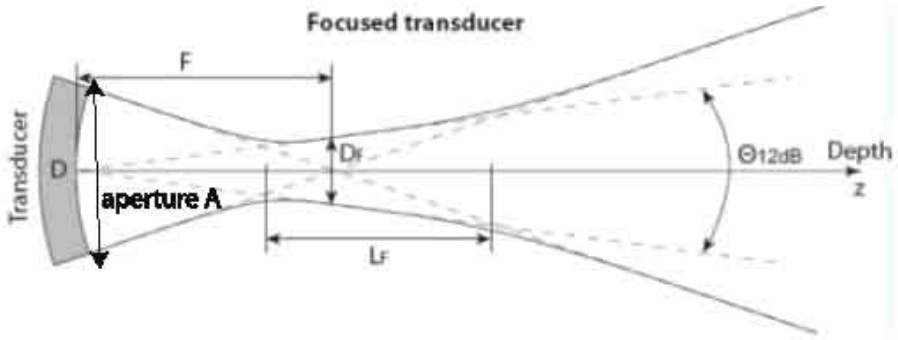

FIGURE 1.15: By applying geometric focusing, a narrow beam can be achieved over a limited depth region. This figure was adapted from [26].

The depth dependent evolution of an ultrasound beam resulting from a focused transducer is shown in fig. 1.15. It should be noted that as the imaging process consists of a transmit and receive part, the actual beam profile results from the overlap of the transmit and receive beamshape. An important parameter determining the beamshape of a focused transducer and hence describing its image quality, is the F-number $F_\#$. This dimensionless parameter expresses the ratio of the focal length F to the aperture A:

$$F_\# = \frac{F}{A} \tag{1.8}$$

The F-number is defined for both the transmit and receive beamforming, and is referred to as the two-way F-number when combining both the transmit (T) and receive (R) process:

$$\frac{1}{F_{\#,2-way}} = \frac{1}{F_{\#,T}} + \frac{1}{F_{\#,R}} \tag{1.9}$$

Large F-numbers mean a decreased acoustic intensity is emitted or received by the transducer. The beamwidth D_F at the in-focus position is related to the wavelength and the F-number $F_\#$ as (cfr. fig. 1.15):

$$D_F = \lambda F_\# \tag{1.10}$$

This is the -3 dB beamwidth, or the beamwidth measured at 70 % of the maximum beam amplitude. The -3 dB beamwidth is also illustrated in fig. 1.14. To describe the quality of focusing, the *focal depth* L_F is used (cfr. fig. 1.15). This is the depth region where the beamwidth, as given at the in-focus position, remains relatively uniform. Hence, the focal

depth describes the region of the image which is focused. Considering the -1 dB beamwidth (the beamwidth measured at 90 % of the maximum beam amplitude) at the in-focus position, the focal depth is defined as the region over which this beamwidth doubles, and is given by:

$$L_F = 4\lambda F_\#^2 \tag{1.11}$$

As can be seen from equations 1.10 and 1.11, small F-numbers are beneficial for the lateral resolution (D_F), but also result in limited focal depths (L_F). Consequently, the F-number is a trade-off parameter in transducer design.

To overcome the limitations of a limited focal depth, a *dynamic focus* and/or *dynamic aperture* is often applied on receive (cfr. fig. 1.16). Dynamic focusing is a technique to electronically sweep the focus on receive. Nowadays, a large number of focal receive zones can be defined so that the transition between zones is indistinguishable on the final image. A dynamic focus can also be applied on transmit, by recording several images with different focal zones, and splicing them together to create a composite image with better resolution. However, this technique slows down the frame rate. Using a dynamic aperture means the size of the aperture is changed throughout depth, with larger apertures for larger depths. This way, the F-number can be kept constant

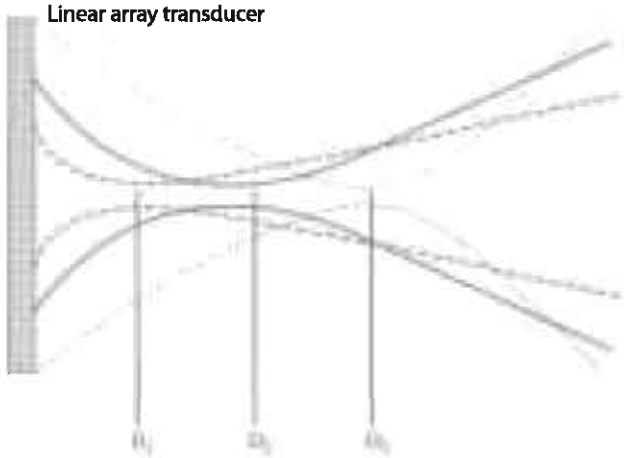

FIGURE 1.16: Three different focusing zones are defined on receive (D1,D2,D3). By applying a dynamic aperture, the in-focus beamwidth is the same for these focusing zones. This figure was adapted from [21].

throughout depth, and hence also the receive beamwidth, resulting in more uniform image properties for the depth region of interest.

As can be seen in fig. 1.14, in addition to the central beam, the ultrasound field also shows *sidelobes*, which degrade the image quality. Strong reflectors positioned in the sidelobes may create false echoes and interfere with the signal from targets on the imaging axis. To decrease the sidelobe levels, *apodization* is applied: an amplitude weighting of the normal velocity across the aperture. For array transducers, apodization is typically accomplished by exciting each array element with different voltage amplitudes. The downside of apodization is the broadening of the main lobe.

For a continuous wave excitation, the weighting of the aperture is related to the far-field beamprofile by a spatial Fourier transform. As an example, a rectangular weighting of the aperture results in a sinc beamprofile. The relationship between the aperture function and the beamprofile is shown in fig. 1.17. This figure also demonstrates that the final beamprofile is found by the overlap of the transmit and receive beam,

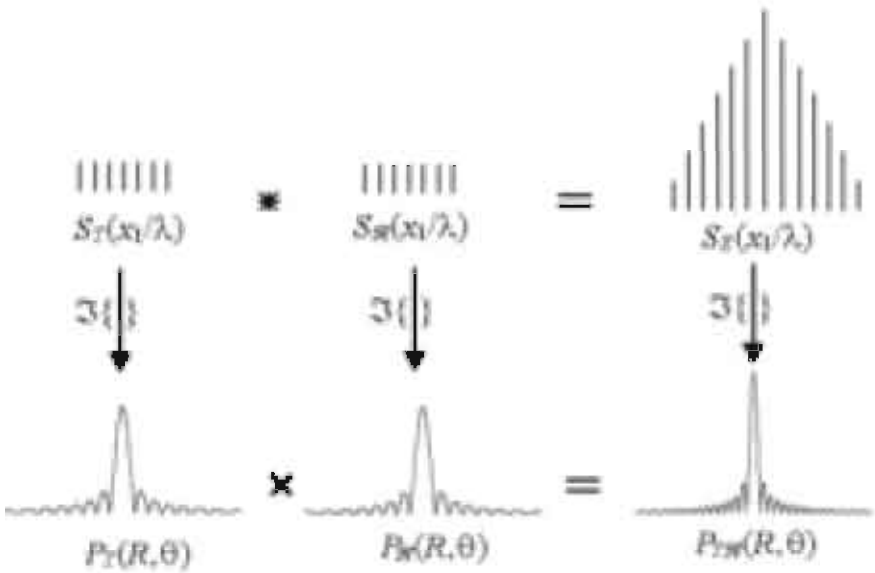

FIGURE 1.17: The relationship between the aperture function and the beamprofile is the spatial Fourier transform. The eventual beamprofile (P_{TR}) is the overlap between the transmit (P_T) and receive beam (P_R), corresponding to a convolution of the transmit (S_T) and receive aperture function (S_R). This figure was adapted from chapter 7 of [20].

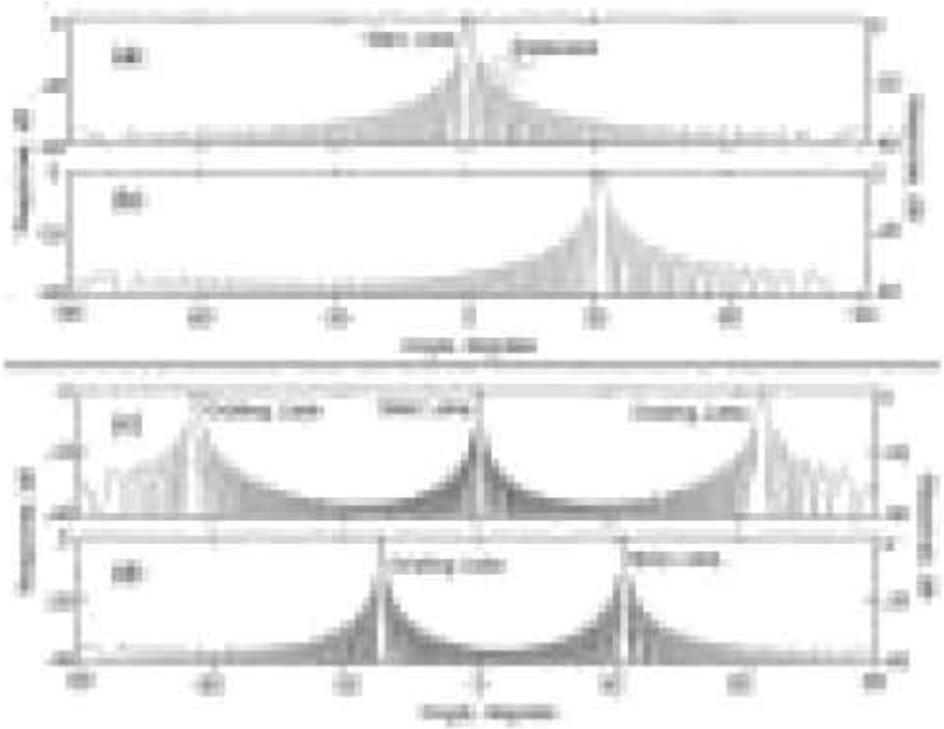

FIGURE 1.18: The normalized far-field pressure amplitude on transmit is shown versus the observation angle. In panel (a) the element spacing is $\frac{\lambda}{2}$ and no steering angle is applied. In panel (b) the beam is steered with 30 degrees. In panel (c) grating lobes are created due to an increased element spacing of 1.1 λ. Panel (d) shows grating lobes come closer to the axial imaging axis because of steering and larger element spacing. This figure was adapted from chapter 7 of [20].

corresponding to a convolution of the transmit and receive aperture functions.

A special beam formation artifact caused by wave interference from the periodically spaced array elements, is the presence of very high side-lobes, called *grating lobes*. This artifact becomes particularly prominent when the array is insufficiently sampled, and is in this sense related to the Nyquist theorem, stating that the sampling frequency should be larger than twice the maximal frequency content of the signal. Therefore, grating lobes can be avoided by using a sufficiently small pitch $\frac{\lambda}{2}$ (e.g. 0.15 mm for a 5 MHz transducer). For too large element spacings, not one but several beams are emitted, as demonstrated in fig. 1.18. The necessary element spacing is ultimately dependent on the steering angle, since the effect of grating lobes increases for larger steering angles, as shown in fig. 1.18. Therefore, grating lobe minimization is more crucial for phased arrays.

Until now, the concept of focusing has been illustrated in the imaging plane. However, the ultrasound beam should also be focused in the elevation plane to reduce the image thickness. For conventional array transducers, this is typically achieved with a lens, but more flexible focusing can be achieved electronically if the transducer has several elements in the elevation direction. For this purpose, 1.5D and 2D arrays were developed as shown in fig. 1.19. A 1.5D array is in between a 1D and 2D array, and is coarsely sampled in the elevation direction, resulting in a number of horizontal strips of elements on the transducer. In this dissertation, 1D arrays were used during simulations and experiments.

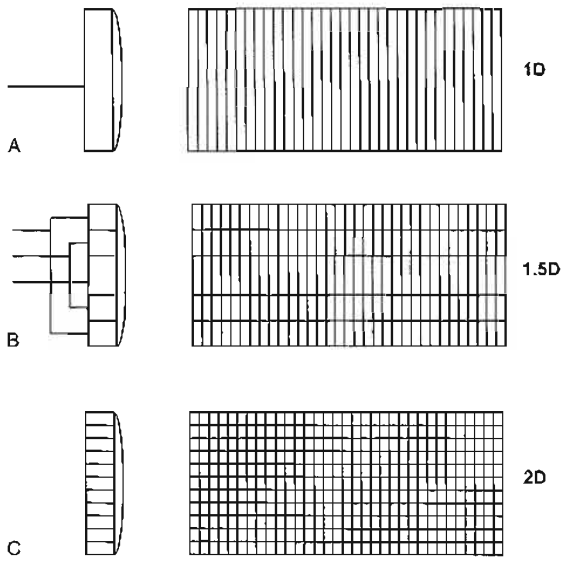

FIGURE 1.19: To improve the focusing in the elevation direction, multidimensional arrays were developed. This figure was adapted from chapter 7 of [22].

1.3.3 Scan acquisition

Different types of scan acquisition will be discussed in the context of linear array transducers, since we used this transducer type to model vascular imaging techniques (cfr. part II, III and IV).

A linear array transducer sequentially scans parts of the tissue, by successively emitting and receiving ultrasound beams in a left-to-right manner. For each emitted and received ultrasound beam, several transducer elements are activated, and the central axis of the beam is referred to as a *scanline*. The spatial sequence with which the ultrasound

beams are fired, as well as the speed of firing beams, highly influence the image quality. An important parameter in this issue is the *frame rate*, i.e. the number of images acquired per second. In the next paragraphs, we will discuss two important scan acquisition methods: parallel receive beamforming and beam interleaving.

With *parallel receive beamforming*, a relatively broad transmit beam is emitted, so that several narrower receive beams can fit inside, as displayed in fig. 1.20. This technique increases the frame rate with the number of receive beams per transmit beam.

Beam interleaved acquisition was developed in the context of ultrasonic velocity imaging (cfr. chapter 2). Measuring tissue and flow velocities with ultrasound requires that several beams, i.e. a *a packet*, are emitted for *each scanline*. This should be executed with sufficient speed in order to capture the highly dynamical behaviour of the heart and blood vessels. The speed with which ultrasound beams are fired is called the *PRF or pulse repetition frequency*. As will be further explained in chapter 2, the PRF is crucial for the properties of the velocity measurement: a higher PRF means a higher maximal measurable velocity, at the cost of less sensitivity for low velocities.

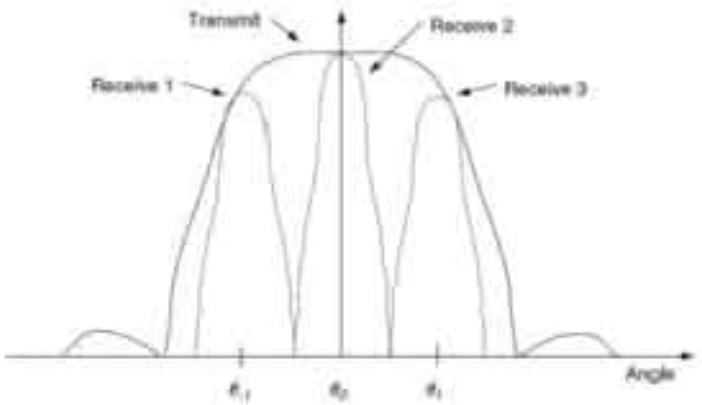

FIGURE 1.20: With parallel receive beamforming, several narrower receive beams fit within a broader transmit beam. The horizontal axis denotes the lateral observation point, represented by the angle between the central beam axis and the line connecting the aperture centre and the observation point. This figure was adapted from chapter 7 of [22].

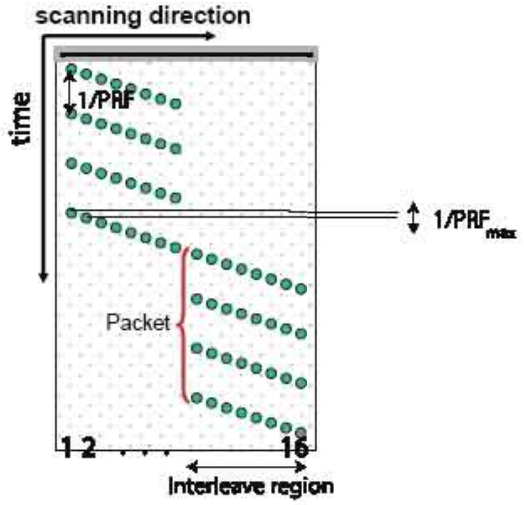

FIGURE 1.21: The terminology used in beam interleaved acquisition is visualized: PRF , PRF_{max} , packet and interleave region.

However, subsequently emitting a packet of pulses is not always optimal. This can be explained as follows. When emitting a pulse, one has to wait a certain time before the next pulse is emitted, because the original pulse should have returned to the transducer before the next one is emitted. For larger imaging depths, one has to wait longer before emitting the next pulse, and hence the PRF is decreased. As such, the imaging depths limit the choice of PRF and hence the possible frame rate.

A special scanning scheme called *beam interleaving* was developed to decrease the waiting time between subsequent pulses in a packet. This technique fires neighbouring beams before emitting the next pulse in the packet. The frequency with which neighbouring scanlines are fired is higher than the firing frequency between pulses in a packet. It is therefore referred to as the maximal PRF or PRF_{max}. This is possible in peripheral vascular imaging because the PRF, determined by the velocity range of interest, is lower than the PRF_{max}, determined by the imaging depth. We indicated this terminology in fig. 1.21, which visualizes the emitted scanlines as dots, as a function of the scanning direction (horizontally) and time (vertically). The time between pulses in a packet, i.e. 1/PRF, is equal to the vertical distance between dots of the same scanline direction. The time between firing neighbouring scanlines, i.e. $1/PRF_{max}$, is the vertical distance between neighbouring dots.

Beam interleaving divides the scanwidth into lateral subregions, called *interleave regions*. In fig. 1.21, the scanwidth, which consists of 16 neighbouring beams, is divided into two interleave regions of each 8 beams. In general, the interleave groupsize IGS is given by:

$$IGS = \left\lfloor \frac{PRF_{max}}{PRF} \right\rfloor \cdot PRB \tag{1.12}$$

with PRB the number of parallel receive beams. With this technique, higher overall frame rates are obtained.

The principles of beam interleaving are also shown in fig. 1.22. In this figure, a packet of 4 pulses is emitted for each scanline, as is indicated by the vertical axis, denoting the beam sequence. The left panel shows the case where no interleaving is applied, which means that the PRF_{max} is chosen equal to the PRF. The right panel shows an interleave group of 3 beams, which means that the PRF_{max} is three times higher than the PRF. The numbering of the beam sequence also shows that the interleave groups are subsequently obtained.

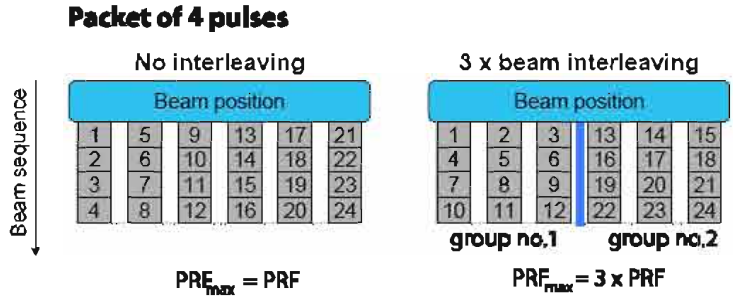

FIGURE 1.22: The beam sequence is shown for an interleaved acquisition scheme where PRF_{max} is equal to PRF (left), and PRF_{max} is 3 times larger than PRF (right). This figure was adapted from [26].

To conclude, we give a practical example, illustrating the benefits of an interleaved scan scheme. Consider a lateral scanwidth of in total 16 beams (#Beams), a packetsize of 5 pulses and a PRF of 2 kHz:

(i) In case of no interleaving, the total frame duration (1/FR with FR the frame rate) is 40 ms, calculated as:

$$1/FR = 1/PRF \cdot packet \cdot \#Beams = 1/2000 \cdot 5 \cdot 16 = 40ms \tag{1.13}$$

(ii) For an interleaved acquisition scheme, dividing the scanwidth in 2 groups of 8 beams (#Beams), the PRF_{max} is 16 kHz according to:

$$PRF_{max} = IGS \cdot PRF = 8 \cdot 2kHz = 16kHz \tag{1.14}$$

The total frame duration (1/FR) is then calculated as:

$$1/FR = 1/PRF_{max} \cdot IGS \cdot packet \cdot noIG = 1/16000 \cdot 8 \cdot 5 \cdot 2 = 5ms \tag{1.15}$$

with noIG the number of interleave groups. Hence, the total frame rate is 8 times faster than if no interleaving is applied.

1.3.4 Image quality

1.3.4.a Signal-to-Noise Ratio

Main noise sources arise from the transducer and the random nature of the background medium. Since the amplitude of the received signal is depth dependent due to attenuation, the Signal-to-Noise Ratio (SNR) is also depth dependent and can be defined as:

$$SNR(z) = \frac{Maximum\ instantaneous\ received\ signal\ power}{Noise\ power} \tag{1.16}$$

The SNR can be improved by optimizing the reception process of the RF-signals and increasing the transmitted energy. Safety issues however limit the maximum transmitted amplitude, and longer transmitted pulses may be an option to increase the emitted energy. However, longer pulses degrade the spatial resolution (see further), but coded excitation has been a promising solution in this context [27].

1.3.4.b Image resolution

The axial resolution is given by the length of the ultrasound pulse, according to equation 1.7:

$$\Delta z = \frac{cT}{2} \tag{1.17}$$

with T the duration of the emitted pulse and c the ultrasound wave speed. The resolution in the lateral and elevation direction is related to the beamwidth in and out of the imaging plane. The resolution further depends on the contrast, which is mainly degraded by beam sidelobes, grating lobes, phase front aberration, and reverberations.

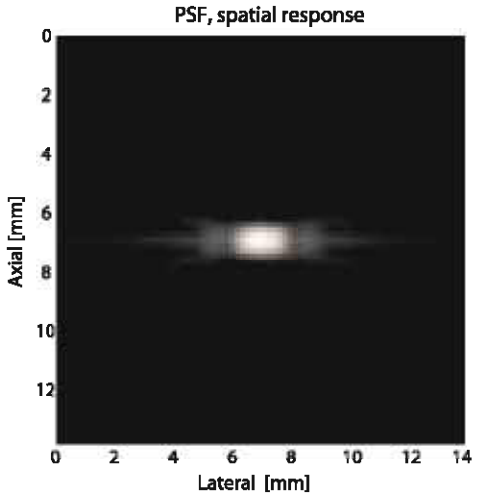

FIGURE 1.23: The point spread function represents the degree of blurring of an imaging system, and is a measure of the quality of the imaging system. This figure was adapted from [26].

The final image resolution of a system is represented by the point spread function (PSF), which is the image response of an infinitely small point scatterer in a particular location. In an ideal imaging system, the image of an infinitely small point is again an infinitely small point. However, real imaging systems induce a blurring of the imaged point. The degree of blurring is a measure of the quality of the imaging system, and is the combined effect of spatial and temporal imaging processes. More specifically, the image of a point is blurred due to:
(i) The *spatial image impulse response*, arising because of the spatially varying beamprofile. The spatial impulse response both on transmit and receive influences the PSF.
(ii) The *electro-acoustic conversion* performed by the piezo-electric element, which smoothens the applied and received voltage signal in time. The transmitted pulse e(t) is therefore convoluted with the electro-acoustic conversion impulse response, which describes the conversion of the applied voltage to the normal transducer velocity and vice versa, denoted as g_T on transmit and g_R on receive:

$$e_{RT} = e(t) *_t g_T(t) *_t g_R(t) \tag{1.18}$$

We can then express the time domain formulation of the point spread

function as the temporal convolution of the spatial impulse responses h_T and h_R, and e_{RT}:

$$PSF(z, x, t) = h_T *_t h_R *_t e_{RT} \tag{1.19}$$

with z and x the axial and lateral coordinate. Figure 1.23 shows the PSF for a 2 MHz centre frequency, an F-number of 2 both on transmission and receive, and a relative bandwidth of 60%.

1.4 Ultrasound imaging systems

1.4.1 Grayscale imaging

The amplitude of the backscattered ultrasound signals is related to the reflection strength of the imaged tissue. Hence, grayscale representation of the received amplitudes allows to investigate the structure and morphology of organs, with higher amplitudes translated in a brighter hue. An example is given for the carotid artery in fig. 1.24. To obtain such a grayscale representation, the RF-signals should be processed according to the following steps:

1. Time gain compensation (TGC): the RF signal is amplified in the receiving transducer, for increasing depths to compensate for attenuation (cfr. section 1.2.3)

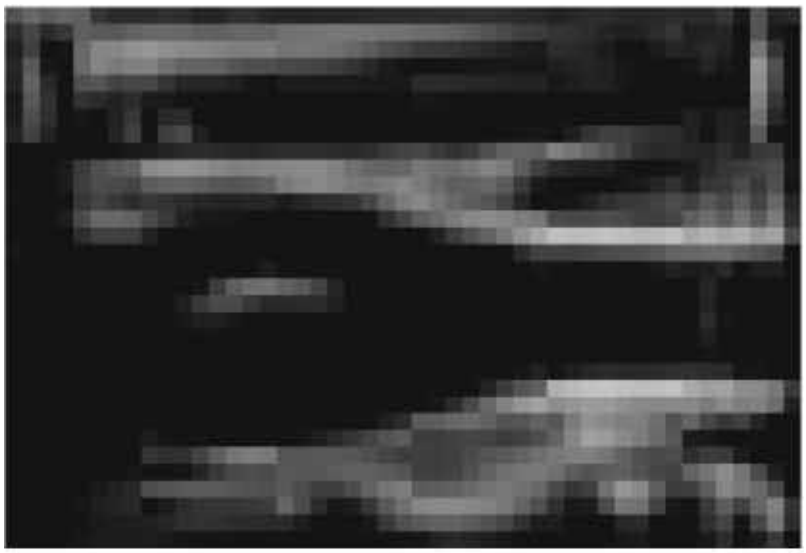

Figure 1.24: B-mode image of the carotid artery. Source: vascularscreening.co.uk

2. Amplitude demodulation of the RF-signal is performed by calculating the signal envelope, as explained in more detail in section 2.1.4.a. It are the variations in the received signal envelope which are translated into gray scale values.
3. The received signals have a large dynamic range, because the imaged structures may differ in scattering nature. For instance, in the case of blood vessel imaging, the blood signal is very weak compared to the reflection strength of the surrounding tissues. To decrease the large dynamic range of the signal, logarithmic compression is performed.
4. A scan converter performs the mapping of the received scanlines to the correct spatial positions.

Different grayscale representations exist. One scanline converted to grayscale values is called A-line (Amplitude) imaging. The two-dimensional (2D) equivalent is known as B-mode (Brightness) imaging, and is obtained by sweeping the ultrasound beam over a 2D region of interest. M-mode (Motion) imaging facilitates the perception of moving structures by showing A-lines received at successive time instants next to each other.

1.4.2 Speckle imaging

Speckle is the granular image appearance, which is created by the interference of the ultrasonic waves backscattered by a dense distribution of scatterers. The characteristic length of speckle does not relate to the macroscopic character of the imaged tissue, but is solely dependent on the resolution of the imaging system. Essential for producing a speckle pattern are a coherent radiation source and many small randomly distributed scatterers. Fully developed speckle is formed when the number of scatterers within the sample volume is large.

Speckle reduces the resolution capabilities of the imaging system, because scatterers are not distinguishable when they are closer to each other than the imaging resolution. Consequently, several methods have been proposed to reduce speckle in B-mode images. Most often, these methods consist of recording several weakly correlated or uncorrelated speckle images and averaging them afterwards to produce a compound image [28]. However, the presence of speckle can also be used to its advantage and new imaging applications were developed since its discovery: (1) assessment of tissue microstructure, (2) measurement of a tissue strain distribution (elastography), (3) blood flow field measurement. In the latter application, the speckle pattern changes with time,

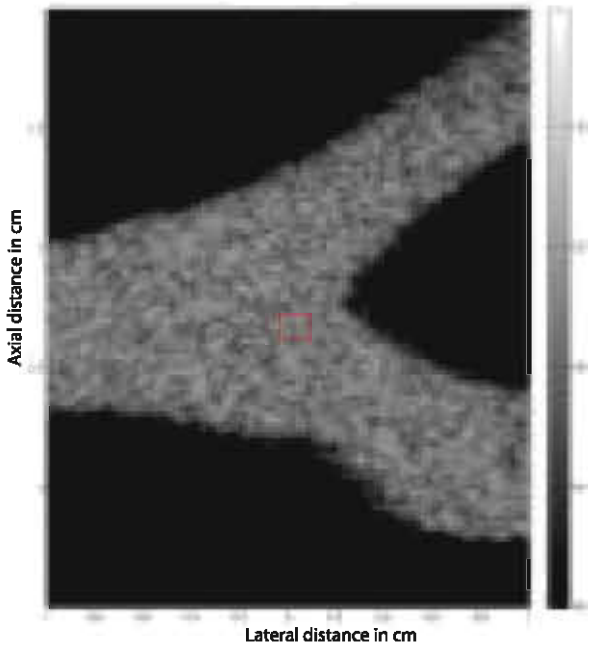

Figure 1.25: An example of a speckle pattern created by blood flow in the carotid artery. This image was obtained with the simulation procedure explained in part II of this dissertation.

and the flow field is estimated by tracking speckle patterns in subsequently acquired speckle images. An example of a speckle pattern created by blood flow in the carotid artery is shown in fig. 1.25. This image was obtained with the simulation procedure explained in part II of this dissertation.

1.4.3 Blood flow imaging

Blood flow imaging techniques will be discussed in detail in chapter 2, but a short overview of the existing methods and research lines is already presented.

Until now, flow imaging systems used in clinical practice consist of 1D velocity estimation, only measuring the flow component in the beam direction. Several flow imaging systems have been proposed the past decades and their applicability depends on the nature of the measurement. The earliest blood flow imaging system was a *continuous wave (CW) system*, using the Doppler effect. The velocity estimate is then based on detecting the frequency shift that the emitted signal experiences, due to the movement of the scattering objects. Such a system

has a transmitting crystal continuously emitting a sinusoidal wave, and a second crystal receiving the backscattered signal. Analyzing the frequency content of the received signal allows to detect the Doppler shift.

Most often, the two crystals in a CW system are close to each other, which hampers detecting the depth in tissue. To overcome this limitation, *pulsed wave systems (PW)* were developed. In contrast to CW systems, pulsed systems do not detect the Doppler shift, but measure the movement of the scatterers by correlating subsequently received signals. For this purpose, a packet of pulses is emitted and the received signals are sampled at a certain depth in the tissue. A received signal in this packet is displaced compared to the preceding one, and detecting this displacement allows to assess the movement of the scatterers. In theory, two pulses are sufficient to detect the displacement of the backscattered signal, but due to the presence of noise (arising from moving vessel walls, thermal noise from the transducer, etc...), several pulses are required to obtain a reliable velocity estimate.

Several methods exist to measure the displacement of the backscattered signals. As for CW-systems, spectral analysis techniques may be employed, especially when one is interested in a specific tissue depth. The basic concept of spectral analysis in PW-systems relies on the fact that a packet of samples is received from a certain tissue depth, giving rise to a 'slow time waveform'. The centre frequency of this wave is related to the velocity of the scatterers. Based on the frequency content of the slow time waveform, a velocity estimate can be obtained for

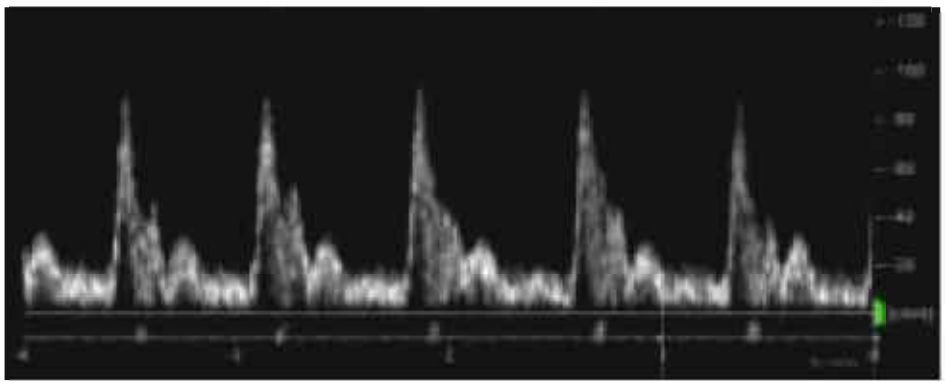

FIGURE 1.26: An example of a sonogram, visualizing the time-dependent velocity profile in the common carotid artery of a healthy volunteer. This image was made for the in-vivo study, mentioned in chapter 8.

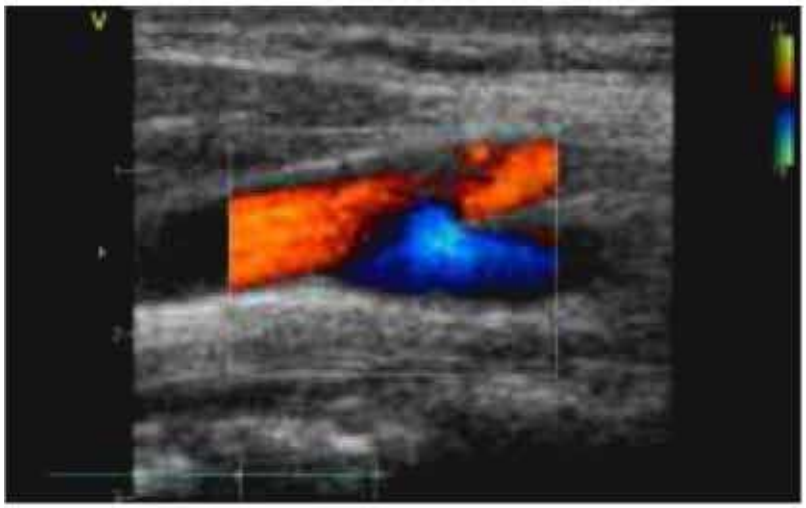

Figure 1.27: An example of a color flow image, visualizing the carotid artery of a healthy volunteer. This image was made for the in-vivo study, mentioned in chapter 8.

the tissue depth under consideration. A sonogram visualizing the time dependent velocity profile, is a common display mode in this context (cfr. fig. 1.26). The brightness is based on the signal power, which is related to the number of red blood cells moving with a particular velocity.

To obtain larger 2D cross-sections portraying blood flow, fast velocity acquisition is necessary, based on just a few samples. Velocities can be rapidly estimated with time-domain formulation techniques, detecting the position shift in the received signals due to the blood movement. This way, flow maps can be acquired in a 2D region of interest, which are color coded to enhance visual interpretation. Different colors are used to show the direction of the flow. This technique is refered to as color flow imaging (CFI), and an example is shown in fig. 1.27. The red colors indicate the measured velocity is towards the transducer, and the blue colors refer to flow away from the transducer. Usually, the flow estimates are averaged both in time and space to reduce the variance on the estimates.

A main limitation of previously discussed flow imaging systems is their 1D-nature, since only the velocity component in the beam direction is measured. Two-dimensional flow imaging systems have been proposed, with speckle tracking and vector Doppler as main research lines. As mentioned in section 1.4.2, the movement of speckle patterns can

be a measure of the flow movement, and using appropriate tracking algorithms, 2D velocity vectors can be derived. Vector Doppler is the two-dimensional extension of the previously discussed 1D color flow imaging technique. RF-signals are received from two different directions and further processed with a phase-shift technique. Velocity vectors can be composed through triangulation of the estimates from the two receive directions.

A more detailed description of flow imaging systems is given in chapter 2.

1.4.3.a Duplex scanning

Often, the flow image is superimposed on a B-mode image, called a duplex scan. An amplitude/power threshold should then be applied to determine whether tissue or flow is visualized. However, some compromises should be made in such a system:

1. To obtain a good axial resolution, the pulse lengths used in B-mode imaging are much shorter than what is conventionally used in flow imaging systems.
2. For good flow measurements, the angle of insonation should be close to the flow direction, while the best angle for B-mode imaging is perpendicular to the vessel walls.

1.5 Advanced ultrasound imaging

1.5.1 Harmonic imaging

When the energy of the transmitted pressure fields is high enough, the non-linear characteristics of the medium can become apparent and higher harmonics can be generated. The higher harmonics can enhance image quality and are utilized in *tissue harmonic imaging*, which shows potential due to decreased side lobes and decreased reverberation effects [29].

Higher harmonics can also be excited using the non-linear scattering properties of contrast agents, which are often organ or tumor specific, and designed to improve image contrast to assess structural or functional information. In *contrast medium imaging*, the contrast agent generates a second harmonic component in the received signal, which

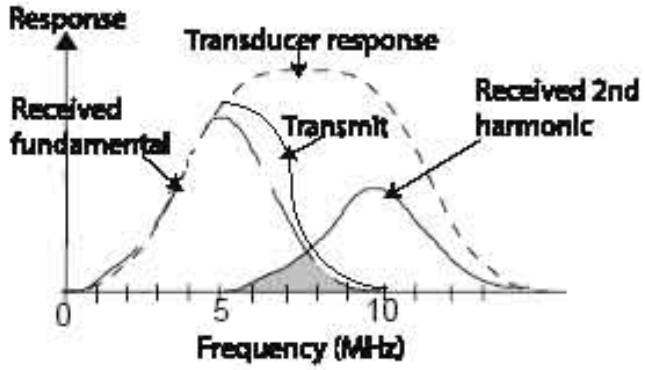

FIGURE 1.28: Illustration of harmonic imaging. The transducer frequency reponse, the transmitted spectrum, the received fundamental and second harmonic component. This figure was adapted from [20].

allows distinguishing the contrast medium from the surrounding tissue. Often the second harmonic and fundamental frequency spectrum overlap, and appropriate system design is mandatory [30]. Fig. 1.28 shows the transducer response together with the fundamental (surrounding tissue) and 2nd harmonic frequency response (contrast agent).

1.5.2 Shear wave imaging

In B-mode imaging, the bulk modulus K mainly determines the image. However, changes in bulk modulus are small compared to changes in shear modulus in the tissue, as illustrated by fig. 1.29. To increase the

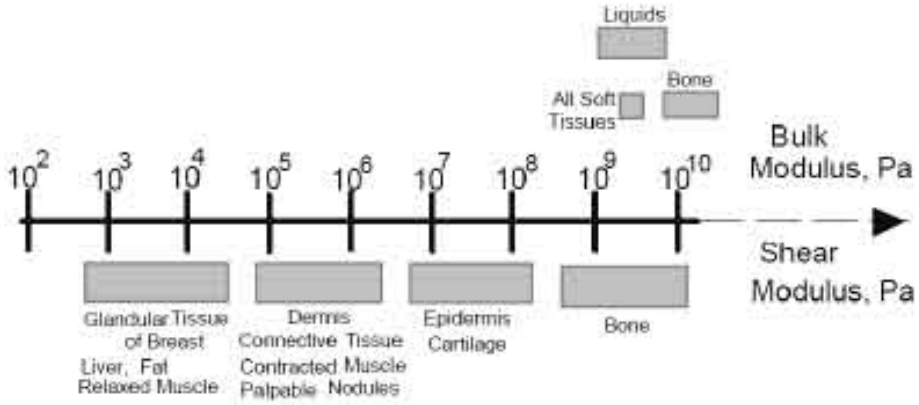

FIGURE 1.29: The range of the shear modulus compared to the bulk modulus for hard and soft tissue. This figure was adapted from [20].

sensitivity of the image to changes in tissue characteristics, imaging of the properties of the shear wave propagation would be a promising approach. Low frequency excitation is necessary due to the rapidly increasing attenuation of the shear waves with frequency.

CHAPTER 2

Velocity imaging with ultrasound

Various measurement methods exist to measure blood flow velocities, depending on whether 1D or 2D velocity information is desired, and whether high spatial or temporal resolution is required. In this chapter, an overview will be given of the commonly applied flow measuring principles. We will first discuss the 1D flow estimators, and both continuous and pulsed wave systems will be investigated. Continuous wave systems are the oldest and simplest approach to ultrasonic flow detection, and are based on the well known Doppler effect. Although a pulsed wave system is also often designated as a 'Doppler method', it does not use the Doppler effect in its true sense, as will be further explained. The applicability of pulsed systems is exemplified through detailed consideration of estimation techniques used in color flow imaging. Finally, we will give an overview of two major research lines in 2D velocity estimation: speckle tracking and crossed-beam vector Doppler.

As for the previous chapter, this overview of velocity imaging is based on several textbooks on ultrasound, and main inspirations were: *Doppler Ultrasound* book of *Evans and McDicken* [19], *Estimation of blood velocities using ultrasound* of *Jensen* [23], and *Ultrasound Imaging: Waves, Signals, and Signal Processing* of *Angelsen* [24].

2.1 CONTINUOUS WAVE SYSTEMS

2.1.1 Doppler effect

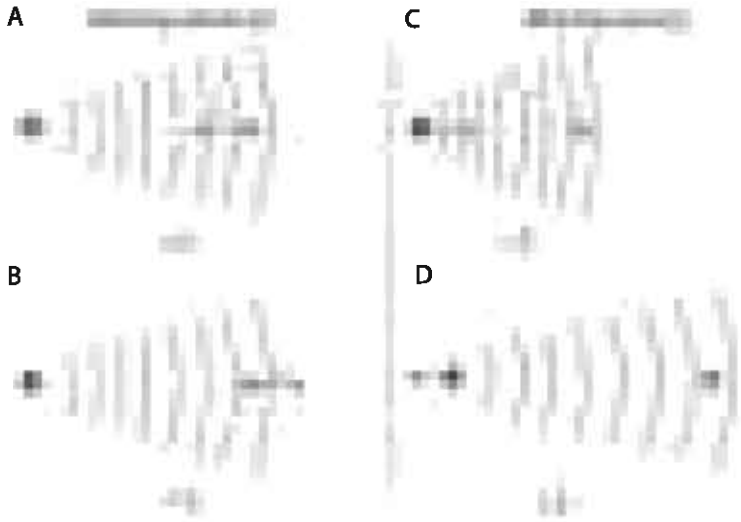

FIGURE 2.1: The Doppler effect describes the change in observed frequency of a wave due to motion. The effect of a moving observer is illustrated in panels A and B, and the effect of a moving source in panels C and D. This figure was adapted from [19].

The basic concept of the Doppler effect is the change in observed frequency of a wave due to motion, as illustrated in fig. 2.1. When an observer moves towards the source of an emitted signal, the frequency increases (cfr. panel A in fig. 2.1). The frequency decreases when the observer moves away (cfr. panel B in fig. 2.1):

$$f_r = f_t \frac{c + v \cdot cos(\theta)}{c} \tag{2.1}$$

with f_r and f_t the received and transmitted frequency respectively, v the velocity of the observer, c the wavespeed and θ the angle between the movement of the observer and the direction of the wave propagation. When a source moves, a similar effect occurs: a source moving in the direction of wave travel compresses the wave (cfr. panel C in fig. 2.1). The wavelength is expanded for a source moving in the opposite direction of wave travel (cfr. panel D in fig. 2.1).

$$f_r = f_t \frac{c}{c - v \cdot cos(\theta)} \tag{2.2}$$

A combination of the phenomena expressed in equations 2.1 and 2.2 appears in medical ultrasound, because the imaging process consists

of both a *transmit* and *receive* part. Considering blood flow applications, the red blood cells will act as moving observers during the transmit part of the imaging process, while the red blood cells will serve as moving sources when receiving the backscattered ultrasound waves. Hence, both equations 2.1 and 2.2 need to be used when deriving the resulting Doppler shift in frequency:

$$f_r = f_t \frac{c + v \cdot cos(\theta)}{c} \frac{c}{c - v \cdot cos(\theta)} \tag{2.3}$$

The Doppler frequency shift is therefore proportional to the velocity of the scatterer (assuming $v << c$):

$$f_d = f_r - f_t = 2 f_t \frac{v \cdot cos(\theta)}{c} \tag{2.4}$$

A scatterer moving towards the transducer increases frequency or the Doppler shift is positive. A scatterer moving away from the transducer causes a negative Doppler shift. The proportionality between the Doppler frequency f_d and the velocity of the observed scatterer is the basis of a continuous wave system. The Doppler shifts for a range of clinically relevant velocities and applied transducer centre frequencies is shown in table 2.1, adapted from [19].

TABLE 2.1: The Doppler shift (kHz) for a clinical range of velocities (cm/s) and transducer centre frequencies (MHz), as adapted from [19]. An angle of insonation of 45 degrees was assumed.

	Transducer centre frequency			
velocity	2 MHz	3 MHz	5 MHz	10 MHz
1 cm/s	0.018	0.027	0.046	0.092
10 cm/s	0.183	0.275	0.459	0.918
50 cm/s	0.915	1.37	2.29	4.59
100 cm/s	1.83	2.75	4.59	9.18

Equation 2.4 shows that *only the flow component in the direction of the received ultrasound beam can be detected.* In case the receive beam direction is perpendicular to the transducer surface, v$cos(\theta)$ is called the axial velocity or v_z. When the flow is expected to be aligned with the axis of the vessel, the actual flow velocity v can be derived by angle correcting with a factor $cos(\theta)$.

2.1.2 The Doppler spectrum

2.1.2.a *Spectral broadening*

When measuring flow velocities, not a single Doppler frequency, but a spectrum of frequencies is present in the backscattered ultrasound waves. A first reason is that not a single scatterer is insonified, but an ensemble of scatterers moving with different velocities. Consequently, the Doppler spectrum represents the distribution of velocities in the sample volume, as illustrated in fig. 2.2. Further, other intrinsic and extrinsic processes also contribute to the broadening of the spectral bandwidth. Intrinsic refers to processes which are inherently related to the measurement and analysis methods. Extrinsic refers to processes associated with the nature of the velocity field.

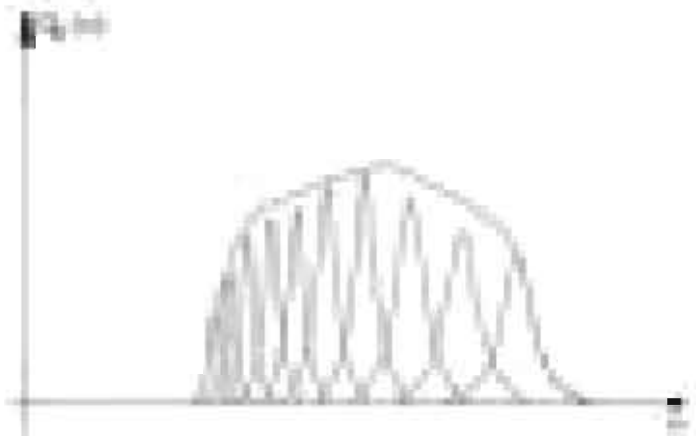

FIGURE 2.2: The Doppler spectrum $G_e(\omega)$ is build up from the contribution of different velocities present within the insonified sample volume. This figure was adapted from [24].

Transit time broadening is the first cause of intrinsic spectral broadening, and arises from the fact that the finite extents of the sample volume limit the observation time of the scatterer, as illustrated in fig. 2.3. A shorter observation time results in a broader spectrum. Both the beam width and the length of the range gate (cfr. section 2.2.3) determine the transit time. Fig. 2.3 shows that for continuous wave systems, the beam width is often limiting while for pulsed wave systems, the length of the range gate is often the determining factor. Whether the beam width or range gate limits the observation time ultimately depends on the direction of the scatterer movement. One should also

note that the ultrasound field in the sample volume might be non-uniform, which modulates the spectrum as the scatterer transverses the sample volume. This can be particularly problematic in the near field of the transducer, where the acoustic pressure field has a very complex shape. However, one aims to position the region of interest in the far field.

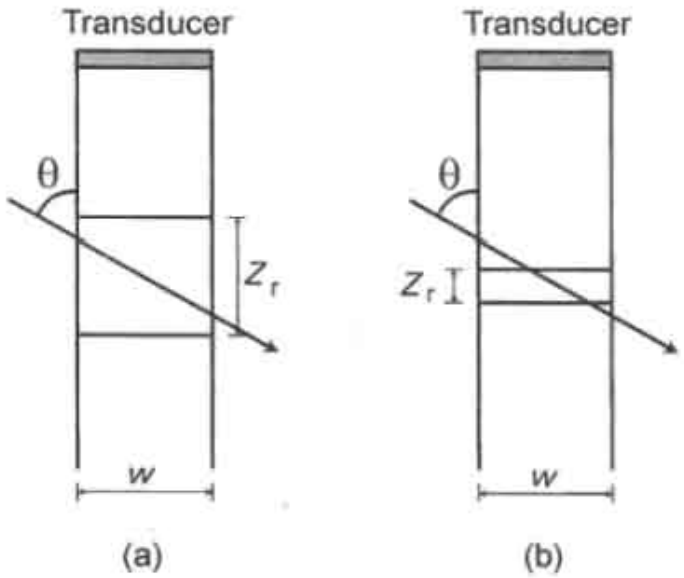

FIGURE 2.3: The finite extents of the sample volume limit the observation time, causing spectral broadening. For continuous wave systems, the beamwidth is the determining factor (panel a). For pulsed wave systems, the short axial sample volume length (range gate Z_r) limits the transit time of the scatterer (panel b). θ indicates the direction of the scatterer movement versus the scanline. This figure was adapted from [19].

Geometrical broadening is another cause of intrinsic spectral broadening. As the scatterer moves through the sample volume, it will see elemental sources on the transducer surface at different angles. Since the Doppler shift is dependent on the angle between the movement of the source (in this case the scatterer) and the wave propagation, a Doppler spectrum is produced, which changes as the scatterer transverses the sample volume. Also on the reception side, this spectrum will be broadened because every point on the receive aperture also consists of a range of angles. These ambiguities on the vector directions, on both transmission and receive side, determine the spectral shape. This phenomenon is displayed in fig. 2.4. It has been shown that close to

the in-focus position, transit time and geometrical broadening basically represent the same phenomenon [31]. Practically speaking, these broadening processes do not affect the accuracy of a mean velocity measurement since the broadening is more or less symmetrical.

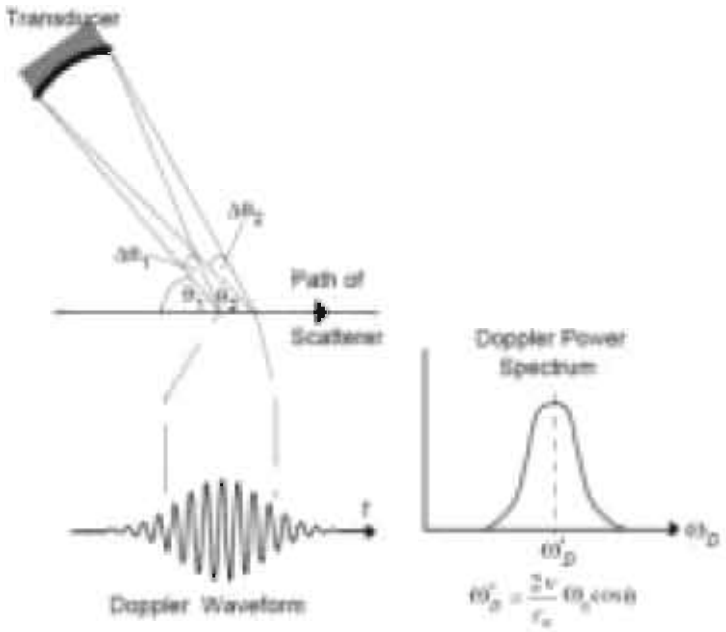

FIGURE 2.4: Geometrical broadening occurs because the scatterer sees elemental sources on the transducer with different angles as it travels through the sample volume. Broadening on the reception side is also present since the receive aperture covers a range of angles as well. This figure was adapted from [20].

Two main factors contribute to *extrinsic spectral broadening*. As mentioned before, an ensemble of scatterers with different velocities in the sample volume broadens the spectrum. The presence of different velocity directions in the sample volume, as is the case in turbulent flow, also contributes to extrinsic broadening.

2.1.2.b *Spectral shape*

The amplitudes in the frequency spectrum are proportional with the number of red blood cells moving with a certain velocity. Hence, the velocity distribution of the red blood cells in the insonated volume corresponds to the Doppler spectrum. Fig. 2.5 shows an example of the correspondence between Doppler-spectra and idealized velocity profiles in a cylinder:

$$v(r) = v_0\left(1 - \left(\frac{r}{R}\right)^{p_0}\right) \tag{2.5}$$

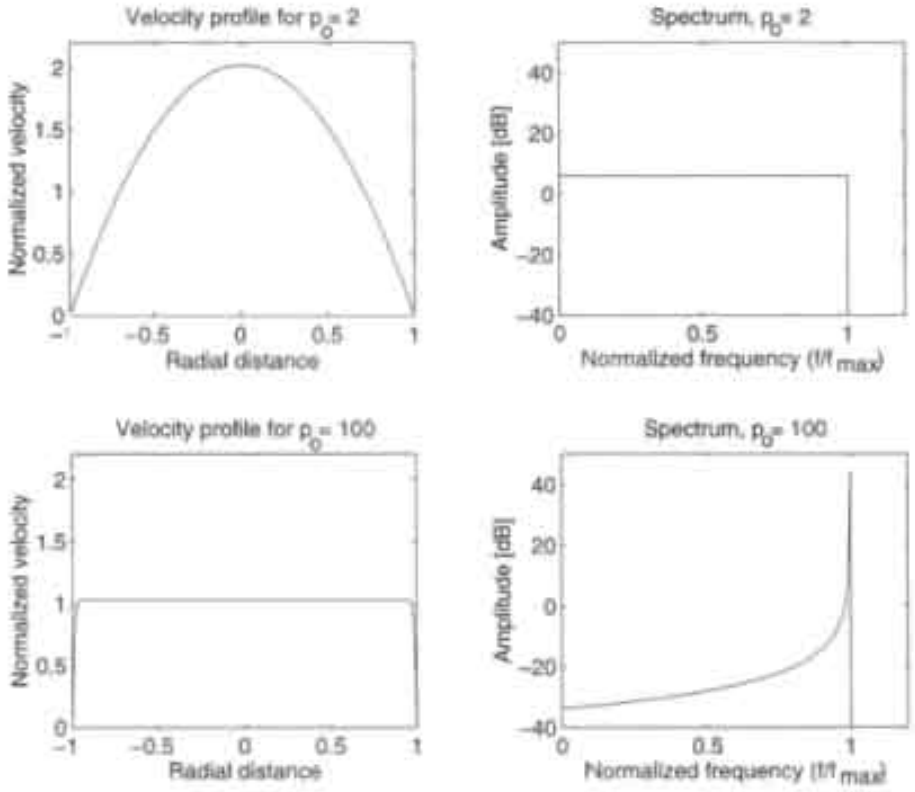

FIGURE 2.5: The Doppler spectra corresponding to idealized velocity profiles. A flatter velocity profile results in a more monochromatically shaped frequency spectrum. This figure was adapted from chapter 5 of [23].

with r denoting the radial position, R the radius of the vessel, v_0 the maximum velocity and p_0 characterizing the velocity profile. Chosing p_0 equal to 2 results in a parabolic profile. For these idealized conditions, it can be shown that the particle density p_v as a function of velocity v is given by [23]:

$$p_v(v) = \frac{2lR^2\pi\rho_p}{p_0 v_0} \frac{1}{\left(1-\frac{v}{v_0}\right)^{\left(1-\frac{2}{p_0}\right)}} \tag{2.6}$$

with l the length of the sample volume (in the lateral direction of the image) and ρ_p the scatterer density. Equation 2.6 can be directly related to the power density spectrum, through equation 2.4. A parabolic profile displays a uniform spectrum because all velocities are equally represented, while a plug flow has a quasi-monochromatic spectrum, with one obviously represented frequency, as shown in fig. 2.5.

2.1.3 Spectral estimation

2.1.3.a Fourier analysis

The Doppler spectrum arises from a number of red blood cells contributing to the observed Doppler shifts. Hence, the received signal is stochastic and only an estimated complex power density spectrum $\Phi(f)$ can be achieved. The power density spectrum represents the total backscattered power in the frequency range of f to $f + df$, with f the Doppler frequency and df an elemental frequency interval.

For this purpose, the received signal is divided into temporal segments using a *window function* (usually non-rectangular), and the power density spectrum is calculated for each of these segments. The Fourier signal is a complex series:

$$S(f) = \sum_{n=0}^{N-1} s(n) exp(-i2\pi f n \Delta T) \tag{2.7}$$

with s(n) the received signal, N the number of samples in the segment, and ΔT the sampling interval. The estimated power density spectrum $\hat{\Phi}(f)$ is then:

$$\hat{\Phi}(f) = \frac{|S(f)|^2}{N} \tag{2.8}$$

Since the analysis is performed for each temporal interval, a 2D array of power estimates is obtained (cfr. panel A of fig. 2.6), which is often graphically represented in a *sonogram* (cfr. panel B of fig. 2.6).

This display mode shows the resulting frequency estimates (vertical axis) side by side for each temporal interval (horizontal axis). Brighter values indicate a higher amplitude in the spectral distribution, meaning a higher number of red blood cells are moving with the considered velocity. The temporal distribution of the velocities can this way be visualized. To show a detailed distribution of the temporal velocity profile, small time segments should be used for the Fourier analysis. However, shorter segments imply a shorter observation time, leading to a larger bandwidth in the frequency domain, and hence a coarser velocity resolution. It is important to note that this approach is only truly valid if the signal is stationary during the temporal segment used in the Fourier analysis.

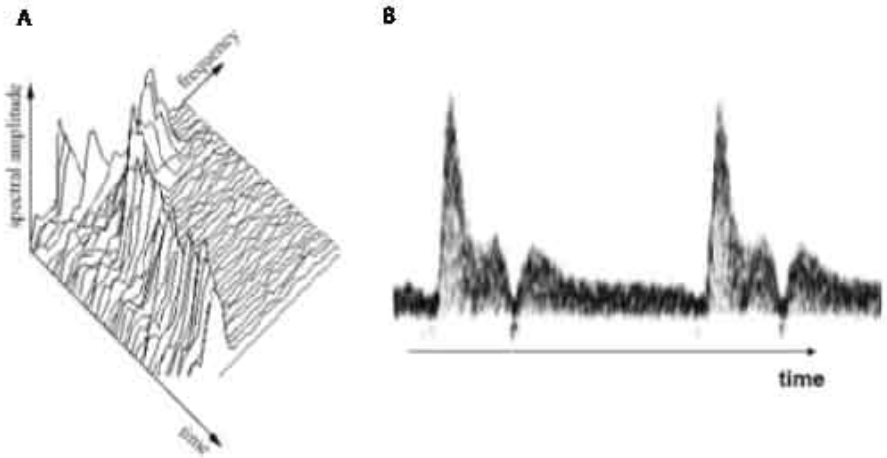

FIGURE 2.6: Panel A shows a 2D array of power estimates is obtained after spectral analysis for each temporal interval. Panel B is the corresponding sonogram, where brighter values are related to higher spectral amplitudes in the 2D array of power estimates. This figure was adapted from [24].

The bias and variance of these spectral estimates should naturally be minimized. The bias is the result from adjacent frequency components affecting the estimated spectrum at a particular frequency, due to the applied window function. The power density spectrum also has a large variance, which can only be decreased by averaging the spectrum. For this purpose, the windowed segment is split further into smaller segments, and the estimated spectra are added afterwards. This is called Bartlett's procedure [32]. Further reduction in the variance can be obtained by overlapping the segments 50%, called Welch's procedure [33]. One can conclude that the choice of the window function is crucial for the bias and variance of the spectrum estimates.

2.1.3.b *Postprocessing the Doppler spectrum*

Three methods to further process the received spectrum are discussed: zero crossing rate, mean and maximum frequency detectors.

The simplest method to assess the most dominant Doppler shift is to measure the *zero crossing rate* of the signal. This technique measures the number of times the signal crosses its mean value per second. Best results are obtained for a monochromatic transmission signal and in the presence of low noise levels. It should be noted that a zero crossing system is a biased estimator, with the bias depending on the shape of the power density spectrum.

The *mean frequency estimator* estimates the mean frequency of the complex power spectral density $\Phi(f)$:

$$\bar{v} = \frac{c}{2f_0 cos(\theta)} \frac{\int_{-\infty}^{\infty} f\Phi(f)df}{\int_{-\infty}^{\infty} \Phi(f)df} \tag{2.9}$$

Since in cilindrical vessels the blood flow Q is determined by $Q = \pi R^2 v$, equation 2.9 has often been used as a basis to measure volume flow in vessels. Volume flow estimation however implies that flow is aligned with the axis of the vessel, and that angle correction (cfr. division by factor $cos(\theta)$ in eq.2.4) as mentioned in section 2.1.1 should be applied.

The *maximum frequency detector* constructs an envelope of the sonogram by summing the absolute minimum and maximum frequency envelope, so that bidirectional flow can be detected. When only forward flow is present, the maximum corresponds to the highest forward velocity. The same principle is valid if only reverse flow is present. When both are present, the envelope detector results in the difference between the maximum forward and minimum backward flow. The detector is however biased since a maximum/minimum frequency can not be univocally determined because of intrinsic broadening processes.

2.1.4 System implementation

A continuous sinusoidal signal is emitted by a transmitter crystal, and the backscattered signal is received by a piezo-electric crystal, usually housed in the same probe, as shown in fig. 2.7. The applied frequency ranges are 1-3 MHz for deeper structures, and 5-10 MHz for more shallow vessels. The narrow bandwidth of the transducers is in the range of 50-100 kHz. A nearly monochromatic signal is excited and this is beneficial for improving SNR (see section 1.3.4.a).

Because the frequency dependent effects of the Doppler shift and attenuation are relatively small, the received frequency spectrum is centred around a frequency close to the transmitted frequency (order MHz). Such a high frequency signal requires a high sampling rate, since the Nyquist theorem states that the sampling frequency should be larger than twice the maximum frequency content in the signal. Although

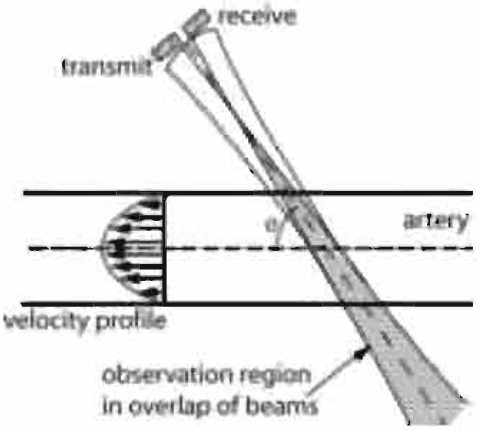

FIGURE 2.7: A continuous wave system has a seperate transmit and receive piezoelectric crystal. The overlap between the transmit and receive beam determines the sample volume. This figure was adapted from [24].

the beamforming is typically performed at such high sampling frequencies, the postprocessing of the signal is nowadays performed at lower sampling frequencies. For this purpose, the frequency content should be downshifted. Using the transmitted frequency f_0 for downmixing, the spectrum is moved to baseband, resulting in a spectrum with the desired Doppler shifts f_d ($f_d = f_r - f_0$ with f_r the received frequency). This procedure does not remove any crucial information since the essential frequency content of the received signal is contained in the signal envelope and not in the higher frequency contents.

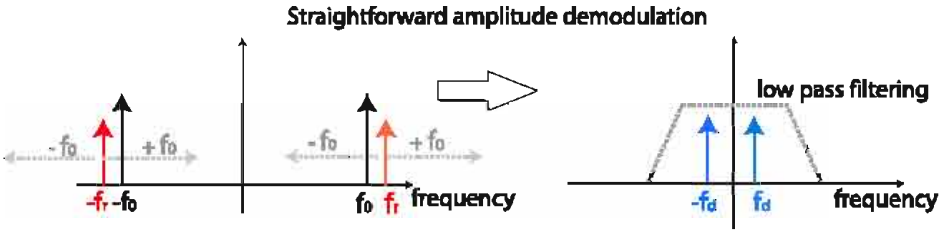

FIGURE 2.8: Straightforward demodulation for a continuous wave system. The Fourier transform of the received signal is symmetric and centred around f_r. By demodulating, the upper and lower sidebands are shifted in frequency. The higher frequency content is low-pass filtered and the remaining frequency spectra are centred around the Doppler shift $-f_d$ and f_d. The fact that the frequency spectrum is still symmetrical after demodulation, makes it impossible to determine the flow direction.

For downmixing the frequency content, *demodulation* is applied, which multiplies the received signal with a sinusoidal signal with a frequency

equal to the transmitted centre frequency f_0. The effect of straightforward demodulation for continuous wave systems is illustrated in fig. 2.8. Demodulation implies multiplying the received signal f(t) with $cos(2\pi f_0 t)$ in the time domain, corresponding to translating the received signal over the distance f_0 in the frequency domain:

$$f(t)cos(2\pi f_0 t) \longleftrightarrow \frac{1}{2}(F(f - f_0) + F(f + f_0)) \qquad (2.10)$$

The received signal f(t) is real, and hence when Fourier transforming it to F(f), an even symmetric spectrum around zero-frequency arises, showing an upper and lower side band, centred around a positive and negative frequency $f_r = f_d + f_0$. The demodulation of the received signal using equation 2.10 gives rise to frequency bands centred around:

1. $-(f_d + f_0) + f_0$ and $-(f_d + f_0) - f_0$ for the lower side band
2. $(f_d + f_0) + f_0$ and $(f_d + f_0) - f_0$ for the upper side band.

The higher frequency content, containing $\pm 2f_0$, is filtered with a low-pass filter. What is left, are two frequency bands containing the desired Doppler shifts. However, because both parts of the symmetric spectrum were downshifted to baseband, the upper and lower side band overlap. This makes distinction between forward and backward flow impossible. A variety of methods have been proposed to extract the forward and reverse components of the Doppler signal and the in-phase quadrature (IQ) technique prevailed.

2.1.4.a *Quadrature demodulation*

Quadrature demodulation is a special type of demodulation, which allows assessing the flow direction, based on determining the phase content of the received Doppler signal. For this purpose, an in-phase and quadrature component of the received signal are derived. The nomenclature *in-phase* and *quadrature* refer to the fact that these signals are 90 degrees out of phase.

The concept can be most easily illustrated based on the earliest system implementation of IQ-demodulation. The received signal was multiplied with a $\cos(\omega_0 t)$ and a $\sin(\omega_0 t)$ signal, with ω_0 the centre frequency of the emitted pulse, to find respectively the in-phase and quadrature component of the signal, i.e. I(t) and Q(t). As such, a complex

form of the received signal was constructed, further referred to as the IQ-signal:

$$IQ(t) = I(t) + iQ(t) \tag{2.11}$$

This complex signal allows assessing the instantaneous amplitude, phase and frequency properties of the signal. Based on trigonometric relationships, the I- and Q-signal can be derived as [20]:

$$I(t) = A_f cos(\omega_f t + \phi_f) + A_r cos(\omega_r t - \phi_r) \tag{2.12}$$

$$Q(t) = A_f cos(\omega_f t + \phi_f + \pi/2) + A_r cos(\omega_r t - \phi_r - \pi/2) \tag{2.13}$$

with A_f and A_r the amplitudes of the forward and reverse flow component in the received signal and ω_f, ω_r, ϕ_f and ϕ_r their respective angular frequencies and phases. It can be readily seen that these two signal components are 90 degrees out of phase.

Further, the forward (V_f) and reverse (V_r) flow components can be derived as [20]:

$$V_f = I(t) + Q(t) = 2A_f cos(\omega_f t + \phi_f) \tag{2.14}$$

$$V_r = I(t) - Q(t) = 2A_r cos(\omega_r t - \phi_r) \tag{2.15}$$

This complex representation of the received signal can also be digitally derived, using a Hilbert transform, as performed nowadays. The

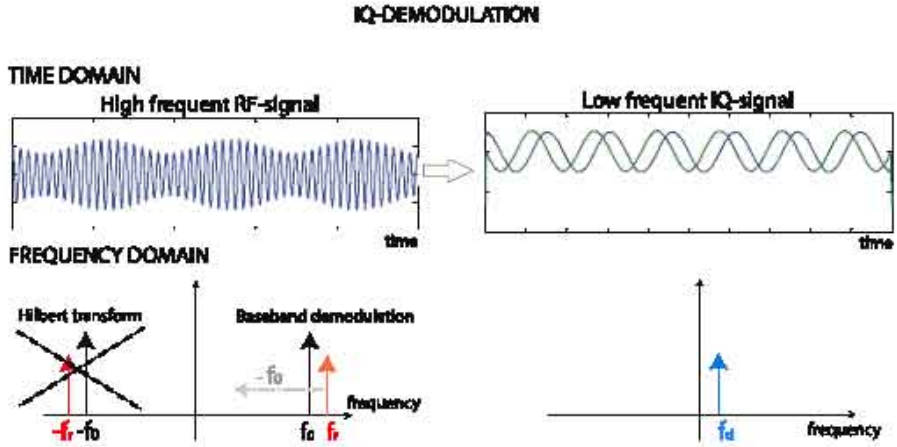

FIGURE 2.9: IQ-demodulation breaks the symmetry of the frequency spectrum by deriving the analytical form of the RF-signal with a Hilbert transform. Because just one side of the frequency spectrum is kept, the direction of flow can be determined.

Hilbert transform has the same amplitude and frequency content as the original data. However, the originally received signal has a symmetric Fourier transform, containing both positive and negative frequencies, while the complex IQ-signal contains only the positive part of the original frequency spectrum. Because the negative frequency spectrum is removed, downshifting the frequency content does allow to determine the flow direction, in contrast to the previously mentioned straightforward demodulation. The IQ-demodulation process is illustrated in fig 2.9. For more details on this method, we refer to [19].

The information given in the complex IQ-signal can be used to assess important image properties. Besides derivation of the flow direction, B-mode imaging also uses the complex IQ-signal to construct the signal envelope A(t) (cfr. fig. 2.10) for gray scale representation, calculated as:

$$A(t) = \sqrt{I(t)^2 + Q(t)^2} \tag{2.16}$$

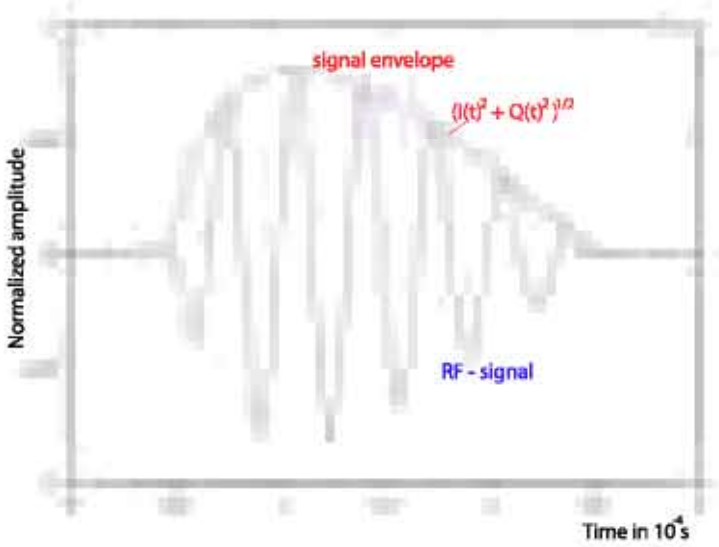

FIGURE 2.10: The envelope of an RF-signal.

2.2 PULSED WAVE SYSTEMS

The main reason why pulsed systems were developed, was to overcome the range ambiguity of the continuous wave systems, which lack the possibility of detecting the depth in tissue. Most often, the transmit and receive crystal in a CW system are close to each other, and the

depth in tissue can not be discriminated. The only depth discrimination possible is based on the fact that signals originating closer to the transducer are less attenuated.

Pulsed systems transmit short bursts of ultrasound at regular intervals. After some time, they receive signals during a well defined time interval. The delay applied before receiving signals determines the depth from which signals are gathered. The velocity measurement performed by a pulsed system is however not based on detecting the classical Doppler shift (order kHz). Due to their pulsed nature, the transmitted signal has a relatively broad frequency spectrum (order MHz), and the pulse spectrum is distorted by attenuation which increases with frequency. Hence, the Doppler shift will be obscured by the frequency downshift due to attenuation. For continuous wave systems, this was not such a problem since a narrow pulse spectrum is much less sensitive to attenuation. Consequently, another physical phenomenon must be used in pulsed systems to detect the velocity.

2.2.1 Principles

The motion of a scatterer introduces a Doppler shift in the received signal, but also a time/phase shift compared to the preceding RF line. In case of a single scatterer propagating through an ultrasound beam, the received signal r(t) has the following form [23]:

$$r(t) = a \cdot e\Big(\underbrace{\frac{c - v_z}{c + v_z} t}_{Doppler effect} - \underbrace{\frac{2d_0}{c + v_z}}_{time shift} \Big) \tag{2.17}$$

with a the amplitude of the scattered signal, e(t) the emitted signal, d_0 the position of the scatterer before emission of the pulse, and v_z the axial velocity of the scatterer. Equation 2.17 shows that in the absence of attenuation, the received signal is a delayed version of the transmitted signal, with a compressed or expanded time scale due to the Doppler effect. The time delay $\frac{2d_0}{c+v_z}$ is caused by the movement of the imaged target in between pulse emissions, and can consequently be used for estimating the scatterer velocity. The axial distance Δz traveled by a scatterer in the time in between transmissions T_{prf} is:

$$\Delta z = T_{prf} v_z \tag{2.18}$$

The time displacement $\Delta\tau$ observed in consecutively received signals can then be derived as, using equation 1.7:

$$\Delta\tau = \frac{2\Delta z}{c} = \frac{2T_{prf}v_z}{c} \tag{2.19}$$

The Doppler effect is just a small artifact of the system, and has a negligible influence on the velocity estimation. This approach is however only valid if the displacement is small, or the product of the scatterer velocity v and the time between successive pulses T_{prf} is small compared to the beam width.

FIGURE 2.11: The principle behind velocity estimation in a pulsed wave system. Panel A: A packet of pulses (n=27) is acquired and sampled at a specific depth, indicated by the vertical line. The time-scale of the received RF-signals is called 'fast time'. Panel B: The sampled waveform obtained from the packet of pulses is in the 'slow time' domain. The slow-time waveform has the same shape as the emitted pulsed but is scaled in time. This figure was adapted from chapter 10 of [20].

To further illustrate that pulsed wave systems detect the target displacement, consider fig. 2.11. A single scatterer is traveling through the sample volume, and a Gaussian modulated shape is emitted. If we neglige any frequency dependent effects in the scattering medium, the received pulse will have the same shape as the transmitted pulse, but shifted in time due to the motion of the scatterer. In fig. 2.11, 27 subsequently acquired RF signals are shown (n=1...27), and the scatterer is moving away from the transducer as can be seen from the increasing

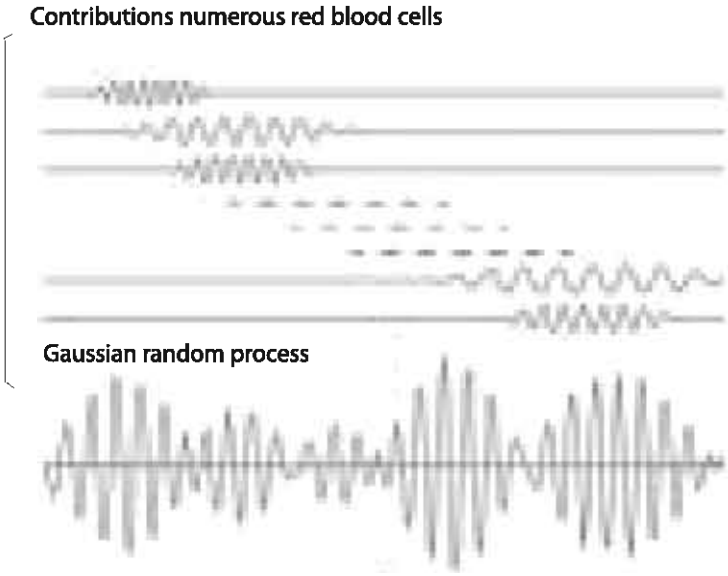

FIGURE 2.12: A complex scattered waveform is obtained due to contributions of numerous red blood cells. This figure was adapted from [24].

time delays. The propagation of the RF signal in the depth direction of the tissue corresponds to a time scale denoted as *'fast time'*. The subsequently acquired RF signals correspond to a time scale called *'slow time'*. Each RF signal is sampled at exactly the same depth, or equivalently at the same time delay from pulse transmission, as indicated by the dashed vertical line in fig. 2.11. As shown in panel B, the sampled signal has the same shape as the transmit pulse but scaled in time. This sampled signal is further called the *slow-time waveform*. The shape of the received spectrum is the same as the transmitted spectrum, but has a scaled frequency axis. It can be derived that the centre frequency of the slow-time wavefrom f_{slow} scales with the transmitted centre frequency f_0 as:

$$f_{slow} = \frac{2 \cdot v \cdot cos(\theta)}{c} f_0 \tag{2.20}$$

with c the ultrasound wavespeed, v the velocity magnitude of the scatterer, and θ the angle between the beam direction and the motion of the scatterer. A sufficient number of lines should be acquired to sample the whole pulse.

The principles of pulsed systems have been shown for a single scatterer, while in reality an ensemble of scatterers with different velocities

is moving through the sample volume. Consequently, the scattered waveform will have a more complex form due to interference effects, and will add up to a Gaussian random process due to the contribution of numerous red blood cells (cfr. fig. 2.12).

2.2.2 Velocity limits

The sampling of the slow-time waveform puts restrictions on the detectable velocity, and imposes both an upper and lower velocity limit. This is in contrast with continuous wave systems, where the measurable velocity was only limited on the lower side by spectral broadening as mentioned in section 2.1.2.

The criterion for the maximum velocity is related to the Nyquist theorem, stating that two or more samples must be obtained within one period of the transmitted centre frequency. During the time between pulses, a scatterer travels an axial distance Δz;

$$\Delta z = \frac{v_z}{PRF} \tag{2.21}$$

with PRF the pulse repetition frequency. This distance Δz is equivalent with a fast time Δt, which can be found using:

$$\Delta t = \frac{2\Delta z}{c} \tag{2.22}$$

or replacing Δz with the previous expression:

$$\Delta t = \frac{2v_z}{cPRF} \tag{2.23}$$

Due to the Nyquist criterion, $\Delta t \leq \frac{1}{2f_0}$ to avoid aliasing. This finally results in:

$$v_{max,z} = \frac{cPRF}{4f_0} \tag{2.24}$$

Actually, the maximal velocity is a bit lower, since the pulse has a certain bandwidth B:

$$v_{max,z} = \frac{cPRF}{2(2f_0 + B)} \tag{2.25}$$

Further, the pulse repetion frequency and the ultrasound wavespeed c determine the maximal depth z_{max} to univocally measure the velocity:

$$\frac{1}{PRF} \geq \frac{2z_{max}}{c} \tag{2.26}$$

For larger depths, it can not be unambiguously derived which emitted pulse gave rise to the backscattered signal. Hence, the PRF should be decreased for large depths, to give the pulses sufficient time for the round journey. This implies that only lower velocities may be detected in deeper vessels.

The minimal velocity which can be measured by a pulsed system is derived from the fact that at least one period of the received slow-waveform should be observed ($\frac{N}{PRF} = \frac{1}{f_{slow}}$):

$$v_{min,z} = \frac{cPRF}{2Nf_0} \tag{2.27}$$

N is the number of pulse transmissions.

2.2.3 Sample volume

The axial resolution of pulsed systems is related to the transmitted pulse (as for B-mode imaging), and the applied range gate. The *range gate* corresponds to the axial division of the scanlines in smaller intervals, called 'range gates' (cfr. fig. 2.13). The RF-data present in the range gate are used for the velocity estimation at a certain depth position. As opposed to the sampling at a specific depth as shown in fig. 2.11, the received signals can also be integrated over the range gate, which can significantly improve SNR.

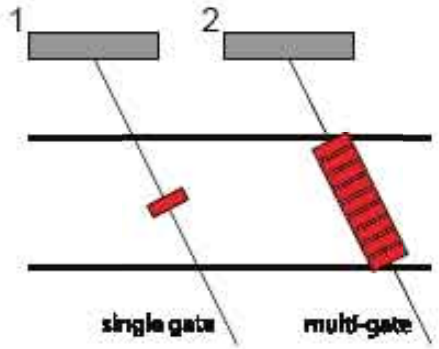

FIGURE 2.13: The scanline is divided into smaller intervals or sample volumes, called range gates. Single-gate and multi-gate (1D and 2D scans) have been developed.

It has been shown that choosing the range gate equal to the length of the transmitted pulse results in the best sensitivity inside the sample volume [34]. However, choosing the pulse length and range gate differently, results in more equal axial weighting inside the sample volume. For the autocorrelation method used in phase shift estimators (cfr. section 2.3), choosing the range gate and pulse length equal is an optimal choice [34]. It should be noted that due to the properties of the transducer and limited bandwidth of the receiving electronics, an ideal rectangular gate shape and pulse are impossible to achieve in practice. Further, the ultrasound beam width also contributes to the sample volume, determining the weighting of the received energy.

2.2.4 Spectral estimation in 1D

2.2.4.a Frequency domain estimation

For CW-systems, Fourier analysis (section 2.1.3) of the demodulated received signals allowed to construct a sonogram, representing the time dependent velocity profile. For pulsed systems, this is also possible by estimating the frequency of the slow-time waveform f_{slow} (cfr. equation 2.20). This estimate becomes more reliable for longer observation times, which are only limited by the stationarity of the flow signal (order 10 ms). However, such long observation times make a full spectral analysis impractical for real-time flow imaging of a 2D sector, as demonstrated by the following example. Let's say we want to image a moving target at a depth of 2 cm with a PRF of 4 kHz. When choosing an observation time, preferably as long as possible (10 ms), a large number of samples enters the Fourier analysis (40 samples). For a 2D sector, a large number of range gates should be scanned, and the large amount of samples required for a reliable Fourier analysis becomes problematic regarding frame rate. Hence, this technique is nowadays mainly used when investigating a single range gate, although multigate systems using parallel processing have been developed to scan several depths at the same time.

2.2.4.b Time domain estimation

The simplicity of time domain velocity estimation, based on just a limited number of samples (range 8-16), makes them highly suitable for real-time flow imaging in a 2D region of interest. Hence, commercial color flow imaging (CFI) systems rely on this type of estimation. CFI does not perform a full spectral analysis of the investigated range gate,

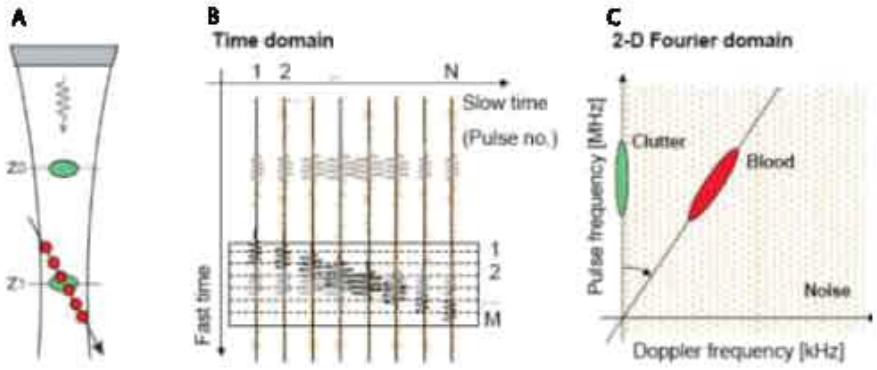

FIGURE 2.14: Pulsed systems are based on a 2D time signal for velocity estimation: the RF-signals are sampled in both the fast-time (depth) and slow-time (packetsize) domain, as indicated by the rectangle in panel B. Panel C illustrates the 2D frequency content of the signal. The blood signal is elliptically shaped and the angle of the major axis of the ellips corresponds to the estimated velocity.

but rather estimates parameters like the mean frequency in the investigated sample volume and the associated spread of velocities. The estimated mean velocities are color-coded with a scale depending on the direction of the flow (red towards and blue away from the transducer). Two important methods were developed to derive the time shift of the backscattered signals due to the scatterer motion: the autocorrelation method for phase shift estimation and the cross-correlation procedure for time shift estimation. These techniques will be discussed further in section 2.3 (phase shift estimation) and section 2.4 (time shift estimation).

2.2.5 Spectral estimation in 2D

The above-mentioned 1D spectral estimators only take into account the correlation of the received signals in the slow time domain. Two-dimensional methods were developed to include the correlation of the signal in the depth range or fast time domain. Indeed, as can be seen in fig. 2.14, the received packet of signals is a 2D signal, ranging in the fast-time domain (depth) and the slow-time domain (packet). The two-dimensional frequency content can be obtained with a two-dimensional Fourier transform of the 2D signal $s(n_1,n_2)$, with the indices n_1 and n_2 referring to the sampling in respectively the slow time and fast time domain.

$$\hat{P}(m_1, m_2) = \frac{1}{N_1 N_2} \sum_{n_1=0}^{N_1-1} \sum_{n_2=0}^{N_2-1} s(n_1, n_2) e^{-i2\pi m_1 n_1/N_1} e^{-i2\pi m_2 n_2/N_2} \quad (2.28)$$

with N_1 and N_2 corresponding to the data length in the slow and fast time domain. Fourier transforming the slow-time dimension results in a slow-frequency axis. Because the centre frequency of the slow-time waveform corresponds to the Doppler shift (cfr. equation 2.20), the slow-frequency is actually the Doppler frequency. Fourier transforming the fast-time dimension (depth dimension) results in the radio frequency axis.

The blood signal in 2D Fourier space has an elliptical shape. The angle of the major axis of the ellips is related to the velocity of the observed scatterers. The 1D Fourier transform can be obtained by projecting the 2D spectrum on the Doppler frequency axis. Compared to the 1D representation of the Doppler spectrum, the 2D Fourier representation

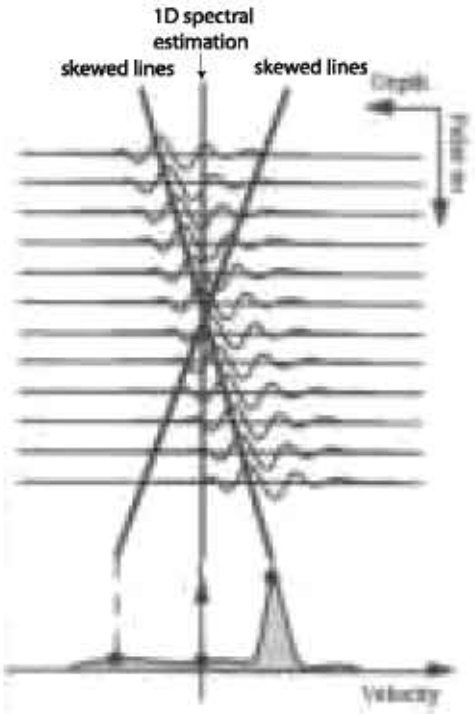

FIGURE 2.15: The principles of the velocity matched spectrum analysis. The spectrum analysis is performed along different skewed lines, corresponding to a set of assumed velocities. This gives rise to a velocity distribution, from which the maximum corresponds to the most reliable Doppler estimate. This figure was adapted from [35].

has the advantage that the effects of spectral broadening can be visualized. Indeed, a frequency spread is observed in the RF-frequency direction due to the finite sample volume length. The limited observation time causes a spread in the Doppler frequency direction.

A method showing great potential in this context is *velocity-matched (VM) spectrum analysis* [35]. While the 1D spectral estimators are based on samples received from a specific depth, the velocity matched spectrum is obtained by using samples from several depths. As shown in fig. 2.15, this means that not only samples from a vertical line, like in 1D methods (cfr. fig. 2.15), are included in the spectral analysis, but also those from skewed lines. This way, the signals are also correlated in the depth direction. After spectral evaluation along different skewed lines, a velocity matched spectrum is obtained, as shown in fig. 2.15. The most accurate estimate of the Doppler shift corresponds to the maximum in this spectrum. This technique suppresses aliasing artifacts, but does not remove it. Further advantage is that the method is insensitive to frequency dependent attenuation.

2.2.6 System implementation

In many aspects, the pulsed wave system is similar to the CW-system, described in section 2.1.4. However, some differences are present, as illustrated in figure 2.16. The same piezo-electric crystal is used for transmitting and receiving the ultrasound waves. Additional circuitry is necessary to sample and hold the RF-signals, corresponding to the depth and range gate of interest. As for CW-systems, the IQ-demodulation process is applied for the spectral analysis techniques (cfr. section 2.2.4.a) and phase shift methods (cfr. section 2.3).

The fact that appropriate demodulation is needed to obtain the flow direction in pulsed wave systems, is illustrated in fig. 2.17. Imagine a scatterer moving with an axial velocity v_z. The subsequently acquired RF-signals show a timeshift due to this motion. However, when sampling the received signals only once per centre frequency period, direction ambiguity may arise, as can be seen in the top row of fig. 2.17. Two possible waveforms may arise after insufficient sampling, corresponding to two different scatterer propagation directions. Directional information may be obtained by acquiring two samples for each received line, spaced $\Delta\tau = \frac{1}{4f_0}$ apart from each other, which guarantees

a unique representation of the signal. This *quadrature sampling* corresponds to a phase shift $\Delta\phi$ of $\frac{\pi}{2}$:

$$\Delta\phi = 2\pi f_0 \Delta\tau = 2\pi f_0 \Delta \frac{1}{4f_0} = \frac{\pi}{2} \tag{2.29}$$

Hence, this sampling procedure is equivalent with in-phase quadrature demodulation, as described in section 2.1.4.a, a method to obtain a version of the received signal 90 degrees out of phase with the original signal.

2.3 COLOR FLOW IMAGING USING PHASE SHIFT ESTIMATION

Phase shift estimation techniques were developed to make real time 2D flow imaging possible, as used in today's color flow imaging (CFI), shown in fig. 1.27. The autocorrelation method as developed by Kasai et al [36] is the most commonly applied phase shift estimator, and allows estimating the velocity based on just a few RF-lines, keeping the frame rate high. As illustrated for the general pulsed wave system in fig.

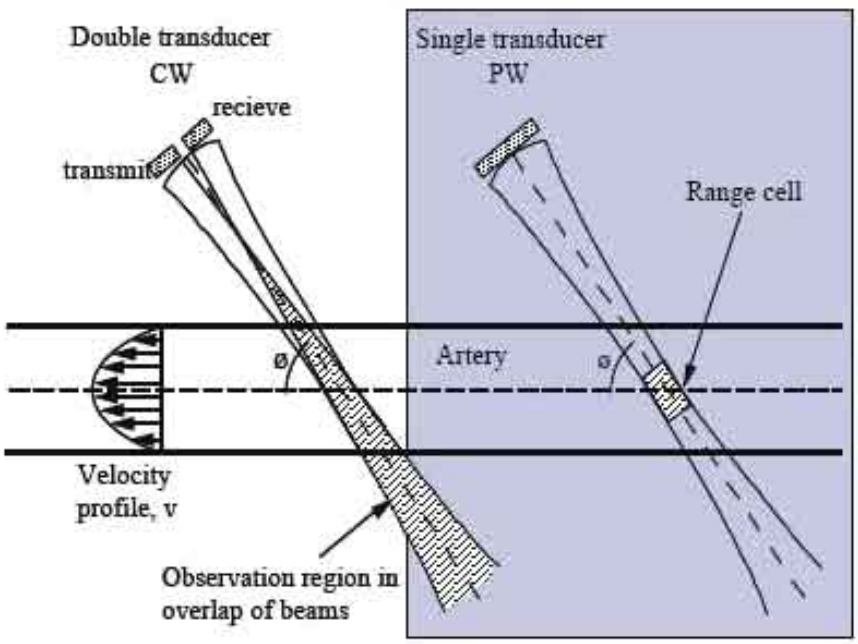

FIGURE 2.16: Comparison of the Continuous Wave system with the Pulsed Wave System. In the PW-implementation, only a limited sample volume is insonified, and the same transducer is used for transmitting and receiving ultrasound waves. This figure was adapted from [24].

2.11, subsequent RF-lines are gathered to estimate the shift in scatterer position, and this is done for a number of lateral scanlines composing the color flow image.

2.3.1 Principles

According to equation 2.20, the velocity of a scatterer is related to the frequency of the slow-time waveform f_{slow}, which is obtained after sampling subsequently acquired RF-signals, as illustrated in fig. 2.11. Consequently, for an ensemble of scatterers, the mean axial velocity $\bar{v}_z$ can be derived from the mean angular frequency $\bar{\omega}_{slow}$, using equation 2.20:

$$\bar{v}_z = \frac{c\bar{\omega}_{slow}}{2\omega_0} \tag{2.30}$$

with ω_0 the angular frequency corresponding to the received centre frequency. Since the velocity estimate is derived from ω_{slow}, it is subject to the velocity limits as presented in section 2.2.2.

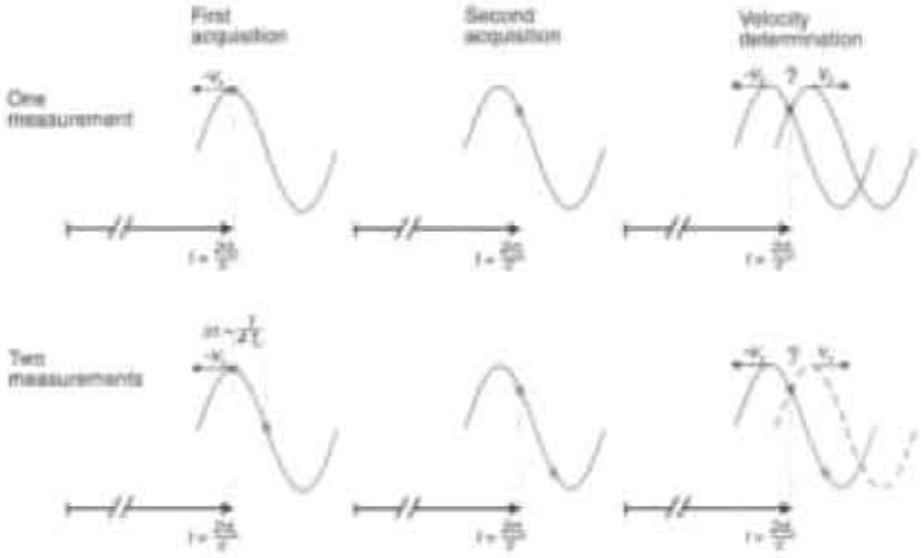

FIGURE 2.17: Appropriate sampling is necessary to determine the flow direction in pulsed wave methods. In case only 1 measurement is performed for each centre frequency period of the received signal, direction ambiguity arises, as illustrated in the top row of the figure. When acquiring two samples per received signal, within a distance of $1/4f_0$, also called quadrature sampling, the direction ambiguity is resolved. This figure was adapted from chapter 6 of [23].

The most intuitive approach in finding ω_{slow} is illustrated below. In case of M pulse emissions, the mean angular frequency for the mth transmission is related to the phase change in the time interval T_{prf};

$$\omega_{m,pw} = \frac{\phi_m - \phi_{m-1}}{T_{prf}} \tag{2.31}$$

The instantaneous phase of the mth received signal is calculated as $atan(\frac{Q(m)}{I(m)})$ using the IQ-demodulated form of the received signal.

$$\omega_{m,pw} = \frac{atan(\frac{Q(m)}{I(m)}) - atan(\frac{Q(m-1)}{I(m-1)})}{T_{prf}} \tag{2.32}$$

This estimate is however only based on two received lines, and often more lines are employed to improve the estimate. Following approach is then considered. The mean angular frequency can be calculated using the power density spectrum $\Phi(\omega)$:

$$\bar{\omega} = \frac{\int_{-\infty}^{\infty} \omega\Phi(\omega)d\omega}{\int_{-\infty}^{\infty} \Phi(\omega)d\omega} \tag{2.33}$$

Estimating the power density spectrum is however a computational complex approach, and the Wiener-Khinchin relation [37] is crucial in solving this issue. This theorem provides a fundamental link between the time- and frequency domain properties of complex processes. It states that the power density spectrum forms a Fourier transform pair with the autocorrelation function $R(\tau)$ of the considered signal:

$$R(\tau) = \frac{1}{2\pi}\int_{-\infty}^{\infty} \Phi(\omega)exp(i\omega\tau)d\omega \tag{2.34}$$

For random processes, the autocorrelation function is the correlation between observations of a process 's' at two different points in time, as a function of the time difference τ. For a process 's' sampled with the pulse repetition period T_{prf}, the autocorrelation function for subsequent observations can be estimated as:

$$\hat{R}(T_{prf}) = \frac{1}{M-1}\sum_{m=1}^{M-1} s(m)s^*(m-1) \tag{2.35}$$

with m corresponding to the m^{th} received signal in a total number of M transmissions.

Since the power density spectrum is related to the autocorrelation function, $R(\tau)$ or its estimate can be used to find ω_{slow}. When calculating the first and second order derivative of the autocorrelation function using equation 2.34 ($\dot{R}(\tau)$ and $\ddot{R}(\tau)$), one can derive the mean angular frequency of the slow time waveform ω_{slow} according to equation 2.33:

$$\hat{\bar{\omega}}_{slow} = -i\frac{\dot{R}(0)}{R(0)} \tag{2.36}$$

The autocorrelation function of the demodulated IQ signal is a complex valued function, and can consequently be written in polar form:

$$R(\tau) = A(\tau)exp(i\phi(\tau)) \tag{2.37}$$

This allows expressing the mean angular frequency ω_{slow} as a function of the phase of the autocorrelation function $\phi(\tau)$, and equation 2.36 can be reformulated as:

$$\hat{\bar{\omega}}_{slow} = \dot{\phi}(0) \tag{2.38}$$

We then obtain the following expression for $\hat{\bar{\omega}}_{slow}$, using a first-order Taylor expansion for $\phi(\tau)$:

$$\hat{\bar{\omega}}_{slow} = \frac{\phi(T_{prf}) - \phi(0)}{T_{prf}} \approx \frac{\phi(T_{prf})}{T_{prf}} \tag{2.39}$$

The last approximation is valid because $\phi(\tau)$ is an odd real function. This can be further linked with the autocorrelation function:

$$\hat{\bar{\omega}}_{slow} = \frac{1}{T_{prf}} arctan\left(\frac{Im(\hat{R}(T_{prf}))}{Re(\hat{R}(T_{prf}))}\right) \tag{2.40}$$

The autocorrelation function in these equations can be approximated using equation 2.35, taking into account s(m) is a complex signal consisting of an in-phase and quadrature component, s(m)=I(m)+iQ(m). The final expression for the velocity estimate is given as:

$$\hat{\bar{v}}_z = \frac{c}{2T_{prf}\omega_0} atan\frac{\sum_{m=1}^{M} Q(m)I(m-1) - Q(m-1)I(m)}{\sum_{m=1}^{M-1} I(m)I(m-1) + Q(m)Q(m-1)} \tag{2.41}$$

The arctan function is limited to the $-\pi \rightarrow +\pi$ interval, confirming the maximal measurable velocity mentioned in section 2.2.2.

As can be seen in equation 2.41, the autocorrelation method estimates the temporal derivative of the phase with a first order difference equation. The derivative could be more closely approximated using a higher order difference equation. But an increased packetsize is needed then, and the averaging is performed over less estimates. Barber et al [38] showed no improvement when using a higher order difference equation to approximate the temporal derivative of the phase.

An important advantage of the autocorrelation method is the absence of a bias on the estimates, even under poor SNR conditions. When taking into account the frequency dependent effects of scattering and attenuation, depth dependent errors may occur in the velocity estimates, although very small for narrowband methods as demonstrated by Evans and McDicken [19]. These frequency dependent mechanisms, however, hamper the use of very short pulses in the autocorrelation method. For time shift estimation techniques (cfr. section 2.4), these frequency dependent errors do not affect results, since merely a time shift is detected.

The quality of the velocity estimate can be assessed through the variance, which also gives an indication of the spread of the velocities in the range gate. A high variance may indicate the presence of turbulent flow. In clinical applications, the variance is often visualized using a green color-code added to the traditional color flow image scale, as shown in fig. 1.27. Using the autocorrelation approach, the variance can be obtained as:

$$\sigma^2 = \frac{\int_{-\infty}^{\infty} (\omega - \bar{\omega})^2 \Phi(\omega) d\omega}{\int_{-\infty}^{\infty} \Phi(\omega) d\omega} \tag{2.42}$$

or using the Wiener-Khinchin theorem:

$$\sigma^2 = \frac{\dot{R}(0)^2}{R(0)} - \frac{\ddot{R}(0)}{R(0)} \tag{2.43}$$

As can be seen in equation 2.43, the power of the received signal R(0) should be calculated to obtain the variance. The variance increases with velocity and decreases with pulse duration. Because a long pulse is beneficial, the autocorrelation method is often referred to as a narrowband method. The variance on the estimate can be further reduced

by spatial averaging and to a lesser extent by increasing the packet size M of transmissions. This is however potentially at the cost of decorrelation of the signal due to scatterers moving in and out of the sample volume. Increasing the packet size also decreases the frame rate.

2.4 Color flow imaging using time shift estimation

2.4.1 Principles

Time shift estimation has been implemented in CFI-systems to overcome the aliasing limitation present in phase shift techniques. However, this comes at the cost of increased computational times and potential spurious detection errors, as will be explained further. For the time shift estimation technique, the scatterer velocity can be derived using equation 2.19:

$$v_z = \frac{c\Delta\tau}{2T_{prf}} \tag{2.44}$$

with $\Delta\tau$ the change in delay between successively received signals due to the scatterer's motion, and T_{prf} the pulse repetition period. Hence, the time shift method is based on reliably estimating $\Delta\tau$.

Cross-correlation is performed between range-gated portions of subsequently acquired RF signals, to find the time shift $\Delta\tau$ that gives the best match between successive lines. The cross-correlation estimate of two successive signals $y_n(t)$ and $y_{n+1}(t)$ over the range gate is calculated as:

$$\hat{R}(s, N_0) = \frac{1}{N_S} \sum_{l=0}^{N_S-1} y_n(N_0 + l) y_{n+1}(N_0 + l + s) \tag{2.45}$$

with N_0 the first sample of the range gate, s denoting the lag between the signals, and N_s the total number of samples within the range gate. As shown in fig. 2.18, the maximum in the cross-correlation function corresponds to the correct $\Delta\tau$ and velocity. This way, the most dominant scatterer movement in the sample volume is detected, rather than the mean velocity as for phase shift methods. To obtain a reliable estime, the time shift should be averaged over several transmissions. A good estimate of the time shift requires that the correlation coefficient is larger than 0.5 [20] (in practice, it will never reach its theoretical

maximum of 1). In general, large transducer bandwidths resulting in high axial resolution, large range gates and an increased number of RF-lines used for averaging the time shift, may improve the estimate.

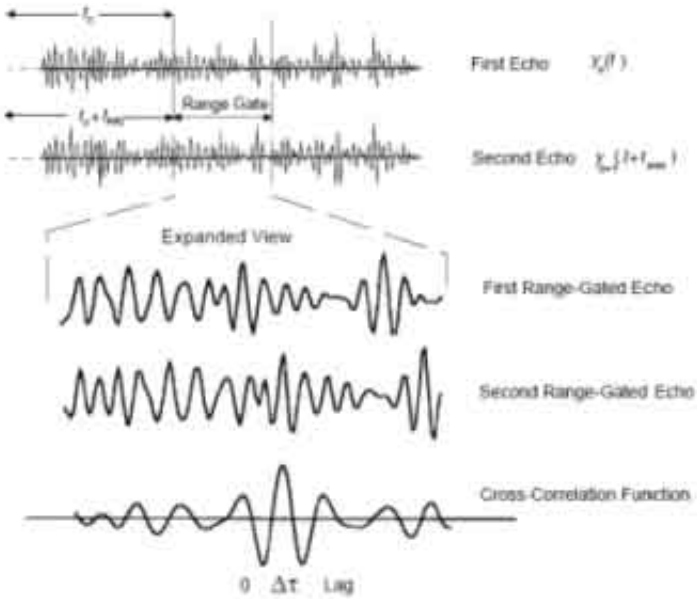

FIGURE 2.18: The cross-correlation procedure used in time shift estimators. The subsequently acquired RF-signals in a range gate give rise to a cross-correlation function. The maximum of this function results in the correct time shift. This figure was adapted from chapter 10 of [20].

However, erroneous peaks may occur in the cross-correlation function, so that a velocity different from the true velocity is detected. Possible decorrelation sources are:

1. Scatterers moving too quickly and leaving the sample volume during the estimation procedure. This may especially occur when the velocity is higher than the Nyquist limit for phase shift estimation.
2. Limitations on the sampling rate. High sampling rates improve the tracking accuracy, but are limited by the hardware of the receiving transducer.
3. High noise levels.
4. Modulation of the RF-signal by the spatially variant beam profile.
5. Velocity dispersion in case of turbulent flow.
6. Clutter filtering: the removal of the tissue signal (cfr. section 2.5). Scatterer velocities near the clutter filter transition region are affected.

2.4.2 Velocity limits

For time shift estimation, the velocity limits differ from what was presented in section 2.2.2 for pulsed wave systems. The maximal velocity is related to the distance traveled by ultrasound in the considered range gate in between pulse transmissions:

$$v_{max} = \frac{l_{range}}{T_{prf}} = \frac{cN_s}{2f_s}\frac{1}{T_{prf}} \tag{2.46}$$

with f_s the sampling frequency of the RF-data. Under favourable SNR conditions, this maximum velocity is typically higher than the Nyquist velocity of phase shift techniques, and is only limited by the need for the scatterers to remain within the sample volume during the observation time. The minimal detectable velocity is related to the sampling frequency f_s:

$$v_{min} = \frac{cPRF}{2f_s} \tag{2.47}$$

However, interpolation techniques are often applied in practice to detect sub-sample shifts.

2.4.3 System implementation

Time shift estimation has some specific implementation issues. It should be noted that the time shift estimator tracks velocities based on the RF-signals, not on the IQ-demodulated signals as in the phase shift estimator. Short pulses (wideband signals) result in high resolution RF-data, improving the tracking accuracy. Hence, the applied pulse lengths are short and similar to those used in B-mode imaging. The sampling frequency of the RF-signals should be high, at least four times the highest frequency component in the signal. This is because the cross-correlation procedure multiplies two signals, introducing a frequency component at the sum of the two frequencies. Interpolation techniques may also help improving the velocity resolution.

2.4.4 Comparison with phase shift techniques

The absence of aliasing artifacts is a main advantage of time shift estimation. Further, its robustness to frequency-dependent mechanisms is an improvement over phase shift estimation. The latter technique uses the RF centre frequency in the velocity estimation (cfr. equation 2.41), most often assumed to be the centre frequency of the transmitted pulse f_0. However, for wideband pulses, the received centre frequency

is affected by frequency dependent attenuation, scattering and random fluctuations of the scatterers in the sample volume. Methods have been proposed to estimate the mean RF frequency of the data in the range gate to correct this [34].

The main disadvantage of time shift estimation, however, is the high computational time. Many computations need to be performed because of the high sampling rates and because all the samples in the range gate are involved in the estimation procedure (only one sample per range gate in phase shift estimation). Methods have been developed to decrease the computational complexity, just using the sign of the RF-signal in the cross-correlation approach [39], showing similar results as the full cross-correlation procedure.

Further, cross-correlation benefits from using short pulses (wideband signals), which are however more susceptible to noise. Under poor SNR conditions, longer pulses are beneficial to increase sensitivity and the bandwidth should be reduced. In this case, the superior performance of the time shift method decreases and has comparable performance to the phase shift method [40]. Still, most commercial systems rely on phase shift techniques, which suggests that any gain resulting from using cross-correlation techniques is not cost effective.

2.5 CLUTTER FILTERING

When imaging blood flow, signal from the surrounding tissue is also present in the vessel lumen due to beam sidelobes and reverberations. However, the amplitude and Doppler frequency content of this tissue signal differs much from the blood signal. First of all, the tissue signal has a much higher amplitude compared to the weak scattering from blood, and is often 20 to 60 dB stronger. Further, the vessel wall tissue is slowly moving compared to blood flow, creating a low frequency component (below 1 kHz) in the Doppler frequency spectrum. This can be particularly troublesome for detecting low blood velocities near the vessel wall. To obtain accurate flow velocities, these *high amplitude-low frequency* clutter signals should be removed. Especially for color flow imaging, using a limited number of samples for velocity estimation, this can be a challenging task. In the next paragraphs, different types of clutter filtering are discussed in the context of CFI.

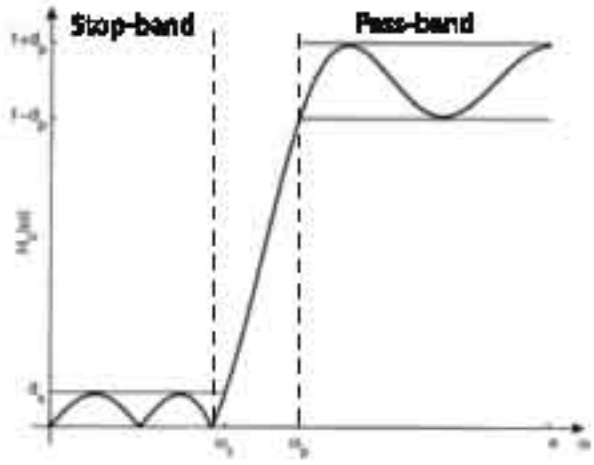

FIGURE 2.19: Characteristics of the frequency response of a high pass clutter filter. This figure was adapted from [41].

2.5.1 Principles

Velocity estimation in CFI is based on transmitting and subsequently receiving a packet of N signals (cfr. section 2.2). This packet of 'slow-time' samples is filtered before the actual velocity estimation, for each beam direction seperately. We will further represent the packet of unfiltered slow-time samples with the vector x=[x(0),x(1)...x(N-1)], and the filtered output with the vector y=[y(0),y(1)...y(M-1)]. Notice that the output has a dimension M, potentially differing from the dimension N of the input vector. If one considers linear filtering, a general filtering operation can be expressed with a matrix multiplication:

$$y(n) = \sum_{k=0}^{N-1} a(n,k)x(k) \tag{2.48}$$

with a(n,k) denoting the filter matrix A.

The effect of the clutter filter on the frequency content in the Doppler signal x, can best be described using the frequency response $H_0(\omega)$ of the filter. Fig. 2.19 shows the frequency response of a high-pass filter for clutter filtering. The range of frequencies attenuated by the clutter filter is called the stopband, which has a cut-off frequency ω_s. The deviation from zero in the stopband (d_s) should be as small as possible to get sufficient attenuation. The range of frequencies, passing unaltered through the filter, is called the passband. For this purpose, the ripple

d_p should be minimized. Finally, the stopband cut-off frequency ω_s should be as close as possible to the passband cut-off frequency ω_p, to obtain a narrow transition band, improving clutter attenuation. In case of a wide transition band, too many blood velocities are attenuated, and only high blood flow can be measured accurately.

2.5.2 Finite impulse response (FIR) filter

In general, the output y(n) of an FIR filter of order K-1 can be written as:

$$y(n) = \sum_{k=0}^{K-1} h(k)x(n-k) \tag{2.49}$$

with h(k) the impulse response of the filter. Equation 2.49 demonstrates that a filtered sample is only dependent on current and past input samples x(n-k). The output is only valid if all the filter registers are filled up with input data. Therefore, if the scan acquisition emits a packet of N signals, and the FIR-filter has an order K-1, the number of valid output samples is N-K+1. Hence, the number of output samples is reduced, which is an important drawback of FIR-filters. Real-time flow imaging techniques like CFI use only a limited number of samples, and decreasing the packetsize increases the variance on the estimate. Using higher order filters has however the benefit that narrow transition bands can be designed.

Note that the FIR-filter is time-invariant: each filtering of a slow-time sample uses the same filtering coefficients for the present and K-1 past samples. This means that each row in the filter matrix A (cfr. equation 2.48) is identical, except for a simple time shift [41].

2.5.3 Infinite impulse response (IIR) filter

An IIR-filter uses past and present input samples, like an FIR-filter, but also uses past output samples:

$$y(n) = -\sum_{k=1}^{K} a_k y(n-k) + \sum_{k=0}^{K} b(k)x(n-k) \tag{2.50}$$

Since past output samples are used, the IIR filter is a system with a feedback loop. Such a system has a transient response, and after a large number of input samples (an infinite number in theory), a steady-state

response is reached. However, in CFI, only a limited number of samples is available, and the steady-state response is not reached in the available observation time. With appropriate initialization, the transient response can be surpressed. Several initialisation techniques have been proposed and we refer to [41] for an overview.

Because more information is used in this filter compared to the FIR-filter, lower order filters can achieve much steeper transition bands. However, because past output samples are used, the IIR-filter is time-variant.

2.5.4 Polynomial regression filter

This approach is based on the fact that the slowly varying clutter signal can be approximated by a low-order polynomial function. The filter models the clutter signal using a set of curve shapes (typically Legendre polynomials), which in a vector space formulation span a subspace of the received signal space, called the *clutter space*. The best least-squares fit of the clutter signal to the proposed polynomial set is calculated. If b_k is a set of orthonormal basis vectors spanning the clutter space (index k referring to the filter order), the filtering procedure can be written as the projection of the received signal x onto the complement of the clutter space:

$$y = (I - \sum_{k=0}^{M-1} b_k b_k^{*T})x \tag{2.51}$$

I is the identity matrix, and M-1 is the order of the filter. Advantage is that there is no loss in output samples, as for FIR-filters, reducing the variance of the estimate. However, the filter is time-variant, which means that each output sample is filtered with a different FIR-filter. In case of a time-invariant filter, each row of the filter matrix is identical, except for a simple time-shift, which means that the filter coefficients are shifted one column for each output sample. However, the symmetrical projection matrix $b_k b_k^{*T}$ does not fulfill this condition.

2.5.5 Overview

The frequency response of the FIR-filter, IIR-filter and polynomial regression filter is shown in fig. 2.20. The exact form of the frequency response of the IIR and regression filter depends on the packetsize. For the IIR-filter, a higher packetsize means more output samples are used

in the feedback loop, increasing the filter performance. For the regression filter, the shape of the clutter curve is better approximated when using a large packetsize. Further, the regression filter has the most attractive transition band, but also the largest bias in this region. In the passband, all filters have negligible bias [41].

2.6 ULTRASONIC FLOW IMAGING IN 2D

2.6.1 Speckle tracking (ST)

The previously presented 1D Doppler methods are hampered by aliasing and the angle dependence between the ultrasound beam and the flow direction. To overcome these limitations, 2D flow imaging methods have been developed, with speckle tracking one of the major research lines. This method is the multidimensional extension of the 1D cross-correlation procedure presented for CFI (section 2.4). Using appropriate pattern matching techniques, the speckle patterns arising from blood can be tracked in the 2D imaging plane or even in the 3D imaging volume, and a map with blood velocity vectors can be derived. Because ultrasound probes for 3D vascular applications have yet to come onto the market, we focus on 2D tracking, but the basic principles can be extended to 3D if one disposes of a 2D linear array probe.

Fig.2.21 shows the basic principles behind speckle tracking. A kernel is identified in a first acquisition, and is tracked inside a surrounding

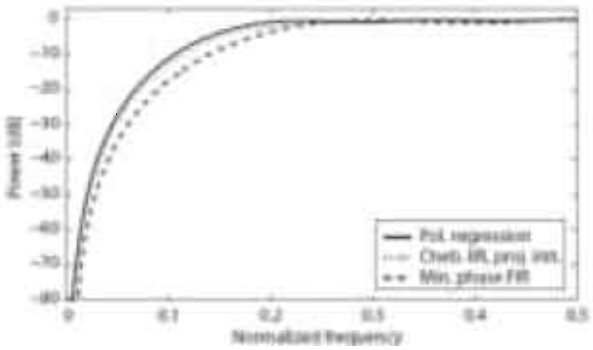

FIGURE 2.20: Comparison of the FIR-filter, a Chebychev IIR-filter (projection initialization, [41]), and polynomial regression filter (fourth order). The attenuation (dB) is shown versus the frequency normalized to the Nyquist limit. This figure was adapted from [41].

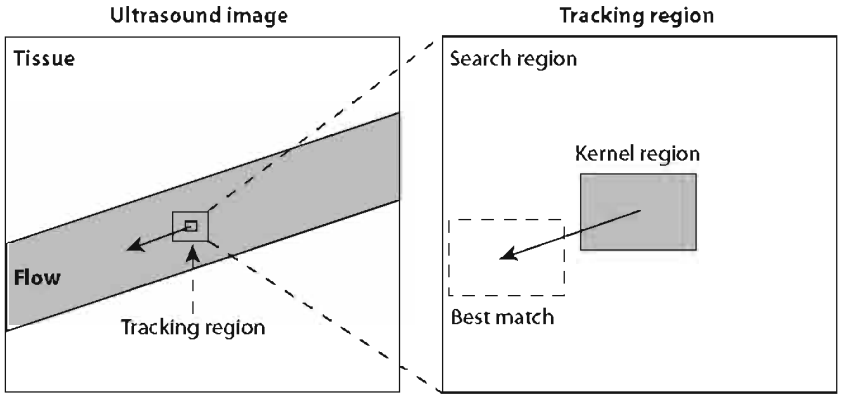

FIGURE 2.21: The basic principles of speckle tracking. A kernel is identified in a first acquisition and a best match is searched for in a search region of a next acquisition. This figure was adapted from [26].

search region in a next acquisition. The 2D velocity vector is determined by the best match of the kernel inside the search region. When this is performed for several kernels in a region of interest, a blood flow velocity map can be generated. The size of the kernel and search region influences the tracking performance. In general, large kernels improve tracking accuracy because they are more unique and less susceptible to noise. However, in the case of large spatial flow gradients, this might not hold anymore. Further, large kernels reduce the spatial resolution of the velocity map. The size of the search region determines the velocity range which can be measured.

Several methods have been proposed to track speckle patterns from blood flow. Cross correlation algorithms have been investigated, trying to match a kernel in acquisition X_0, inside a search region of the next acquisition X_1:

$$\rho(\alpha,\beta) = \frac{\sum_{i=1}^{l}\sum_{j=1}^{k}(X_0(i,j)-\bar{X}_0)(X_1(i+\alpha,j+\beta)-\bar{X}_1)}{N} \tag{2.52}$$

and the normalization factor N is:

$$N = \sqrt{\sum_{i=1}^{l}\sum_{j=1}^{k}(X_0(i,j) - \bar{X}_0)^2} \cdot \sqrt{\sum_{i=1}^{l}\sum_{j=1}^{k}(X_1(i+\alpha, j+\beta) - \bar{X}_1)^2} \quad (2.53)$$

The cross-correlation coefficient $\rho(\alpha, \beta)$ is calculated for each possible kernel displacement (α, β) in the search region. $\bar{X}_0$ and $\bar{X}_1$ are the spatial mean values of the corresponding regions, and l and k are the lateral and axial dimensions of the kernel.

However, the sum-absolute-difference (SAD) algorithm is nowadays preferred, since it is less computationally complex, and produces similar results as the cross-correlation method as demonstrated by [42]:

$$e(\alpha, \beta) = \sum_{i=1}^{l}\sum_{j=1}^{k}(X_0(i,j) - X_1(i+\alpha, j+\beta)) \quad (2.54)$$

with e the SAD-coefficient, representing the error of matching a kernel X_0 inside a search region X_1. For each possible kernel displacement (α, β), the SAD-coefficient is calculated, resulting in an SAD-matrix. The minimal value in the SAD-matrix corresponds to the (α, β) displacement used to calculate the velocity magnitude and angle.

The performance of these speckle tracking methods may depend on whether RF-data or envelope data are used during tracking. The 1D cross-correlation procedure presented in section 2.4 was based on the RF-data, but showed limitations with respect to sampling requirements and spurious detection errors. For the sake of computational simplicity, envelope data may be used in 2D. Furthermore, it has been demonstrated that using high frequency transducers and limited sampling rate, the envelope data may result in superior performance over RF-data [43].

When tracking rapid displacements as in arterial blood flow, spatial and temporal resolution of the imaging system is crucial. The spatial resolution of the estimated scatterer movement is limited to an integer number of beam and range samples. Especially in the poorly sampled

lateral direction, interpolation techniques become important. Interpolation may be performed on the envelope data, and tracking accuracy can be further increased by interpolating the SAD-matrix.

High temporal resolution can be obtained using the beam interleaved acquisition, mentioned in section 1.3.3. Speckle images are then obtained in smaller lateral subregions at a rate of PRF. The tracking algorithm is performed within the interleave group since there is no correlation between interleave groups. Another option is to track the speckle patterns within regions of simultaneously received beams [44]. We refer to section 1.3.3. for more explanation about parallel receive beamforming. Final alternative is to use plane wave imaging [45], allowing very high frame rates of the complete lateral scanwidth, but the downside is the unfocused ultrasound beam.

Decorrelation of the speckle pattern is the major limitation of this 2D flow imaging technique, and may potentially be caused by:

(1) blood flow out of the imaging plane, further called 'out-of-plane flow'
(2) high spatial velocity gradients
(3) high temporal velocity gradients.

As for the CFI-techniques, clutter filtering is crucial for proper functioning of the speckle tracking methods. IIR and polynomial regression filter are not suitable for speckle tracking due to their time-variant nature. Time-variant means that each output sample is basically filtered with a different FIR filter. The speckle pattern may therefore change for each output sample within a packet, and the basis for tracking is therefore suboptimal. Hence, using an FIR-filter is appropriate due to its time-invariant nature. Clutter filtering can however be hampered when only lateral flow is present. The Doppler shift is then about zero and traditional clutter filters will remove most of the blood signal.

2.6.2 Compound Doppler

By combining Doppler measurements from different angles, a multidimensional velocity estimate can be obtained. The past decades, several systems have been proposed to receive Doppler signal from two different directions. Single and multiple transducer setups have been used, but in the context of CFI, two main methods are relevant [46]:

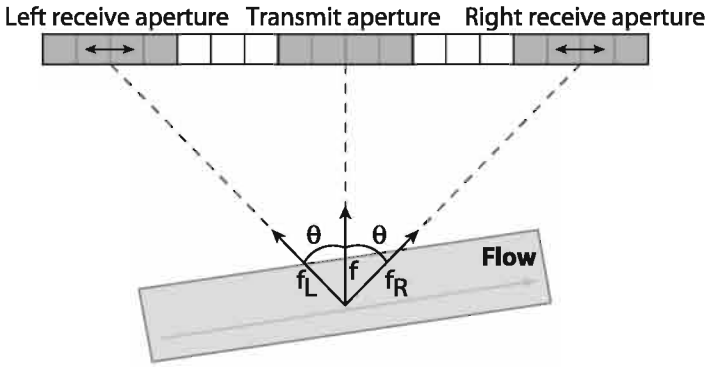

FIGURE 2.22: The crossed-beam vector Doppler technique: a single transducer is seperated in a central transmit aperture and two receive apertures on the side. The Doppler shifts received by both receive apertures are combined to obtain the lateral and axial velocity estimate. This figure was adapted from [26].

(1) regular CFI measurements are performed along different scanning directions and the estimates for the different angles are combined afterwards
(2) a transducer is split into a central transmit aperture and two receive apertures on the sides, allowing to simultaneously perform measurements along two different scanning directions (cfr. fig.2.22)

Since the latter technique is applied in this dissertation, we will further focus on this method, referred to as crossed-beam vector Doppler (VD). For a full overview on previously proposed vector Doppler systems we refer to [46]. The axial v_{ax} and lateral velocity v_{lat} component can be derived using the following equations [47]:

$$v_z = \frac{c(f_l - f_r)}{2f_0 sin(\theta)}, v_x = \frac{c(f_l + f_r)}{2f_0(1 + cos(\theta))} \tag{2.55}$$

with θ the angle between the transmit and receive aperture, and f_l and f_r the Doppler shifts from the left and right receive aperture, as estimated by the phase shift estimator used in CFI (cfr. section 2.3). To obtain constant image properties throughout depth, the angle should be kept constant throughout depth by sliding the receive apertures towards the edges of the transducer for larger depths. A sufficient angle θ should be applied to achieve reasonable lateral velocity estimates. However, the finite size of the transducer limits the possible angles, as well as the applied aperture sizes.

2.7 Vessel wall tracking based on an autocorrelation technique

Finally, we also want to briefly mention that the autocorrelation technique, as previously discussed for blood flows, is also employed to assess vessel wall mechanics. Rabben et al [5] developed a method to measure arterial distension, based on a modified autocorrelation estimator, which accurately estimates the tissue velocity by compensating for a potential downshift of the received centre frequency due to attenuation. The vessel wall motion is then tracked by integrating the tissue velocities:

$$z(t + \Delta t) = z(t) + v(t)\Delta t \tag{2.56}$$

with z(t) the position in the vessel wall, v(t) the estimated tissue velocity, and Δt the time resolution of the measurement method or more specifically the packetsize times the pulse repetition frequency. As the tissue velocity is typically much slower than arterial flow velocity, the PRF is chosen lower than in blood flow applications. Also the required packetsize is smaller since higher order clutter filters are not necessary. In general, a high resolution imaging setup, entailing short pulses, is necessary to track the tissue velocities due to the narrow vessel wall thickness. The accuracy of this method is assessed in chapter 9.

CHAPTER 3

Ultrasound simulations

3.1 Introduction

Computational simulations of medical images have proven useful in comprehending and ameliorating existing imaging techniques. When of a sufficient realism, they may provide a flexible and versatile tool in the design and development of existing and new imaging modalities. Besides ultrasonic imaging, the development of other imaging disciplines like computed tomography (CT) [48] and magnetic resonance imaging (MRI) [49] has also been supported by simulations.

In this dissertation, the Field II ultrasound simulation software developed by Jensen et al [17, 18] was applied, which is based on physical models for ultrasonic wave propagation. By means of a numerical approximation of the spatial impulse response of the transducer, this type of simulator allows to model arbitrary transducer geometries, scansequencing and beam formation with great flexibility. The tissue (including blood, vessel wall, ...) is modeled as a homogeneous medium represented by an ensemble of point scatterers on which the ultrasound waves reflect. The reflection strength of each point varies according to a scattering amplitude distribution.

This chapter is mainly based on the course notes *Linear description of ultrasound imaging systems* by Jensen [50].

3.2 Field II ultrasound simulation model

3.2.1 Concept of the spatial impulse response

The Field II software developed by Jensen [17, 18] simulates the backscattered RF-signals using a linear description of ultrasound imaging systems. A linear time-invariant system is fully characterized by its impulse response h, which allows to calculate the system's output signal y for an arbitrary input signal x via the following convolution:

$$y(t) = h(t) * x(t) = \int_{-\infty}^{+\infty} h(\tau)x(t-\tau)d\tau \tag{3.1}$$

The impulse response of an ultrasound imaging system can be found by exciting each array element of the transducer with a delta pulse, and measuring the generated pressure field with a hydrophone. The spatially dependent part of the impulse response is further referred to as $h(\vec{r}_1, t)$, with $\vec{r}_1$ representing the observation point. The Field II program uses a numerical derivation of the system's spatial impulse response to calculate the emitted and received pressure fields. The impulse response measured with a hydrophone however also includes the electro-acoustical excitation.

3.2.1.a Emitted pressure field

For any excitation of the transducer, the *emitted pressure field* p_e can be found by temporal convolution of the spatial impulse response (m/s) with the excitation pulse $e(t)$, also taking into account the conversion of electrical to acoustic energy with the electro-acoustic conversion impulse response $g_T(t)$ (cfr. section 1.3.4):

$$p_e(t) = e(t) * g_T(t) * h(\vec{r}_1, t) \tag{3.2}$$

The convolution of the excitation pulse and the impulse response of the electro-acoustic coupling results in a transducer vibration, characterized by a velocity v_n normal to the transducer surface. Based on the Rayleigh diffraction integral for a rectangular piston, it can be shown that the emitted pressure field is then given by [51]:

$$p_e(\vec{r}_1, t) = \rho_0 \frac{\partial v_n}{\partial t} * h(\vec{r}_1, t) \tag{3.3}$$

with $\frac{\partial v_n}{\partial t}$ the acceleration of the transducer surface and ρ_0 the density of the medium.

3.2.1.b *Received pressure field*

The spatial impulse response is also used for calculating the *received pressure signal* p_r. It can be derived that p_r is a temporally and spatially smoothed version of the backscattered signal $f_m(\vec{r}_1)$, arising due to inhomogeneities in the tissue, i.e. density ($\Delta\rho$) and propagation velocity (Δc) perturbations, located in the field at $\vec{r}_1$.

$$f_m(\vec{r}_1) = \frac{\Delta\rho(\vec{r}_1)}{\rho_0} - \frac{2\Delta c(\vec{r}_1)}{c_0} \tag{3.4}$$

with ρ_0 and c_0 the mean density and wavespeed of the medium. The received field $p_r(\vec{r}_2, t)$ can then be formulated as the *temporal* convolution ($*_t$) of the inhomogeneity term f_m with the electro-acoustical excitation, as well as a *spatial* convolution ($*_r$) of f_m with the pulse-echo spatial impulse response $h_{pe}(\vec{r}_1, \vec{r}_2, t)$:

$$p_r(\vec{r}_2, t) = v_{pe}(t) *_t f_m(\vec{r}_1, t) *_r h_{pe}(\vec{r}_1, \vec{r}_2, t) \tag{3.5}$$

with $\vec{r}_2$ denoting the position of the transducer (cfr. fig. 3.1). Equation 3.5 can be further explained as follows. The term $v_{pe}(t)$ is the pulse-echo wavelet including the electro-acoustical impulse response on transmit and receive, $g_T(t)$ and $g_R(t)$ respectively:

$$v_{pe}(t) = \frac{\rho_0}{2c^2} g_R(t) *_t g_T(t) *_t \frac{\partial^3 v}{\partial t^3} \tag{3.6}$$

The pulse-echo spatial impulse response is defined as the temporal convolution of the spatial impulse response on transmit and receive:

$$h_{pe}(\vec{r}_1, \vec{r}_2, t) = h(\vec{r}_1, \vec{r}_2, t) *_t h(\vec{r}_2, \vec{r}_1, t) \tag{3.7}$$

It should be noted that equation 3.5 does not include multiple scattering.

As demonstrated in the previous paragraphs, the spatial impulse response plays a crucial role in calculating the emitted and received pressure fields, and the exact form of h can be found using *Huygens' principle*. This theorem states that each point on the radiating surface is the origin of an outgoing spherical wave. The principle is demonstrated in fig. 3.1, showing that each point on the transducer emits a spherical wave with radius $|\vec{r}| = ct$, at a fixed time instance t. Each spherical wave is given by:

$$p_{spherical} = \frac{\delta(t - \frac{|\vec{r}_1 - \vec{r}_2|}{c})}{2\pi |\vec{r}_1 - \vec{r}_2|} \tag{3.8}$$

Figure 3.1: Panel A shows the imaging setup: $\vec{r}_1$ denoting the field point and $\vec{r}_2$ indicating the transducer. Huygens' principle is illustrated in panel B: the transducer is a collection of point sources simultaneously radiating spherical waves, with a radius $|\vec{r}| = ct$. The impulse response is more compact on the imaging axis compared to off-axis. This figure was adapted from [50].

with δ denoting the Dirac delta function. As indicated in fig. 3.1, $\vec{r}_1$ is the field point and $\vec{r}_2$ is the position of the transducer. For a rigid baffle, the spatial impulse response is then found by observing a point in time, and summing all the emitted spherical waves passing by:

$$h(\vec{r}_1, t) = \int_S \frac{\delta\left(t - \frac{\vec{r}_1 - \vec{r}_2}{c}\right)}{2\pi \left|\vec{r}_1 - \vec{r}_2\right|} dS \tag{3.9}$$

The ultrasound probe induces a spatial variance in the impulse response, demonstrated in fig. 3.1, with a more compact response on the imaging axis, and a longer response off-axis.

3.2.2 Numerical calculation of the spatial impulse response

Calculating the surface integral described in equation 3.9 becomes challenging for complex transducer shapes and apodizations. Therefore, the Field II program simplifies the calculation procedure using the *acoustic reciprocity theorem*. This principle states that the source and receiver can be interchanged in an unchanging environment, in case of a small source and receiver. In our setup, switching source and receiver means that the emitting aperture turns into a receiver and an observation point in the field becomes a source.

Using this approach, the spatial impulse response is calculated by finding, for each time instance, the intersection of the aperture with the

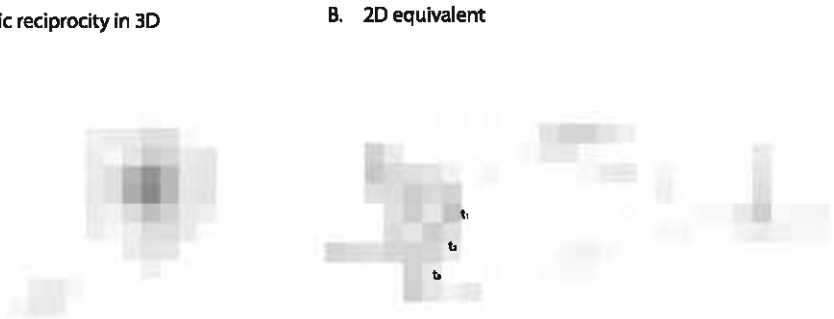

FIGURE 3.2: Panel A shows the principle of acoustic reciprocity for a radiating triangle. The field point becomes the source, emitting spherical waves intersecting the aperture. Panel B shows the 2D equivalent of panel A. Each time instance t (see t_1, t_2 and t_3), the relative length of the intersection determines the spatial impulse response. This figure was adapted from [50].

spherical wave originating from a field point. This principle is illustrated in panel A of fig. 3.2. The field point (acting as source) is projected on the plane of the aperture, and the intersections of the emitted spherical waves with the aperture are determined. Each time instance t_i, a different circular intersection contributes to the spatial impulse response (cfr. panel B of fig. 3.2), and it is the *relative length* of these intersections which determines the spatial impulse response. Indeed, it can be derived that the spatial impulse response at time t is equal to:

$$h(\vec{r}_1, t) = \frac{(\theta_2 - \theta_1)c}{2\pi} \tag{3.10}$$

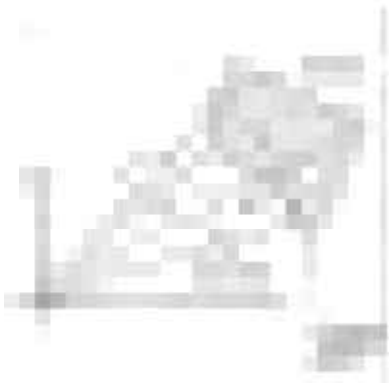

FIGURE 3.3: Indication of the θ-angles determining the intersection of the spherical wave, and hence the spatial impulse response. This figure was adapted from [50].

with θ_1 and θ_2 the angles marking the beginning and ending of the circular intersection (cfr. fig. 3.3). As the impulse response is dependent on the angular spread of the intersecting arc, discontinuities only occur in $h(\vec{r}_1, t)$ when an edge or corner of the aperture is met. The impulse response has been derived for circular and polygonal aperture shapes in [52].

Fig. 3.4 gives an example of an impulse response for a rectangular aperture and an observation point on the imaging axis. As long as no spherical waves reach the aperture, the response is zero. When the first spherical wave arrives, the impulse response becomes equal to the wavespeed c. The response remains constant as long as the intersections are fully closed circles. When the edges of the aperture are met, discontinuities occur, and the impulse response decreases, until it finally drops off to zero (cfr. fig. 3.4).

When calculating the spatial impulse response off the imaging axis for several lateral positions, a spatial impulse response as illustrated in fig. 3.5 is obtained (example of an unapodized circular transducer). It can be seen that the impulse response depends on the spatial observation point, with lower and slower responses further from the imaging axis. In general, the spatial impulse response is calculated for several observation points in the field, and this for each element in the aperture. The final impulse response of an aperture element is then found by summing all the contributions of the intersections (total number of

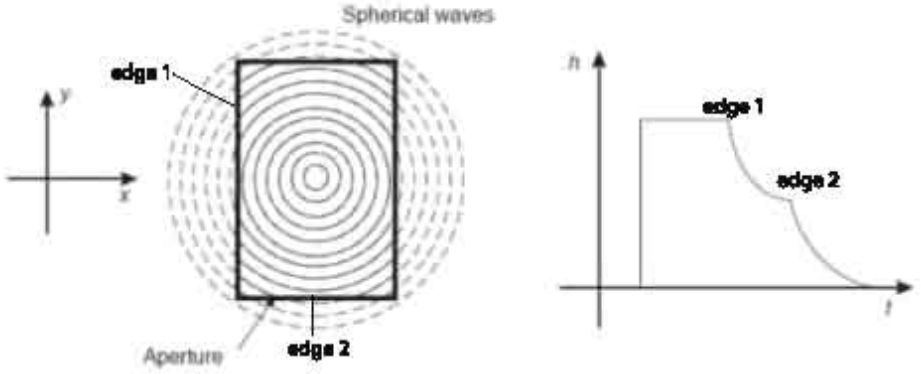

FIGURE 3.4: The spatial impulse response on the imaging axis from a rectangular aperture element. This figure was adapted from [50].

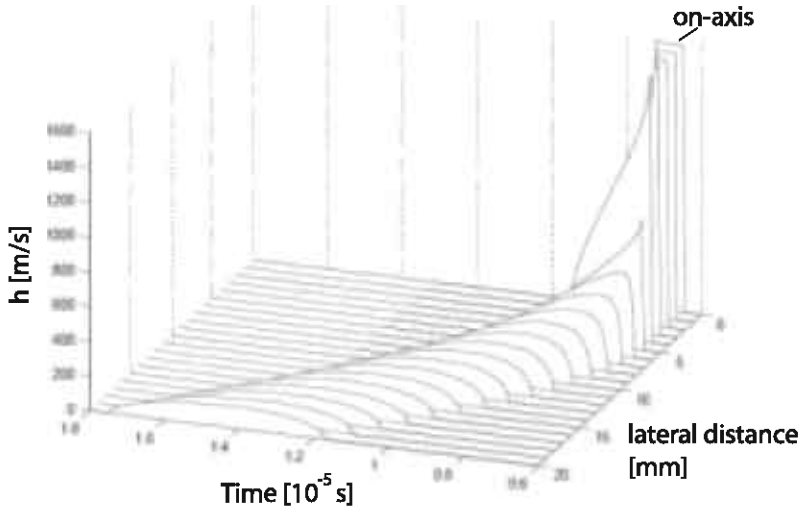

FIGURE 3.5: Spatial impulse response from a circular non-apodized aperture. This figure was adapted from [50].

N(t)) at a given time instance t:

$$h(\vec{r}_1, t) = \frac{\sum_{i=1}^{N(t)} (\theta_2^i(t) - \theta_1^i(t))c}{2\pi} \tag{3.11}$$

3.2.2.a *Far field approximation*

Simulation-wise, it is convenient to work with a far-field approximation of the spatial impulse response, which means that the ultrasound waves can no longer be represented as spheres, but a plane wave approximation is more correct. This means that the intersections of the ultrasound waves with the aperture are lines instead of circles. Fig. 3.6 compares the near field situation (circular intersections) with the far field approximation (linear intersections). Because of the linear intersections in the far field, the spatial impulse response has a trapezoidal shape (cfr. fig. 3.6).

For the far-field approximation to be valid, the observation point should be in the far-field of the emitting and receiving transducer elements. As such, the elements should be sufficiently small, and often the physical transducer elements have to be divided into smaller mathematical elements, according to:

$$l >> \frac{w^2}{4\lambda} \tag{3.12}$$

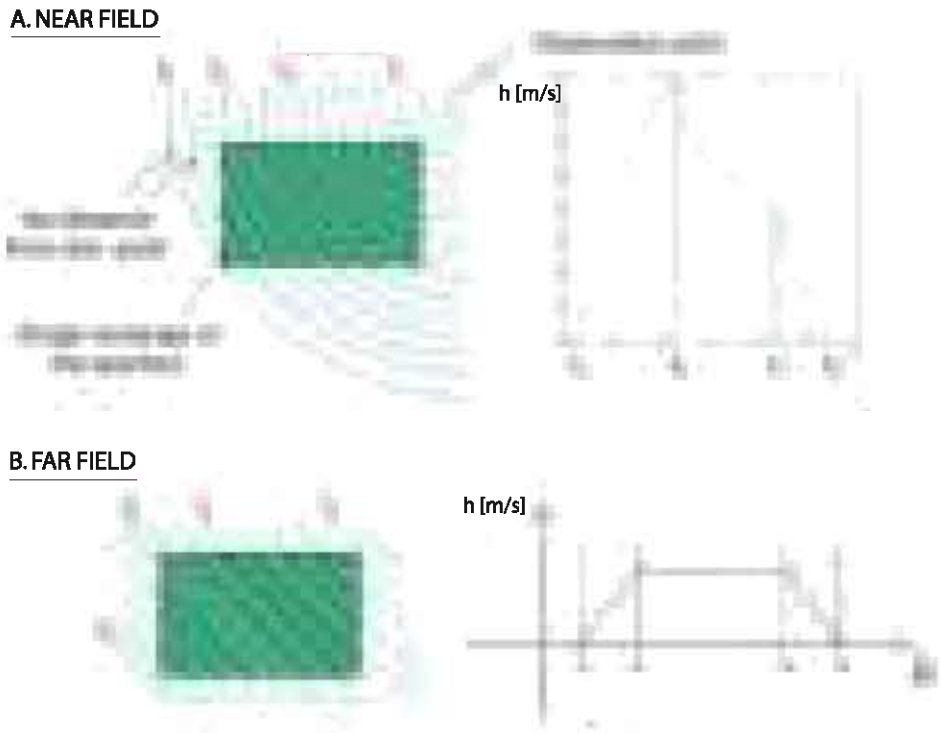

FIGURE 3.6: Panel A shows the near field situation for calculating the spatial impulse response. Panel B shows the far field approximation used in the Field II calculation procedure of the spatial impulse response.

with l the distance of the centre of the aperture to the observation point, w the largest dimension of the mathematical element, and λ the wavelength. The subdivision of the transducer elements into smaller rectangles is illustrated in fig. 3.7 for a 1.5D array. The spatial impulse response of a particular aperture element is then found by summing the responses from each mathematical element, a valid assumption because the imaging system is considered linear.

Apodization and *focusing* can be easily implemented by respectively weighting and delaying the responses from each sub-rectangle. *Attenuation* can be included by convolving the Huygens integral of equation 3.9 with a distance dependent attenuation impulse response.

3.3 ALTERNATIVE SIMULATION APPROACHES

The Field II program is an extensively validated ultrasonic imaging simulator, resulting in realistic ultrasound data for linear imaging setups, but comes at the cost of high computational times, especially in

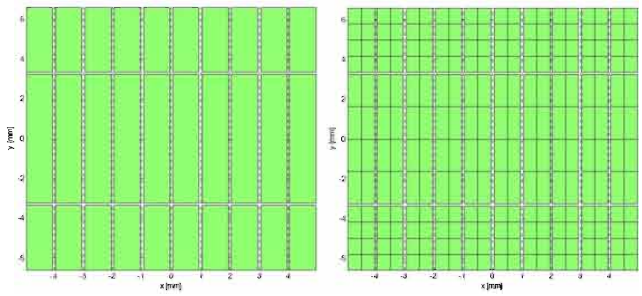

FIGURE 3.7: Subdivision of physical transducer elements into mathematical elements for a 1.5D array.

case of large 3D scatterer phantoms. Depending on the imaging application, such a high accuracy as offered by Field II is not needed, and simplified ultrasound simulation approaches have been developed. We mention in particular the COLE [53] and FUSK [54] method, which simulate RF-signals based on a spatially invariant point spread function. In case of the COLE method, the scatterer ensemble is convolved with the point spread function in the spatio-temporal domain. The FUSK method is also a convolution-based technique, but is performed in the spatial frequency domain. Both methods result in a seriously decreased computational cost compared to the Field II method (in the order 10^3 times faster), but neglect the spatial variant properties of the imaging system.

3.4 Field II in practice

Field II consists of a compiled C-program which has a Matlab interface. The imaging and simulation setup can be programmed using Matlab-routines which call the C-program. Often, simulations with different imaging setups and variable simulation strategies are performed to investigate and optimize the imaging method of interest. However, a straightforward Matlab code based on the Field II-routines is rather prone to error, because one should keep track of a large amount of imaging and simulation parameters. For this purpose, an object-oriented approach to Field II was developed in Matlab, to provide a more flexible interface to the Field II-program. This Matlab-environment is called *FieldSim*, and was developed by Dr. Lasse Lovstakken (Department of Circulation and Medical Imaging, NTNU, Norway).

The Field II-simulations mentioned in this dissertation were performed with the FieldSim-approach, and the code was extended to provide a link between on the one hand the Field II ultrasound simulations, and on the other hand the flow velocity and structural displacement fields as obtained from CFD or FSI simulations (sections 4.2 and 4.4). For the studies of multidimensional flow estimation, as mentioned in part III of this dissertation, the cross-beam vector Doppler strategy was also implemented in FieldSim. A more detailed explanation of the FieldSim simulation procedure will be given in the next paragraphs.

3.4.1 FieldSim

FieldSim uses an object-oriented approach to Field II, to implement the imaging and simulation setup in a Matlab-code. Different *objects* can be distinguished in the ultrasound simulation model:

(i) the object Probe, defining the transducer
(ii) the object Scan, describing the scanning scheme
(iii) the object FieldSim, defining the simulation strategy
(iv) the object Phantom, describing the ensemble of point scatterers on which the ultrasound waves reflect.

The implementation of Field II in Matlab will be further explained using these objects. Before starting a Field II-simulation, these objects should be properly initialized, and certain scanning and simulation features (e.g. apodization, focusing, phantom composition,...) are updated during the simulated scan procedure. A descriptive overview of the FieldSim approach will be given, including a summary of the object definitions and an outline of the simulation procedure. For a more concrete implementation based on the Field II-routines, we refer to the Field II-manual [55].

3.4.1.a Probe class

The Probe object describes the properties of the transducer, and following parameters should be defined:

1. The transducer type: linear array transducer, phased array transducer, etc. ...
2. The number of elements of the probe.
3. The size of the elements in the lateral and elevation direction, and

the kerf.
4. The centre frequency.
5. The focus position in the depth and elevation direction.
6. The F-numbers on transmit and receive. The minimal and maximal aperture which may be used during imaging should also be defined.
7. The electro-acoustic impulse response.

3.4.1.b Scan class

As for the probe object, several parameters are necessary to define the scanning scheme:

1. The type of scanning: continuous or beam interleaved acquisition
2. The beginning and end position of the scan.
3. The angle of the scanlines.
4. The packetsize.
5. The PRF_{max} and PRF.
6. The number of parallel receive beams (PRB).

The FieldSim program can then define the scanning scheme. We mention in short the scan definition followed by FieldSim, in case of a beam interleaved scan acquisition:

1. The distance between scanlines Δx is defined. This is chosen according to half the Rayleigh resolution criterion, i.e. the distance between scanlines corresponds to:

$$\Delta x_{init} = \frac{\lambda F_{\#,in-focus}}{2}, \tag{3.13}$$

with $F_{\#,in-focus}$ the F-number defined as:

$$F_{\#,in-focus} = \frac{D_F}{A_{2-way}} \tag{3.14}$$

with D_F the focus distance and A_{2-way} the two-way aperture width.
2. The number of interleave groups is determined. For this purpose, an initial number of scanlines L_{init} is calculated based on the scanwidth (W) and the beamdensity:

$$L_{init} = round(\frac{W}{\Delta x_{init}}) \tag{3.15}$$

The number of interleave groups (No_{IGS}) is then the ratio of L_{init} and the interleave groupsize (IGS):

$$No_{IGS} = round(\frac{L_{init}}{IGS}) \tag{3.16}$$

with IGS defined as:

$$IGS = \left\lfloor \frac{PRF_{max}}{PRF} \right\rfloor \cdot PRB \tag{3.17}$$

The final number of scanlines L_{final} is then the multiplication of the IGS and the number of interleave groups:

$$L_{final} = IGS \cdot No_{IGS} \tag{3.18}$$

The distance between beams should be updated accordingly:

$$\Delta x_{final} = \frac{W}{L_{final}} \tag{3.19}$$

The exact position (m) of the transmit and receive beams can then be defined, as well as the corresponding time of beam reception.

3.4.1.c FieldSim class

For the simulation setup, the following modeling aspects are needed:

1. The division of each physical element of the transducer into a number of mathematical elements. The exact number of mathematical elements in the lateral and elevation direction is required.
2. The type of mathematical elements: rectangular or triangular elements can be chosen.
3. The sample frequency of the RF-signal in the depth direction.
4. Inclusion of attenuation in the model: yes or no. If yes, the degree of frequency dependent attenuation (dB/MHz cm) should be defined.
5. Definition of the wavespeed.

The FieldSim object also defines certain aspects of the image formation:

1. The excitation pulse of the transducer, i.e. the amplitude, frequency, shape and number of periods of the pulse.

2. The type of apodization applied on transmit and receive. Different apodization windows are possible, like rectangular, hanning, hamming and tukey (cosine tapered).
3. Implementation of a dynamic aperture: yes or no. FieldSim takes into account that the aperture should always be defined symmetrically with respect to the centre axis of the beam.

3.4.1.d Phantom class

The imaged medium is represented by a phantom, consisting of an ensemble of random point scatterers with varying scattering amplitude. The number of point scatterers is related to the imaging resolution, and the scattering amplitude is typically defined with a normal distribution.

The phantom should be correctly positioned versus the transducer, knowing that the centre of the probe is always positioned in the origin of the coordinate system. The Field II coordinate system is further defined as follows: the X-axis denotes the lateral direction, the Z-axis the axial or depth direction, and the Y-direction the elevation direction.

3.4.1.e Running a simulation

Running a Field II-simulation is similar to the actual physical scanning procedure performed by a true ultrasound probe. The scanlines are sequentially simulated, by looping over all the scanlines:
1. For each scanline, the apodization is updated accordingly, so that the transducer elements are appropriately activated and weighted.
2. The focussing scheme is updated for each beam, so that correct delays are applied to the considered elements.
3. The position of the scatterers in the phantom is updated. The scatterers are created *on the fly*, meaning that the positions of the scatterers are derived during the scanning procedure, for each beam seperately. Only the scatterers used during simulation of the previous beam (k-1) are saved in a temporary file, so that the scatterers at the currently simulated beam (k) are correctly propagated:

$$\vec{x}_k = \vec{x}_{k-1} + \vec{v}_{k-1} \cdot \frac{1}{PRF_{max}} \tag{3.20}$$

with $\vec{x}$ and $\vec{v}$ the position and velocity of the scatterers, and PRF_{max} the pulse repetition frequency. This reduces the memory necessary to perform simulations.
4. When the currently simulated beam entails the start of a new interleave group, the scatterer ensemble is refreshed, meaning that a new random distribution is created. As long as the same ensemble of scatterers is simulated, the amplitudes of the scatterers do not change. In case of multiple line acquisition, the scatterers are only propagated when the position of the transmit beam changes.
4. The simulation time can be decreased by limiting the number of scatterers contributing to the signal of a scanline. Scatterers far from the transmit/receive beam have little influence, and are not included in the simulation of the considered beam.
5. The RF-signal from the ensemble of scatterers is simulated.

3.4.1.f Simulation output

When the complete scanning procedure is finished, the data from all the scanlines are interpolated to the same temporal grid. The timescale of each RF-signal starts as soon as signal is picked up, and is therefore related to the position of the scatterers which are closest to the transducer. Hence, the timescale of each scanline is different, and temporal interpolation is necessary in order that all RF-signals correspond to the same timescale.

To find the correct timescale, one should also compensate for the *filter lag*. Because of all the filtering processes involved to obtain the backscattered signal, the position of the imaged phantom in the simulated image is slightly translated compared to the true position of the phantom, as defined during the input-stage of the simulation.

Further, the sample frequency may be decimated to reduce the necessary storage capacity. Finally, if the IQ-demodulated data are desired, a Hilbert transform is performed on the RF-data followed by a demodulation with the centre frequency of the pulse. Once the RF- or IQ-data are obtained, appropriate signal processing should be applied according to the imaging technique of interest.

3.5 Simulating ultrasonic blood flow imaging

Jensen et al. [56] introduced synthetic blood flow phantoms for the Field II simulation program, demonstrating its abilities in realistically

simulating color flow and pulsed wave Doppler imaging. A *blood flow phantom* in the Field II software is defined as a random distribution of point scatterers. Different types of flow profiles can be simulated by updating the scatterer position every emitted beam. The scattering amplitude of the point scatterers is defined with a normal distribution [57]. The variance of this distribution is related to the backscattering cross-section of the tissue. The mean value influences the relative brightness of the different tissue types present in the simulated image.

The number of scatterers is dependent on the imaging resolution, with 10 scatterers per resolution cell showing satisfying results [58]. Because the signal from blood flow can be considered as a Gaussian random process, a sufficient number is attained as soon as the RF-signal has a Gaussian distribution. Hence, not every physical particle should be represented by a scatterer, which seriously decreases computational times. The number of scatterers may be further reduced during simulation since scatterers far from the main lobe of the beam have little effect on the image.

Fig. 3.8 shows examples of ultrasonic flow simulations performed by Jensen et al [56]. Panel A in fig. 3.8 shows a color flow image resulting from a steady flow phantom representing parabolic flow in a carotid

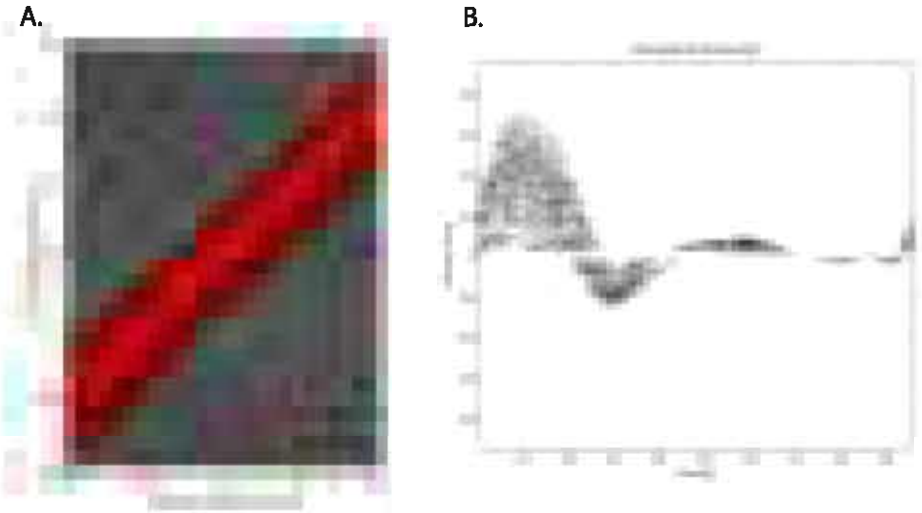

FIGURE 3.8: Examples of flow simulations with Field II, performed by Jensen et al [56]: Panel A shows a simulated color flow image based on a carotid artery phantom and panel B a sonogram from a femoral artery phantom. This figure was adapted from [50].

artery. An example of pulsatile flow in the femoral artery is shown in the sonogram of panel B in fig. 3.8. The scatterers in this simulation were propagated according to a Womersley flow profile.

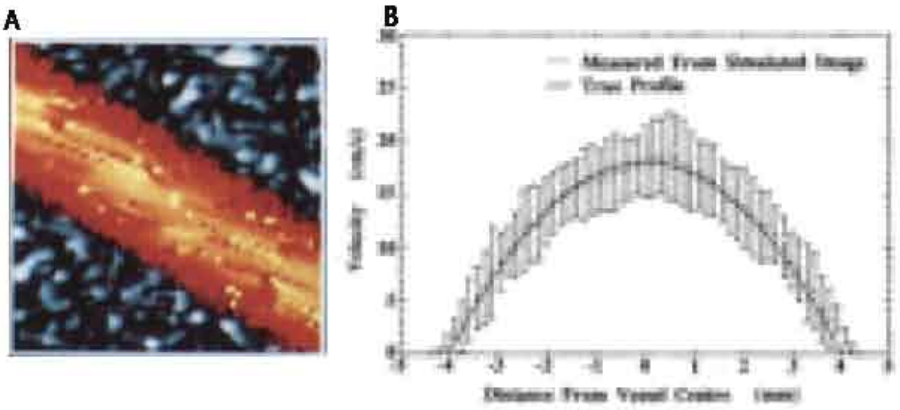

FIGURE 3.9: Panel A shows the simulation of a color flow image resulting from a cylindrical vessel with parabolic flow, according to the method of Kerr et al [59]. Panel B compares the flow profile as estimated from the ultrasound simulations with the true one.

Kerr et al [59] developed a simulation method for color flow images, also based on retrieving the acoustic signal from an ensemble of point scatterers using the spatial impulse response. Hence, this method is quite similar to the Field II program, but it was specifically developed for the validation of ultrasonic flow imaging. Panel A in fig. 3.9 shows an example from their work: a simulated color flow image overlaid on a B-mode image from static background structures. The computer phantom was constructed as a cylindrical vessel inside a scattering background, and the point scatterers were moved according to a static parabolic flow profile. Panel B in fig. 3.9 compares the flow profile as estimated from the ultrasound simulations with the true one.

The blood velocity fields arising in the cardiovascular system are however very complex, and the analytically described flow phantoms previously mentioned do not suffice. Therefore, Oung et al [60] combined the spatial impulse response approach for ultrasound simulations with a realistic blood flow model based on a finite element technique for solving the Navier-Stokes equations (cfr. section 4.2.1). This allowed a wide range of flow patterns and transducer geometries to be simulated. Oung et al focused on obtaining Doppler spectra from a limited sample volume, and other ultrasonic flow imaging methods were not

investigated.

Khoshniat et al [61] also developed a method to simulate Doppler signals from a realistic blood flow field. Complex blood velocities were obtained with computational fluid dynamics (cfr. section 4.2), and integrated with an empirical model of Doppler ultrasound physics, which accounted for the effects of sample volume, finite temporal sampling window, and intrinsic spectral broadening. The Doppler ultrasound simulations worked in *real-time* for the purposes of teaching and training. Realistic Doppler spectograms were obtained, but as for Oung et al [60], the method did not allow to investigate a generic ultrasonic flow estimator.

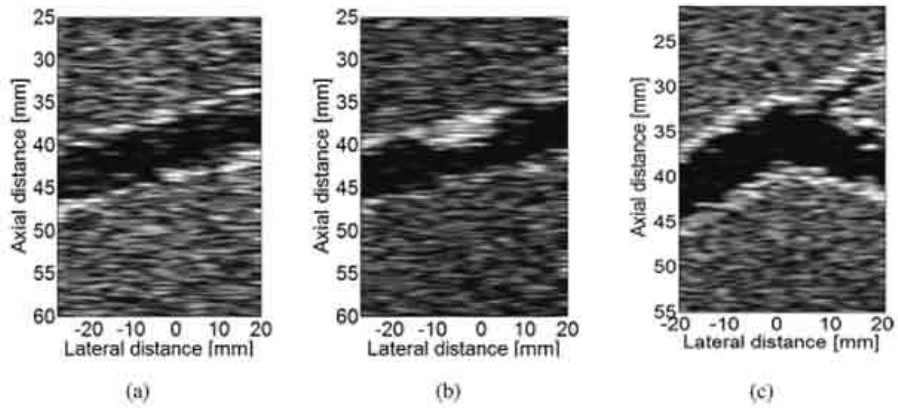

FIGURE 3.10: Examples of B-mode simulations of blood vessels during diastole performed by Balocco et al [62]. Panel (a) shows a healthy vessel, (b) a stenosed vessel and (c) a bifurcation.

A first attempt to fully integrate the complex blood vessel behaviour with the Field II software was made by Balocco et al [62]. Both realistic blood flow and vessel wall movement were simulated, and their complex fluid-structure interaction (cfr. section 4.4) was taken into account in the Comsol Multiphysics software. The FSI-simulations were coupled with the Field II model, but little elaboration was made on how the blood vessel physics were integrated with the ultrasound simulations. Simulated B-mode images from different types of blood vessel phantoms are shown in fig. 3.10.

Although ultrasound images in general can be quite noisy, the visual appearance of the simulations is still quite different from clinical images (cfr. fig. 1.24). The exact reason for this is unclear, as the imaging

setup as defined in [62] provides very little detail.

Also, the construction of the scatterer phantom is unclear. As such, we feel that Balocco et al focussed immediately on applications in more complex arterial configurations (although the ultrasound imaging applications themselves were rather basic), but that they did not provide detail on the applied methodology so that it is available for replication by other research teams.

3.5.1 Conclusion

Due to the shortcomings of previously mentioned work, we aim to implement a more advanced coupling between computational fluid dynamics and Field II ultrasound simulations, based on a model of a carotid artery. This entails modeling a highly realistic ultrasonic imaging setup, mimicking transducers as used in clinical practice. Further, this also requires to investigate how Field II scatterer phantoms based on CFD-simulations can be constructed, so that complex flow fields as present in the carotid artery can be used as input to the ultrasound simulations. This is an important aspect of advanced ultrasonic flow imaging simulations, which has not been reported in literature before. Finally, we intend to extend our ultrasonic simulation environment based on CFD-simulations to FSI-simulations. This then allows to simulate ultrasound images of both the blood flow field and vessel wall.

Besides elaborating on the CFD/FSI-ultrasound coupling techniques (chapters 5, 6 and 9), we will demonstrate that we obtain a high degree of realism in the simulated ultrasound images, more particularly in 1D and 2D flow images as well as ultrasonic wall distension measurements. Our advanced simulation environment will then allow to validate and develop new imaging techniques, as will be reported in chapters 7, 8 and 9 of this dissertation.

CHAPTER 4

Numerical modeling of the blood vessel

4.1 Introduction

When validating and developing ultrasonic imaging methods for blood flow and vessel wall visualization, it is important to get an accurate picture of the flow field and vessel wall behaviour. Due to the complex arterial geometry and tissue properties, the flow field and tissue deformation are of an intricate nature. This hampers an analytical solution of the complex equations governing the vascular hemodynamics and tissue mechanics. Therefore, numerical techniques are required to solve these equations in an iterative approach, converting the continuous formulation of these equations to a discrete domain, both in time and space. The numerical techniques used to solve problems involving fluid flows are often lumped together in the term *computational fluid dynamics* or *CFD*, and an overview is given in section 4.2. The numerical methods used to get insight in tissue mechanical problems involve structural mechanics, and are often referred to as *computational structure dynamics (CSD)*. An overview is given in section 4.3.

Solving the hemodynamics and tissue mechanical problem is complex, and it becomes even more complicated when realizing that the behaviour of the blood flow and vascular wall is a coupled problem.

The blood flow field influences the vessel wall mechanics, and on the other hand, the vessel wall movement also determines the flow field. Sophisticated numerical algorithms are needed to solve this complex *fluid-structure-interaction*, or *FSI*. In this dissertation, an in-house FSI-code was applied, as developed by [63, 64], coupling two commercial solvers for respectively the fluid (Fluent) and structural (Abaqus) problem. In our case, the fluid and structural solver were *black-box solvers*, as the coupling procedure was hampered by the limited accessibility to the calculation procedures used in both solvers. Hence, an overview of FSI coupling techniques will be provided in the context of integrating two black box solvers (section 4.4).

4.2 COMPUTATIONAL FLUID DYNAMICS: NUMERICAL MODELING OF BLOOD FLOW

4.2.1 The Navier-Stokes equations

In this dissertation, blood flow is modeled as an *incompressible Newtonian fluid*, which is governed by the principles of mass and momentum conservation. The mathematical formulation of these principles will be explained in the following paragraphs.

4.2.1.a Conservation of mass

Consider a general control volume (c.v.) through which fluid flows. The conservation of mass states that the rate of net mass flux *through* a control volume and the rate of mass accumulation *in* a control volume should compensate each other:

$$\underbrace{\int_{c.s.} \rho_f (\vec{v} \cdot \vec{n}) dA}_{\text{rate of net mass flux}} + \underbrace{\frac{\partial}{\partial t} \int_{c.v.} \rho_f dV}_{\text{rate of mass accumulation}} = 0 \tag{4.1}$$

with ρ_f the fluid density, $\vec{v}$ the velocity vector field and $\vec{n}$ the normal on the surface of the control volume (c.s.), pointing outwards of the control volume. In differential formulation, the conservation of mass is expressed as:

$$\nabla \cdot (\rho_f \vec{v}) + \frac{\partial \rho_f}{\partial t} = 0 \tag{4.2}$$

with ∇ the nabla-operator. This can be reformulated as:

$$\frac{D\rho_f}{Dt} + \rho_f \nabla \cdot \vec{v} = 0 \tag{4.3}$$

The substantial derivative $\frac{D\rho_f}{Dt}$ is the sum of a temporal derivative $\frac{\partial}{\partial t}$ and a convective derivative $v \cdot \nabla$, the latter one expressing changes in a scalar quantity caused by the flow motion of the vector field $\vec{v}$:

$$\frac{D\rho_f}{Dt} = \underbrace{\frac{\partial \rho_f}{\partial t}}_{temporal\ change} \underbrace{+ v_x \frac{\partial \rho_f}{\partial x} + v_y \frac{\partial \rho_f}{\partial y} + v_z \frac{\partial \rho_f}{\partial z}}_{convective\ change} \tag{4.4}$$

For an incompressible fluid, i.e. the density of the fluid is not dependent on changes in pressure and temperature, the substantial derivative of the density is zero. Equation 4.3 reduces to:

$$\nabla \cdot \vec{v} = 0 \tag{4.5}$$

4.2.1.b Conservation of momentum

The conservation of momentum can be derived in a similar way and is the expression of Newton's second law of motion: the temporal rate of change in momentum ($\rho_f \vec{v}$) is equal to the net force acting on the system ($\sum F$).

$$\underbrace{\int_{c.s.} \rho_f \vec{v}(\vec{v} \cdot \vec{n}) dA}_{rate\ of\ net\ momentum\ flux} + \underbrace{\frac{\partial}{\partial t} \int_{c.v.} \rho_f \vec{v} dV}_{rate\ of\ momentum\ accumulation} = \sum F \tag{4.6}$$

The external forces F can be separated into:
(i) body forces f_f, like gravitational or electromagnetic forces
(ii) forces due to normal and shear stresses acting on the control volume, represented by the tensor $\overline{\sigma}_f$
For an incompressible fluid, the differential notation of the conservation of momentum is:

$$\rho_f \nabla \cdot \vec{v}\vec{v} + \rho_f \frac{\partial \vec{v}}{\partial t} = \nabla \cdot \overline{\sigma}_f + f_f \tag{4.7}$$

The diadic tensor $\vec{v}\vec{v}$ arises from the net momentum flux and is given by:

$$\vec{v}\vec{v} = \begin{bmatrix} v_x v_x & v_x v_y & v_x v_z \\ v_y v_x & v_y v_y & v_y v_z \\ v_z v_x & v_z v_y & v_z v_z \end{bmatrix} \tag{4.8}$$

The divergence of this dyadic tensor is:

$$\nabla \cdot \vec{v}\vec{v} = \vec{v} \cdot \nabla \vec{v} + (\nabla \cdot \vec{v})\vec{v} \tag{4.9}$$

For incompressible flows, the second term on the righthand side is zero due to the conservation of mass. The first term on the righthand side contains $\nabla\vec{v}$, which is the velocity gradient tensor:

$$\nabla\vec{v} = \begin{bmatrix} \frac{\partial v_x}{\partial x} & \frac{\partial v_y}{\partial x} & \frac{\partial v_z}{\partial x} \\ \frac{\partial v_x}{\partial y} & \frac{\partial v_y}{\partial y} & \frac{\partial v_z}{\partial y} \\ \frac{\partial v_x}{\partial z} & \frac{\partial v_y}{\partial z} & \frac{\partial v_z}{\partial z} \end{bmatrix} \tag{4.10}$$

Hence, the rate of net momentum flux, described by the divergence of the dyadic tensor, is solely determined by the convective derivatives of the velocity components in respectively the x, y and z-directions:

$$\nabla \cdot \vec{v}\vec{v} = \vec{v} \cdot \nabla\vec{v} \tag{4.11}$$

The forces acting on the control volume can also be simplified and reformulated. First of all, the body forces f_f (e.g. gravitational forces) are neglected for biomechanical applications. Further, for an incompressible Newtonian fluid, the stress tensor $\overline{\sigma}_f$ has contributions from:
(i) the pressure p
(ii) the shear stress tensor $\overline{\tau}_f$ due to the viscosity μ_f:

$$\overline{\sigma}_f = -pI + \overline{\tau}_f \tag{4.12}$$

Considering the reformulation of the external forces (equation 4.12) and of the rate of net momentum flux (equation 4.11), the following form of the conservation of momentum is obtained:

$$\rho_f \frac{\partial\vec{v}}{\partial t} + \rho_f\vec{v} \cdot \nabla\vec{v} = -\nabla p + \nabla \cdot \overline{\tau}_f \tag{4.13}$$

Using the definition of the substantial derivative (equation 4.4), the conservation of momentum can be expressed for the x, y and z-directions as:

$$\rho_f \frac{Dv_x}{Dt} = -\frac{\partial p}{\partial x} + \frac{\partial \tau_{xx}}{\partial x} + \frac{\partial \tau_{yx}}{\partial y} + \frac{\partial \tau_{zx}}{\partial z} \tag{4.14}$$

$$\rho_f \frac{Dv_y}{Dt} = -\frac{\partial p}{\partial y} + \frac{\partial \tau_{xy}}{\partial x} + \frac{\partial \tau_{yy}}{\partial y} + \frac{\partial \tau_{zy}}{\partial z} \tag{4.15}$$

$$\rho_f \frac{Dv_z}{Dt} = -\frac{\partial p}{\partial z} + \frac{\partial \tau_{xz}}{\partial x} + \frac{\partial \tau_{yz}}{\partial y} + \frac{\partial \tau_{zz}}{\partial z} \tag{4.16}$$

For an incompressible Newtonian flow, the shear stress tensor $\overline{\tau}_f$ can be defined using the velocity gradient tensor:

$$\overline{\tau}_f = \mu_f(\nabla\vec{v} + \nabla\vec{v}^T) \tag{4.17}$$

4.2.1.c Conclusion

We derived in this section a set of coupled non-linear partial differential equations, called the Navier-Stokes equations, expressing conservation of mass and momentum for an incompressible and viscous:

$$\nabla \cdot \vec{v} = 0 \tag{4.18}$$

$$\rho_f \frac{\partial \vec{v}}{\partial t} + \rho_f \vec{v} \cdot \nabla \vec{v} = -\nabla p + \nabla \cdot \overline{\tau}_f \tag{4.19}$$

The Navier-Stokes equations can also be formulated in integral form:

$$\int_S \vec{v} \cdot \vec{n} dS = 0 \tag{4.20}$$

$$\rho_f \frac{\partial}{\partial t} \int_V \vec{v} dV + \rho_f \int_S \vec{v}\vec{v} \cdot \vec{n} dS = -\int_S p \cdot \vec{n} dS + \int_S \vec{n} \cdot \overline{\tau}_f dS \tag{4.21}$$

4.2.2 Finite volume method

For most practical cases, an analytical solution of the Navier-Stokes equations is not possible. Hence, numerical techniques are required to convert the continuous formulation of the equations to a discrete domain, and approximate the solution in an iterative way. In the next sections, we provide a detailed description of the finite volume method for incompressible flow, as used in the commercial CFD package Fluent.

The finite volume method solves the integral form of the Navier-Stokes equations, mentioned in (4.20) and (4.21), by dividing the fluid domain into a number of control volumes, resulting in a *grid* of small cells. Through discretization and linearization of the integrals, algebraic equations are obtained for each control volume. This system of linear equations is then solved with an iterative approach, i.e. the equations are solved in an iterative loop until the numerical solution has converged within a predefined tolerance.

4.2.3 Grid formulation

For CFD-calculations in fluid domains with rigid walls, the finite volume method is performed using an Eulerian grid formulation. This means that the grid is fixed in space as the fluid flows. The flow variables change with time for each grid cell, and mass flows from cell to cell. This grid formulation is one of the important differences with

computational solid mechanics (cfr. section 4.3), which is based on a Lagrangian grid formulation. In this approach, the grid is fixed to the material and moves corresponding to the material deformation. Both grid formulations are illustrated in fig. 4.1.

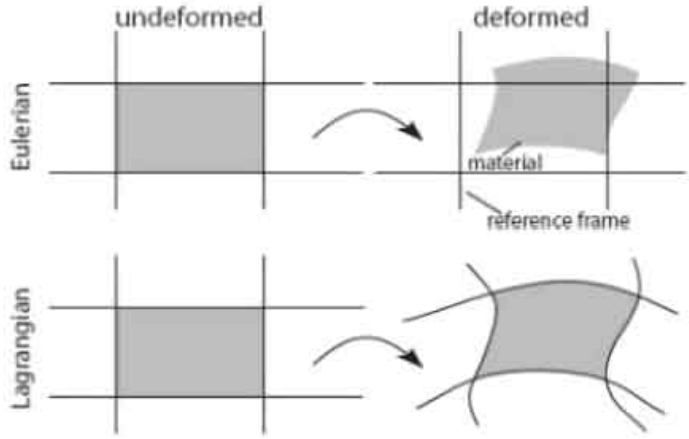

FIGURE 4.1: Illustration of the Eulerian and Lagrangian grid formulation in 2D. This figure was adapted from [65].

4.2.4 Discretization in space

Fluent uses a *collocated scheme*, meaning that both pressure and velocity are stored in the centre of the grid cell. This shows a high practical advantage, both for structured and unstructured grids, but has an important disadvantage. The pressure distribution shows a zig-zag or checkerboard variation throughout the mesh, due to a second order accurate central discretization of the pressure gradient in the momentum conservation law.

A method has been proposed by Rhie and Chow [66] to avoid this pressure checkerboarding by appropriate discretization of the mass fluxes in the conservation of mass equation. As the velocities are only stored in the cell centres, Rhie and Chow developed a technique to calculate mass fluxes at the cell faces using a momentum-balance interpolation technique, instead of the linear interpolation of neighbouring cell centre values. The basic concept of this method is that the mass flux of a cell face J_f can be written as the sum of two terms:

(i) a term J_f^* containing the influence of the velocities in the two neighbouring cells (c0 and c1)

(ii)a term containing the contribution of the pressures in the two neighbouring cells (co and c1):

$$J_f = J_f^* + d_f(p_{co} - p_{c1}) \tag{4.22}$$

with d_f a coefficient (m/s) calculated according to [66]. Further details on this averaging method are beyond the scope of this work and we refer to [66].

The convective terms in the equation for momentum conservation also require the knowledge of scalar quantities ϕ_f on the faces of the grid cell. As for the conservation of mass, the face values are unavailable because of the collocated scheme. Therefore, a *second order upwind scheme* is used, meaning that the face value is obtained with a Taylor expansion of the cell-centred solution. For this purpose, the cell-centre value upstream of the considered face is taken:

$$\phi_f = \phi_{c-up} + (\nabla\phi)_{c-up} \cdot \vec{r} \tag{4.23}$$

with ϕ_{c-up} the scalar value in the upstream cell-centre, $(\nabla\phi)_{c-up}$ the gradient of the scalar in the upstream cell-centre, and $\vec{r}$ the vector denoting the displacement from the upstream cell centre to the centre of the face. The gradient $(\nabla\phi)_{c-up}$ is calculated with a least-squares cell-based gradient evaluation, and we refer to the Fluent User's manual for more details on this discretization scheme.

4.2.5 Discretization in time

A first-order temporal discretization scheme is used in Fluent, called a *backward Euler* scheme. This can be explained as follows. The temporal derivative of a scalar quantity ϕ can be written as a function of the spatial discretization terms $F(\phi)$:

$$\frac{\partial\phi}{\partial t} = F(\phi) \tag{4.24}$$

The first order backward Euler scheme discretizes this equation as:

$$\frac{\phi^{n+1} - \phi^n}{\Delta t} = F(\phi^{n+1}) \tag{4.25}$$

with n the current time step where the solution of the Navier-Stokes equations is known, and $n+1$ the future time step with unknown flow field. This equation is implicit since the variable ϕ^{n+1} at a given cell is a function of unknown values ϕ^{n+1} in neighbouring cells through the term $F(\phi^{n+1})$. The advantage of implicit time integration is that it is in theory a stable scheme irrespective of the chosen time step size Δt.

4.2.6 Pressure-velocity coupling

For CFD-simulations of incompressible flow, we used the *pressure-based segregated solver* in Fluent. This means that the conservation of mass and momentum are solved *sequentially*, and we used the SIMPLE (Semi-Implicit Method for Pressure-Linked Equations) algorithm for this purpose. More specifically, the momentum equations are solved *first*, to find a velocity field v^*, based on an initial guess of the pressure field p^*. Next, the mass conservation law is solved. However, the velocity vector field v^* does not satisfy this equation due to the assumed pressure field p^*. For this purpose, a correction term is added to the mass flux J_f. If J_f^* is the mass flux as calculated from the velocity field v^*, then the corrected face flux J_f can be written as:

$$J_f = J_f^* + J_f^{'} \tag{4.26}$$

with $J_f^{'}$ the mass flux correction term. In the SIMPLE method, it can be seen that this correction flux is solely dependent on a cell pressure correction $p^{'}$:

$$J_f^{'} = d_f(p_{c0}^{'} - p_{c1}^{'}) \tag{4.27}$$

After substitution of equations 4.26 and 4.27 in the mass conservation law, the equation can be solved in terms of the unknown pressure correction $p^{'}$. Next, the velocities are updated according to the pressure correction, and convergence of the numerical solution is checked. If no convergence is met, the momentum equations are solved again based on the corrected pressure and velocity field to obtain a new solution for the velocity field. Next, the pressure-velocity coupling is performed again to find a new corrected pressure field through the conservation of mass. This *iterative loop* is performed until the numerical solution converges with a satisfying tolerance. For more details on the SIMPLE method, we refer to [67].

4.2.7 Underrelaxation

Momentum and pressure variables are transferred from one iteration to the next, as described in the previous paragraph. However, these flow variables are not transferred directly from one iteration to the other, but *underrelaxation* is performed. This tempers the change of the scalar quantity ϕ when advancing to the next iteration, according to the following equation:

$$\phi_i = \phi_{i-1} + \alpha(\phi_{new} - \phi_{i-1}) \tag{4.28}$$

with ϕ_{i-1} the value from the previous iteration *i-1*, ϕ_{new} the value at the current iteration *i* as calculated from the discretized Navier-Stokes equations, and ϕ_i the value at the current iteration i after underrelaxation of the update with a factor α. For pressure and momentum, the underrelaxation factors in Fluent are respectively 0.3 and 0.7 by default.

4.2.8 Practical setup

A first step in setting up a CFD-problem consists of making a grid or mesh of the fluid volume of interest. In case of blood vessels, a 3D geometry and mesh is most often reconstructed from medical scans. The number of grid cells is related to the particular problem, i.e. geometry and flow conditions. Therefore, a mesh dependency study should be performed to determine whether the solution is dependent on the chosen grid refinement or not.

As the blood vessel is a complex geometry, one opts most often for unstructured meshes consisting of tetrahedral cells. In recent work [68], algorithms have been developed to make structured hexahedral meshes for complex shaped geometries. A structured grid has the advantage that the hexahedral cells are aligned with the flow, reducing the error due to numerical diffusion. Further, it seriously reduces computational times.

Besides the geometrical description of the flow problem, the hemodynamical condition should also be prescribed at the in- and outlet boundaries of the fluid volume. Different kinds of boundary conditions exist, with prescribed pressure and flow profiles in space and time the most common types. Recently, impedance boundary conditions have been developed, a more accurate solution since they impose a relationship between flow and pressure. The impedance Z is defined as the ratio between pressure P and flow Q, and can be expressed in both the time and frequency domain. We refer to [69] for more details. The boundaries of the fluid volume which do not act as in- or outlet are, in case of rigid walls, most often described with a no-slip condition, i.e. the velocity is zero at the wall.

It should be noted that for incompressible flow modeling, the pressure field is not determined in absolute terms, and an arbitrary constant value can be added to the pressure field. Moreover, for time-dependent

simulations, as is the case for the pulsatile blood flow field, this constant may be chosen differently for each timestep, because the Navier-Stokes equations (4.18 and 4.19) do not contain a temporal derivative of the pressure.

Figure 4.2 shows an example of a CFD-setup for a carotid artery bifurcation, as applied in chapter 5 of this dissertation. A velocity profile measured in a healthy volunteer was applied at the inlet of the geometry, and an outflow division of 45-55 % was imposed at the two outlets.

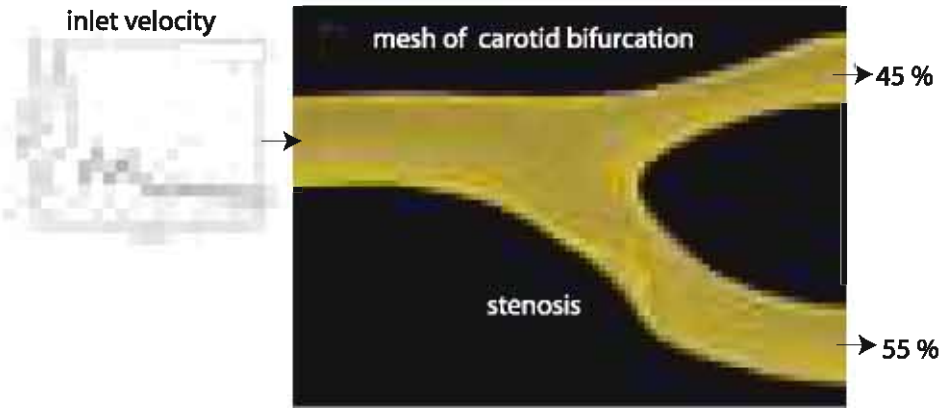

Figure 4.2: A CFD-setup for a carotid artery bifurcation, as applied in chapter 5 of this dissertation. A velocity profile was applied at the inlet of the geometry, and an outflow division was imposed between the two outlets.

4.3 Computational structure dynamics: numerical modeling of vascular tissue

4.3.1 Conservation of momentum

The deformation of the vessel wall is governed by the conservation of mass and momentum. As for the fluid flow, the complex mathematical formulation of these principles is solved by dividing the solid domain in smaller volumes. In contrast to the Eulerian grid formulation used in fluid mechanical problems, a Lagrangian formulation is used when numerically solving solid mechanical issues. This means that the grid moves as the material deforms, and hence no mass flows through the cells. Therefore, the conservation of mass is implicitly fulfilled and only the momentum equation is solved.

The conservation of momentum for a solid is given by:

$$\nabla \cdot \overline{\sigma}_s + \rho_s \vec{f} = \frac{D(\rho_s \vec{v})}{Dt} \tag{4.29}$$

with ρ_s the density of the solid, $\vec{v}$ the velocity of the material, $\vec{f}$ the external forces on the solid and $\overline{\sigma}_s$ the Cauchy stress tensor. This symmetric tensor is the most physical interpretation of the stresses present in a solid. More specifically, it is the force acting per unit area of deformed solid. This stress tensor is commonly applied for *small deformations* (strains smaller than 5 %). Other formulations of the stress tensor, like the first and second Piola-Kirchoff tensor, are used for *large deformations*. We refer to specialized literature for further details [70].

In the next paragraphs, the numerical solution of the momentum equation will be discussed in the context of the methods applied in the finite element software Abaqus.

4.3.2 Finite element method

As in fluid mechanical problems, the momentum equation is solved by integration over each cell volume in the solid mesh. However, the numerical method used for this purpose is different from the finite volume method used in fluid problems (cfr. section 4.2.2). A *finite element method* is used, which is based on the weak formulation of the momentum equation. The derivation of the weak formulation is out of the scope of this work, and we refer the interested reader to [71] for more details. A finite element method can also be used for fluid mechanical problems, but most often this is a too complex approach for the large grid sizes typically used in CFD.

The weak formulation of the momentum equation allows to discretize equation 4.29 in space using interpolation functions, also called *shape functions*. This makes it possible to express, at an arbitrary material point, the variable of interest (e.g. displacement, temperature, ...) as a linear combination of the shape functions:

$$a = \sum_i N_i a_i \tag{4.30}$$

with a the variable of interest, a_i the value of this variable at node i of the cell, and N_i the i^{th} shape function. The summation is performed

over all nodes of the considered cell.

It is important to note that the grid cells in a solid, i.e. the *finite elements*, are defined by a number of nodes, which can be different from the number of vertices of the cell. Indeed, extra nodes can be defined on the edges of the considered cell volume. The reason for this is that the number of nodes is related to the order of the shape functions. Naturally, higher order shape functions result in more accurate solutions.

An illustration of shape functions is given for a 2D rectangular element in fig. 4.3. The upper panel of fig. 4.3 shows the element, described in a local coordinate system with the parameters r and s. The element is quadratic, i.e. each edge has a node on its centre, resulting in quadratic shape functions. Because the element has eight nodes, eight shape functions are used to describe the variables in the cell. Each shape function N_i is 1 at node i, and 0 elsewhere, as illustrated by the following shape functions:

$$\begin{aligned}
h_1(r,s) &= -\frac{1}{4}(1+r)(1+s)(1-r-s) & h_5(r,s) &= \frac{1}{2}(1-r^2)(1+s) \\
h_2(r,s) &= -\frac{1}{4}(1-r)(1+s)(1+r-s) & h_6(r,s) &= \frac{1}{2}(1-r)(1-s^2) \\
h_3(r,s) &= -\frac{1}{4}(1-r)(1-s)(1+r+s) & h_7(r,s) &= \frac{1}{2}(1-r^2)(1-s) \\
h_4(r,s) &= -\frac{1}{4}(1+r)(1-s)(1-r+s) & h_8(r,s) &= \frac{1}{2}(1+r)(1-s^2)
\end{aligned} \tag{4.31}$$

The lower panel of fig. 4.3 shows the shape functions for node 1 and 7.

Using the shape functions, the weak formulation of the momentum conservation can be reformulated as a system of linear equations. We illustrate this for a static analysis of small deformations in case of a linear elastic material. The following system of equations is to be solved for a single finite element:

$$\overline{K}\vec{u}_d = \vec{F} \tag{4.32}$$

with $\vec{u}_d$ the displacements of the nodes in the element, $\overline{K}$ the stiffness matrix and $\vec{F}$ the forces acting on the finite element.
Stiffness matrix: For a linear elastic material, the stiffness matrix can be defined by the following integral over the element volume V:

$$\overline{K} = \int_V \overline{B}^T \overline{C}\overline{B} dV \tag{4.33}$$

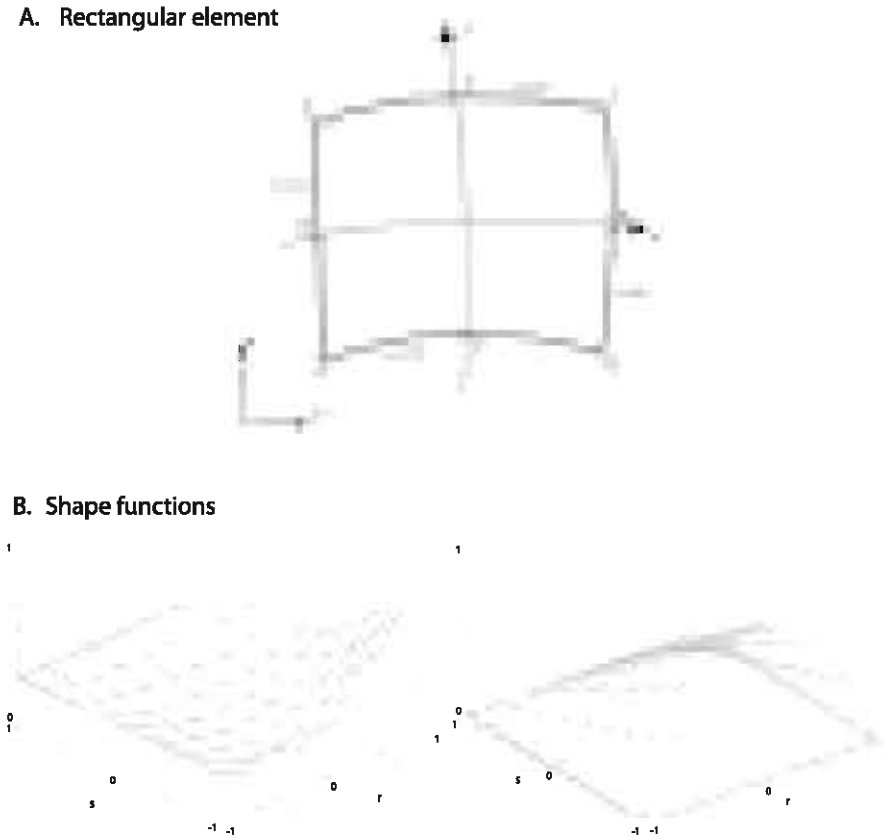

FIGURE 4.3: Illustration of the shape functions used in finite element methods for a 2D rectangular element. This figure was adapted from [65]

with $\overline{C}$ the tensor relating the stresses and strains in a linear manner as:

$$\vec{\sigma} = \overline{C}\vec{e} \tag{4.34}$$

with $\vec{\sigma}$ the vector containing the six independent stresses of the symmetric stress tensor, and $\vec{e}$ the vector containing the six independent strains of the symmetric strain tensor. $\overline{B}$ is the tensor containing the spatial derivatives of the shape functions. Hence, the stiffness matrix contains only known variables, depending on the geometry, material properties and shape functions of the element.

Force matrix: The forces acting on the element can be split into external body forces $\vec{f}$ (e.g. gravity), and a term containing the surface forces $\vec{t}$ acting on the element. These surface forces are present due to the loading on the boundary of the structure.

$$\overline{F} = \int_S \overline{N}^T \vec{t} dS + \int_V \rho_s \overline{N}^T \vec{f} dV \tag{4.35}$$

with $\overline{N}$ the tensor containing the element's shape functions.
In case of non-linear behaviour of the structure, due to non-linear material properties and/or geometrical non-linearities, a similar approach can be followed, but this is out of the scope of this work.

To conclude, any finite element method for solid mechanical applications consists of the following steps:
1. Reformulate the momentum equation with shape functions according to the weak formulation and solve for the unknown nodal displacements $\vec{u}_d$
2. Calculate the strains from the displacements $\vec{u}_d$. Strains can be obtained from the displacement vector $\vec{u}$ using the Green-Lagrange strain tensor, defined as:

$$E = \frac{1}{2}(\nabla\vec{u} + \nabla\vec{u}^T + \nabla\vec{u}^T\nabla\vec{u}) \tag{4.36}$$

In case of small deformations, the Green-Lagrange tensor can be linearized, i.e. the last term in equation 4.36 can be neglected.
3. Stresses are computed from the strains using a constitutive law, which describes the response of a material to an imposed load. A constitutive law for a linear elastic material was given in equation 4.34, but often more complex material models are necessary to realistically describe the blood vessel behaviour. A more accurate description of the vessel wall tissue is possible with a hyperelastic material [72].

4.3.3 Dynamic analysis

Performing a dynamical analysis means that the inertia term in the momentum conservation should be included. Equation 4.32 then contains a term of the form:

$$M\frac{\partial^2 u}{\partial t^2} \tag{4.37}$$

with M the mass matrix, only dependent on the shape functions of the element, and $\frac{\partial^2 u}{\partial t^2}$ the second order derivative of the displacement, further written as $\ddot{u}$. While the previously discussed shape functions take care of the spatial discretization of the solution, the inertia term also requires discretization in time. Abaqus uses an implicit time discretization scheme, called the Hilber-Hughes-Taylor scheme, which is unconditionally stable. Temporal discretization of the first order and second order derivative of the displacement is then defined as:

$$u^{n+1} = u^n + \Delta t\dot{u}^n + \Delta t^2((1 - \frac{1}{2}\beta)\ddot{u}^n + \beta\ddot{u}^{n+1}) \tag{4.38}$$

$$\dot{u}^{n+1} = \dot{u}^n + \Delta t((1-\gamma)\ddot{u}^n + \gamma\ddot{u}^{n+1}) \tag{4.39}$$

with

$$\beta = \frac{1}{4}(1-\alpha)^2 \tag{4.40}$$

$$\gamma = \frac{1}{2} - \alpha \tag{4.41}$$

The advantage of this scheme is that high-frequent noise, potentially induced when advancing in time, can be numerically damped. The parameter α is then varied between the values 0 (no damping) and -1/3 (maximal damping). This way, only the physical low-frequency response of the structure is obtained.

4.3.4 Practical setup

As for the fluid mechanical problem, a solid mesh should be constructed, preferably based on high-resolution medical scans, necessary to capture the small dimensions of the blood vessel wall. However, the choice of the element type requires more attention compared to the CFD-setup. As will be discussed further, two important modeling aspects determine the choice of element in Abaqus:

1. Order of the shape functions
2.Accuracy of the integration scheme

First of all, the element type is determined by the *order of the shape functions* (cfr. section 4.3.2). Both linear and quadratic elements are available in Abaqus, with quadratic elements more accurate but requiring more computational time.

Choosing an element type is also linked with the choice of the *integration scheme*. As can be seen in equations 4.32 and 4.35, the integrals should be evaluated over the finite element in a discrete way, and for this purpose, different calculation procedures are available . Most element types use a Gaussian quadrature scheme, i.e. a weighted sum of function values within the integration domain.

The elements can be divided in two groups according to the accuracy of the integration scheme. Elements with *full integration* schemes are most accurate, but most of them are not suitable for modeling incompressible material. *Reduced integration* elements evaluate the integrals at a set of optimally chosen integration points, requiring less

computational time. However, reduced integration only models contributions to the strain field which are one order less than the order of the shape functions. All tetrahedral elements use the full integration scheme. Both full and reduced integration are available for hexahedral elements.

Besides the element choice, one should also choose a deformation formulation. Previously, the small deformation analysis was discussed, as this is the most intuitive approach to explain solid mechanics. However, biological tissues demonstrate typically large deformations. For this purpose, Abaqus allows to model these geometrical non-linearities with the theory of large deformations, as briefly discussed in section 4.3.1. Finally, the loads and constraints experienced by the structure should be appropriately applied. Typically, a pressure load is imposed on the inner surface of the blood vessel wall.

4.4 FLUID-STRUCTURE INTERACTION: NUMERICAL MODELING OF INTEGRAL BLOOD VESSEL BEHAVIOUR

Simulations of fluid-structure interaction (FSI) model the complex blood flow and structural displacement field, taking into account their mutual effect on each other. Indeed, the flow field influences the structural displacement, but the movement of the structure also influences the flow field. In the next paragraphs, common FSI terminology and principles are explained, more particularly in the context of the in-house FSI-code applied in this dissertation [63, 64].

4.4.1 Coupling the fluid and structural domain

To find the solution of a coupled fluid-structure problem, the equations governing the fluid flow and structural displacement should be solved. The *fluid solver* numerically solves the Navier-Stokes equations determining the fluid flow (cfr. section section 4.2). The momentum equation governing the structural deformation is solved by the *solid solver* (cfr. section 4.3). In this work, the commercial software packages Fluent and Abaqus were respectively used as fluid and solid solver.

Choosing two commercial software packages has the disadvantage that coupling both solvers is hampered by the limited accessibility to the source code. Therefore, the applied fluid and solid solver can be considered as *black-box solvers*. On the other hand, coupling two black box

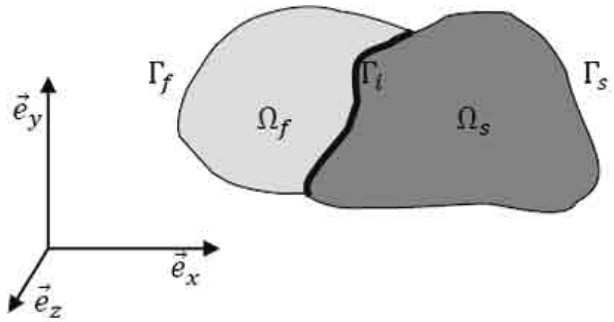

FIGURE 4.4: Abstract visualization of an FSI-problem. The solution domain is divided into a fluid Ω_f and solid domain Ω_s which share an interface Γ_i. This figure was adapted from [73].

solvers has the advantage that sophisticated codes, specifically developed and optimized for fluid and structural problems, can be applied.

An abstract visualization of an FSI-problem is given in fig. 4.4. The solution domain can be divided into a fluid domain Ω_f and a solid domain Ω_s. The boundaries of the domain are denoted as Γ_f and Γ_s, and the fluid-structure interface Γ_i is the intersection of both.

To solve the coupled fluid-structure problem, an appropriate grid formulation of the fluid and solid solution domains is required. Typically, the *Arbitrary-Lagrangian-Eulerian (ALE) formulation* is used for the fluid domain, as illustrated in fig. 4.5. In contrast to the Eulerian approach mentioned for CFD-problems with rigid walls (cfr. section 4.2.3), the fluid solver now uses a moving grid. The velocity of the fluid grid nodes is arbitrary, hence the name of the grid formulation. A common method is to move the fluid grid nodes according to a spring analogy, with a spring constant inversely proportional to the edge length. This causes a smooth redistribution of the nodes in the fluid domain, but care must be taken when large deformations are present. The latter requires a remeshing of the fluid domain, associated with interpolation errors. For the structural domain, a Lagrangian approach is taken (cfr. section 4.3.1), which means that the grid moves as the material deforms.

Typically, the grid resolution of the solid and fluid domain is quite different, which results in a *non-conforming mesh* on the interface. A

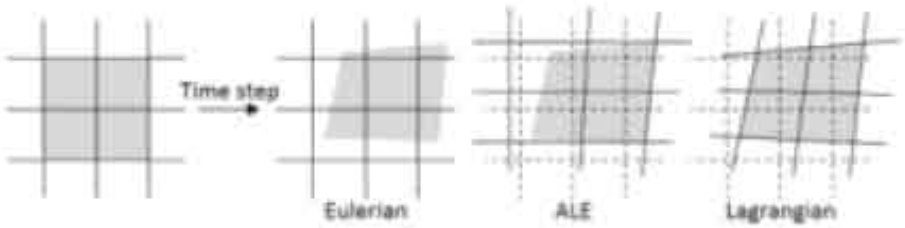

FIGURE 4.5: The ALE-grid formulation compared to the Lagrangian and Eulerian approach. The medium (fluid or solid) is indicated in grey, and the dashed line refers to the original grid. The grid is stationary for the Eulerian approach, and moves with the material for the Lagrangian formulation. With the ALE-grid formulation, the grid moves at an arbitrary velocity compared to the velocity of the medium. This figure was adapted from [73].

non-conforming mesh means that the elements of the solid and fluid grid do not coincide on the interface, as illustrated in the left panel of fig. 4.6. If gaps and overlays occur between the elements at the interface, the grid is called *non-matching*, shown in the right panel of fig. 4.6. Non-conforming and non-matching grids require appropriate interpolation of the flow and structural variables to the considered nodes, with an interpolation technique based on radial basis functions applied in this work [74].

4.4.2 Monolitic approach

In the monolitic approach, the equations governing the fluid and solid domain are solved simultaneously as one big set of equations. This is a straightforward *strongly coupled* FSI-approach, particularly suited for

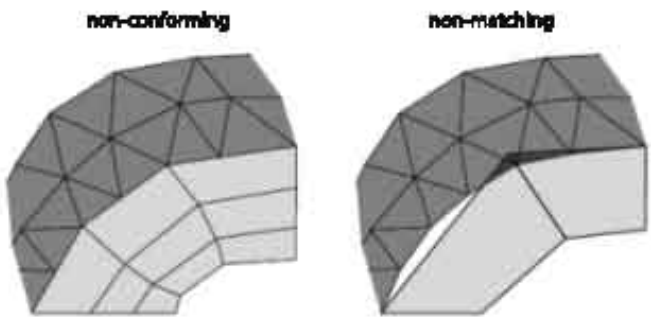

FIGURE 4.6: The left panel shows a non-conforming but matching grid at the interface. The right panel shows a non-conforming and non-matching grid. This figure was adapted from [73].

simple FSI-problems. However, the disadvantage is that specific solution methods for complex fluid and/or solid mechanical problems may no longer be applied.

If we represent the flow equations by F, and the structural equations by S, the system of equations solved by a monolitic solver can be written as:

$$\begin{aligned} F(\mathbf{v}, \mathbf{u}) &= 0 \\ S(\mathbf{v}, \mathbf{u}) &= 0 \end{aligned} \tag{4.42}$$

with $\mathbf{v}$ the flow variables and $\mathbf{u}$ the structural variables. This system of non-linear equations is often solved with *Newton-Raphson iterations*. The Newton-Raphson method is a popular approach to find the root of a non-linear function. For a one-dimensional function $f(x)$, the method searches for better approximations of the root with an iterative approach, based on an initial guess x_0. As illustrated in fig. 4.7, successive approximations are found using a first order Taylor series expansion of the function $f(x)$ around the root approximation x_k:

$$f(x) = f(x_k) + f'(x_k)(x - x_k) = 0 \tag{4.43}$$

Using this equation, the root approximation in iteration $k+1$ is found with the solution of iteration k as :

$$x_{k+1} = x_k - \frac{f(x_k)}{f'(x_k)} \tag{4.44}$$

A block formulation of the Newton-Raphson method is necessary to solve the system of non-linear equations of (4.42):

$$\underbrace{\begin{bmatrix} \partial_v F & \partial_u F \\ \partial_v S & \partial_u S \end{bmatrix}}_{\textit{Jacobian matrix}} \cdot \begin{bmatrix} v_{k+1} - v_k \\ u_{k+1} - u_k \end{bmatrix} = - \begin{bmatrix} F(v_k, u_k) \\ S(v_k, u_k) \end{bmatrix} \tag{4.45}$$

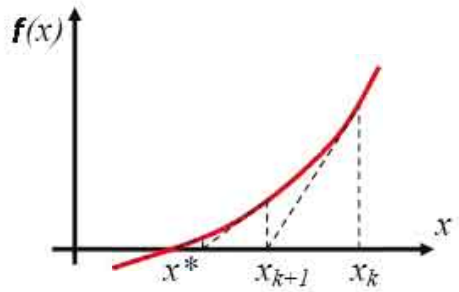

FIGURE 4.7: Illustration of the Newton-Raphson method. This figure was adapted from [73].

As can be seen in equation 4.45, the multidimensional formulation of the Newton-Raphson method requires the use of the Jacobian matrix of the system. More specifically, a monolitic solver calculates a Jacobian block matrix, which consists of (i) the partial derivatives of the flow solver with respect to the flow variables ($\partial_v F$) and structural variables ($\partial_u F$), (ii) the partial derivatives of the structural solver with respect to the flow variables ($\partial_v S$) and structural variables ($\partial_u S$).

4.4.3 Partitioned approach

In this dissertation, we used an in-house FSI-code [63, 64] coupling two black box solvers, entailing a *partitioned approach* to the fluid-structure interaction problem. This means that the flow and structural equations are solved *separately*, which requires that the coupled problem is decomposed in two sub-problems. A common approach in this matter is the *Dirichlet-Neumann decomposition*, which divides the FSI-problem into the following flow and structural problem:

(i) the flow equations are solved for a given displacement of the fluid-structure interface
(ii) the structural equations are solved for a given stress at the interface

When representing the displacement of the nodes at the interface as a vector $\vec{x}$, and the stress at the interface as a vector $\vec{y}$, the Dirichlet-Neumann decomposition can be mathematically formulated as:

$$\begin{aligned} \vec{y} &= F(\vec{x}) \\ \vec{x} &= S(\vec{y}) \end{aligned} \tag{4.46}$$

with F and S respectively representing the flow and structural equations. This system of equations can be interpreted as follows:
(i) For the *flow problem* $\vec{y} = F(\vec{x})$, the fluid grid is updated for a given displacement $\vec{x}$ of the interface, according to the chosen moving grid approach. The flow equations can then be solved to extract a stress $\vec{y}$ on the interface.
(ii)The formulation of the *structural problem*, $\vec{x} = S(\vec{y})$, shows that a stress $\vec{y}$ is imposed as a boundary condition on the interface, and the structural equations are solved to find the displacement vector $\vec{x}$ of the interface.

The Dirichlet-Neumann decomposition of the FSI-problem, described

by (4.46), can be solved in a *strongly coupled* or *weakly coupled* manner. The strongly coupled approach imposes an equilibrium condition on the interface, as was implicitly the case for the monolitic method, while in the weakly coupled approach, no equilibrium is enforced at the interface. The equilibrium condition at the interface can be defined as:

$$\begin{aligned} \vec{x} &= S(F(\vec{x})) \\ \vec{y} &= F(S(\vec{y})) \end{aligned} \tag{4.47}$$

Equation 4.47 states that the fluid and solid domain are in equilibrium with each other if the interface displacement and stress are. The weak and strong coupling strategy will be further explained in the next paragraphs.

4.4.3.a Weak or explicit coupling

Solving the partitioned approach in a weakly coupled manner means that no equilibrium condition is imposed on the interface. The flow and structural equations are solved just once per timestep, and the size of the timestep is limited to stabilize this technique. Hence, this technique is also referred to as an *explicit coupling* of partitioned FSI-solvers.

The most basic weak coupling approach solves the system of equations (4.46) as follows. The fluid solver is used to find the interface stress $\vec{y}$ at the new timestep $n+1$, based on the interface displacement $\vec{x}$ from the previous timestep n. Using this stress condition y_{n+1} as an input to the solid solver, the interface displacement $\vec{x}$ at timestep $n+1$ is found:

$$\begin{aligned} \vec{y}_{n+1} &= F(\vec{x}_n) \\ \vec{x}_{n+1} &= S(\vec{y}_{n+1}) \end{aligned} \tag{4.48}$$

However, this approach is not stable for incompressible fluids and compliant structures, and hence is not useful for modeling arteries [75, 76].

4.4.3.b Strong or implicit coupling

The partitioned technique can also be solved in a strongly coupled manner, i.e. the equilibrium conditions from (4.47) are imposed on the interface, and several *iterations per time step* are performed to find a converged solution of (4.46). This technique is also referred to as an *implicit coupling* of partitioned FSI-solvers.

During the iteration procedure, convergence is judged for every iteration k, by calculating the L2-norm of the residuals on the interface, and comparing it to a predefined tolerance. The interface displacement $\vec{x}$ should be in equilibrium with both the fluid and the solid, and for this purpose, the L2-norm of the residual r_x is calculated as:

$$r_x = \frac{1}{N_n}\sqrt{\sum_{i=1}^{N_n} |\vec{x}_{k+1} - \vec{x}_k|^2} \tag{4.49}$$

with k the current iteration, k-1 the previous iteration and N_n the number of nodes on the interface. Equilibrium is also demanded for the stresses on the interface $\vec{y}$, which is checked by the L2-norm of the residual r_y:

$$r_y = \frac{1}{N_f}\sqrt{\sum_{i=1}^{N_f} |\vec{y}_{k+1} - \vec{y}_k|^2} \tag{4.50}$$

with N_f the number of faces on the interface

The strongly or implicitly coupled partitioned solvers can be further classified according to the explicitness or implicitness of the applied iteration procedure. Two important iteration methods will be further discussed: (i) the explicit Gauss-Seidel iterations and (ii) the implicit Newton-Raphson method.

4.4.4 Iterative approaches for implicitly coupled partitioned solvers

4.4.4.a Explicit iteration approach - Gauss-Seidel iterations

As mentioned in the previous paragraph, partitioned solvers need an iterative approach to obtain an FSI-solution where the fluid and solid domain are in equilibrium. The most basic approach in this matter are the Gauss-Seidel iterations between the fluid and structural solver. This method sequentially solves the equations describing the Dirichlet-Neumann decomposition (cfr. equation 4.46).

During a particular timestep, the iteration procedure works as follows. First, the fluid problem is solved as:

$$\vec{y}_{k+1} = F(\vec{x}_k) \tag{4.51}$$

Next, the structural equations are solved as:

$$\vec{x}_{k+1} = S(\vec{y}_{k+1}) \tag{4.52}$$

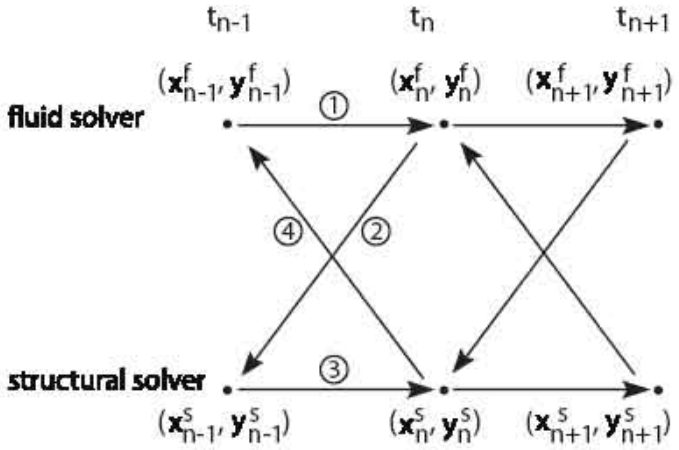

FIGURE 4.8: The Gauss-Seidel iteration scheme. The index f denotes the fluid solver, the index s the solid solver, and the index n the timestep. The displacement and stress vectors at the interface are respectively defined as x and y. This figure was adapted from [65].

This iterative approach is illustrated in fig. 4.8. For each iteration k, the convergence criteria calculated according to (4.49) and (4.50), are checked. If convergence is met, one proceeds to the next time level. As can be noticed in equation (4.51), the first iteration ($k = 0$) requires an appropriate choice for the initial interface displacement x_0. Typically, this value is extrapolated from the previous timesteps.

During the iteration process, different displacement modes of the interface arise. We illustrate the concept of displacement modes in fig. 4.9 for an FSI-problem in a straight tube with length L, visualizing the scaled interface displacements obtained from the first 6 iterations. An implicit iteration approach (see further) was taken in this matter, and for the further setup of the simulation, we refer to [77]. In the case of an implicit iteration approach, fig. 4.9 shows that the low wavenumber modes are the first to appear in the iteration process.

The Gauss-Seidel iterations converge very slowly for incompressible fluids, and often do not converge at all. This can be intuitively understood, as an incompressible fluid has difficulties compensating the required fluid volume change when the interface displaces. Considering a simple tube, new fluid has to enter the domain when the tube dilates, and vice versa, fluid has to leave the domain when the tube

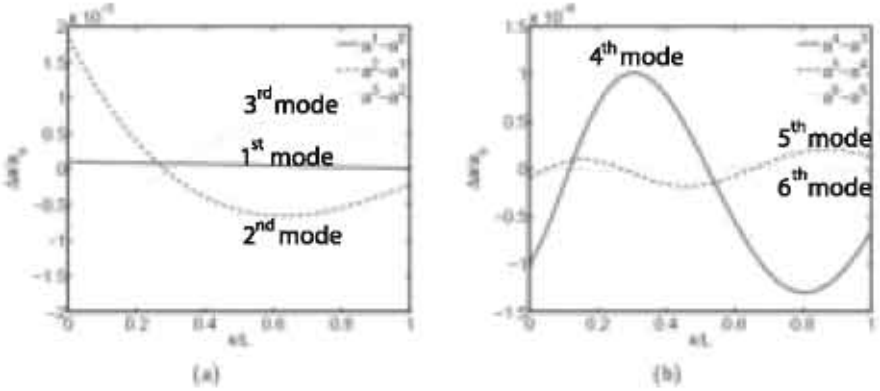

FIGURE 4.9: For a partitioned FSI-problem with implicit iterations, the scaled displacement modes at the interface are shown for the first 6 iterations. The low wavenumber modes are most unstable and are the first to appear. This figure was adapted from [77].

contracts. One method to stabilize Gauss-Seidel iterations is a technique called *Interface Artificial Compressibility* (IAC). This method introduces some fluid compressibility close to the interface, by adding a source term in the mass conservation equation for the control volumes next to the interface. For more details on IAC, we refer to [78].

How well the Gauss-Seidel iterations converge, depends on several factors, like geometry, stiffness of the structure, the ratio of the fluid density to the solid density, and the chosen timestep. In this context, Degroote et al [77] analyzed stability of the Gauss-Seidel iterations in an analytical manner, based on Fourier decomposition of the error on the interface displacement. The error is decomposed into a number of modes, each with their own spatial wavenumber. The wavenumber of the error mode corresponds to the wavenumber of the interface displacement mode. The stability of the modes was theoretically predicted by calculating the amplification factor μ of the error, as the ratio of the amplitude of the error mode at current iteration k to the amplitude of the error mode in the previous iteration k-1, with $\mu \leq 1$ referring to a stable mode.

The study was performed in a one-dimensional model of a tube with length L, which consisted of N independent structural cells and N fluid cells, neglecting structural inertia. To study the convergence as a function of structural stiffness and size of the timestep, the dimensionless

stiffness (κ) and timestep parameter (τ) were defined:

$$\kappa = \frac{\sqrt{\frac{Eh}{2\rho_f r_0} - \frac{p_0}{2}}}{v_0} \tag{4.53}$$

$$\tau = \frac{v_0 \Delta T}{L} \tag{4.54}$$

with E the Young elasticity modulus of the structure, h the structural thickness, ρ_f the fluid density and ΔT the timestep size. The parameters r_0, p_0 and v_0 respectively refer to the tube radius, pressure and flow velocity around which the structural behaviour is linearized.

It was demonstrated that stability is decreased for small timesteps (in case the structure is assumed massless) and flexible structures. This is shown in fig. 4.10, visualizing the error amplification factor μ versus the spatial wavenumber θ. For a large timestep size (left panel), the error amplification increases for smaller stiffnesses κ. For a small timestep size (right panel), the modes are less stable compared to the large timestep, with unstable modes appearing for the lowest wavenumbers.

Another important conclusion of [77] is that interface displacements with a low spatial wavenumber destabilize the iteration procedure. The low wavenumber modes hamper convergence, while the high wavenumber modes are naturally damped. This is visible in the decreasing trend

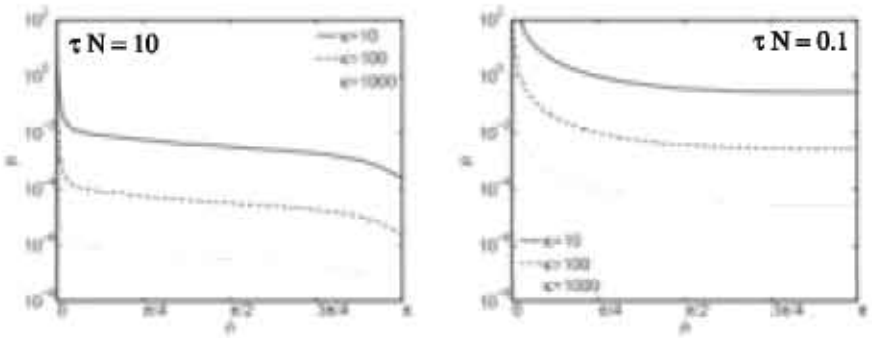

FIGURE 4.10: The amplification factor μ of each error mode, shown for different degrees of stiffness (κ=10,100,1000), versus the spatial wavenumber θ. The left panel shows a large timestep size (τN = 10) and the right panel a small timestep size (τN = 0.1). This figure was adapted from [77].

of the error amplification factor μ in fig. 4.10. This can be attributed to the large global fluid accelerations induced by the low wavenumber interface displacement modes, which are difficult to compensate for by incompressible fluids. On the other hand, high wavenumber modes cause smaller, local fluid accelerations, which are more easily balanced by the fluid volume.

Convergence is eased if implicitness is introduced into the iteration procedure (see further). The explicitness of the Gauss-Seidel iterations is evident when realizing that the flow equations are solved for a *given* interface displacement, and the displacement does not change as the flow pressure changes. The same is valid for the structure, which is solved for a *given* interface stress, without considering the interplay between stress and deformation during the iteration. Implicit iteration approaches take into account these *interplay* effects between interface displacement and stress, as will be explained in the next paragraph.

4.4.4.b Implicit iteration approach - Newton-Raphson iterations

The discussed partitioned approach entails a transfer of variables *at the interface*. More particularly, a stress transfer is performed from the fluid to the solid domain, and a displacement transfer from the solid to the fluid domain. However, a straightforward implementation of this coupling principle causes instabilities, as was previously discussed for the Gauss-Seidel iterations. Introducing implicitness in the iteration approach eases convergence, as it tempers the displacement and stress transfer at the interface. This is achieved by performing a sensitivity analysis, i.e. investigating the interplay between the displacement ($\Delta\vec{x}$) and stress changes ($\Delta\vec{y}$) at the interface, and accounting for their sensitivity during the iteration procedure. Further details on the implicit iteration approach will be discussed in the context of the IBQN-LS (Interface-Block-Quasi-Newton Least-Squares) model, as this is the technique applied in this dissertation.

4.4.5 IBQN-LS method

The IBQN-LS approach simultaneously solves the system of non-linear equations of (4.46), representing the Dirichlet-Neumann decomposition of the FSI-problem:

$$\begin{aligned} F(\vec{x}) - \vec{y} &= 0 \\ S(\vec{y}) - \vec{x} &= 0 \end{aligned} \tag{4.55}$$

A *block Newton-Raphson method* (cfr. section 4.4.2) is used for this purpose:

$$\begin{bmatrix} \frac{d\hat{F}}{d\vec{x}} & -I \\ -I & \frac{d\hat{S}}{d\vec{y}} \end{bmatrix} \cdot \begin{bmatrix} \Delta\vec{x} \\ \Delta\vec{y} \end{bmatrix} = - \begin{bmatrix} F(\vec{x}) - \vec{y} \\ S(\vec{y}) - \vec{x} \end{bmatrix} \tag{4.56}$$

The following matrices and vectors can be found in this equation:
(i) $\frac{d\hat{F}}{d\vec{x}}$: the Jacobian of the flow solver. This matrix expresses how the interface stress obtained from the flow solver reacts to changes in the interface displacement. Using black box solvers, the exact expression of the Jacobian can not be obtained, hence the hat-notation.
(ii) $\frac{d\hat{S}}{d\vec{y}}$: the Jacobian of the solid solver. This matrix expresses how the interface displacement obtained from the solid solver reacts to changes in the interface stress. Using black box solvers, the exact expression of the Jacobian can not be obtained, hence the hat-notation.
(iii) $\Delta\vec{x}$: the update in interface displacement. Considering an iteration k, the displacement update can be written as:

$$\vec{x}_{k+1} = \Delta\vec{x}_k + \vec{x}_k \tag{4.57}$$

(iv) $\Delta\vec{y}$: the update in interface stress. Considering an iteration k, the stress update can be written as:

$$\vec{y}_{k+1} = \Delta\vec{y}_k + \vec{y}_k \tag{4.58}$$

In the following paragraphs, the approach used to solve (4.56) will be explained step by step.

4.4.5.a Newton-Raphson iterations of the Gauss-Seidel type

Newton-Raphson iterations are performed to solve (4.56) for the *change* in interface displacement $\Delta\vec{x}_k$ and the *change* in interface stress $\Delta\vec{y}_k$ at iteration k. For this purpose, the block Newton-Raphson iterations are performed in a *Gauss-Seidel* manner. This means that, as for the explicit Gauss-Seidel iterations, the flow equations are solved first:

$$\tilde{\vec{y}}_{k+1} = F(\vec{x}_k) \tag{4.59}$$

and subsequently, the structural equations are solved:

$$\tilde{\vec{x}}_{k+1} = S(\vec{y}_{k+1}) \tag{4.60}$$

The *tilde* indication ($\tilde{}$) in the output of the flow and structural solver demonstrates that the coupling approach is not performed in a straightforward manner. In contrast to the explicit Gauss-Seidel iterations, the output of the solvers, $\tilde{\vec{y}}_{k+1}$ and $\tilde{\vec{x}}_{k+1}$, are intermediate values, which are *not* directly used as input to the structural solver or flow solver in a next step of the iteration procedure. Instead, the true input to the solvers is implicitly calculated, using the intermediate values $\tilde{\vec{y}}_{k+1}$ and $\tilde{\vec{x}}_{k+1}$. This tempers the displacement and stress transfer at the interface, hence avoiding instabilities.

Now the Gauss-Seidel character of the Newton-Raphson iterations is established, the righthand side of equation 4.56 can be formulated for iteration k as:

$$\begin{bmatrix} F(\vec{x}) - \vec{y} \\ S(\vec{y}) - \vec{x} \end{bmatrix} = \begin{bmatrix} \tilde{\vec{y}}_{k+1} - \vec{y}_{k'} \\ \tilde{\vec{x}}_{k'} - \vec{x}_{k} \end{bmatrix} \tag{4.61}$$

with the index k' arising because of the Gauss-Seidel character of the iteration approach. Indeed, as can be seen in equation 4.59, the index k changes when solving for the interface stress based on a given interface displacement.

4.4.5.b Implicit iteration approach

The difference between the implicit and explicit iteration approach is illustrated below considering the calculation procedure for updating the interface stress. For the update of the interface displacement, the same principles are valid.

(i) *Explicit iterations*: the interface stress is found as a direct solution to the flow equations, as expressed by equation 4.51. This approach only takes into account the effect of a change in interface displacement $\Delta\vec{x}$ on the output of the flow solver $\Delta\vec{y}$: $\Delta\vec{x} \overset{?}{\Rightarrow} \Delta\vec{y}$
(ii) *Implicit iterations*: the interface stress is found by considering the mutual effect of the interface displacement and stress: $\Delta\vec{x} \overset{?}{\Leftrightarrow} \Delta\vec{y}$. Compared to the explicit approach, this method also takes into account how the interface displacement changes for a varying interface stress. An implicit approach is achieved with a sensitivity analysis, investigating the effect of changes in the interface displacement on the interface stress, and vice versa.

With the implicit iteration procedure, the straightforward equations

of the Gauss-Seidel iterations (4.51 and 4.52) are no longer valid and a more complex form is obtained by manipulating the system of equations in (4.56). Formulating these equations for iteration k, and taking into account the Gauss-Seidel character of the Newton-Raphson iterations (equation 4.61), the following linear system is obtained:

$$\begin{bmatrix} \frac{d\hat{F}_k}{d\vec{x}} & -I \\ -I & \frac{d\hat{S}_{k'-1}}{d\vec{y}} \end{bmatrix} \cdot \begin{bmatrix} \Delta\vec{x}_k \\ \Delta\vec{y}_k \end{bmatrix} = - \begin{bmatrix} \tilde{\vec{y}}_{k+1} - \vec{y}_{k'} \\ \tilde{\vec{x}}_{k'} - \vec{x}_k \end{bmatrix} \tag{4.62}$$

This system is first solved for the update of the interface stress $\Delta\vec{y}_k$, using $k' = k$. For this purpose, the displacement update $\Delta\vec{x}_k$ is eliminated from the system, resulting in the following equation:

$$(I - \frac{d\hat{F}_k}{d\vec{x}} \frac{d\hat{S}_{k-1}}{d\vec{y}}) \Delta\vec{y}_k = \tilde{\vec{y}}_{k+1} - \vec{y}_k + \frac{d\hat{F}_k}{d\vec{x}} (\tilde{\vec{x}}_k - \vec{x}_k) \tag{4.63}$$

Equivalently, the interface displacement update $\Delta\vec{x}_k$ can be calculated, eliminating $\Delta\vec{y}_k$ from the system, with $k' = k + 1$:

$$(I - \frac{d\hat{S}_k}{d\vec{y}} \frac{d\hat{F}_k}{d\vec{x}}) \Delta\vec{x}_k = \tilde{\vec{x}}_{k+1} - \vec{x}_k + \frac{d\hat{S}_k}{d\vec{y}} (\tilde{\vec{y}}_{k+1} - \vec{y}_{k+1}) \tag{4.64}$$

The practical explanation and implementation of equations 4.63 and 4.64 is discussed in the next paragraphs.

4.4.5.c Approximation of the Jacobian

Equations 4.64 and 4.63 show that the Jacobian of the flow and solid solver are required to perform implicit iterations. The exact form of the Jacobian can not be obtained since black box solvers are used in the coupling procedure. Therefore, the Jacobians are approximated with a *reduced order model* of the flow and solid solver on the interface.

A reduced order model of the solvers is built by performing a sensitivity analysis. We illustrate this for the Jacobian $\frac{d\hat{F}_k}{d\vec{x}}$ of the flow solver, but the same principles are valid for the solid solver. The approximate Jacobian of the flow solver at subiteration k describes how the interface stress changes ($\Delta\vec{y}_k$) for a given perturbation of the interface displacement ($\Delta\vec{x}_k$):

$$\Delta\vec{y}_k = \frac{d\hat{F}_k}{d\vec{x}} \Delta\vec{x}_k \tag{4.65}$$

The reduced order model states that an arbitrary perturbation of the interface displacement $\Delta\vec{x}$ can be written as a linear combination of the displacement perturbations of the previous k iterations:

$$\Delta\vec{x} \approx \sum_{i=1}^{k} \alpha_i \Delta\vec{x}_i \tag{4.66}$$

The stress change $\Delta\vec{y}$ induced by the displacement perturbation $\Delta\vec{x}$ can also be written as a linear combination of the interface stresses from the previous k iterations, using the same α-coefficients:

$$\Delta\vec{y} \approx \sum_{i=1}^{k} \alpha_i \Delta\vec{y}_i \tag{4.67}$$

The coefficients α_i can be found with a *least-squares (LS) approximation*, since the dimension of the interface displacement is typically much larger than the number of iterations k.

To perform the least-squares approximation, the perturbations of the interface displacement and the associated changes of the interface stress should be stored during the iteration process. More particularly, if $k+1$ iterations have been performed, k displacement perturbations and k stress changes at the interface are available:

$$\Delta\vec{x}_{k-1} = \vec{x}_k - \vec{x}_{k-1} \tag{4.68}$$

$$\Delta\tilde{\vec{y}}_k = \tilde{\vec{y}}_{k+1} - \tilde{\vec{y}}_k \tag{4.69}$$

Per iteration of a particular timestep, these vectors are stored column-wise in the matrix V_f^k for the displacements and in the matrix W_f^k for the stresses, with the index f denoting the fluid solver. Equation 4.66 and 4.67 can then be reformulated as:

$$\Delta\vec{x} \approx V_k \alpha \tag{4.70}$$

$$\Delta\vec{y} \approx W_k \alpha \tag{4.71}$$

The α-coefficients are found using an economy-size QR-decomposition of the matrix V_k:

$$V_k = Q_k R_k \tag{4.72}$$

For details on this matrix decomposition technique, we refer to [79]. Using the QR-decomposition of V_k, the α-coefficients are defined as:

$$\alpha = R_k^{-1} Q_k^T \Delta\vec{x} \tag{4.73}$$

This definition of the α-coefficients can also be used to describe the perturbation of the interface stress:

$$\Delta\vec{y} = W_k\alpha = \underbrace{W_k R_k^{-1} Q_k^T}_{Jacobian}\Delta\vec{x} = \frac{d\hat{F}_k}{d\vec{x}}\Delta\vec{x}_k \tag{4.74}$$

To conclude, the Jacobian of the flow solver can be calculated according to:

$$\frac{d\hat{F}_k}{d\vec{x}} = W_k R_k^{-1} Q_k^T \tag{4.75}$$

The same procedure can be followed to calculate $\frac{d\hat{S}_k}{d\vec{y}}$, keeping track of the in- and outputs of the structural solver during the iteration procedure.

4.4.5.d Overview IBQN-LS algorithm

For a given iteration k of timestep n, the following steps are performed during the iteration procedure of the IBQN-LS method, to find the solution at iteration k+1:

1.) The updated interface displacement $\vec{x}_k$ is used as input to the flow solver: $\tilde{\vec{y}}_{k+1} = F(\vec{x}_k)$.

2.) Using the output of the flow solver, $\tilde{\vec{y}}_{k+1}$, the reduced order model of the flow solver is updated with one extra mode.

3.) The update of the interface stress ($\Delta\vec{y}_k$) is calculated according to equation 4.63, using the reduced order models of the flow and solid solver. The interface stress at iteration $k+1$ is then: $\vec{y}_{k+1} = \Delta\vec{y}_k + \vec{y}_k$

4.) The updated interface stress $\vec{y}_{k+1}$ is used as input to the solid solver: $\tilde{\vec{x}}_{k+1} = S(\vec{y}_{k+1})$.

5.) Using the output of the solid solver, $\tilde{\vec{x}}_{k+1}$, the reduced order model of the solid solver is updated with one extra mode.

6.) The interface displacement is updated according to: $\vec{x}_{k+1} = \Delta\vec{x}_k + \vec{x}_k$, with $\Delta\vec{x}_k$ obtained with the implicit approach of equation 4.64, using the updated reduced order models of the flow and solid solver.

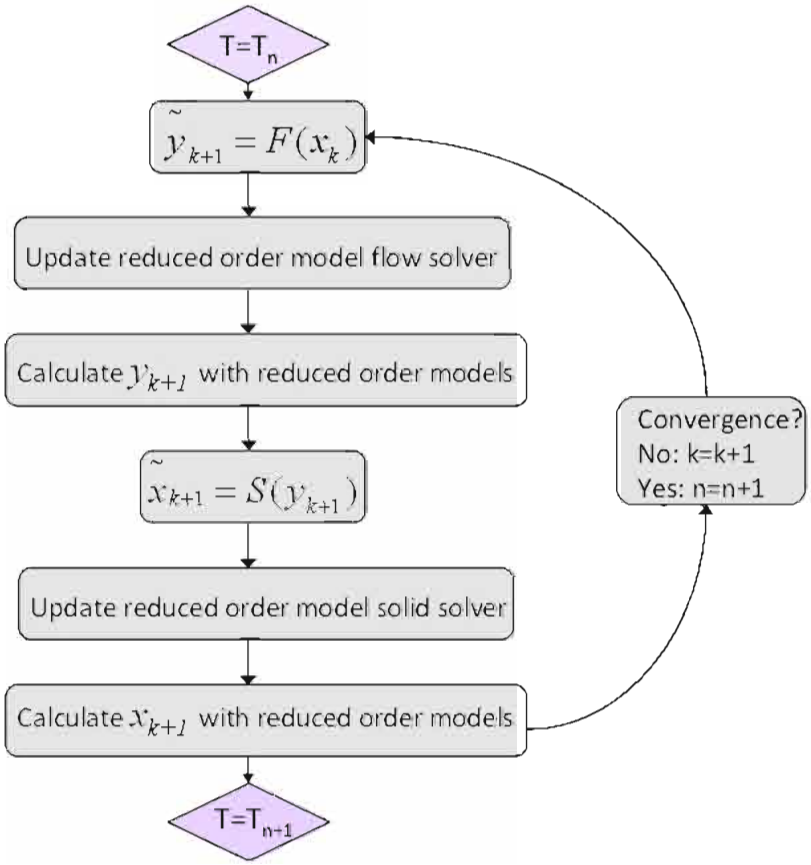

FIGURE 4.11: Illustration of the iteration procedure used in the IBQN-LS method.

7.) The convergence criteria for the interface displacement and stress, as described in equations 4.49 and 4.50, are checked. If convergence is met, the timestep is increased to $n+1$. If not, the iteration loop is repeated from step 1.

This iteration procedure is also illustrated in fig. 4.11.

First iterations of a timestep: It should be noted that this iteration procedure can not be performed for the first two iterations of a timestep, i.e. k=1 and k=2. As could be deduced from the construction of the reduced order models, at least two iterations are necessary to construct a single mode. Therefore, the procedure followed in the first two iterations is different. Indeed, explicit Gauss-Seidel iterations are performed for the first two iterations, as no reduced order model can be constructed yet. More particularly, the following steps are followed at the beginning of each timestep n:

1.) Each timestep starts with an initial guess of the displacement of the interface ($\vec{x}_0$), based on extrapolation of the results from the previous timesteps.

2.) Using this initial interface displacement, the interface stress is calculated as: $\vec{y}_1 = F(\vec{x}_0)$. No tilde-notation is used now, since the output of the flow solver will be directly transferred to the solid solver, as for the explicit Gauss-Seidel iterations.

3.) The output of the solid solver is calculated as $\tilde{\vec{x}}_1 = S(\vec{y}_1)$. The obtained displacement of the interface is not directly transferred to the fluid solver. Since no reduced order model can be constructed yet, underrelaxation (cfr. section 4.2.7) with a factor ω is performed to temper the transfer: $\vec{x}_1 = \vec{x}_0 + \omega(\tilde{\vec{x}}_1 - x_0)$

4.) Using the interface displacement $\vec{x}_1$ obtained in step 3, the interface stress is calculated as: $\vec{y}_2 = F(\vec{x}_1)$.

5.) The reduced order model of the flow solver can be built with one mode, using the input-output couples of the flow solver: $\vec{x}_1 - \vec{x}_0$ and $\vec{y}_2 - \vec{y}_1$.

6.) The interface stress $\vec{y}_2$ is directly transferred to the solid solver, and the interface displacement is calculated as: $\tilde{\vec{x}}_2 = S(\vec{y}_2)$.

7.) The reduced order model of the solid solver can also be built now, using the input-output couples of the solid solver: $\vec{y}_2 - \vec{y}_1$ and $\tilde{\vec{x}}_2 - \tilde{\vec{x}}_1$.

8.) Now the reduced order models of both solvers are available, the iteration procedure previously explained and illustrated in fig. 4.11 can be applied.

4.4.6 Conclusion

Developing algorithms for tackling fluid-structure interaction problems is a complex domain in itself. Many coupling methods exist, and their stability is depending on the investigated situation. For blood vessel modeling, the explicit Gauss-Seidel iterations are not advantageous due to the compliant vessel walls and the similar fluid and solid density. Implicit iteration approaches are required for this application domain,

and both the interface artificial compressibility and the IBQN-LS method can be used, with the latter one applied in this dissertation. For a complete overview on these and other coupling techniques, we refer to the PhD-thesis of Degroote [73].

Two

Integrating computational fluid dynamics and ultrasound simulations

CHAPTER 5

Ultrasound Simulation of Complex Flow Velocity Fields Based on CFD

In this chapter, we elaborate on the creation of CFD-based phantoms for ultrasound simulations of complex blood flow. We simulate ultrasonic flow images with the Field II software, which models blood as a collection of point scatterers on which the ultrasound waves reflect. Doppler signals can then be retrieved by moving the point scatterers according to a realistic blood flow field. Instead of using analytically described flow behaviour, as used in previous research, we derive complex blood movement from velocity fields obtained with computational fluid dynamics (CFD). The coupling of such a computed flow field with an ultrasound model offers flexible control of both flow and ultrasound imaging parameters, ideally suited for improving and developing imaging algorithms.

We validate the proposed method in a straight tube with a stationary parabolic velocity profile, and further exemplify it by an eccentricly stenosed carotid bifurcation. We show that the estimated flow velocities are in good agreement with the CFD reference, both for color flow imaging and pulsed-wave Doppler simulations.

This chapter is based on the IEEE-TUFFC paper *"Ultrasound Simulation of Complex Flow Velocity Fields Based on Computational Fluid Dynamics."*, vol. 56, p. 546-556, 2009.

5.1 Introduction

Common vascular diseases such as aneurysms and arterial stenosis are most often associated with atherosclerosis. This disease appears to preferentially originate in regions with disturbed flow velocity and wall shear stress patterns such as on the downstream side of bifurcations and on the inner curvature of bends [6, 80, 81]. When flow departs from a laminar unidirectional pattern, shear forces exerted on the vascular endothelium become more complex. Also, residence time of circulating particles in susceptible regions will increase and may enhance the development of arterial plaque. An accurate understanding and efficient imaging of these disturbed flow fields can thus help in diagnosing arterial disease in an early stage and contribute to our understanding of atherogenesis and progression of cardiovascular disease.

Diagnostic ultrasound imaging has proven valuable when screening for cardiovascular disease, offering a non-invasive way of imaging pathology related both to the vessel wall and vessel flow. Using Doppler based techniques such as pulsed-wave (PW) Doppler or color flow imaging (CFI), one can visualize the flow velocity components parallel to the ultrasound beam. However, these methods are not always able to portray the true flow behavior, especially for complex vessel geometries and non-axial flow patterns such as vortex formations. In previous work, methods have been proposed to estimate the true velocity vector with ultrasound, based for instance on speckle tracking algorithms [82] or crossed beam Doppler [46, 47]. We refer to [83, 84] for an overview. For the complex flow patterns which can occur in the vicinity of an arterial stenosis or aneurysm, the performance and clinical applicability of these methods remain however to be established. Consequently, there is a need for a controlled and realistic environment where experimental techniques can be validated and compared to established methods.

In the study of flow behavior, computational fluid dynamics (CFD) plays an important role. CFD allows obtaining realistic flow fields in

complex geometries by solving the non-linear equations of mass and momentum conservation in a discretized form. A truthful reconstruction of the flow and wall shear stress patterns in physiological and pathological conditions can then be obtained by using complex geometries and boundary conditions derived for example from magnetic resonance imaging (MRI) [85–87]. The complex flow fields existing in carotid arteries and aneurysms have been extensively studied using CFD [88, 89].

In this work, we present a framework that couples CFD and ultrasound simulations, and which allows generating ultrasound signals resulting from realistic flow patterns in complex vessel geometries. In particular, blood is modelled as a collection of point scatterers moving with velocities given by the CFD velocity field and the Field II simulation package is used to generate the backscattered ultrasound signals.

Some references on this topic can be found in literature. Jensen et al introduced synthetic computer phantoms with moving scatterers for generating ultrasound B-mode and color flow images with Field II [56]. Kerr et al described a computer method for simulating Doppler color flow also by representing blood and tissue as 3D point scatterers [59]. However, these computer phantoms were analytically described and there is a need for computer models accounting for complex 3D flow fields in anatomically and physiologically realistic conditions, and the associated complex scatterer movement. Balocco et al proposed a 3D-model of a pulsating vessel where both 3D flow and wall displacements simulations were coupled with the Field II-software [90]. However, little elaboration was made on how the scatterer phantom was derived from the flow and mechanical simulations.

Consequently, the aim of this work is to present a fully elaborated method on generating CFD based phantoms for ultrasound simulations and in this framework obtain Doppler signals of realistic flow for method development and validation. Vessel wall movement was not included in the current model. However, simulating ultrasound images from realistic arterial flow based on CFD is considered a first step towards a more complete model also including fluid structure interactions (FSI), where fluid flow influences the wall motion and vice versa. In this paper we will focus on carotid arteries due to the complexity of the local flow field, their susceptibility to atherosclerosis, and

because the location is easily accessible with ultrasound. The performance of the simulation environment will be evaluated through both PW-Doppler and CFI examples.

In section 5.2, we elaborate on the applied CFD and ultrasound procedures. The issues arising when coupling a CFD flow field with ultrasound software will be presented. In section 5.3, we will show results on how well the CFD and estimated ultrasound velocity fields correspond. In first instance, the coupling of flow simulations with the ultrasound environment will be validated using stationary flow simulations in a straight tube before going thoroughly into the carotid artery. To compare the velocity fields over time, PW-Doppler simulations will be assessed. In section 5.4, the potential usefulness and limitations of CFD generated phantoms will be discussed as well as the limitations to our specific approach. Possible clinical applications and future work will also be mentioned.

5.2 Methods

5.2.1 Flow mechanics and CFD simulations

5.2.1.a Straight tube

To verify the ultrasound simulations of a CFD-generated phantom, stationary flow was simulated in a 5 cm tube created in the modeling software Gambit 2 (Fluent Inc., Sheffield, UK), with a diameter of 6 mm to be comparable with carotid dimensions. The geometry was meshed with 628902 tetrahedrons, resulting in a high density mesh where we could acquire mesh independent results and also had sufficiently accurate information on the flow field compared to the ultrasound resolution. The commercial CFD software Fluent 6.2 (Fluent Inc., Sheffield, UK) was used to numerically solve the Navier-Stokes equations with a finite volume method. Standard pressure discretization and second order upwind momentum discretization were used. The pressure-velocity coupling scheme was SIMPLE [67]. Blood was modeled as an incompressible Newtonian fluid with dynamic viscosity μ and density ρ respectively set to 3.5 mPas (3.5cP) and 1050 kg/m^3. Rigid walls were assumed and a parabolic velocity profile with a maximum velocity of 0.5 m/s was chosen as an inlet boundary condition. The outlet boundary condition was a constant pressure of 100 mmHg.

5.2.1.b Carotid artery

The carotid artery was based on a geometry of a healthy volunteer in which we artificially added an eccentric plaque in the interna. Starting from CT-scans, the geometry could be three-dimensionally reconstructed and meshed with appropriate software (Mimics, Materialise Leuven, Belgium), eventually resulting in a tetrahedral grid of 669409 elements. At the level of the common carotid artery, we imposed an inlet velocity profile which we measured in a healthy subject with pulsed-wave Doppler measurements using a 7L 3-7 MHz linear array transducer for vascular imaging applications (Vivid 7 PRO, GE VingMed Ultrasound, Horten, Norway). Since fully developed flow [91] may be assumed at this location, the inlet area was sufficiently extended to meet this condition. A constant [92] 45-55% outflow division between external and internal carotid artery was imposed as outlet boundary condition [93]. The CFD-package Fluent assumes fully developed flow at outflow boundaries and cylindrical extensions were therefore matched to the outlet surfaces. The Womersley and maximal Reynolds number in the common carotid artery were calculated to be approximately 3.8 and 605. The cardiac cycle (length 1s) was divided into 200 equally spaced timesteps and three cycles were computed to obtain results fully independent of any transient effects. The calculation took 220 hours on a 64-bit, 2.4 GHz Intel Core 2 Duo processor. The same numerical schemes as for the stationary simulation were used.

5.2.2 Ultrasound simulation model

For ultrasound simulations, the Field II software created by Jensen et al [17, 18] was employed. This simulation software makes it possible to model arbitrary transducers and to use realistic image scan sequencing. It is restricted to linear wave propagation and operates in the Born approximation regime, but may include frequency dependent attenuation. The approach is based on spatial impulse response estimation as described by Tupholme [94] and Stepanishen [95], and makes use of linear system theory to determine the ultrasound field based on an excitation pulse, the temporal impulse responses of the transmitting and receiving transducers, and the spatial impulse response at a given point.

In Field II tissue is modelled as a collection of point scatterers. Blood can in this setting be modelled as randomly distributed point scatterers with a density that, according to the central limiting theorem, results in

Gaussian distributed RF-signal amplitudes. The total number of scatterers then needed is related to the resolution of the imaging system determined by the pulse length and the lateral and elevation beamwidth, which avoids the extreme computational effort needed for representing each red blood cell by separate point scatterers. Dynamic objects are achieved by moving the point scatterers during simulation. Each ultrasound beam is simulated individually, and it is therefore possible to update the position of moving scatterers between beam acquisitions: $\Delta\vec{R} = \vec{V}\frac{1}{PRF}$ with $\Delta\vec{R}$ the displacement vector and $\vec{V}$ the velocity vector of the scatterer.

Field II simulation times are mainly related to the number of point scatterers, the axial sampling frequency, and the number and shape of mathematical subelements used for modelling the transducer.As shown in a simplified example in [96], 94% of the Doppler energy can be contributed to the main lobe of the beam. The number of scatterers significantly contributing to the RF-signal is therefore determined by the beam intensity and can thus be reduced by only including scatterers in the vicinity of the main lobe without significantly affecting results. The Nyquist criterion determines in theory the axial sampling frequency. However, a higher sampling frequency is typically necessary to represent the simulated spatial impulse responses [97], and may otherwise induce significant sidelobes in the Doppler spectrum as shown in fig. 5.2B for a sampling frequency of 40 and 100 MHz respectively. Finally, the transducer should be divided into smaller mathematical subelements such that every scatterer imaged is in the far field of each subelement [17] ($l >> \frac{w^2}{4\lambda}$ with l the distance to the imaged point, w the largest dimension of the element and λ the wavelength), and such that a sufficiently accurate field representation is obtained when using a fixed elevation focus.

5.2.3 Ultrasound simulation setup

An illustration of the imaging setup is shown in fig. 5.1. The CFD phantom of both the straight tube and the carotid artery was imaged with a one-dimensional (1-D) 192 element linear array transducer having a center frequency of 5 MHz, a relative bandwidth of 64%, an azimuthal pitch of 0.25 mm, and an elevation element width of 6 mm. In our setup each transducer element was divided into four rectangular shaped mathematical elements in the elevation direction. This choice lowered simulation times while keeping the far field of each mathematical element at an axial distance of 1.8 mm, and ensuring an accurate

focused elevation field from about 0.5 cm in depth. The most shallow point scatterers were located at about 0.75 cm in depth. The azimuth focus was fixed at 2 cm in depth with an F-number of 2.5 on transmit, and dynamic focus and expanding aperture was used on receive to retain an F-number of 1.4. Further, a fixed elevation focus at 3.2 cm was used. Rectangular and cosine tapered apodization were applied on transmit and receive respectively.

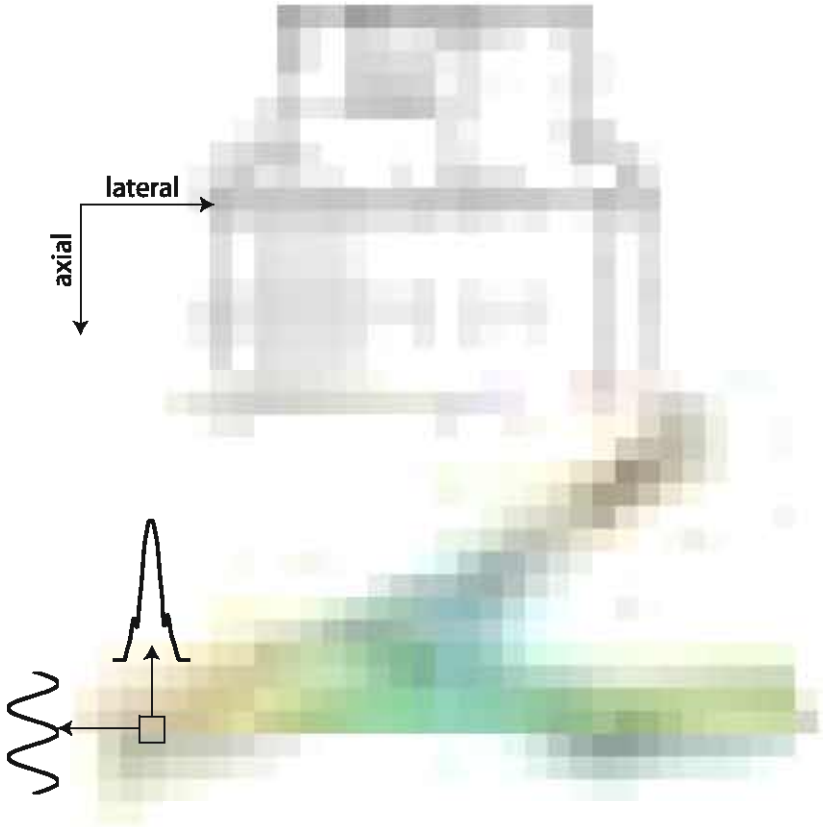

FIGURE 5.1: An illustration of the imaging setup. A straight tube or a carotid bifurcation (indicated) was imaged using a 3-7 MHz linear array transducer. An example of beam interleaved scan sequencing as used in the CFI simulations is also shown, where the numbers indicate the beam sequence. The imaging objects were angled 20^o to obtain non-zero Doppler shifts. Markers 1, 2 and 3 indicate the common, external and internal carotid artery and refer to the locations where pulsed-wave (PW) Doppler simulations were executed. The horizontal markers indicate the PW-Doppler sample volumes, in our examples 1.5 mm.

The required density of the scatterers is determined by the imaging system bandwidth, with approximately 10 scatterers per resolution cell assuring Gaussian distributed RF-signals. A similar number has previously been reported in literature [58]. The resolution cell was in our

case defined as the volume covered by the axial pulse length and the one-way -3dB beam widths in lateral and elevation direction respectively.

The simulation time was further reduced by only including scatterers at a distance of $k = 12$ times the receive beam width, equal to about ±5 mm in the azimuth direction. This rather conservative value still reduced the number of scatterers to one third the original amount. To demonstrate the effect of only including scatterers in the vicinity of the main lobe, the Doppler spectrum of one scatterer traversing the beam (velocity = 10 cm/s) was simulated. Fig. 5.2 shows the Doppler spectrum for no limitation of the included scatterers and for limiting scatterers to k=1 and k=12 times the receive beamwidth. The choice of

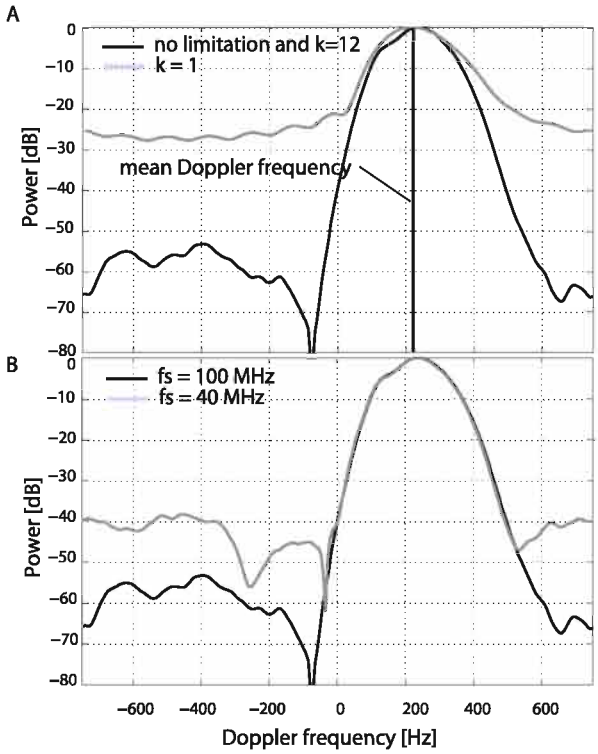

Figure 5.2: A. The effect on the Doppler spectrum of limiting the imaged scatterers to the vicinity of the main lobe. Simulations of one scatterer traversing the beam were executed and showed that k = 12 times the receive beamwidth, as chosen in the final simulation set-up, keeps the Doppler spectrum undisturbed. B. The influence of different sampling frequencies was studied by simulating Doppler spectra of one scatterer traversing the beam and sampling the received RF-signal with respectively 40 MHz and 100 MHz. A sampling frequency of 40 MHz significantly increases the Doppler sidelobe levels.

k = 12 keeps the Doppler spectrum undisturbed.

The sampling frequency of the RF-signal was set to 100 MHz during simulation, and was decimated to 25 MHz for the in-phase and quadrature (IQ) signals during postprocessing. This proved sufficient to keep Doppler spectrum sidelobes at about -50 dB. The influence of the sampling frequency can also be studied in fig. 5.2 where the Doppler spectrum was simulated for one scatterer traversing the beam with velocity 10 cm/s. A sampling frequency of 40 MHz significantly increases the Doppler sidelobe levels compared to 100 MHz as chosen in our final set-up. No frequency dependent attenuation was included for the purpose of our examples but can be included in the Field II simulation program at the expense of higher simulation times or can be approximated during postprocessing. Thermal noise was not included either, but can easily be applied to the simulated RF-signals during postprocessing. For a summary of simulation parameters please see Table 5.1.

5.2.3.a Straight tube validation setup

Halfway across a straight tube angled 20^o with respect to the lateral direction, 600 pulses were fired at a PRF of 4 kHz using a 2.5 period sinusoidal excitation. For each packet N_p of 15 pulses, a new random distribution of scatterers was created to obtain 40 statistically independent realizations. Velocities along the arterial cross-section were estimated using the autocorrelation algorithm developed for ultrasound applications by Kasai et al [36]. This is an estimator of the mean axial velocity $\hat{v}_z$ based on the phase of the autocorrelation function at lag one, $\hat{R}(1)$, as given by,

$$\hat{v}_z = \frac{c \cdot PRF}{4\pi f_0} \arctan\left(\frac{Im\left\{\widehat{R}(1)\right\}}{Re\left\{\widehat{R}(1)\right\}}\right), \tag{5.1}$$

where $N_p - 1$ correlation function estimates were averaged for each slow-time signal vector in range. The autocorrelation estimator is known to be unbiased for narrowband and in general symmetrical Doppler spectra, and to have a variance that increases with the spectrum bandwidth [98, 99].

A mean-subtraction clutter filter was employed for each signal vector prior to velocity estimation. Based on the 40 axial velocity profile realizations, the bias and variance of the estimates were investigated.

5.2.3.b *Color flow imaging setup*

In the color flow imaging simulation setup, a 3-by-4 cm scan was made using a 2.5 period sinusoidal excitation pulse, fired at a pulse PRF of 3.75 KHz for a packet size of 12. Beam interleaved acquisition [100] was applied to ensure that the waiting time between beam acquisitions was always given by the maximum PRF available, as limited by the image scan depth. This scanning technique is typically used in CFI to maximize the imaging frame rate when the Doppler PRF is chosen lower than the maximum imaging PRF available, as is most often the case in peripheral imaging. A number of neighbouring beams are then acquired sequentially at PRFmax while maintaining the Doppler PRF in the slow time domain (cfr. fig. 5.1). To get a reasonable frame rate, each image frame consisted of a total of 108 scanlines, equal to 27 interleave groups of size 4. This resulted in a frame rate of 11 frames per second. For a summary of the ultrasound simulation parameters, we refer to table 5.1. Axial velocities were estimated using the autocorrelation algorithm as described for the straight tube. In addition, the autocorrelation function estimates were spatially averaged over 2 pulse lengths in the axial direction and for 3 beams in the lateral direction. The CFI simulations for the stationary straight tube and the dynamic carotid took 3 hours 40 minutes and 8 hours 38 minutes per frame respectively on a 3.4 GHz Pentium IV processor.

5.2.3.c *Pulsed wave Doppler setup*

To investigate the Doppler signal through the cardiac cycle, PW-Doppler simulations were performed. For these simulations, 4000 sinusoidal

Table 5.1: The ultrasound set-up for CFI

Probe parameters		**CFI simulation setup**	
center frequency	5 MHz	excitation	sinusoidal
relative bandwidth	65%	pulse periods	2.5
number of elements	192	PRF_{max}	15 kHz
element pitch	0.25 mm	PRF	3.75 kHz
element height	6 mm	packetsize	12
transmit focus Az	2 cm	scanlines	108
transmit focus El	3.2 cm	interleave group size	4
dynamic receive focusing	yes	$F_{\#}$ transmit / receive	2.5 / 1.4
expanding aperture	yes	IQ sample rate	25 MHz

pulses of 2.5 periods were fired at a PRF of 4 kHz at fixed locations before and after the carotid bifurcation apex. Sample volumes of 1.5 mm were chosen at appropriate depths as shown in fig. 5.1. The mean frequency of the Doppler spectrum G(ω) was calculated according to the formula (scaled to velocity):

$$v_z = \frac{c \cdot PRF}{4\pi f_0} \frac{\int_{-\pi}^{\pi} \omega \cdot G(\omega) d\omega}{\int_{-\pi}^{\pi} G(\omega) d\omega}. \tag{5.2}$$

The formula was calculated as a discrete sum at frequencies $\omega(n) = \frac{2\pi}{N}(n - \frac{N-1}{2})$, with $n = 0..N-1$ where N is the number of data samples. To reduce the variance of the spectrum estimates, the final Doppler spectrum was estimated by averaging power spectra from several individual range samples within the sample volume. The PW-Doppler simulation took 61 hours 16 minutes on a 64 bit, 2.80 GHz Intel Xeon processor.

5.2.4 Coupling of CFD and ultrasound simulations

Some aspects related to the coupling of the CFD and ultrasound simulations need to be addressed. First, constructing the point scatterer phantom for a complex shaped geometry like the carotid bifurcation requires accurate knowledge on the geometry boundaries. However, in this work this was circumvented by inserting scatterers in a bounding box enclosing the carotid and further removing the scatterers with zero velocity in the CFD-grid.

Further, to couple the CFD velocity field information to the positions of the point scatterer distribution, three-dimensional (3-D) spatial interpolation of the CFD velocity vectors was executed in Matlab (The Mathworks, Natick, Ma, USA). Since 3-D interpolation in Matlab requires monotonic coordinates delivered in a rigid format, the velocity vectors in the complex tetrahedral CFD grid were first transformed to a regular grid. The CFD velocity vectors known in these regular grid points were subsequently interpolated to the randomly distributed scatterers as is shown in fig. 5.3A.

Also, due to the large disparity in time scales between the CFD and ultrasound simulations, directly coupling the CFD velocities to the ultrasound scatterers is a much too crude approach. As mentioned, the CFD calculations were based on a timestep of 5 ms, while ultrasound

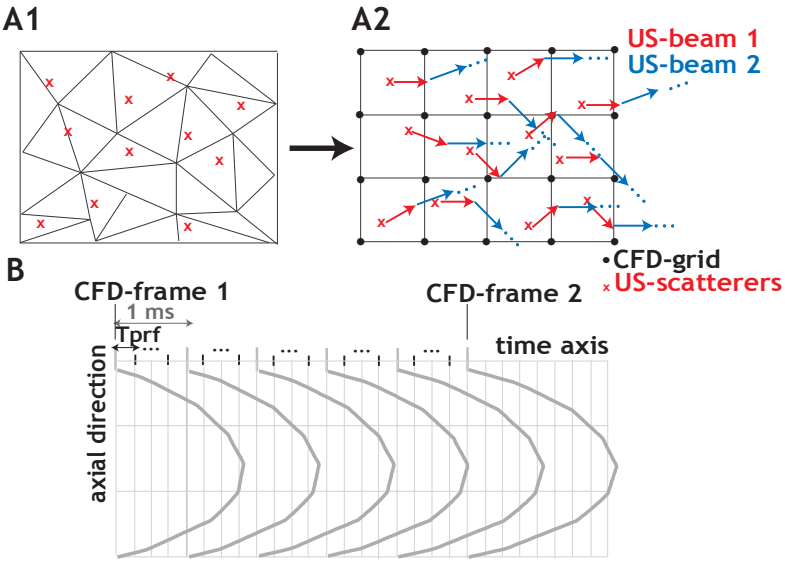

Figure 5.3: Panels A1 and A2 shows a 2D representation of the spatial interpolation used to assign scatterers during the ultrasound simulation. The velocities at the CFD grid points are interpolated to the random positions of the ultrasound scatterers for every ultrasound beam. Panel B further illustrates the temporal interpolation of the CFD flow profiles in the common carotid artery during systolic acceleration. Due to the large timescale disparity between ultrasound and CFD simulations, the CFD velocity profiles should be interpolated to the timesteps of subsequent ultrasound beam emissions in order to provide the correct motion of the scatterers.

uses a much smaller timescale between pulse excitations ($\frac{1}{15kHz}$ = 0.067 ms in our examples). Hence, besides interpolating velocities in 3D-space, temporal interpolation between CFD-frames is also required. This concept is illustrated in fig. 5.3 B. For every pulse repetition period (T_{prf}), the velocities are interpolated linearly between subsequent CFD-frames, and scatterers are propagated to the next position. A complete CFI frame had a duration of 86.4 ms (108 scanlines with a packetsize of 12 and a PRF_{max} of 15 kHz), and therefore 18 CFD-frames were necessary to constitute one color flow image.

An artificial dilution and aggregation of point scatterers may form due to the relatively long scanning time. To avoid such problems, the scatterer phantom should be reset to its original scatterer density sufficiently often, while preserving the beam-to-beam correlation inherent for a given imaging technique. In this work, the scatterer distribution was refreshed between the acquisition of individual interleave regions. A random point distribution was thus created for the first beam of each

interleave group in the color flow image. For subsequent beams, the random scatterers were propagated by calculating the displacement from 3D spatial and temporal interpolation of the CFD velocity vectors. This way the position of the point scatterers was updated every beam.

Rigid walls were assumed in the CFD simulations and no vessel wall or tissue movement was present. However, the no-slip boundary condition at the vessel wall caused however quasi-stationary scatterers to be present which can bias the velocity estimates if not attenuated. During postprocessing, a simple fixed target cancelation was therefore applied by subtracting the mean value of the signal vectors for all simulation cases.

5.3 Results

5.3.1 Straight tube

As described in Section 5.2, stationary parabolic flow was simulated in a straight tube to validate the coupling of the ultrasound and CFD setup. The results are shown in fig. 5.4A, where the velocity profile calculated using the autocorrelation algorithm was averaged over 40 realizations. As can be observed the velocity profile has a parabolic shape close to the CFD simulated profile. At the vessel centre, velocity is underestimated due to the influence of scatterers with low velocity in the vicinity of the high-speed core. At the vessel walls, the opposite occurs and velocity is overestimated. In this region, the clutter filter will also lead to an increased overestimation. The average standard deviation of the estimates is 8.25% and the average bias is 5 % compared to the maximal axial velocity. Further details of the spatial velocity field can be retrieved using contour plots of the ultrasound and CFD velocities as shown in the lower plots in fig. 5.4. In the color flow images, the parabolic velocity field can be observed to be in good agreement with that obtained from the CFD simulations. The variance and bias present for the given simulation setup may explain the rather spotted appearance.

5.3.2 Carotid artery

As for the stationary simulations, contour plots of the estimated ultrasound and CFD velocities are a good way to illustrate the performance of the simulation environment in producing accurate Doppler

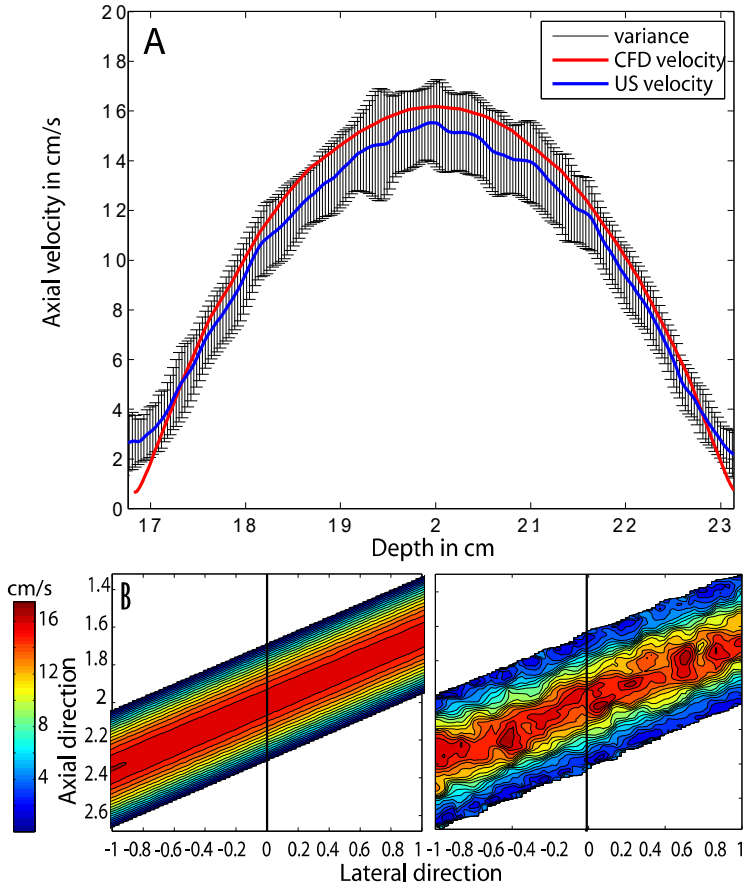

Figure 5.4: *A*: The average (N=40) and standard deviation of the parabolic velocity profile as estimated with the autocorrelation algorithm compared to the reference CFD profile. A packetsize of 15 was used, and 40 realizations were available for averaging. The errorbars indicate ± the standard deviation. *B* & *C*: A contour plot comparison between the CFD and ultrasound velocity field for the parabolic profile. Panel B shows the CFD velocities and panel C the ultrasound velocities. The vertical line indicates the location where panel A was retrieved.

signals. Since the ultrasound color flow mode delivers dynamic images, we also took into consideration the acquisition time of the image for the CFD contour plots. The CFD velocities were interpolated to the exact same locations as in the ultrasound image at the time instances the involved pulses were fired. In this way, a series of 12 (=packetsize) velocity profiles were obtained for each beam direction and subsequently averaged. The resulting contour plots are shown in fig. 5.5 during 3 important phases of the cardiac cycle: systolic acceleration, systolic deceleration and diastole. The estimated velocity fields in the color flow images show good agreement with the CFD results for all 3 frames, with a slight underestimation of the velocities estimated by

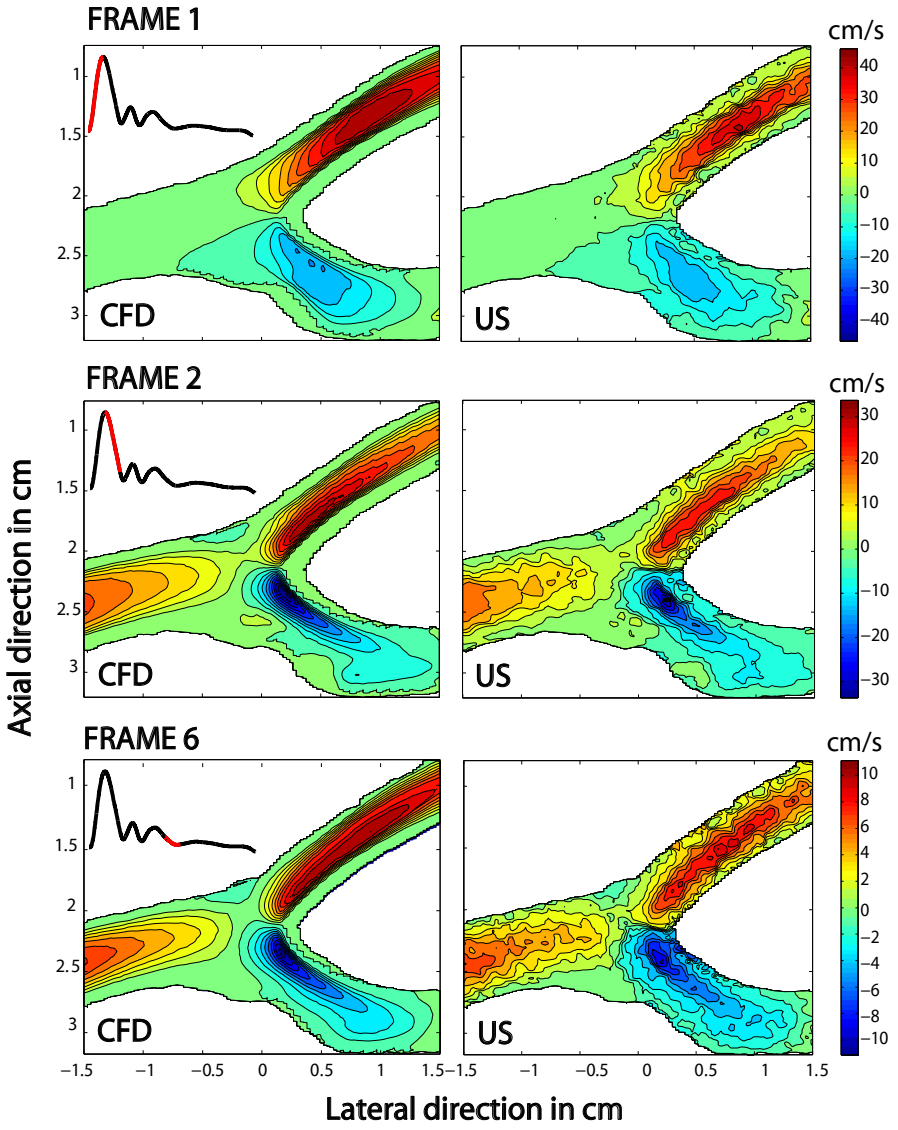

FIGURE 5.5: Contour plots of the axial velocity field from CFD and US simulations at different cardiac phases: systolic acceleration/deceleration and diastole. The complex flow fields from the US simulations show good agreement with the CFD reference.

ultrasound noticeable.

Due to the realistic scan sequencing used in the simulations, timing artifacts can be observed in fig. 5.5 (frame 1), where varying flow velocities during the scanning of one color flow image causes seemingly unnatural flow behavior. This can typically be observed in vivo during dynamic phases of the cardiac cycle. During the systolic acceleration

in fig. 5.5 (frame 1), the velocities are low at the start of the scan for the common carotid, while high at the end of the scan for the external and internal carotid, which in reality is due to a scanning time lag. The part of the cardiac cycle imaged is indicated by the red portion of the velocity inlet curve for each frame.

Due to the Nyquist criterion, the velocity range measurable without aliasing is limited to 29 cm/s . For the ultrasound contour plots presented in fig. 5.5 the aliased velocities were unwrapped to present the comparison as clearly as possible. In the CFD contour plots, a border of zero velocities may be noticed. Due to the effect of beam sidelobes, the transducer also receives signal from outside the carotid geometry. With the appropriate amplitude thresholding, this effect can be minimized. However, since the CFD velocities are plotted at the same locations as the ultrasound estimated ones, a slight overestimation of the carotid geometry is present in the CFD contour plot.

Realistic color flow images are shown for the three phases of the cardiac cycle in fig. 5.6. Velocities in the direction of the transducer are represented in the red spectrum of the color scale, and those in the direction away from the transducer are in the blue spectrum. These images can be compared with corresponding vector plots originating from the CFD calculations below. As was the case for the contour plots, the acquisition time of the ultrasound image is taken into account when representing the CFD vector field. In the first frame the flow field is quite undisturbed, although aliasing artifacts can be observed in the external carotid artery. In the second color flow image frame, a suspicion may arise of more complex flow present in the bifurcation and in the internal carotid artery. This is confirmed by the CFD vector plot showing vortex formations in the concerned regions and has also been demonstrated in vivo [45]. A very small zone of aliasing may also be noticed in the internal branch. During diastole in the third example (frame 6), a large zone of swirling flow is still present in the bifurcation together with a smaller one at the opposite side. This information, although not clearly revealed, may also be interpreted from the axial velocities shown in the color flow image.

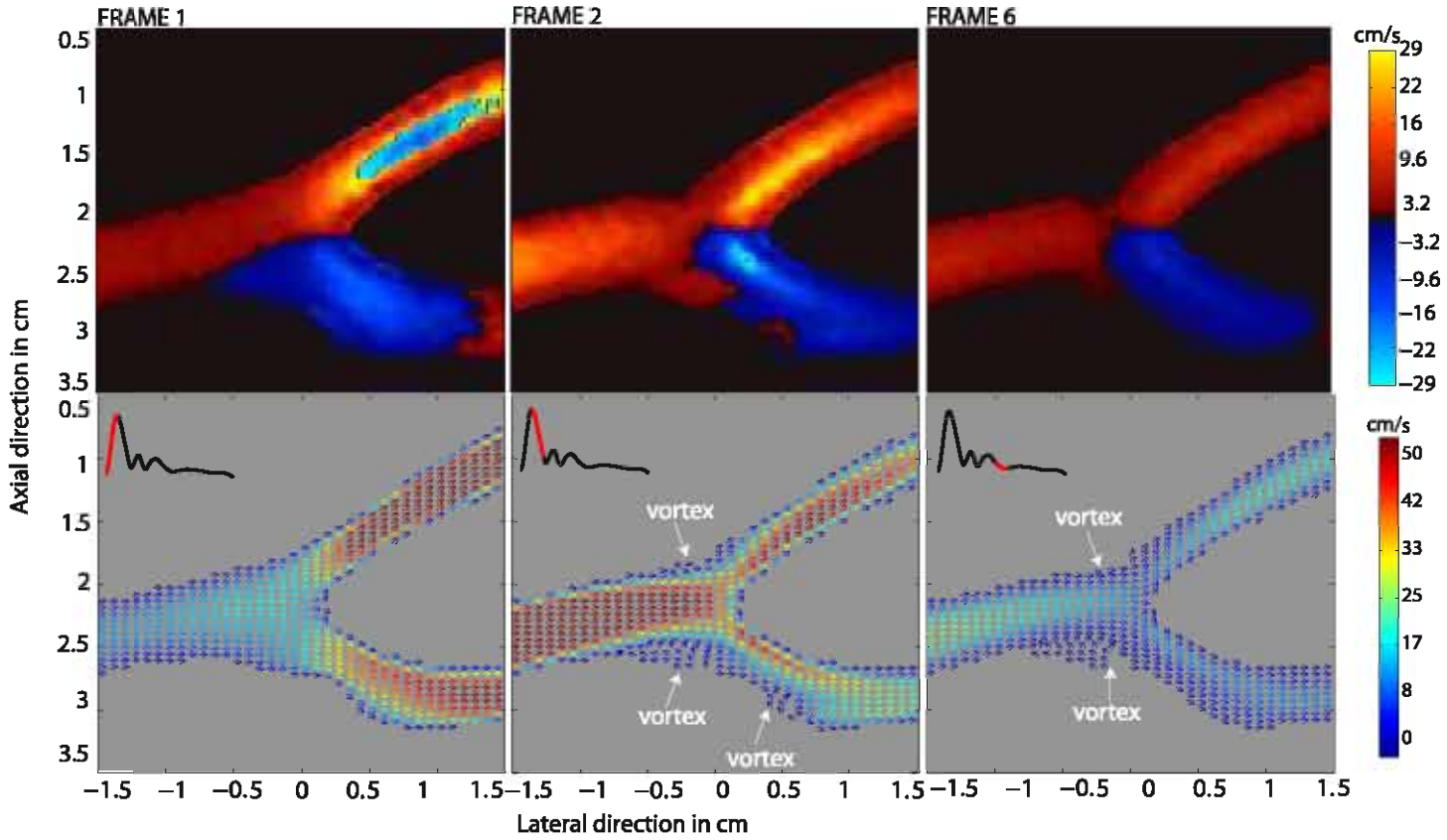

FIGURE 5.6: Comparison between color flow images and dynamic CFD vector plots at different moments of the cardiac cycle: systolic acceleration, systolic deceleration and diastole. The suspected presence of vortices in the color flow images are confirmed by the swirling velocity vectors in the CFD calculations.

The swirling flow present in frame 2 is more clearly illustrated in fig. 5.7. Panel A shows the complex swirling flow field as given in-plane when the ultrasonic scanning sequence is taken into account. In panel B the actual flow field generated from CFD is shown at a time halfway through the scan sequence. Due to scanning time lags this instantaneous velocity field cannot be captured.

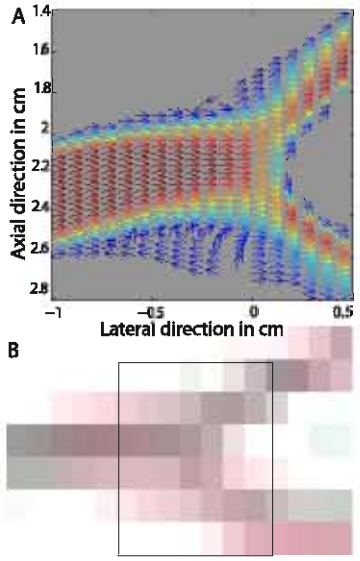

Figure 5.7: Panel A shows the complex swirling flow field as given in-plane when the ultrasonic scanning sequence is taken into account. In panel B the actual flow field generated from CFD is shown at a time halfway through the scan sequence. Due to scanning time lags this instantaneous velocity field cannot be captured.

Besides the spatial comparison of the velocity fields computed with CFD and ultrasound, a detailed parallel in time is also desired. For this purpose, PW-Doppler simulations were performed to increase the temporal resolution at three locations: the common (1), external (2), and internal (3) carotid artery as indicated in fig. 5.1. As can be seen in fig. 5.8, the CFD velocity profile and mean frequency estimates from the Doppler spectra compare to an acceptable range. The velocity trace obtained with the color flow imaging simulation is also indicated by dots in fig. 5.8. As can be observed, the temporal resolution is too poor to show an accurate velocity profile over time, especially in the external branch. The aliased velocities in the color flow images were unwrapped in the external carotid artery for the first frame.

5.4 Discussion

In this work a new ultrasound flow simulation environment based on CFD generated velocity fields has been presented. This tool makes it possible to simulate ultrasound signals resulting from realistic flow fields, which can enhance the development and validation of new flow

related ultrasound algorithms. The aim of this study has been to describe and validate the simulation environment, and further to show how it can be used to generate color flow images and PW-Doppler spectra of complex flow patterns in a stenosed carotid bifurcation.

The coupling of ultrasound and CFD simulations was verified for stationary parabolic flow in a straight tube. In fig. 5.4, a small bias could be observed in the autocorrelation estimates compared to the CFD reference. This can be explained by the inherent spatial smoothing of the ultrasound point spread function, but is also explained by the mean subtraction clutter filter for lower velocities. The variance observed can for our setup mostly be attributed to the short observation time of the scatterers as they move laterally through the ultrasound beam. As we used relatively low F-numbers, this variance can be expected to be relatively significant.

Following, flow in the carotid artery bifurcation was investigated. Except for some small deviations near the vessel walls and at locations where aliasing occurred, ultrasound and CFD velocities showed a good qualitative agreement as clear from the contour plots in fig. 5.5. Although the most interesting use of the simulation environment perhaps is to validate new algorithms, it can also be beneficial for investigating how conventional color flow images portray complex flow patterns. Comparing the corresponding vector plots generated from the CFD velocity field to the color images in fig. 5.6, one can observe that vortex formation in the bifurcation and the internal carotid is not readily available from only axial velocity information. This indicates the need for more refined techniques that are also able to resolve the lateral velocity component. Fig. 5.7 illustrates the complex flow field as given in the imaging plane when the ultrasonic scanning sequence is taken into account (for frame 2) and this compared to the realistic flow conditions present in the carotid artery. In case of dynamic flow conditions, as present in the carotid artery during systole, CFI images give a time-smoothed impression of the flow field as was also clearly apparent in the contourplot of frame 1 in fig. 5.5. The CFD pathline plot displays how massless particles follow the vector field simulated at a time instance halfway the imaging sequence of frame 2. When analyzing CFI-images, it is important to bear in mind this dynamic character of the images as opposed to the realistic flow field present at a certain point in time.

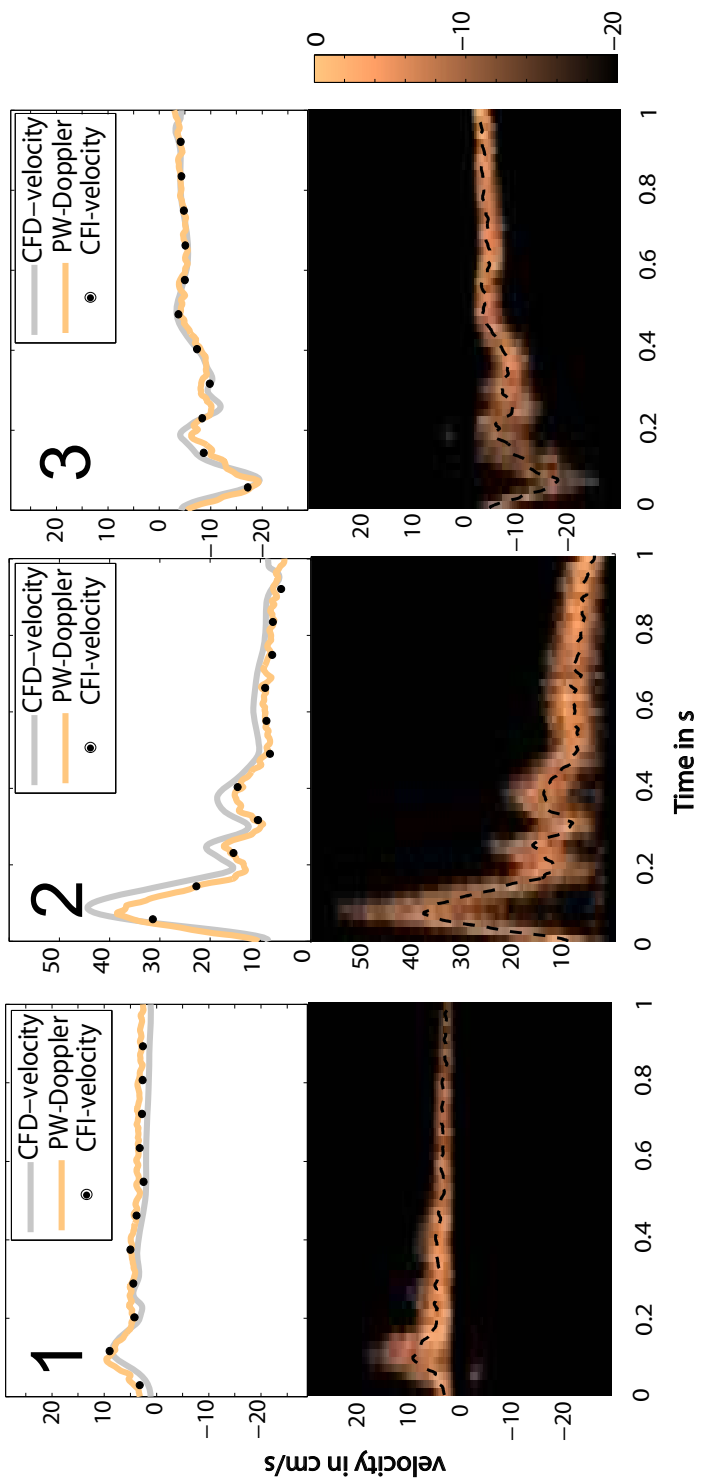

Figure 5.8: PW-Doppler simulations for sample volumes of 1.5 mm located in 1) The common carotid, 2) the external carotid, and 3) the internal carotid. The upper panels show the estimated mean axial velocity vs. time, for the color flow and PW-Doppler simulations compared to the CFD reference. The lower panels show the Doppler spectrum sonograms with a dynamic range of 20 dB. The mean velocity of the spectra has been indicated with a dashed black line.

However, this aspect will improve when using parallel receive beams or synthetic aperture imaging [101].

A comparison of the flow velocities over time was possible with PW-Doppler simulations. A good agreement was found between the CFD and PW-Doppler mean velocity estimates as shown in fig. 5.8. As can also be seen from fig. 5.8, the CFI setup resulted in only 11 frames per cardiac cycle, and therefore could not accurately track the rapid changes in flow velocity, especially in the external branch. However, in modern high-end systems, parallel receive beamforming is available to at least double the frame rate of a conventional imaging setup.

Although results have demonstrated the capabilities of the simulation environment, there are limitations to the setup that need to be addressed. For the CFD part, the behaviour of blood was approximated as an incompressible Newtonian fluid. For investigating wall shear stress distributions, using a non-Newtonian fluid model would be more accurate, but will increase simulation times. Further, certain limitations arise due to the fact that CFD treats blood as a continuum, which cannot adequately incorporate the realistic mesoscale behaviour of blood [102]. The deformation of red blood cells is not included, and electrochemical interactions between red blood cells are ignored. Interaction with leukocytes or vessel walls is also neglected [103]. The CFD setup further assumes that red blood cells follow the flow field passively, and no realistic aggregation model is incorporated. It is also assumed that red blood cells are equally distributed in the vessel which can trouble modelling complex phenomena like the Fahraes-Lindqvuist effect, where red blood cells migrate to the vessel centre and a plasma layer is formed near the wall. Although most of these phenomena appear at microvascular level, they should still be borne in mind when modeling relevant applications.

Concerning ultrasound simulations, the Field II method has some limitations. First of all, non-linear propagation of ultrasound waves and multiple scattering is not included. Non-linear harmonic distortions due to wave propagation are typically suppressed by the receive filter in conventional flow imaging. However, to obtain realistic clutter signals in the vessel lumen, simulating multiple scattering from surrounding tissue structures would indeed be interesting. Field II puts restrictions on the nature of the scatterers since the disc shaped red blood cells are

represented by random point scatterers. Frequency dependent scattering was not included in our work but can be incorporated in the pulses set in the Field II simulation environment.

By only including signal contributions from scatterers in the vicinity of the beam main lobe, potential signal from beam side lobes and grating lobes is neglected. Further, no vessel walls or surrounding tissue were included in our examples, which of course is a crude approximation. Stationary scatterers are often 40 dB stronger than blood scatterers. Hence, Doppler techniques incorporate stationary echo canceling filters to minimize their contribution but which may also degrade the performance of the blood velocity estimator. However, the current model can still be very useful for studying fundamental flow related limitations of imaging algorithms. Assuming no clutter leakage, the influence of clutter filters can also be studied. In previous work [104], analytically described tissue and vessel wall motion has been incorporated into Field II simulations. However, to be able to realistically model the complex mechanical properties of the layered hyperelastic vascular wall, and to incorporate the mutual influence between the flow field and the vessel wall, simulation of fluid-structure interactions (FSI) needs to be performed. The current model presented is considered an important step towards more complete ultrasound simulations including both realistic flow fields and surrounding vessel wall and tissue movement.

Compared to the ultrasound simulations, CFD is by far the most computationally intensive. However, generating a CFD phantom will typically be done once, and can subsequently be incorporated in many different imaging setups. The ultrasound simulation times can be further shortened for instance by including scatterers in a smaller vicinity of the beam main lobe. Still, by using computer clusters and distributing one CFI frame simulation per computer node, a complete cardiac cycle using the current setup can be generated in less then 10 hours. This is expected to further decrease due to the continuing increase in computational power of desktop CPUs.

The proposed simulation environment offers flexible control of flow and ultrasound imaging parameters, and can hence be interesting for numerous applications. Estimation of velocity vectors using crossed-beam Doppler or speckle tracking techniques could be evaluated in

a controlled manner for realistic flow patterns. The accuracy of ultrasound wall shear stress estimation could be assessed, which might be of great importance when assessing plaque rupture risk in carotid arteries. Also, research on methods for future 3-D vascular imaging could be investigated.

5.5 Conclusion

Ultrasound signals from realistic blood flow can be acquired based on velocity fields generated from computational fluid dynamics. Axial velocities estimated from stationary parabolic flow as well as from a stenosed carotid bifurcation were in good agreement with the CFD reference. In the carotid bifurcation, simulated color flow images did not readily portray vortex formation, indicating the need for imaging methods that also resolve the lateral velocity component. Therefore, we believe the simulation environment will be beneficial for investigating the performance of current as well as future algorithms for flow imaging using ultrasound.

CHAPTER 6

Assessing simulation strategies for color flow imaging: coupling CFD and ultrasound simulations based on an in-vitro carotid artery model

In the previous chapter, we demonstrated that computational fluid dynamics (CFD) can play an important role in assessing the performance of ultrasonic flow imaging methods. We simulated established ultrasonic flow estimators, like color flow imaging and pulsed wave Doppler, by coupling velocity fields from CFD-simulations with the Field II ultrasound simulation software. However, ultrasound images of blood flow can also be mimicked by directly processing CFD simulations, without using an ultrasound simulation model. In this chapter, we study both approaches in the clinically relevant setting of a carotid artery using color flow images (CFI). We investigate a first order approach, which consists of producing ultrasound images by color-coding CFD velocity fields. Further, we compare results of the first order approach with our previously discussed second order approach, which simulates CFI by integrating CFD with the Field II ultrasound simulation model.

We assess the realism of the different simulation approaches by measuring color flow images in an experimental setup of the same carotid geometry. Results show that during dynamic stages of the cardiac cycle, realistic ultrasound data can only be achieved when incorporating both the dynamic image formation and the measurement statistics into the simulations.

This chapter is based on the paper "*Assessment of Numerical Simulation Strategies for Ultrasonic Color Blood Flow Imaging, Based on a Computer and Experimental Model of the Carotid Artery*", published in Annals of Biomedical Engineering, vol. 37, p. 2188-2199, 2009.

6.1 INTRODUCTION

Ultrasonic imaging is widely applied for visualization of blood flow in the heart and superficial vessels such as the carotid and femoral arteries, often making use of color flow imaging (CFI). This is a Doppler based velocity estimation technique which estimates the phase-shift between the ultrasonic waves backscattered by the moving red blood cells (but it does not estimate the phase shift between the emitted and backscattered signal as a pure Doppler technique). The resulting velocities are color-coded to enhance visual interpretation. Such Doppler techniques are however hampered by several limitations and the link between the data in an ultrasound image and the real flow characteristics is not always straightforward.

Firstly, fundamental 1D Doppler limitations arise since flow velocities are only measured parallel to the ultrasound beam, and the maximum measurable velocity is limited by the Nyquist limit leading to aliasing artifacts in the image [105]. Secondly, the applied velocity measurement method also entails inherent statistical limitations. The received signal has a stochastic nature since it is generated by independent random blood particles, creating a speckle pattern due to their dense distribution compared to the wavelength used in diagnostic ultrasound. Furthermore, statistical properties arise from the measurement method itself. The Doppler phase-shift is estimated based on a packet of received ultrasound signals, and is as such encumbered with a variance due to the limited observation time and the ultrasound beam width. Finally, the ultrasound imaging process also exhibits limitations due to

the ultrasound beam forming physics and signal processing. In effect, color flow imaging does not result in an instantaneous snapshot of the flow field but in a dynamic image where different regions of the field of view are acquired at different times. The reason for this is twofold: (1) the region of interest typically acquired in CFI-mode is large and (2) the observation time should be sufficiently long to reduce the variance on the velocity estimates. Hence, high spatial resolution is obtained at the cost of low temporal resolution. This can however be partially compensated by receiving several beams in parallel (multiple line acquisition [106]).

Since these limitations hamper the use of ultrasound measurements for more quantitative analysis and assessment of relevant hemodynamic parameters (such as flow-derived pressure gradients, velocity profiles or wall shear rate), we want to better understand the relationship between the ultrasound image and the actual flow dynamics. Therefore, computational fluid dynamics (CFD) may play an important role. CFD solves the non-linear equations for conservation of mass and momentum in a discretized form and allows simulating complex flow fields in realistic, patient specific geometries. Ultrasound images derived from such CFD-solutions would offer great possibilities to validate and develop ultrasound flow imaging modalities. Until now, ultrasound flow imaging is most often investigated with experimental flow phantoms and a nice overview is given by Hoskins [107]. However, the actual flow field in these experimental phantoms should also be validated by other reliable imaging techniques. In this respect, ultrasound images based on computed flow fields are more interesting since they directly offer knowledge and insight on the imaged flow field. Jensen et al. introduced synthetic computer phantoms with moving ultrasound scatterers for generating ultrasound B-mode and color flow images with Field II [56]. Kerr et al. described a computer method for simulating Doppler color flow also by representing blood and tissue as 3-D point scatterers [59]. However, these computer phantoms were based on analytical flow behavior while there is a need for computer models accounting for complex 3D flow fields in anatomically and physiologically realistic flow conditions. Balocco et al. proposed a 3-D-model of a pulsating vessel where both 3-D flow and wall displacements simulations were coupled with the Field II software [62]. Khoshniat et al. presented a real-time numerical simulation technique of Doppler ultrasound spectograms for complex flow. CFD velocity fields were coupled to a simplified empirical model of Doppler ultrasound physics,

which accounted for the effects of sample volume, finite temporal sampling window and intrinsic spectral broadening [61].

One approach to link the CFD data to the ultrasound image is to directly process the CFD simulations and mimic ultrasound CFI by color coding the component of the CFD velocity vectors in the ultrasound beam direction [108]. In particular for color flow imaging and interpretation of colour M-mode images, Vierendeels et al and Nakamura et al [108, 109] directly applied this first order approach and processed CFD simulations by color-coding the component of the CFD-velocity vectors in the ultrasound beam direction. This first order approach, however, does not account for the dynamics and statistics of the ultrasound imaging process. This is why we recently introduced a novel approach [110], linking CFD results to software which can model realistic ultrasound probes and image scan sequencing. This second order approach allows retrieving radiofrequent (RF) signals from complex flow fields, with flexible control of both the flow and imaging parameters while in previous work simplified assumptions on the flow (analytical flow behavior) and/or imaging process (simplified ultrasound physics) were present. In [110], we focused on the CFD-ultrasound coupling procedure and elaborated on the ultrasound simulation setup and signal processing. We applied this second order approach to the carotid artery, a location prone to atherosclerosis, easily accessible with ultrasound and hence of great clinical interest. We demonstrated that realistic-looking ultrasound images of pulsed wave Doppler and color flow images are obtained.

Although our previously described method [110] allows retrieving Doppler signals from realistic and complex flow fields, simpler methods exist to mimic CFI. We did not yet assess in detail to what extent the more complex procedure of fully coupling CFD and ultrasound differs from the previously described first order approach of simply color coding the instantaneous CFD velocity vectors. Further, the images generated by this CFD-based ultrasound simulation environment have not yet been compared to measured ultrasound images. The aim of this study is therefore 1) to compare color flow images in the carotid artery obtained with the first order and second order approach, and 2) to further support our results with experimentally measured ultrasound images.

6.2 Methods

The general outline of the study is illustrated by the flowchart in fig. 6.1. We first recorded experimental ultrasound images in an in-vitro silicone model of the carotid artery subjected to pulsatile flow conditions. These measurements provided the necessary input for CFD simulations. The silicone model was scanned using CT to create the geometry and the mesh for CFD-simulations. The CFD velocity fields were then subsequently used to produce ultrasound images. Two main approaches were tested (i) a first order approach where the CFD velocity vectors are directly projected on the ultrasound beam direction, and (ii) a second order approach previously described in detail by Swillens et al [110] which uses CFD velocity fields as an input to an ultrasound simulation model (Field II). The simulated CFI images and information obtained via these two approaches will be compared to the experimental measurements.

Figure 6.1: This flowchart illustrates the general outline of the study. CFI-images were recorded on an in-vitro carotid model. Next, CFD-simulations were performed, simulating the experiment. These CFD-data could be directly processed to mimic CFI or were further coupled to an ultrasound simulation model.

6.2.1 In-vitro carotid flow model

A 3D geometry was reconstructed from CT-scans of the carotid artery of a healthy volunteer (Mimics; Materialise, Leuven, Belgium), and a mould of the carotid lumen was created through rapid prototyping. From this mould, a silicone model of the carotid artery was constructed and inserted in a mock loop. The position of the external and internal carotid artery (cfr. fig 6.2) was switched compared to the anatomical situation to obtain optimal image quality. The carotid

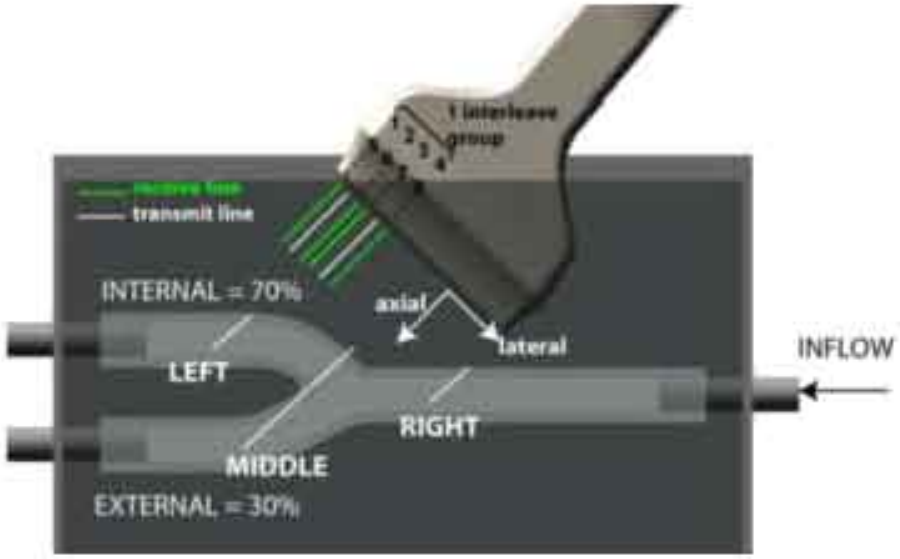

FIGURE 6.2: The probe position is shown together with the applied scan sequencing and multiple line acquisition. The axial (parallel with US-beam) and lateral (perpendicular to US-beam) directions are indicated. The positions where the 1st order color-coded CFD data and 2nd order simulations are evaluated (cfr. fig.6.4) are presented with 'left', 'middle' and 'right'.

artery was contained in a water reservoir which fits the in- and outlets of the silicone carotid model and connects them to the ducts in the loop. In this way, the carotid model could be submerged into water, serving as an echo-translucent medium for the ultrasound probe, while flow was generated within the carotid lumen by pumping an echogenic blood mimicking fluid [111] through the mock loop. The other components in the loop, i.e. a windkessel model, backpressure reservoirs, a bypass duct and clamp resistances made it possible to tune the pulse output of the pulsatile pump to generate realistic dynamic carotid flow pulses. Ultrasound data were recorded with a Vivid 7 ultrasound system (GE Vingmed Ultrasound, Horten, Norway) using a 12L linear array transducer for vascular imaging procedures with a centrefrequency of 5.7 MHz (GE Medical Systems, Milwaukee, WI), positioned under an angle of approximately 40 degrees to the axis of the common carotid artery to optimize the ultrasound images (see fig. 6.2). Raw RF data were stored which allowed post-processing the recorded ultrasound data in the exact same way as the simulated RF data (see further). An artificial triggering signal was generated by the piston pump (Harvard apparatus) and was sent to the ECG input channel on the scanner to provide a reference in time. The data used in this paper were recorded at a pump rate of 60 beats/minute, and peak flow

velocity in the common carotid artery (measured using pulsed Doppler with angle correction) was 0.8 m/s. The flow division, measured gravitationally, was 30% to the external and 70% to the internal carotid artery.

6.2.2 CFD-simulations

The silicone model, connected to the water reservoir and loaded to the same constant mean pressure as in the experiment, was scanned in a clinical CT scanner to ensure that the geometry used for the CFD simulations matches as closely as possible the experimentally tested geometry. From these CT-scans, the geometry was 3-dimensionally reconstructed and meshed with dedicated software (Mimics; Materialise, Leuven, Belgium) resulting in a high-quality triangular mesh after optimizing the mesh quality based on skewness and smallest/largest edge length. This surface mesh was further processed by Gambit (Ansys, Canonsburg, Pennsylvania) to create a volume mesh of 477570 tetrahedrons. The commercial CFD software Fluent 6.2 (Ansys, Canonsburg, Pennsylvania) was used to numerically solve the Navier-Stokes equations with a finite volume method. The CFD boundary conditions were measured during the experimental protocol. At the level of the common carotid artery, we imposed the measured time-varying parabolic inlet velocity profile with the pulsed wave Doppler trace as maximal velocity. The flow division between external and internal carotid artery (30%-70%) was imposed as a traction-free outflow boundary condition, and was assumed constant throughout the cardiac cycle [112]. Although the flow towards the external carotid is relatively low, this flow distribution is still within the physiological range [93], and provided experimental ultrasound images with minimal artifact near the bifurcation region. Blood was modeled as an incompressible fluid with density 1050 kg/m^3 and viscosity 3.5 mPas. The maximal Reynolds number in the common carotid artery was 1185 and the Womersley number 3.76. The cardiac cycle (length 1 s) was divided into time steps of 5 ms, and 3 cycles were computed to obtain results fully independent of any transient effects. Residuals dropped at least 4 orders of magnitude and suffice iterations were set to obtain steady residuals at the end of each timestep. The calculation took 61.8h on an 8GB quad core machine (Intel(R) Core(TM) 2 Quad CPU Q6600 2.4 GHz).

6.2.3 Ultrasound imaging and simulations

The Field II software created by Jensen et al [17, 18] was employed to simulate the RF-signals resulting from the carotid blood flow. This

simulation software allows modeling arbitrary ultrasound transducers and realistic image scan sequencing. For further details on the software background, we refer to [17, 18]. Field II models tissue (in our case blood) as a collection of random point scatterers. The required scatterer density is related to the imaging system resolution, with 10 scatterers per resolution cell assuring Gaussian distributed RF-signals [58]. This avoids the extreme computational effort of representing each individual red blood cell by a single point scatterer. Dynamic objects are achieved by moving these point scatterers during simulation. Each ultrasound beam is simulated individually, and it is therefore possible to update the position of moving scatterers between beam acquisitions.

The ultrasound simulation setup was matched to the experiments. The 12L linear array probe used in the measurements was implemented, with a center frequency of 5.7MHz and a focal depth position of 3.25 cm. A 4.5 period sinusoidal excitation pulse (0.7875 μs) was applied and each transducer element was divided into four smaller rectangular mathematical elements so that the backscattered signal from each point scatterer was simulated with sufficient accuracy. A dynamic focus and expanding aperture was used on receive to retain constant imaging properties throughout depth. To reduce beam sidelobes, apodization was applied (amplitude weighting of the receiving transducer elements).

The color flow imaging application measured the velocities in the axial direction (direction in which the ultrasound pulse is emitted, cfr. fig. 6.2) using the autocorrelation algorithm described for ultrasound applications by Kasai et al. [36]. An ensemble of pulses was fired along the arterial cross-section and the phase-shift (proportional to the mean axial velocity) between the backscattered ultrasonic waves was estimated. Before processing the RF-data, a clutter filter (fixed target cancellation, [113]) was applied to remove the influence of quasi-stationary scatterers near the vessel wall, as is also the case on clinical scanners. Next, the axial velocity v_z was calculated by estimating the mean frequency of the Doppler power spectrum. This spectrum arises since a dense distribution of red blood cells is insonated. The autocorrelation method estimates the mean Doppler frequency as:

$$\frac{2\hat{v}_z f_0}{c} = \frac{PRF}{2\pi} \arctan\left(\frac{Im\left\{\widehat{R}(1)\right\}}{Re\left\{\widehat{R}(1)\right\}}\right), \tag{6.1}$$

with PRF the pulse repetition frequency of the emitted ultrasound beams, f_0 the center frequency of the ultrasound pulse and $\widehat{R}(1)$ the estimated autocorrelation function at lag 1. The autocorrelation function can be approximated with N-1 pairs of complex samples Z.

$$\widehat{R}(1) = \frac{1}{N-1} \sum_{i=1}^{N-1} Z(i-1)Z^*(i), \tag{6.2}$$

This induces broadening of the Doppler spectrum due to a finite observation time. The autocorrelation estimates were spatially averaged over 3 beams (lateral direction=X, cfr. fig. 6.2) and 2 pulselengths (axial direction=Z, cfr. fig. 6.2). The origin of this coordinate system is the centre position of the transducer surface.

For peripheral vascular applications (as in this case), CFI most often incorporates a scanning procedure called beam interleaved acquisition. Beam interleaving ensures that the waiting time between beam acquisitions is minimized, thus maximizing the imaging frame rate when the Doppler PRF is chosen lower than the maximally possible PRF (PRF_{max}), which is restricted by the image depth. We refer to [100] for further details. The interleaving and packet-size in our simulations were chosen to match with the frame rate obtained in the experiments. The PRF_{max} was set to 10 kHz and the PRF to 5 kHz, resulting in an interleave-group of 2 beams. To further increase the frame rate, 2 beams were received in parallel with a technique called multiple line acquisition (MLA) [106], a technique commonly used in high-end systems, which doubled the interleave-group-size. The applied scan sequencing is shown in fig. 6.2. The resulting frame rate was about 15 frames per second (fps).

6.2.4 From CFD to simulation of ultrasound images

6.2.4.a First order static approach: Instantaneously color-coded CFD

The CFD-simulations based on the in-vitro setup were directly processed by color-coding the component of the CFD-velocity vectors in the beam direction. Hence no scanning procedure or velocity estimator statistics are included. To compare this approach with the second order approach of full coupling of CFD and ultrasound simulations, we first color-coded the CFD-frames which were at a time point halfway the CFI-scanning procedure. Since this procedure is based on static CFD information, these data are labeled *'1st order static'* in the results section.

6.2.4.b *First order dynamic approach: Dynamically color-coded CFD*

As the previous approach ignores the fact that it takes some time to build an ultrasound image from the left to the right (67 milliseconds at a frame rate of 15 fps), we also followed another approach, which somewhat holds the middle between instantaneously color-coding CFD and the fully coupled US-CFD approach described below. In this case, we still color-code the CFD component in the direction of the ultrasound beam, but the image is built up from left to right using CFD information corresponding to the moment that a particular scan line is sampled. Hence, about 14 CFD-frames are necessary to compose an image. These results will be labeled as *1st order dynamic.*

6.2.4.c *Second order approach: fully coupled US-CFD*

Field II allows updating the position of the point scatterers for every ultrasound beam. Since CFD provides detailed information on the flow field, this information can be used to propagate the scatterers, ensuring realistic scatterer movement. Integrating CFD and ultrasound simulations entails however a few challenges. Three-dimensional spatial interpolation is necessary to extract the CFD info from the irregularly spaced grid to the random point scatterers. Temporal interpolation is performed to account for the discrepancy between the ultrasound and CFD timescale (100 μs versus 5ms). For further details on coupling CFD and ultrasound simulations, we refer to [110]. For this second order approach, two strategies will be followed in fully coupling US and CFD: 1. one CFD-frame halfway the scan sequence will be used as input to Field II, further named *2nd order static*, 2. several CFD-frames will be used as input to Field II, accounting for the dynamic image formation, further named *2nd order dynamic.*

6.2.5 Comparing measurements and simulations

The CFI-simulation approaches described above and the experimentally measured color flow images were compared to each other, which was possible since all 4 methods were based on the same flow situation. One important issue is however the timing at which simulated and measured images are compared. With a frame rate of 15 fps, one frame spans 67 milliseconds, which is significant in highly dynamic and pulsatile flow conditions. The simulation timescale started at the onset of the cardiac cycle, which was derived from the measured pulsed wave Doppler trace in the common carotid. The timing of the experimental CFI-images was arbitrary but the phase in the cardiac cycle could

be determined by combining information from the ECG-triggering on the CFI and pulsed-wave Doppler application. This way the autocorrelation estimates of the velocities were interpolated from the simulation timescale to the experimental timescale.

Comparison of the numerical and experimental study was further improved since the experimentally recorded RF-data were processed in the exact same way as previously described for the simulations: 1. a fixed target cancellation filter was applied, 2. the power of the demodulated RF-data was threshold so that only blood flow data were visualized, 3. velocities were estimated with the same autocorrelation algorithm and spatially smoothed in the same way.

6.3 Results

The contourplots in fig. 6.3 are a good way to compare the first order approach (static and dynamic) with the second order dynamic approach. The axial velocities (in the beam direction) are shown for 3 cardiac phases as indicated by the red part on the inlet flow condition. The *'1st order static'* column displays instantaneous CFD-data color-coded in the ultrasound beam direction. The *'1st order dynamic'* data show the axial CFD velocities at the timings the ultrasound pulses are fired, which are interpolated to the exact same locations as in the ultrasound image. The *'2nd order dynamic'* contourplots show the fully coupled US-dynamic CFD simulations, which show far more irregular contrours due to the inherent statistical properties of the velocity estimator. Especially in frame 1 and 2, the 1st order static approach appears insufficient to capture the real flow dynamics. During the acceleration phase, the flow velocity in the internal carotid artery (utmost left in the image) is overestimated while in the common carotid artery (utmost right in the image) an underestimation is apparent. This can be attributed to the steep flow increase present in those frames. Scan positions near the extremes of the image will show the most severe deviations because the instantaneous CFD-frame was chosen halfway the scanning procedure. For frame 7, little difference is noticeable between the 1st order static and dynamic plots because little flow variation is present. For all frames, color-coding CFD-solutions obviously lacks the statistical properties of the ultrasound velocity estimator. One should notice that in the color-coded CFD contour plots, a border of zero velocities is present. Due to the effect of beam side lobes, the transducer

FIGURE 6.3: Contourplots are presented during three frames of the cardiac cycle. The first column corresponds with 1st order static, the second column are 1st order dynamic data and the third column shows the 2nd order dynamic approach.

also receives signal from outside the carotid geometry. With the appropriate amplitude thresholding, this effect can be minimized. However, because the CFD velocities are plotted at the same locations as the ultrasound estimated ones, a slight overestimation of the carotid geometry is present in the 2nd order dynamic contour plots, as is also the case with in vivo imaging.

A more quantitative comparison between the first and second order approach is made in fig. 6.4. The three strategies are compared at 3 locations of the ultrasound scan as indicated in fig. 6.2 and fig. 6.3 (X=-1.4cm, X=-0.16cm, X=1.4cm). Frame 1 and 2 demonstrate the effect of the accelerating flow with the 1st order static curve overestimating at the left of the image and underestimating at the right of the image. Frame 7 has slightly decelerating flow and the opposite effect can be noticed. In the middle of the scan, the 1st order static and dynamic

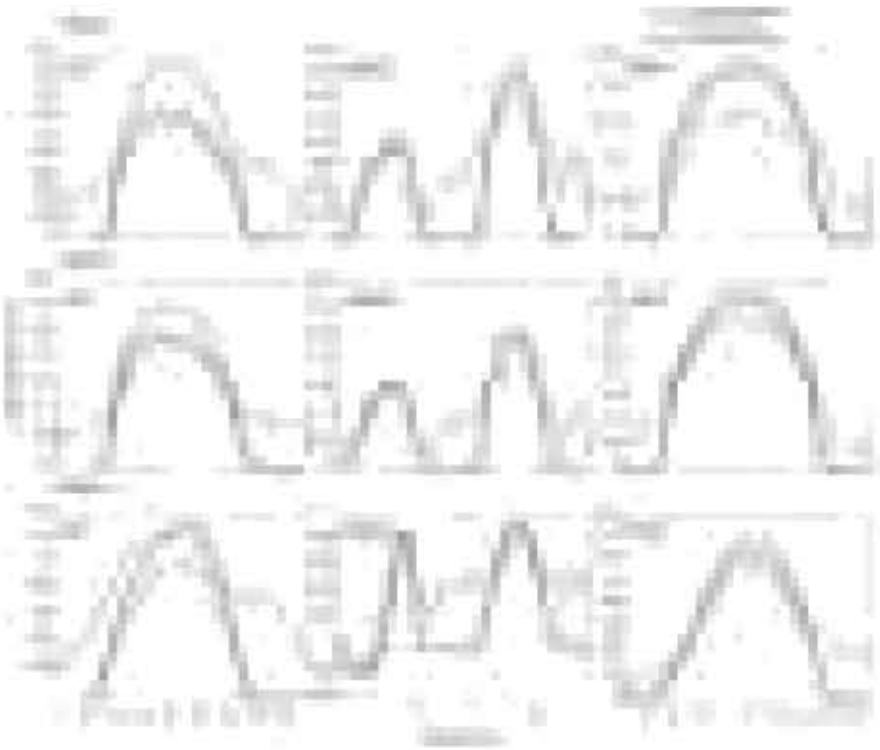

FIGURE 6.4: For three frames of the cardiac cycle, a quantitative comparison is shown between the different simulation methods. The dashed and full black curves represent the 1st order static and dynamic approach respectively. The gray curve shows the 2nd order dynamic approach. The left, middle and right position are indicated in Figs. 2 and 3. For the sake of clarity, the absolute value of the axial velocity (parallel with ultrasound beam) is shown, explaining the positive values (and the difference with fig. 6.3).

curves almost coincide. The curves obtained from 2nd order dynamic simulations show a more irregular character due to the statistics behind the velocity estimation. Ultrasound also has quite some trouble to capture correct velocities near the vessel wall, even after use of a clutter filter.

The more conventional way of portraying color flow imaging is shown in fig. 6.5, for the same cardiac phases as in fig. 6.3. The first column *'2nd order static'* demonstrates the result of Field II simulations based on just one CFD-frame corresponding to a time point halfway the scanning sequence. Compared to the 1st order static contourplots of fig. 6.3, these color flow images take into account the statistical prop-

erties of ultrasound imaging but neglect the dynamics of the scan procedure. In contrast, the *'2nd order dynamic'* plots incorporate the dynamical flow field during scanning and originate from our previously discussed simulation environment [17]. Note that in this case the velocity information is the same as in the right column of fig. 6.3, but using the CFI color scale and containing effects of aliasing (it would of course also be possible to generate CFI images from the 1st order static and dynamic data displayed in fig. 6.3 by simply applying the CFI color scale, but this would provide no additional information).

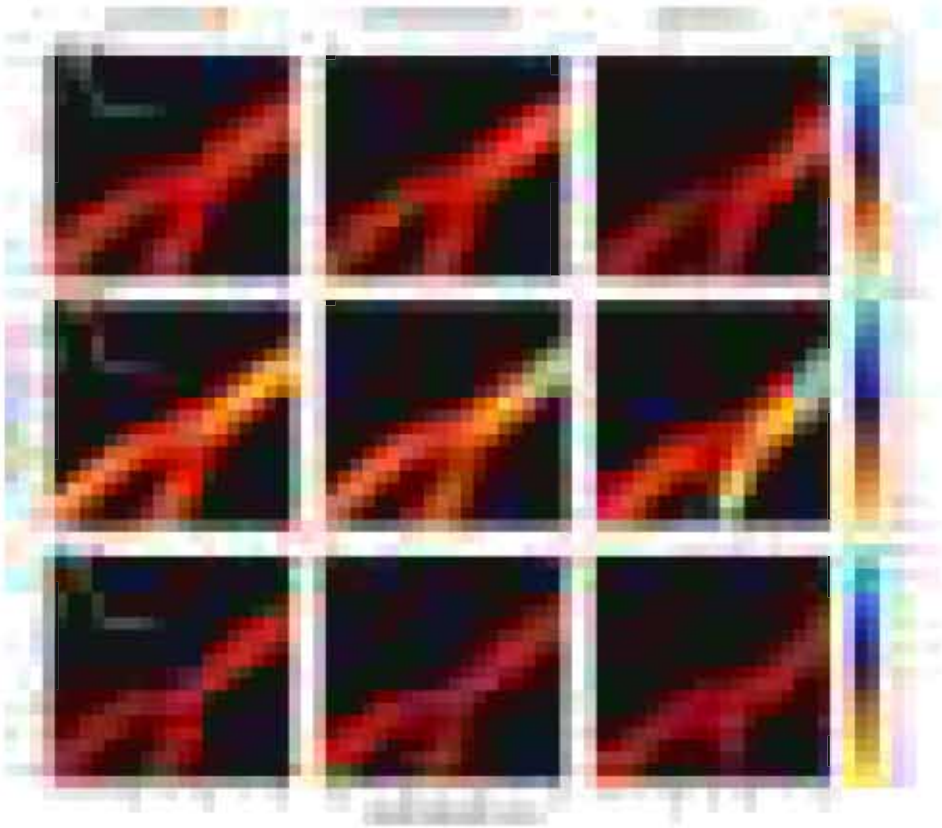

FIGURE 6.5: Conventional color flow images are shown for 3 frames of the cardiac cycle. The first column displays the 2nd order static, using just 1 CFD-frame. The second column shows the 2nd order dynamic, using 14 CFD-frames to account for the scanning time. The third column shows the corresponding experimentally measured CFI-data.

Both second order approaches can then be compared to the experimentally measured CFI images. The same flow characteristics can be observed in the experimental CFI as in the simulated images for all frames. Similar velocity magnitudes, locations of aliasing and vortices are present. The difference between the 2nd order static and dynamic

FIGURE 6.6: For frame 1, the colormaps of the differences between 2nd order simulations (static and dynamic) and the experiment are shown, as well as the difference between the 2nd order static and the 2nd order dynamic approach.

data is less noticeable due to the non-linear color scale. However, in frame 2 the difference is most obvious since the velocities in the common carotid are close to the Nyquist limit. fig. 6.6 shows the distribution of the differences in velocity estimation for frame 1 between respectively, (1) 2nd order static and the experiment, (2) 2nd order dynamic and the experiment, (3) 2nd order static and dynamic. By mapping differences between 2nd order static and the experiment, a color-gradient appears, most visible along the common carotid - internal carotid pathway (note that the yellow color in the external carotid is generated by the artifacts in the measurements). This gradient is greatly reduced in the color map showing the differences between 2nd order dynamic and the experiment. This gradient is due to the timing artifacts related to using instantaneous CFD-data, which is clearly demonstrated when coloring the difference between the two second order approaches.

Finally, fig. 6.7 compares the 2nd order simulations to the experimentally measured velocity profiles in the common carotid artery (at the lateral position X=1.5 cm). A location in the common carotid artery was chosen since velocity estimates closer to the bifurcation are more corrupted by the strongly attenuating silicone wall. For the 2nd order dynamic approach, there is a good qualitative agreement between experimental and simulated data, both in the acceleration (frame 1 and 2) and deceleration (frame 7) phase of the flow. The 2nd order static results show underestimation in the accelerating phase and overestimation in the decelerating flow phase due to the previously discussed timing artifacts. Both the experimental and simulated ultrasound curves have troubles estimating velocities near the wall.

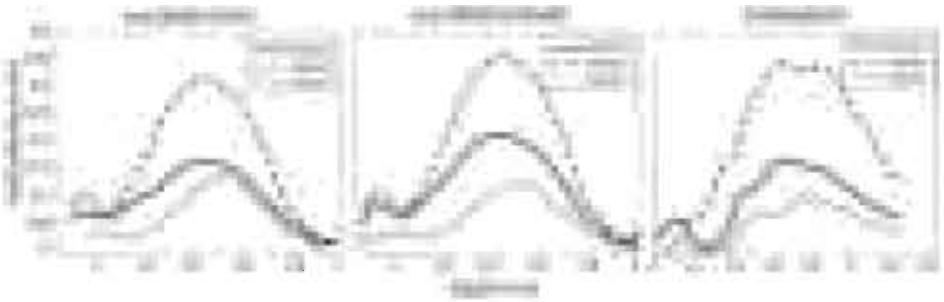

FIGURE 6.7: The comparison between the 2nd order simulations (static and dynamic) and the experiment is shown for the previously shown three cardiac phases, using axial velocity profiles at lateral position X=1.5 cm. For the sake of clarity, the absolute value of the axial velocity (parallel with ultrasound beam) is shown, explaining the positive values (and the difference with fig. 6.3).

6.4 DISCUSSION

In this work we compared both the first order and second order approach using a CFD-based ultrasound simulation environment, supported by experimental CFI-measurements on an in-vitro setup of a carotid flow model. CFD-simulations were performed based on this experimental model and were subsequently employed to mimic ultrasound images. This strategy allows direct comparison between simulated and experimentally acquired ultrasound data, and hence assessing the level of realism that is obtained by the different approaches. We demonstrated that during dynamic phases of the cardiac cycle (e.g. systolic acceleration), the dynamical image formation should not be neglected. Simply color-coding one CFD-frame is inadequate compared to dynamically processing CFD-data (cfr. Contourplots in fig. 6.3). Conventional color flow images showed this to a lesser extent due to the non-linear color-scale. Fig. 6.4, however, demonstrated in a more quantitative way the influence of the dynamical imaging formation using cross-sectional velocity profiles at 3 locations in the carotid bifurcation. Further, realistic ultrasound simulation models like Field II offer the possibility of incorporating the ultrasound velocity estimator statistics, which has a significant effect on the ultrasound images as is apparent in fig. 6.3. The irregular character of the estimated velocity curves in fig. 6.4 is a consequence of this as well. Additionally, simulated (2nd order) and measured ultrasound images may show difficulties measuring correct velocities near the vessel wall, as can be observed by the overestimation present in fig. 6.4 and 6.7. The overestimation is here caused by a spatial averaging effect due to the extents of

the imaging point spread function. In real life, tissue signal from the vessel wall is present, which will typically lead to an underestimation of flow velocities if not properly attenuated through filtering prior to flow velocity estimation. This signal from the vessel wall can also be used to mask the flow image in order to make the spatial averaging effect less prominent. In general, color flow images directly obtained from CFD give an idealized view compared to realistically simulated ultrasound images since the physics of the imaging process are not incorporated. Besides the lacking of the statistics of the velocity estimator, one should note that the spatial imaging resolution in case of CFD is in-effect zero. The imaging process, however, is the result of convoluting a 3D-object and the point spread function of the imaging system (determined by the pulse length and the beam width), hence color-coding CFD assumes a perfect imaging system where no spatial blurring effect due to the point spread function is present. The mentioned limitations of directly processing CFD-data were further supported by the experimental CFI-measurements, demonstrating similar flow patterns as in the 2nd order simulations both in terms of CFI images (fig. 6.5) as well as derived velocity profiles (fig. 6.7).

However, we should note that although the 1st order approach shows limitations, intermediate solutions are possible as described by Khoshniat et al [61], where the CFD velocity field is interrogated at N points within a temporal sampling window and within a spatial sample volume. Velocities are weighted with the power distribution in the sample volume and intrinsic spectral broadening is accounted for by convolving each velocity with a semi-empirical broadening function. This offers a middle ground between the 1st order and more computationally expensive 2nd order approach (CFD calculation: ± 2 days for 3-cycle simulation, ultrasound simulation: 9h for each frame). The final choice of the simulation strategy is however dependent on the research objective. For validation and development of ultrasound imaging algorithms, a 2nd order strategy is indispensable. A 1st order dynamic or intermediate approach is sufficient to obtain a general impression of CFI.

This study is up to some level related to the recent work of Funamoto et al., who integrate ultrasound measurements and numerical blood flow simulations to fully resolve the flow field in vivo, for instance in an aortic aneurysm [114]. They use ultrasound measurements as part

of an iterative loop where they run numerical simulations of a given flow field until ultrasound images derived from this calculated flow field match with the ultrasound measurements. If an optimal match is reached, the CFD data provides all 3D-details of the flow field, and provides the necessary data to calculate hemodynamic parameters such as the wall shear stress distribution. Although the aim of our work is different (to construct an as realistic as possible ultrasound simulation environment), the results presented here may be relevant within the context of ultrasonic-measurement-integrated simulation. When applying this method to highly dynamic flow conditions, it may be necessary to include especially the dynamics (and potentially also the statistical features) of the image formation into the optimization procedure to allow better matching between measured and CFD-derived ultrasound information.

Although both experiments and simulations were based on the same in-vitro flow setup and were identically post-processed, a direct comparison was still hampered by several limitations. Firstly, small differences between the experimental and simulated frame durations (14.9 frames/s and 14.6 frames/s for the simulations and experiments respectively) are present. It is virtually impossible to obtain a perfect match without full disclosure of all information on the employed ultrasonic probes and the sequencing, which is kept confidential by the ultrasound companies. Secondly, the positioning of the ultrasound phantom in the simulations is not exactly the same as in the experiments since the coordinates and angle of the probe position were not measured in the experiments. Positioning of the probe in the ultrasound simulation was obtained via trial-and-error, aiming to get a 2D plane as close as possible to the imaging plane in the experiments. Clear landmarks on the scatterer phantom of the carotid artery (e.g. bifurcation and intersections of the internal and external carotid artery with the image boundaries) were chosen to match with the experimental images. Also the diameters of the common, internal and external carotid artery phantom were compared with the measured image and further adjusted by rotating the phantom. Although both are close, the imaging plane of the experiments and simulations are not identical, as can be seen in the color flow images of fig. 6.5 and the underestimation of the experimental velocity profiles in fig. 6.7. Thirdly, artifacts in the experimental images impede a correct flow field representation. This is why the experimental velocity profiles in fig. 6.7 are cut off near the

posterior wall. Obvious artifacts are also visible in fig. 6.5 where velocity estimates in the experiments are corrupted when the ultrasound beams need to cross the silicone carotid wall more than once. Hence a noticeable alteration in velocity estimates in the external carotid (at lateral position X=0). These artifacts were however not reproduced by the simulations as can be seen in fig. 6.5. Further, differences in the acoustic properties of the in-vitro and simulated model may influence our results. The soft tissue surrounding the blood vessel was represented by water, which has an attenuation coefficient and wave speed differing from the real-life situation (attenuation=0.002 dB/cm for water and 0.5 dB/cm for soft tissue, wave speed=1480 cm/s for water and 1540 m/s for soft tissue). The differing wave speeds in blood and tissue may cause a small shift in the calculation of the depth position ($r = ct/2$ with c the wave speed, t the time and r the depth), which was not taken into account in the simulations. The fact that the acoustic properties differ in the different materials could not be included in the Field II-simulations. The effect of non-linear wave propagation is also more significant in water than soft tissue. However for blood flow imaging, these non-linear or higher-harmonic contents are removed by the receive filter and will not influence the image. Other limitations are due to the CFD-based ultrasound simulation strategy and the ultrasound simulation model. The Field II method does not include multiple scattering, and it also puts restrictions on the nature of the scatterers because the disc-shaped red blood cells are represented by random point scatterers. No attenuation of the ultrasound waves was included in the ultrasound simulations but in our case this assumption is close to the in-vitro setup due to the very low attenuation coefficient of water. However the scanner compensates for attenuation by using a demodulation frequency (a shifted center frequency due to attenuation), based on expected signal from blood or tissue. Hence, the demodulation frequency on the scanner will be slightly differing from the one which should be used when scanning water, and as a consequence the estimated velocities will be slightly offset (f_0 is part of the equation for the autocorrelation estimate). Finally, our CFD-simulations assume rigid walls and hence wall distension had to be minimized in the experimental model by appropriate tuning of the boundary conditions to obtain an optimal match. Incorporating vessel walls or surrounding tissue is intended for future work. For further details on limitations of coupling CFD and ultrasound, we refer to [110]. The overall result of matching simulations to experiments can be observed in fig. 6.6 where

distributions in the velocity estimation difference between simulation and experiment are shown for the second order approaches.

6.5 Conclusion

In conclusion, we have shown that our recently developed CFD-based simulation environment yields realistic color flow images, containing all features of experimentally measured ultrasound data. However, this level of realism can only be achieved by incorporating both the dynamics of the image forming, as well as the statistical features of the velocity estimators in the simulations. A full coupling of CFD and ultrasound is indispensable to capture dynamic arterial flow and the spotted appearance of the estimated velocity field.

Three

Analysis of 2D ultrasonic blood flow estimators based on CFD-based ultrasound simulations and in-vivo data

CHAPTER 7

2D blood flow estimation: speckle tracking versus vector Doppler based on CFD simulations in a carotid artery

In part II of this manuscript, we focused on clinically established methods to image blood flow with ultrasound. However, these techniques are still limited to 1D flow visualization, and therefore a logical continuation of our work is to investigate multidimensional flow estimation. In particular, we compare two techniques being explored by the medical ultrasound community: speckle tracking (ST) and vector Doppler (VD). However, these techniques have yet to be validated for complex flow patterns as may arise in diseased arteries. In this chapter, the properties of ST and crossed-beam VD are compared with a ground truth for clinically relevant flow using our ultrasonic simulation environment coupling the output from computational fluid dynamics (CFD) with the Field II ultrasound simulation model.

The statistical properties of ST and VD are first evaluated for stationary flow in a tube for varying vessel positions and angles, and for varying noise levels. Further, performance is evaluated for pulsatile flow conditions in a stenosed carotid bifurcation model. A linear regression

analysis shows that both methods overall are in good agreement with the CFD reference. However, VD suffers from more spurious artifacts and is severely hampered by aliasing during parts of the cardiac cycle. ST is less accurate in estimating the axial component, but prevails in estimating velocities well beyond the Nyquist range. Our simulations indicate that both methods may be used to image complex flow behavior in the carotid bifurcation, however, considering also scanning limitations of VD, ST may provide a more consistent and practical approach.

This chapter is based on "*Two-dimensional blood velocity estimation with ultrasound: speckle tracking versus crossed-beam vector Doppler based on flow simulations in a carotid bifurcation model*", as published in IEEE-TUFFC, vol. 57, no. 2, p. 327-339, 2010.

7.1 Introduction

Ultrasound is a frequently used non-invasive tool for blood flow visualization. Standard clinical procedures include pulsed-wave (PW) Doppler measurements and color flow imaging (CFI), based on classical one-dimensional (1D) velocity estimation. These methods have been extensively validated but show fundamental limitations [19]. Aliasing artifacts often occur for higher velocities, and the velocity measured is further dependent on the angle between the ultrasonic beam and flow direction. As blood flow in diseased arteries often includes swirling and complex secondary flow patterns, important markers of vascular disease are not properly portrayed using conventional methods. More accurate imaging methods also capturing these complex flow features could potentially improve early cardiovascular diagnosis, provide insight into the atherogenesis and progression of vascular diseases, and prove useful for a more accurate quantification of blood flow and flow-field derived parameters (e.g. vorticity, wall shear stress).

Several multi-dimensional flow velocity estimators for resolving complex flow patterns by estimating both the axial and lateral velocity component have been proposed. Two major research lines in this respect have investigated the use of speckle tracking (ST) [115] and vector Doppler (VD) [46]. Speckle tracking relies on tracking the movement of speckle patterns generated due to constructive and destructive interference of the backscattered ultrasonic waves from blood [42, 116]. On

the other hand, vector Doppler is the natural extension of 1D Doppler techniques, based on the illumination of a sample volume along different angles, and the composition of a velocity vector through triangulation. In this line, several vector Doppler systems have been proposed, including both single and multiple transducer setups [46, 47, 117]. An excellent review of the different configurations is provided by Dunmire [84].

Studies have been performed to evaluate ST and VD for analytically described flow patterns as well as for *in vitro* flow phantoms [43, 118–122]. Both methods have further also been tested *in vivo* in human vessels [44, 121, 123, 124], demonstrating the abilities of both methods in healthy flow conditions. Despite these efforts, neither ST or VD have yet been established for clinical use.

In order to study the true performance of these two-dimensional (2D) flow estimators for clinically relevant flow conditions, knowledge on the true velocity field for complex flow patterns is necessary. Computational fluid dynamics (CFD) allows calculating complex flow fields occurring in realistic geometries by solving the Navier-Stokes equations in a discretized form. In [110], we developed a simulation environment which couples the output of CFD with ultrasonic simulations (Field II). The simulation environment provided RF-signals resulting from realistic flow patterns, with flexible control of the flow and imaging conditions, and was validated through examples of color flow imaging and PW-Doppler.

In this work, the CFD based ultrasound simulation environment will be used to evaluate ST and crossed-beam VD towards a ground truth for pulsatile flow in a 3D model of a stenosed carotid bifurcation. Further, fundamental aspects potentially hampering the performance of the methods will be investigated statistically in a parameter study of stationary flow in a tube, including varying signal-to-noise ratio (SNR), vessel depth and in- and out-of-plane angle. Clutter filtering in 2D velocity estimation is a particular challenge, and will be treated separately.

In section 7.2, details regarding the CFD and ultrasound simulation setups will be given, and the applied speckle tracking and vector Doppler algorithms will be described. In section 7.3, results from the comparison between speckle tracking and vector Doppler for stationary

and pulsatile flow will be given. In section 7.4, the performance of both methods will be discussed and related to the applied imaging and post-processing setups. Further, the benefits and disadvantages of both methods will be discussed in the context of vascular imaging.

7.2 Methods

7.2.1 Ultrasound Flow Phantoms

Blood scatterer movement can be calculated analytically for simplified flow patterns in cylindrical tubes as for instance given by the Poiseuille and Womersley equations [125]. However, in order to mimic realistic and complex flow behavior such as swirling flow and secondary flow effects occurring in vessel curves / branches and for stenotic conditions, numerically computed flow fields are necessary to propagate the scatterers correctly. In [110] we presented a method to couple the output from computational fluid dynamics with ultrasound simulations, where the scatterer positions are updated according to the CFD velocity vector field. In this approach, 3-D spatial interpolation is utilized to transform the irregular CFD grid to the point scatterer positions, and temporal interpolation is used to match the significantly differing time scales of CFD (5ms) and ultrasound (62.5 μs for a pulse repetition frequency of 16kHz). For further details on aspects related to the coupling between CFD and ultrasound simulations we refer to [110].

Backscattered ultrasonic signals are generated using the Field II software [17, 18], which is based on the spatial impulse response estimation as described by Tupholme [94] and Stephanishen [95]. Blood tissue is modeled as a collection of randomly distributed point scatterers with normally distributed scattering amplitude. The required density of the scatterers is related to the imaging system bandwidth, with approximately 10 scatterers per resolution cell assuring Gaussian distributed RF-signals. The scatterer positions are updated for each individual beam acquisition.

7.2.1.a Stationary tube phantom

To investigate the fundamental statistical performance of the 2D velocity estimators for varying imaging conditions, repeated simulations (N=80) were performed of blood moving in a straight tube with radius 3mm (R_{max}). Point scatterers were moved analytically according to the

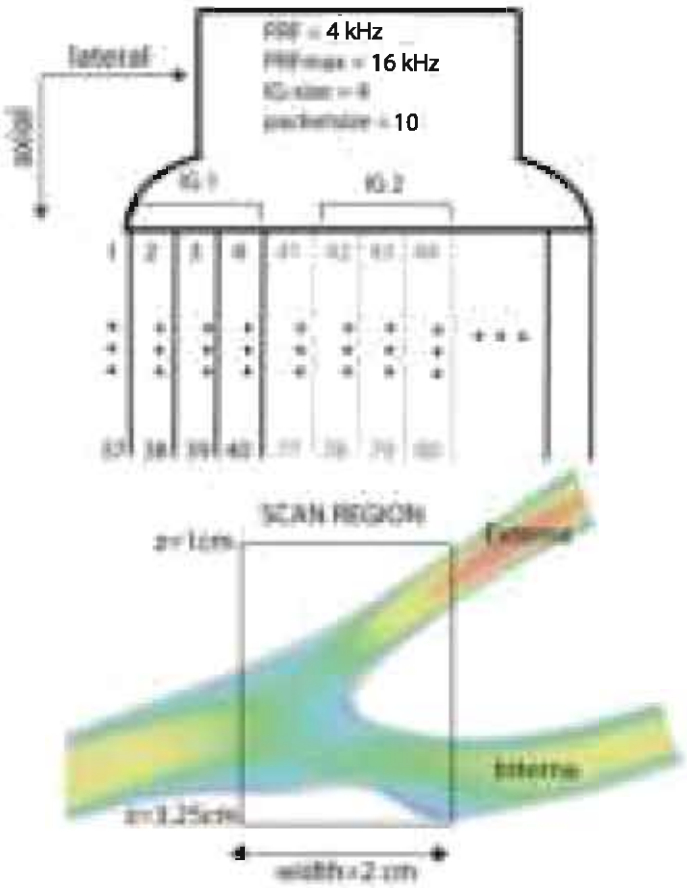

FIGURE 7.1: The stenosed carotid bifurcation model used to compare speckle tracking and crossed-beam vector Doppler is shown, together with an imaging setup demonstrating the principles of beam interleaved acquisition.

Pouseuille equation: $v = v_{max}(1 - (\frac{R}{R_{max}})^n)$, with v the velocity at radial position R, v_{max} the maximal velocity (50 cm/s), and using $n = 2$ to obtain a parabolic flow profile. Performance was quantified in terms of mean bias and standard deviation across the vessel compared to the analytical reference for varying in-plane and out-of-plane flow angles, varying vessel depths, and different signal-to-noise ratios (SNR).

7.2.1.b Pulsatile carotid phantom

A carotid artery bifurcation model was 3D reconstructed from MRI scans of a healthy volunteer (Mimics, Leuven, Belgium), in which we artificially added an eccentric plaque in the internal carotid branch. This resulted in a mildly stenosed bifurcation model as shown in Fig. 7.1. The commercial CFD software Fluent 6.2 (Ansys, Canonsburg, Pennsylvania) was used to numerically solve the Navier-Stokes equations

with a finite volume method. A pulsatile velocity profile measured with PW-Doppler in a healthy volunteer was imposed at the common carotid artery and a 45-55% flow division was assumed at the bifurcation of the external and internal carotid artery. Blood was modeled as an incompressible Newtonian fluid with dynamic viscosity μ and density ρ respectively set to 3.5 mPas and 1050 kg/m^3. CFD velocity fields for a full cardiac cycle were simulated. For further details on the CFD simulations and the phantom construction, we refer to [110].

7.2.2 Ultrasound Simulation Setup

Details regarding the ultrasound simulation setup in general and for ST and VD specifically can be found in Table 7.1. A 1-D, 192 element linear array transducer model with a fixed elevation focus, and a center frequency of 5 MHz was employed for all simulations. A simulation sampling frequency of 100 MHz was used, and each transducer element was divided into 4 mathematical elements in the elevation direction, ensuring that every scatterer imaged was in the far field of each individual element. To further reduce simulation times, the number of scatterers included for each beam acquisition was substantially reduced by only including scatterers within a distance of $k = 12$ times the receive beam width. Also, no frequency dependent attenuation was included in the simulations.

The ultrasound imaging setup was optimized separately for speckle tracking and vector Doppler due to different restrictions imposed by transducer width, scanning depth, and sampling / frame rate requirements. The final setup was determined based on a requirement of achieving a 2x4 cm scan (width x depth) for a frame rate of at least 20 Hz.

7.2.3 2D Velocity Estimators

7.2.3.a Speckle Tracking (ST)

Two-dimensional speckle tracking is applied by searching for the best match of a kernel image region from acquisition X_0 at time t_0, inside a larger search region from a later acquisition X_n at time t_n, as illustrated in Fig. 7.2 (Speckle Tracking-A). The distance to the best match corresponds to the kernel displacement in the time $T = t_n - t_0$ between acquisitions. To reduce the computational demands of 2D cross-correlation, the best match was determined using the sum-of-absolute-

TABLE 7.1: The ultrasound setup for ST and VD

Probe parameters		**Simulation setup**	
center frequency	5 MHz	excitation	sinusoidal
relative bandwidth	65%	pulse periods	2.5
number of elements	192	PRF_{max}	16 kHz
element pitch	0.25 mm	PRF	2 & 4 kHz
element height	6 mm	packetsize	10
transmit focus Az	2 cm	MLA ST / VD	2 / 1
transmit focus El	3.2 cm	IG size ST / VD	16 & 8 / 8 & 4
dynamic receive focusing	yes	$F_\#$ transmit ST / VD	2.5 / 3
expanding aperture	yes	$F_\#$ receive ST / VD	1.4 / 2.85

differences (SAD) method, given by

$$\delta(\alpha, \beta, n) = \sum_{i=1}^{l} \sum_{j=1}^{k} |X_0(i, j) - X_n(i + \alpha, j + \beta)| \tag{7.1}$$

with δ the SAD coefficient, l and k the lateral and axial dimension of the kernel in beam and range samples, and (α,β) defining a kernel displacement in the lateral and axial direction. The kernel displacement (α_m,β_m) is estimated by finding the minimum SAD value, and the 2D velocity vector is then calculated according to:

$$V_n = \frac{\sqrt{(\alpha_m \Delta x)^2 + (\beta_m \Delta z)^2}}{nT}, \Theta_n = atan \frac{\alpha_m \Delta x}{\beta_m \Delta z}, \tag{7.2}$$

with Δx and Δz the lateral and axial sampling distances and T the time between subsequent acquisitions. Due to the fundamental mismatch between the lateral and axial spatial resolution and sampling, 4x linear lateral interpolation was used on the signal envelope to obtain a higher tracking accuracy. Also, local parabolic fitting around the SAD matrix minimum was employed to achieve subpixel accuracy [126].

To achieve a sufficiently high frame rate for tracking the blood speckle movement, beam interleaved acquisition [100] was used as illustrated in Fig. 7.1. Beam interleaving ensures that the waiting time between beam acquisitions is minimized, thus maximizing the imaging frame rate when the Doppler PRF is chosen lower than the maximally possible PRF (PRF_{max}), which is restricted by the image depth. Neighbouring beams in lateral subregions of the image are acquired at PRF_{max},

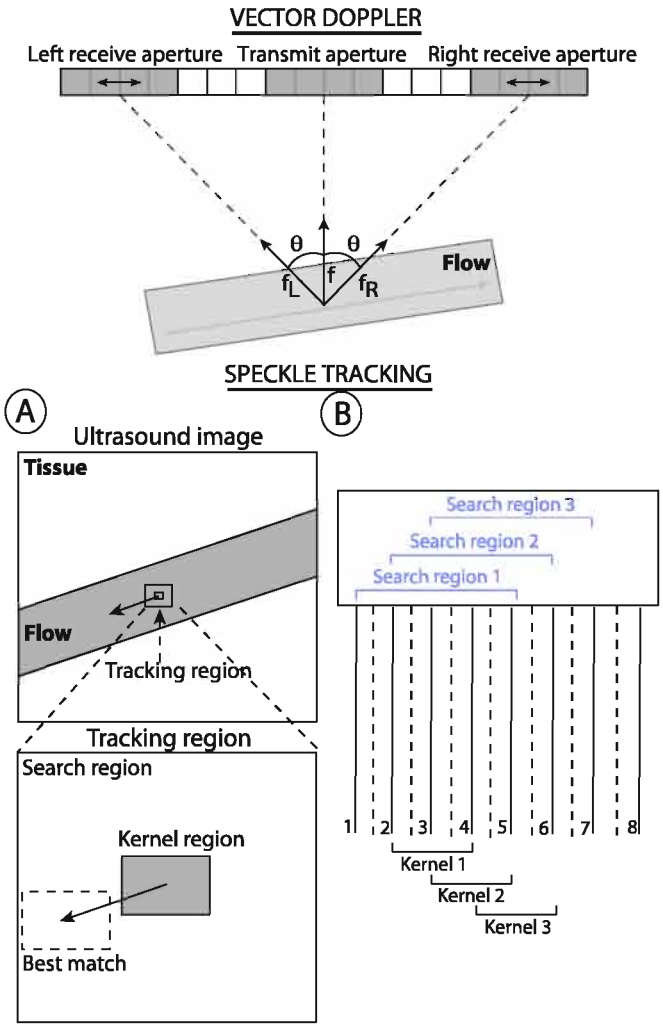

Figure 7.2: The working principles of crossed-beam *vector Doppler* and speckle tracking are illustrated. Crossed-beam vector-Doppler was implemented by using a common transmit aperture, and two simultaneous receiving apertures on each side, sliding across the transducer for increasing depth. Panel A of the *speckle tracking* images demonstrates the principle of tracking a kernel inside a search region. Panel B shows how 3 kernels with corresponding search region are placed inside an interleave group, based on the hypothetical case of a kernel region=3, search region=5 and overlap=2 original receive beams. The solid lines indicate the original receive beams and the dashed lines the interpolated lines.

while a beam in a given direction is acquired at the slow-time PRF. A packet of these speckle subregions is acquired (packetsize=10). The frame rate of such a speckle subregion is then given by the slow-time PRF, typically in the kHz range. The interleave group size, i.e. the num-

ber of beams in each subregion, is given by

$$IGS = \left\lfloor \frac{PRF_{max}}{PRF} \right\rfloor \cdot MLA, \tag{7.3}$$

where MLA is the number of beams received in parallel (multiple line acquisition). This is a technique commonly used in high-end systems, to increase the frame rate [106]. The choice of MLA, lateral beam overlap, packet size, and PRF_{max} will determine the overall frame rate for a given scan width. Two different tracking setups were used corresponding to a PRF of 2 and 4 kHz. Parallel receive beamforming (MLA=2) was utilized to double the interleave region width, thereby doubling the maximum trackable lateral velocity. The PRF_{max} was fixed to 16 kHz which resulted in an interleave group size of 16 and 8 beams for 2 and 4 kHz PRF respectively.

For an interleaved acquisition scheme, the kernel size is dependent on: (1) the desired number of kernels in the interleave group for averaging and (2) the maximal trackable velocity. Fig. 7.2 (Speckle Tracking-B) illustrates for the sake of clarity a hypothetical case where 3 kernels consisting of 3 original receive lines are positioned, with a search region of 5 lines and a kernel overlap of 2 lines. The centre of each kernel is positioned corresponding to an original receive line. Specifically, for both our tracking setups, the kernel size was chosen so that three kernels offset by ±1 receive beam could fit inside an interleave group for averaging purposes. The kernel and search region was further optimized so that a maximal trackable velocity of 62 cm/s for both PRF-setups was obtained. This resulted in a kernel size of 0.52 x 0.88 mm and 0.25 x 0.88 mm for the 2 kHz and 4 kHz setup respectively. The applied search regions had a size of 1.15 x 1.53 mm and 0.56 x 1.19 mm for 2 and 4 kHz respectively. An ensemble of nine single-lag velocity estimates was acquired and the median of the lateral (v_x) and axial (v_z) components was calculated. The median was preferred over the mean in this case to reduce the effect of spurious tracking errors. These v_x and v_z estimates were further averaged in space in a 3x3 kernel region.

Optimizing the ST-algorithm also entails optimizing the imaging setup to obtain images with a high spatial resolution (see Table 7.1). We used a setup with a fixed transmit focus at 2 cm in depth and an F-number of 2.5. Dynamic focus and expanding aperture was used on receive to

retain an F-number of 1.4. Rectangular and cosine tapered apodization were applied on transmit and receive respectively. A pulse length of 2.5 periods was chosen as a trade-off between spatial resolution and penetration depth.

7.2.3.b Vector Doppler (VD)

The 2D vector Doppler technique was implemented by separating a linear array transducer electronically into three subapertures: a central transmitting aperture surrounded on either side by two receiving apertures, all three operating simultaneously [47] (cfr. fig 7.2). This technique is often referred to as crossed-beam vector Doppler, and the axial and lateral velocity components can then be calculated according to [47]:

$$v_x = \frac{c}{2f_0 sin\theta}(f_2 - f_1) \tag{7.4}$$

$$v_z = \frac{c}{2f_0(1 + cos\theta)}(f_1 + f_2), \tag{7.5}$$

where f_0 is the center frequency of the received pulse, θ the steering angle, c the ultrasound wave speed, and f_1 and f_2 are the mean Doppler shifts from the left and right receive aperture respectively. In practice, f_1 and f_2 are estimated using the autocorrelation approach [36].

The crossed-beam vector-Doppler approach was evaluated for a 2x4 cm scan setup as for speckle tracking, and also for two different PRFs of 2 and 4 kHz. In order to achieve the required scan width, a receive steering angle $\theta = 12^o$, and a satisfactory overlap between the transmit and receive beams, trade-offs were needed with regards to setting the transmit and receive apertures. In our setup, the transmit aperture was focused at 2 cm depth with $F_{\#}$=3, at an angle of 0^o, while the two receive apertures were steered at a constant angle of 12^o towards the transmit direction, with an $F_{\#}$ of 2.85. By sliding the receive apertures towards the edges of the transducer, and using expanding apertures and dynamic focusing, an extensive depth range could be covered. A constant receive angle was ensured for depths up to 2.4 cm for the 2 cm scan width. By allowing the angle to decrease for larger depths, a scan depth of 4 cm was achieved. The Nyquist velocity for VD was 15.4 cm/s and 30.8 cm/s for the 2 and 4 kHz setup respectively, effective along the lines angled $\pm\ \theta/2$.

7.2.3.c *Clutter Filtering*

In order to avoid biased velocity estimates and flashing artifacts in tissue regions, clutter filtering prior to velocity estimation is necessary to attenuate signals from near-stationary tissue [41]. This has conventionally been approached by high-pass filtering the slow-time signal from each range gate. For 2D velocity estimation obtained either from speckle tracking or vector Doppler, this filtering process can be particularly troublesome, and may cause errors both in the velocity magnitude and direction. When the flow is perpendicular to the ultrasound beam, the signal from blood will be centered around zero Doppler frequency, and consequently be severely attenuated by traditional clutter filters. For ST, a substantial portion of the signal may be lost, and the remaining signal will have a band pass and therefore an oscillating nature as described in [41]. For VD, the Doppler signal will be centered around zero Doppler frequency when the flow is perpendicular to the line along half the transmit-receive angle (the vector sum of either transmit and receive beam directions). When the signal from either receive aperture is distorted this will lead to bias in the compounded velocity estimates.

In our simulations clutter was not present, but the effect of clutter filtering on the blood signal is included by assuming that all clutter is attenuated by the filter. For the carotid scans, a 5th order finite impulse response (FIR) mean subtraction filter was used, with a frequency response shown in fig. 7.3. The filtered data are obtained by convolution of the received signal and the filter coefficients of a 5th order FIR filter. Hence, 5 temporal samples were available for averaging in subsequent velocity estimation. This FIR filter type was chosen as it is time-invariant, ensuring that speckle images within a slow-time ensemble were identically processed. To ensure fair comparisons, this filter was also used for the VD approach. However, time-variant approaches such as polynomial regression filtering [41] with sharper transition regions and without initialization requirements could then also be used. For the straight tube analysis, we did not use a clutter filter in order to highlight the effect of the other fundamental error sources in 2D velocity estimation.

7.2.3.d *Performance Analysis*

The fundamental performance of ST and VD was first assessed statistically for N=80 realizations by estimating cross-sectional velocity profiles at a section halfway the straight tube. The mean bias and standard

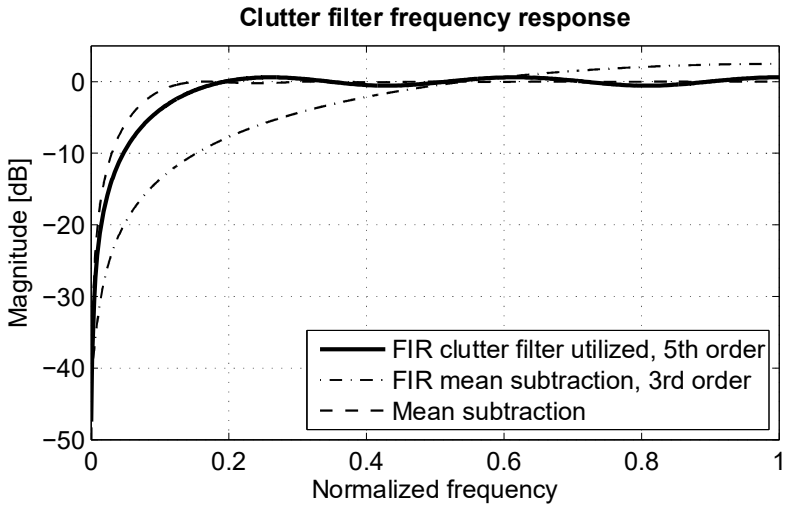

Figure 7.3: The frequency response of the 5th order FIR filter used to simulate the effect of clutter filtering in the simulations, compared to a 3rd order FIR filter and the time-variant mean subtraction filter.

deviations were calculated as percentages of the maximum axial or lateral CFD reference velocity. Further in the 2x4 cm scans of the carotid artery, performance was assessed through a linear regression analysis where velocities at all spatial positions and throughout the cardiac cycle were included. Also, a temporal error analysis was performed by calculating the mean absolute deviation normalized to the maximum axial or lateral velocity component for each frame throughout the cardiac cycle. For both ST and VD, a 3x3 spatial averaging mask was used to reduce variance of the velocity estimates. For ST the tracking estimates were averaged, while for VD the autocorrelation function estimates were averaged. In order to allow for a direct comparison of the two methods in time, we used the same PRF and PRF_{max}, and the same packet size for both methods. However, as only one velocity profile was obtained per interleave group for ST in our setup, the denser spaced VD velocity estimates were spatially interpolated to the speckle tracking positions in the comparisons.

7.3 Results

7.3.1 Speckle Tracking vs. Vector Doppler: Statistical Comparison in a Straight Tube

The parameter study was performed for stationary flow in a tube using the 4 kHz simulation setup. Different factors possibly degrading

the performance of ST and VD were investigated: 1) varying depth of the vessel (for a fixed transmit focal position), 2) in-plane vessel angle, 3) out-of-plane vessel angle, and 4) varying signal-to-noise ratio (SNR). Noise was added during post-processing to normalized signals from the ST and VD acquisitions. The default tube was positioned at

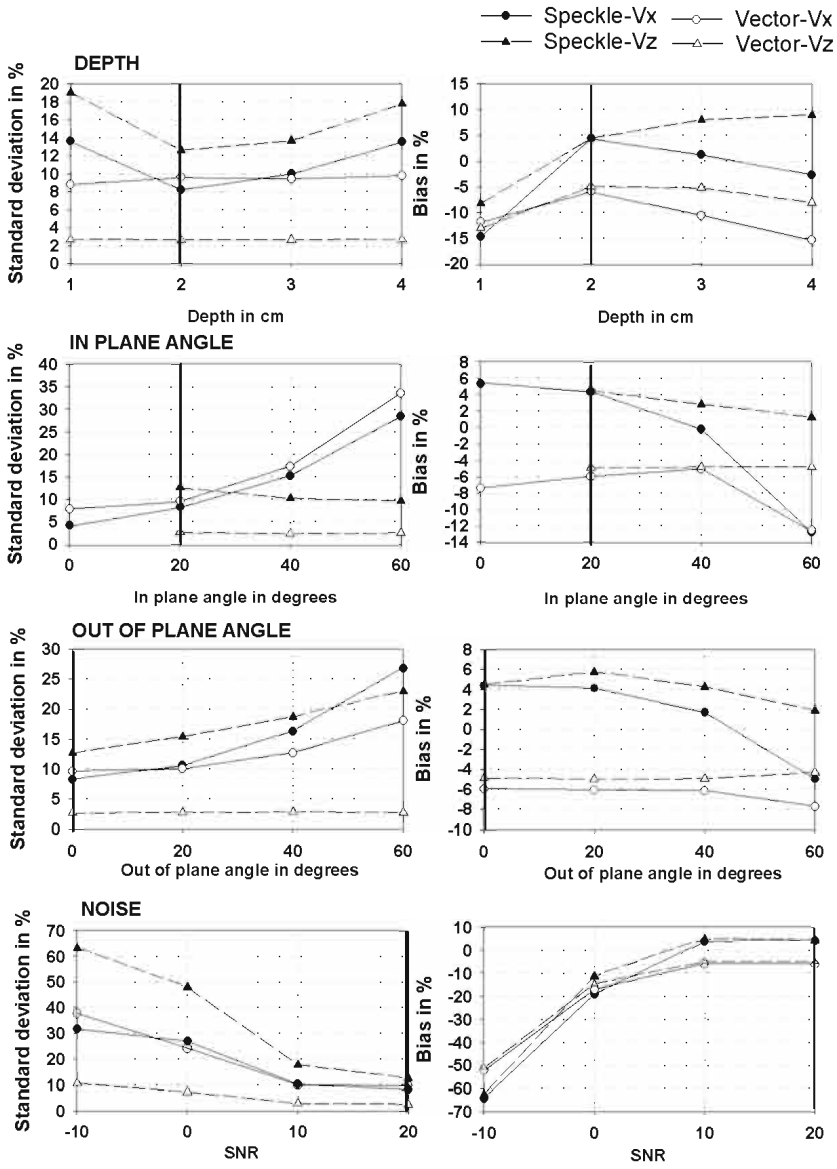

FIGURE 7.4: Results from the parameter study of factors possibly degrading the performance of speckle tracking and vector Doppler, based on ultrasound simulations of stationary flow in a tube (PRF=4 kHz). Vessel depth, noise level, in-plane and out-of-plane angle were investigated. Bias and standard deviation are expressed as a percentage of maximal lateral or axial CFD-velocity.

2 cm depth, angled with 20^o in-plane and 0^o out-of-plane, and with 20 dB SNR. In Fig. 7.4, black and white symbols are respectively used for ST and VD estimates, while triangles represent axial velocity (v_z) and circles lateral velocity (v_x) estimates. Default parameter values are indicated with bold vertical lines.

7.3.1.a Vessel depth

VD estimates were quite unaffected with std=10% and 3% throughout depth for v_x and v_z respectively. For ST, a variation in depth was observed for both velocity components, varying from 8–14% and 13–20% for v_x and v_z respectively. The bias was positive for ST and negative for VD, with similar absolute values in depth.

7.3.1.b In-plane vessel angle

For both techniques an increased underestimation and an increased standard deviation was observed for the lateral velocity estimates with angle, the standard deviation ranging from 4 – 29% (ST) and 8 – 34% (VD). The axial velocity component was not significantly influenced for either method.

7.3.1.c Out-of-plane vessel angle

Out-of-plane scatterer motion affected the standard deviation for both methods, gradually increasing for increasing angle. For ST both velocity components suffered, while for VD the axial velocity component remained unaffected. The VD bias was largely unaffected. For ST, lowered values and in the end underestimation of the lateral velocity component was observed when approaching 60^o angles.

7.3.1.d Signal-to-noise ratio

Bias magnitude increased similarly for both methods up to 50% and higher when noise dominated (SNR=-10dB). In terms of standard deviation, the VD axial velocity estimates were quite robust compared to ST. The lateral velocity estimate degraded similarily for both VD and ST.

7.3.2 Speckle Tracking vs. Vector Doppler: Pulsatile Carotid Artery Flow

To investigate the ability to capture the highly varying carotid flow dynamics (exceeding 90 cm/s in the external carotid), a complete cardiac cycle of ST and VD images was simulated (22 frames in total) for two

different PRFs of 2 and 4 kHz. Fig. 7.5 and 7.6 respectively show the 2 kHz and 4 kHz results for three phases of the cardiac cycle: systolic acceleration, onset of diastole, and mid-diastole, as indicated by the red part on the flow curve of the common carotid artery. The first column shows the reference flow field as obtained from the CFD simulations. The reference CFD vector plots take into account the temporal lags inherent in the image formation by interpolating the CFD data to the

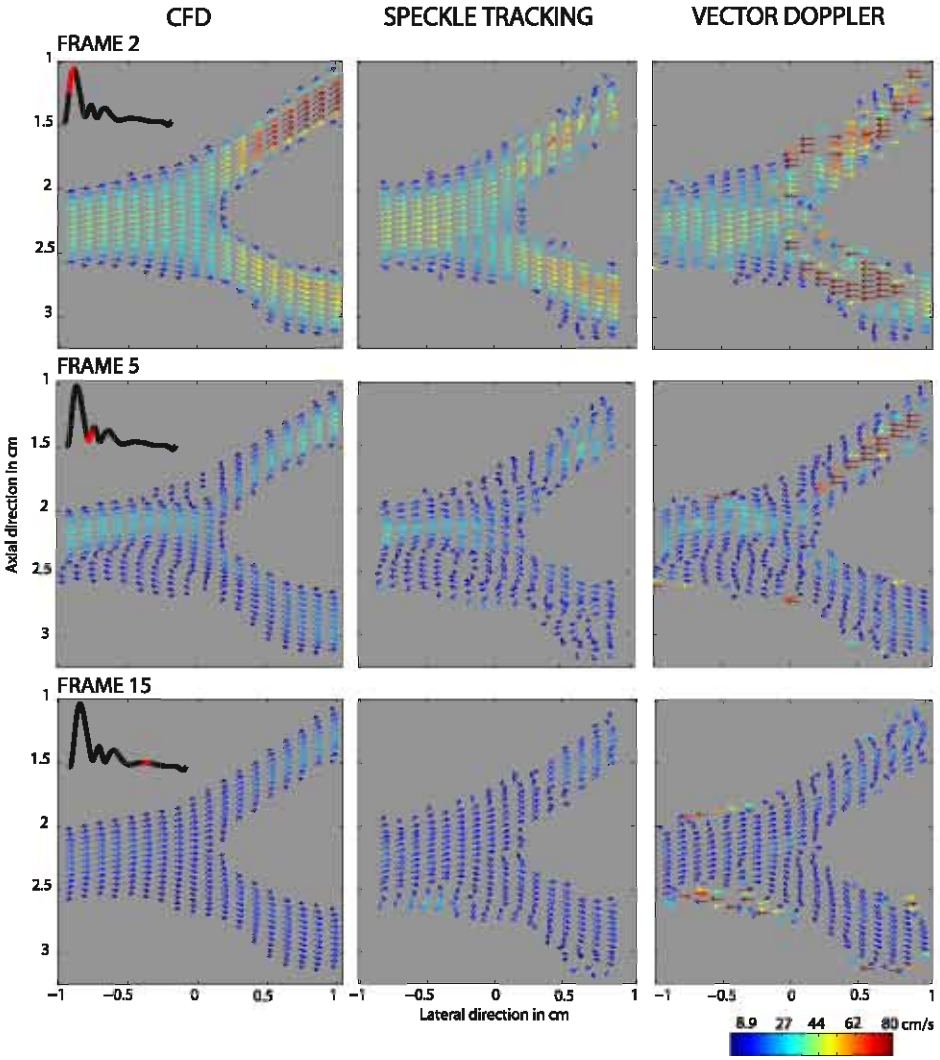

FIGURE 7.5: Results for 2kHz simulations of flow in the carotid bifurcation for speckle tracking and vector Doppler compared to the reference CFD velocity field. Three different frames during the cardiac cycle are shown: systolic acceleration, onset of diastole, and mid-diastole, as indicated by the red part on the flow curve of the common carotid artery. As can be observed, both methods are able to portray the swirling flow in frame 5. Further, vector Doppler performance was severely deteriorated by aliasing in the external (frame 2 and 5) and internal (frame 2) carotid artery.

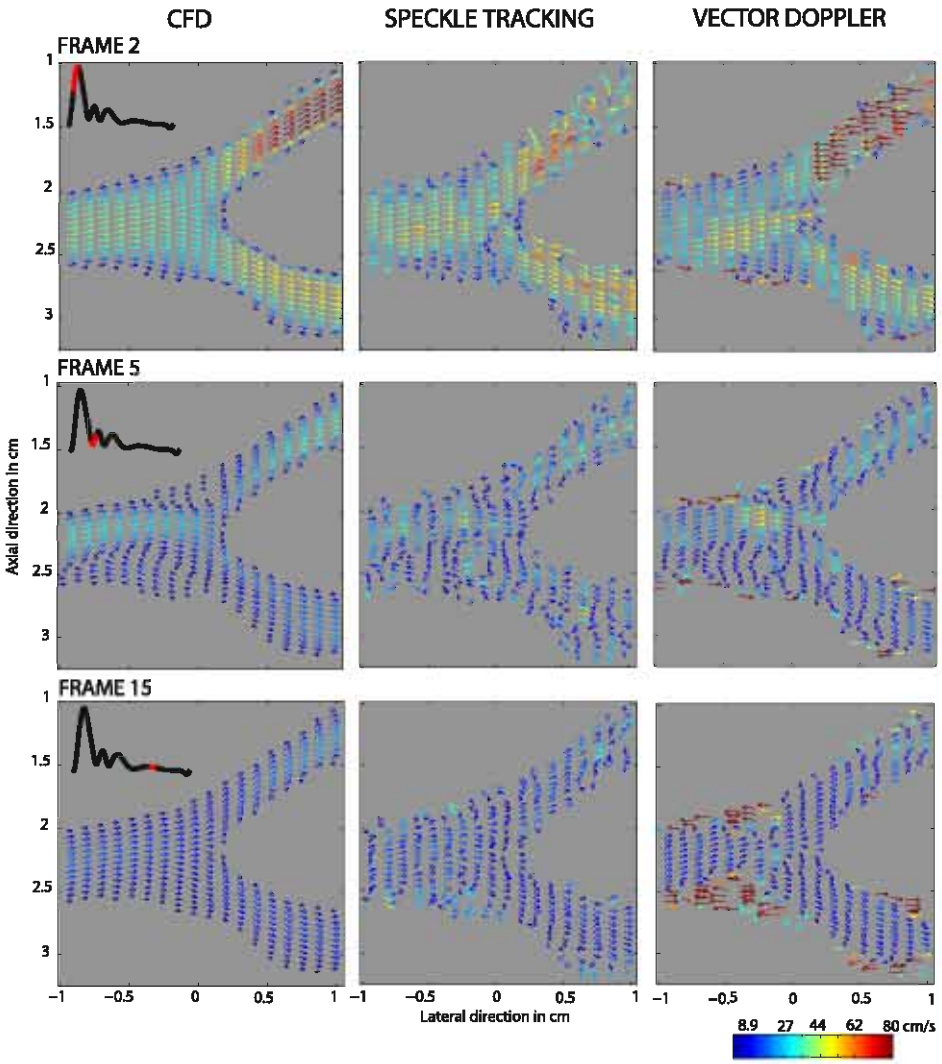

Figure 7.6: Results for 4 kHz simulations of flow in the carotid bifurcation for speckle tracking and vector Doppler compared to the reference CFD velocity field. Three different frames during the cardiac cycle are shown: systolic acceleration, onset of diastole, and mid-diastole, as indicated by the red part on the flow curve of the common carotid artery. As can be observed, speckle tracking performance is severely degraded compared to the 2 kHz setup. The higher PRF infers less aliasing artifacts for vector Doppler, but also leads to an increased amount of clutter filter artifacts as can be seen in the posterior wall in the bifurcation for frame 15.

time instances the involved ultrasound beams were fired.

Comparing fig. 7.5 and 7.6, the 2 kHz scan sequencing proved beneficial for speckle tracking with all three cardiac phases showing good agreement with the reference flow field. Both the lower and higher velocity regions were in general well estimated, with the swirling flow zones in

frame 5 accurately detected by the tracking algorithm. The highest velocities in the external carotid were above the trackable limit, leading to underestimation and a higher variance for these estimates. Some errors can further be noticed near the vessel wall where the velocity becomes close to zero and are attenuated by the clutter filter. For the 4 kHz setup, the ST performance deteriorated significantly during all phases of the cardiac cycle. Tracking errors resulted in seemingly more chaotic flow in the complete bifurcation, with the vortices in fig. 7.6 hardly distinguishable.

Considering only flow velocities within the Nyquist range, vector Doppler provided reasonable results for both the 2 and 4 kHz setups. However, as for conventional Doppler-based methods it is severely hampered by aliasing in parts of the cardiac cycle. For the 4 kHz setup the zones affected by aliasing artifacts were reduced to only occur in the

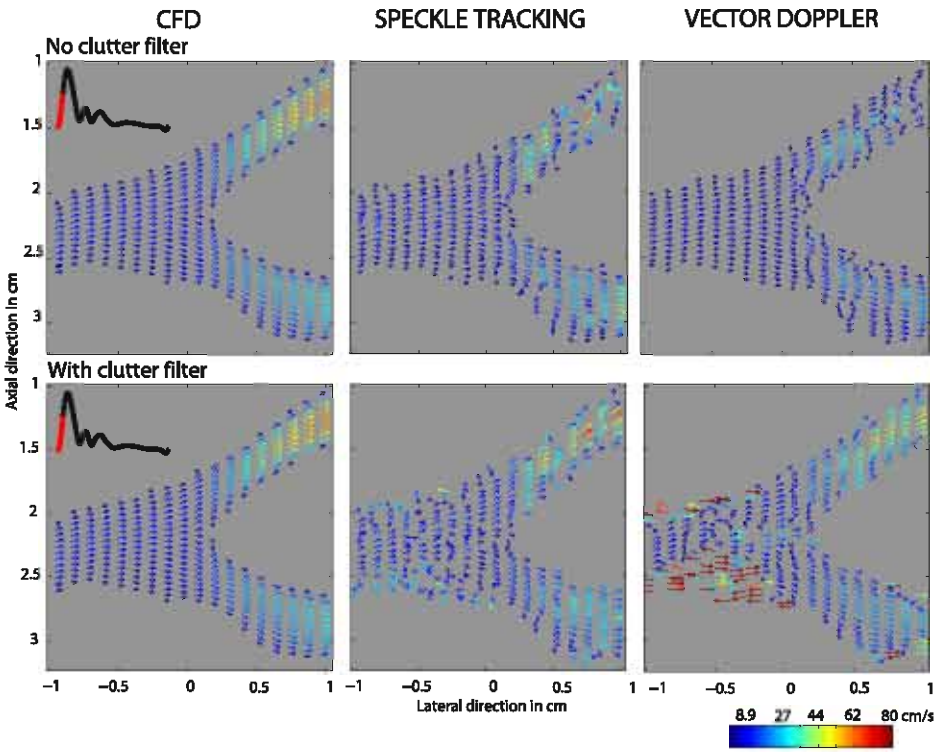

FIGURE 7.7: The effect of using a 5th order FIR clutter filter for both speckle tracking and vector Doppler velocity estimates, compared to the true flow situation. Results are shown for systolic acceleration and for the 4 kHz setup. For speckle tracking, a more chaotic flow picture is obtained due to clutter filtering, and a bias compared to the theoretical estimates is also noticeable. For vector Doppler, low flow zones are transformed into seemingly high flow zones because of the clutter filter.

external carotid, however at the expense of more prominent clutter filtering artifacts for lower velocities. Although the range of velocities measurable was more limited. For VD, both setups allowed distinguishing the swirling flow depicted in frame 5.

The influence of clutter filtering is shown further in fig. 7.7. The top row of images was obtained without clutter filtering, while the bottom row contains images from using the 5th order FIR filter. Results are shown for the systolic acceleration phase of frame 1, imaged with a

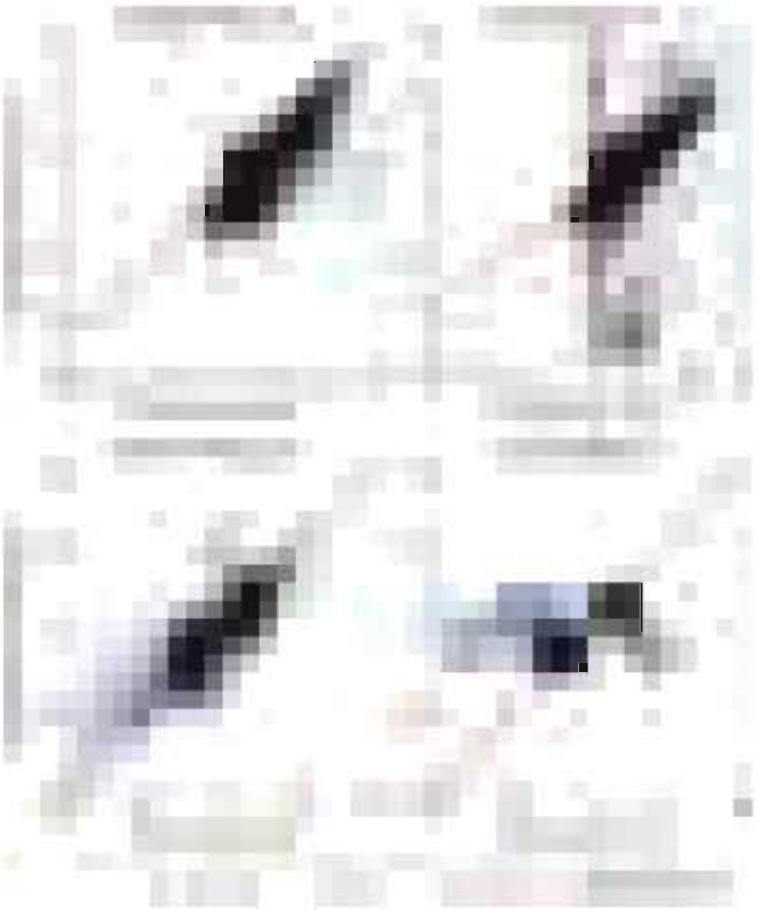

Figure 7.8: Scatter plots showing the relation between reference (CFD) and estimated velocities (ST/VD) for the 2 kHz case. Velocities at all spatial positions in the carotid bifurcation model and throughout the cardiac cycle are included. Three different sets of velocities have been indicated with different colors/symbols: 1) velocities below the clutter filter pass band v_c (red/stars), 2) velocities above the VD Nyquist range v_N (blue/diamond), and 3) velocities in the *normal range* above v_c and below v_N. Regression analysis was performed on the velocities in the normal range, and the resulting regression line has been added to each plot given as a dashed red line.

PRF of 4 kHz. Comparing the top and bottom panels, the low velocity regions present in the carotid bifurcation are clearly disturbed by the clutter filter for both methods, however VD estimates suffer most dramatically.

The performance of ST and VD can be further quantitatively analyzed in the scatter plots shown in fig. 7.8 for the 2kHz setup. Velocities at all spatial positions and throughout the cardiac cycle have been included, and three different sets of axial and corresponding lateral velocity components have been indicated with different colors and symbols: 1) axial velocities below the clutter filter pass band region, 2) axial velocities above the VD Nyquist range, and 3) axial velocities in the clutter filter pass band and below the Nyquist limit for VD, termed further as the normal range of velocities. As can be observed in the scatter plots, ST overall seems to be a more robust lateral velocity estimator with less spurious errors as observed for VD. It can also be observed that ST is able to track velocities beyond the Nyquist range, where the VD lateral velocity estimates are significantly overestimated with a wide spread. On the other hand, considering velocities in the normal range results indicate VD to be a more accurate axial estimator.

To quantify the performance observed in the scatter plots, linear regression analysis was performed on the normal range of velocities. Outliers more than 3 standard deviations from the mean were removed from the data set. Results are shown in Table 7.2 for both the 2 and 4kHz setup, where the parameters $\overline{m}$ (mean), β (slope), σ (standard

TABLE 7.2: Linear regression analysis for the complete cardiac cycle of v_x and v_z as estimated by speckle tracking and vector Doppler compared to the CFD reference. Data were analyzed based on the normal range of velocities, i.e. not influenced by clutter filtering and within the Nyquist range, and is reported for both imaging setups (PRF=2 and 4kHz).

	Speckle Tracking				**Vector Doppler**			
	2 kHz		4 kHz		2 kHz		4 kHz	
	v_x	v_z	v_x	v_z	v_x	v_z	v_x	v_z
$\overline{m}$ (cm/s)	3.9	-0.33	8.9	-1.1	6.3	-0.15	7.3	-0.17
σ (cm/s)	4.1	2.9	7.1	5.0	6.3	1.6	7.3	1.9
β $(slope)$	0.84	0.98	0.61	0.86	0.71	1.05	0.76	1.06
$R^2(gof)$	0.82	0.84	0.60	0.80	0.53	0.95	0.58	0.97

deviation), and R^2 (goodness-of-fit) are reported. The resulting regression line has been added in each scatter plot as a dashed red line. The quantitative results support VD as being a more accurate axial estimator, with approximatively half the standard deviation compared to ST and a better linear fit to the range of velocities present. Further, ST does a better job estimating the lateral component with an overall standard deviation of 4.1 cm/s compared to 6.3 cm/s for VD.

The distribution of errors over the cardiac cycle is shown in fig. 7.9, where the mean absolute deviation has been calculated for velocities in the normal range (outliers removed) individually for each frame. The deviations were normalized by the maximum axial and lateral velocity for each frame. For both methods the normalized deviations gradually increase in diastole where the velocities decrease. ST performance is severely degraded for 4kHz setup for both velocity components. Considering the 2kHz setup, ST is the better lateral velocity estimator while having about twice the mean deviation for the axial component com-

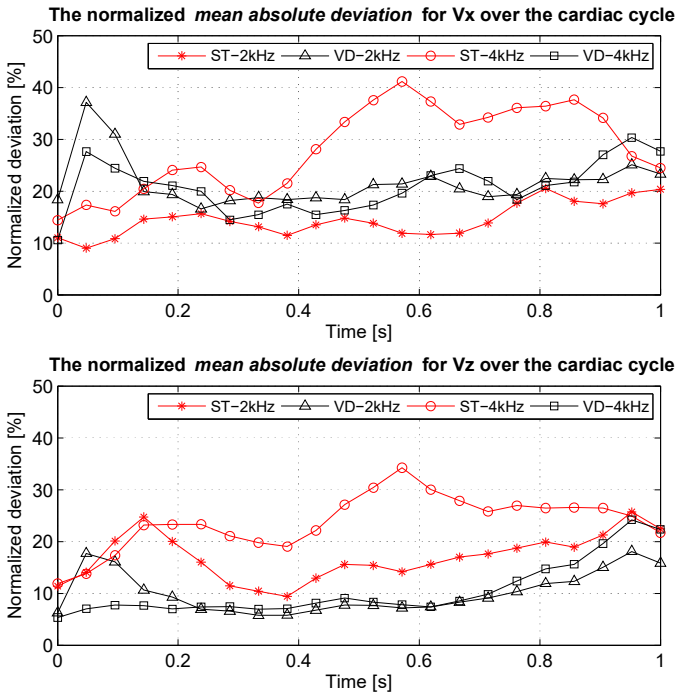

Figure 7.9: The mean absolute deviation of v_x / v_z estimates compared to the CFD reference velocities, calculated individually for each frame throughout the cardiac cycle and for both imaging setups (PRF=2 and 4 kHz). The deviation has been normalized to the maximum axial and lateral velocity component for each frame.

pared to VD. By averaging the absolute deviations over the cardiac cycle, we obtained deviations of 15% and 17% for ST (2kHz) and 21% and 10% for VD (4kHz), for the lateral and axial velocity component respectively.

7.4 Discussion

The development of multi-dimensional flow velocity estimators has been an active field of research for over 30 years [84]. Such methods may potentially offer new information related to vascular disease and more accurate cardiovascular imaging tools compared to conventional 1-D Doppler-based methods. The applicability of ST and VD techniques has previously been evaluated through simplified simulations, for *in vitro* flow rigs, and *in vivo* in healthy vessels. Bohs et al [44] demonstrated the ensemble tracking method based on parallel receive beamforming with promising results. Recently, Udesen et al [127] evaluated speckle tracking based on plane wave emissions in a healthy carotid artery, achieving good agreement for estimated volume flow curves compared to those obtained with MR techniques. A comprehensive overview of early vector Doppler validations can be found in Dunmire [84], where it is reported that reference velocity measurements used to validate VD have been limited to PW-Doppler, existing volumetric flow devices or expected values listed in literature. In [120], a novel rotating flow phantom was developed to evaluate and compare compound and crossed-beam VD, demonstrating a good potential for resolving the 2D velocity vector. Recently, Hansen et al [128] evaluated the related transverse oscillation method by comparing estimated stroke volume with MR phase contrast angiography. Further, Pastorelli et al [121] demonstrated their real-time VD system on human carotid arteries, reporting the lack of true reference as a challenge in the validation process.

To our knowledge, none of the 2D velocity estimators introduced has yet reached clinical use. Reasons for this may include a lack of robustness and accuracy for complex flow patterns in pathological cases. In this respect tools are needed for developing and validating experimental methods towards a ground truth for clinically relevant flow. In this work, a simulation framework for this purpose, coupling the output of computational fluid dynamics with an ultrasound simulation model, was used to study speckle tracking and vector Doppler for

multi-dimensional blood velocity estimation in a stenosed carotid bifurcation model. One of the current limitations of this simulation environment is the absence of vessel wall movement. A useful extension of the model will therefore be to incorporate fluid-structure interactions (FSI), coupling mechanical and fluid dynamic simulation tools. A simplified approach to this concept was recently described by Balocco et al [62].

Both ST and VD have intrinsic limitations for use in blood velocity vector estimation. The main challenges for ST are related to the acquisition of high frame rate speckle images, and the rapid speckle decorrelation due to flow gradients [129] degrading tracking performance. In this work, we used an interleaved acquisition mode, effectively acquiring sub image ensembles for tracking at a frame rate equal to the PRF. A more flexible setup is achieved by tracking within a group of parallel receive beams [44], acquiring instantaneous snapshots of the blood speckle for every emission. Also, by using plane wave emissions (PWE) [127], a high frame rate for tracking and larger search regions can be achieved on the expense of reduced resolution and penetration. On the other hand, VD is limited by aliasing as conventional Doppler, determined by the PRF and angle of flow relative to either transmit-receive direction. Further, the accuracy of the estimated lateral velocity component is determined by the angle between the transmit and receive beams, and a trade-off is therefore given between accuracy and scan region width and depth due to the finite transducer footprint.

In this work a practical approach was taken when selecting the parameter setup for ST and VD, requiring a scan sector of 2x4 cm (WxD) and an overall frame rate of 20 Hz to be achieved. This restricted the receive F-number for VD, and beam sampling and ensemble size for both methods. For ST, the search region size was limited laterally to the interleave group width, and 2 parallel receive beams were required to achieve the maximum tracking velocity of 62 cm/s for the 4kHz PRF setup. A higher number of parallel receive beams could be used to increase this limit, but is currently associated with severe image artifacts [44, 130] degrading tracking performance. The ST approach can be regarded as an extension of the wide-band 1D cross-correlation technique, and its performance is therefore expected to improve for shorter pulses and higher frequencies. We chose to work at a frequency often required for satisfactory carotid imaging in patients, with a small

compromise in pulse length to achieve a deeper penetration. For VD, the 12^o transmit-receive angles could only be achieved for a 2x4 cm scan by reducing receive apertures compared to a conventional Doppler setup, degrading both resolution and penetration. Further, the VD sector width rapidly diminish for increased depths, and it would not be possible to move the region of interest within a larger B-mode scan plane without manually moving the probe. Finally, a 4cm scan depth could be achieved by reducing the angle from a depth of 2.4 cm, deteriorating the velocity estimates at these larger depths. However, a detailed study of this phenomenon is considered beyond the scope of this work. Overall, the values used for ST and VD were in the range used in previous investigations, however, future work is needed to establish whether more accurate results might be achieved for a different setup.

Results from the stationary flow simulations showed that VD estimates of the axial velocity were quite robust with regards to standard deviation compared to ST for all parameters varied, while the lateral velocity estimates were comparable. With regards to bias, overall ST overestimated and VD underestimated the velocities in the tube with similar magnitudes for our setup. However, the lateral ST estimates were more influenced for variations of in-plane and out-of-plane angles, most likely due to an increased speckle decorrelation. VD estimates were more resistant to high thermal noise levels. As noise was added during post processing it is not established how the different sample volumes used for the two methods influence results. However, the larger sample volumes used for VD are expected to further increase the robustness of VD compared to ST in this respect. Overall, the results of the stationary flow phantom simulations were in the range of previous experimental studies [43, 120].

For the carotid bifurcation simulations, both ST and VD were able to portray complex swirling flow patterns present in parts of the cardiac cycle. This is information that previously was shown to not be readily available from color flow images generated from the same model [110]. For ST, the 2kHz setup proved beneficial for tracking accuracy of low velocities due to the shorter speckle displacements and smaller kernel regions present for the 4kHz setup. In other cases, a higher PRF may be beneficial for tracking high velocity and complex blood movement leading to a rapid speckle decorrelation. This can in general for instance take place for jet flow, but can also be observed in our carotid

model when investigating the external carotid artery during systole. Multi-lag tracking might be useful in this respect to increase overall accuracy. One should also note that a higher PRF is applicable without altering the kernel or search region when using an increased amount of parallel receive beamforming. This is for instance the case for the plane wave emission method [127]. However, for high PRFs the quality of the low velocity estimates will deteriorate due to the coarser velocity resolution given. The optimal choice of PRF for speckle tracking is not straightforward and should be given attention in further work. For VD, the velocity range measurable is a trade-off between aliasing and clutter filter artifacts. However, in both the 2 and 4kHz setup the swirling flow near the stenosis was portrayed.

The linear regression and temporal deviation analysis showed that within the normal range of velocities (in the clutter filter pass band and below the Nyquist limit), VD was the more robust axial estimator and ST a more robust lateral velocity estimator. It could also be observed that VD suffered more from spurious errors for the lateral component. VD was further severely hampered by aliasing in parts of the cardiac cycle, as is expected in Doppler imaging for a 2-4 kHz setup in this application. Errors due to aliasing are more complex for VD compared to 1-D velocity estimation. In particular, when only one receive signal aliases, a large difference in Doppler frequencies will occur leading to a large and dominant lateral component. This may explain the aliasing artifacts becoming more dominant for the 4kHz results in the external carotid artery. In this respect ST was more consistent, tracking velocities well above the Nyquist limit, and degrading more robustly when meeting the tracking limit. As conventional CFI can be generated from the ST data acquisition, it may be possible to utilize this combined information to increase the robustness for ST.

Clutter filtering is a major challenge in 2D velocity estimation, due to the fact that the Doppler signal is centered at zero frequency and therefore attenuated for flow perpendicular to the transmit-receive beam direction. As this may often be the case for flow in arteries and for swirling flow patterns, important information may be removed in a slow-time filtering process. Although no clutter was present in the vessel lumen, the effect of filtering on the flow signal was investigated assuming no clutter leakage. As shown in fig. 7.7, the effect can be quite disturbing for both methods, however, most dramatic effects were seen

for VD. For ST reasonable tracking results may be achieved as long as there is sufficient signal remaining after filtering. This can be important when parts of the flow signal are in the transition region of the clutter filter. This transition region width can be significant, extending about 10% of the Nyquist range in our case. For VD, time-variant filters such as polynomial regression filters [41] could be employed, decreasing the filter transition region width and avoiding the loss of samples for averaging due to filter initialization. This approach may therefore decrease the variance of VD estimates. However, to ensure fair comparisons with regards to post processing effects the same filter and averaging was used for both methods in this work.

Implementation wise, we believe both VD and ST can be implemented on todays high end scanners. For VD, two parallel receive beamformers will be required and about twice the processing is needed compared to conventional CFI. For ST, conventional acquisition can be used for vascular imaging where interleaving is possible. Further, the SAD procedure is included as part of the extended multi-media instruction sets in modern CPUs, boosting performance for real-time operation.

Considering estimator performance, both methods may be suitable for 2D flow velocity estimation for clinically relevant flow, with VD as the superior axial velocity estimator. However, also considering the practical scanning limitations present for VD and the ability of ST to consistently portray a higher dynamic range of velocities, ST may be a more consistent and practical approach. Future work will focus on the refinement and evaluation of ST for *in vivo* data recordings and a CFD model generated from patient data with a significant carotid stenosis.

7.5 Conclusion

By coupling the output of computational fluid dynamics with an ultrasound simulation model, the performance of experimental blood velocity estimators can be evaluated for complex and clinically relevant flow patterns. Comparing speckle tracking and crossed-beam vector-Doppler, both methods were able to resolve the axial and lateral velocity components for complex flow in a stenosed carotid bifurcation. Results overall demonstrated that VD was the superior axial velocity estimator, while ST was the better lateral velocity estimator. Overall, considering also practical limitations present for VD with regards to

scanning flexibility and aliasing, ST may provide a more consistent and practical approach to 2D velocity estimation in the carotid bifurcation. However, it is important to note that our conclusions are based on simulations and future work should entail in-vitro and in-vivo validation of these results.

CHAPTER 8

2D flow imaging in the carotid bifurcation using a combined speckle tracking and phase-shift estimator, based on ultrasound simulations and in-vivo analysis

In the previous chapter, we demonstrated that ST is the better lateral flow velocity estimator, and VD the better axial flow velocity estimator. Therefore, we present in this chapter a 2D blood velocity imaging method, combining speckle tracking (ST) and phase-shift estimation (PE) to respectively measure lateral (v_x) and axial (v_z) velocities. This may result in a clinically more robust 2D flow visualization technique. Estimator properties are assessed in a carotid bifurcation using our CFD-based ultrasound simulations, allowing validation towards a ground truth. Simulation results are further supported with in-vivo data of a carotid artery of a healthy volunteer.

ST and PE estimates are combined as: 1) v_x from ST and v_z from PE, 2) v_x from ST and v_z from PE with aliasing correction based on ST, 3) v_z from PE and only lateral speckle tracking to obtain v_x. Linear regression analysis shows that using PE to estimate axial velocities results

in a more robust method than applying only ST. Aliasing correction based on ST improves results but also introduces spurious artifacts. A marginal decrease in performance is observed when only tracking laterally.

This chapter is based on "*Two-dimensional flow imaging in the carotid bifurcation using a combined speckle tracking and phase-shift estimator: a study based on ultrasound simulations and in-vivo analysis*", as submitted for publication.

8.1 Introduction

Ultrasonic blood flow imaging is commonly applied in clinical practice, although still mainly limited to 1D Doppler-related techniques like Pulsed Wave Doppler (PWD) and Color Flow Imaging (CFI). Multidimensional flow imaging is however desirable since complex flow fields are present throughout the arterial system in bends, bifurcations and especially in diseased arteries showing obstructive plaques. Better assessment of the flow field and its associated hemodynamic parameters would potentially improve cardiovascular risk assessment and increase the understanding of the origin and development of cardiovascular disease. In particular, clinically relevant hemodynamic parameters like wall shear stress, well known as a stimulus of endothelial function and involved in atherosclerosis [6], could be derived from multidimensional flow measurements.

Extensive research has been done on 2D flow imaging, mainly focusing on two research lines: speckle tracking (ST) [115] and crossed-beam vector Doppler (VD) [46]. The former relies on tracking the movement of speckle patterns, created by the interference of the ultrasonic waves backscattered by the red blood cells. The latter is the natural extension of 1D Doppler techniques, insonifying the blood vessel in two different directions, allowing construction of the velocity vector through triangulation. The performance of these estimators has been analyzed for analytically described flow patterns as well as in-vitro flow phantoms (e.g. [44] for ST and [120] for VD). Both methods have also been preliminary tested in healthy in-vivo conditions (e.g. [127] for ST and [121] for VD). However, to our knowledge these methods have yet to reach clinical practice, perhaps owing to a lack of robustness or practical applicability.

To investigate the accuracy and applicability of these techniques, accurate knowledge on the actually imaged flow field is indispensable. For this purpose, we developed an ultrasound (US) simulation environment based on computational fluid dynamics (CFD), which allows solving the Navier-Stokes equations and thus flow fields in complex geometries. The phantom for the ultrasound simulations (Field II) is built from random point scatterers representing the red blood cells, which are propagated for each emitted ultrasound beam according to the CFD velocity field. In [110, 131], we described and validated this CFD-based ultrasound simulation environment in detail. We further used our multiphysics environment to compare the estimator properties of speckle tracking and vector Doppler [132]. The ST-estimates were obtained by applying a sum-absolute-difference algorithm on the envelope data. Crossed-beam VD was implemented using one linear array transducer with a central transmit aperture and two sliding receive apertures to keep a fixed angle in depth. For each receive direction, the phase-shift was estimated with the autocorrelation method [36], as commonly applied in CFI. We demonstrated ST to be the better lateral (perpendicular to US beam) velocity estimator and crossed-beam VD the better axial (parallel to US beam) estimator, based on a statistical analysis of Poiseuille flow in a tube and velocity estimations in a carotid bifurcation model [132].

In this paper, we present a natural extension of this work by combining speckle tracking and phase-shift estimation in one 2D flow estimator. A single scan procedure similar to conventional CFI-scanning is applied, and the received US-signals are processed with an ST-algorithm for the lateral flow component and with a phase-shift estimation (PE) method (autocorrelation technique) for the axial flow. In a first step, we analyze the combined estimator in a carotid bifurcation using our CFD-based ultrasound simulation environment, allowing direct comparison of the estimated flow with the reference CFD flow field. Finally, in-vivo data measured in the carotid bifurcation of a healthy volunteer will be analyzed using our different estimator setups to validate and support simulation results.

8.2 METHODS

8.2.1 Data acquisition

Both for the simulations and the in-vivo data, we maximized the frame rate by using a scan acquisition scheme typically used in conventional color flow imaging (CFI), called beam interleaving [100]. This technique is used when the chosen pulse repetition frequency (PRF) of the emitted ultrasound beams is lower than the theoretical maximum (PRF_{max}), as determined by the imaging depth. In case of shallow depths like in peripheral vascular imaging (e.g. carotid artery), the Doppler PRF is typically much lower than the maximum available PRF_{max}, so that sufficient sensitivity is obtained for the expected range of blood velocities.

Interleaving refers to the division of the image into lateral subregions or interleave groups (IG), where the neighbouring beams within the interleave group are acquired at a rate of PRF_{max} and the frame rate of the interleave group corresponds to the slow-time Doppler PRF. The number of beams in an interleave group, i.e. the interleave group size (IGS), is given by:

$$IGS = \left\lfloor \frac{PRF_{max}}{PRF} \right\rfloor \cdot PRB \tag{8.1}$$

where PRB (Parallel Receive Beams) is the number of beams received in parallel for each beam emission, as commonly applied in high-end ultrasound systems.

8.2.2 2D velocity estimation

8.2.2.a Phase-shift estimation (PE)

The autocorrelation method for phase-shift estimation was applied, as proposed for ultrasound applications by Kasai et al [36]:

$$v_z = \frac{cPRF}{4\pi f_0} atan\left(\frac{Im(\hat{R}(1))}{Re(\hat{R}(1))}\right), \tag{8.2}$$

with v_z the estimated axial velocity, c the ultrasound wave speed in blood (1540 m/s), PRF the pulse repetition frequency of the emitted ultrasound beams, f_0 the center frequency of the ultrasound pulse and $\hat{R}(1)$ the estimated autocorrelation function at lag 1. The $\hat{R}(1)$ estimate was averaged over an ensemble of slow-time samples. The factor $\frac{cPRF}{4f_0}$

is the Nyquist velocity limit of the autocorrelation method. A velocity higher than the Nyquist velocity will alias, i.e. wrap around the velocity scale and show with incorrect magnitude and direction.

8.2.2.b Speckle Tracking (ST)

Speckle tracking is applied by identifying a kernel region in a first image acquisition and searching for a best match inside a search region of a later acquisition, as illustrated in fig. 1-B. In this work, the match between the kernel inside the search region was determined using the sum-of-absolute differences (SAD) algorithm, given by:

$$e(\alpha, \beta, n) = \sum_{i=1}^{l} \sum_{j=1}^{k} |X_0(i, j) - X_n(i + \alpha, j + \beta)| \tag{8.3}$$

with e the SAD coefficient, l and k the lateral and axial dimension of the kernel in beam and range samples, (α,β) defining a kernel displacement in the lateral and axial direction, and n referring to the lag between the acquisitions used for tracking. Using the kernel displacement corresponding to the minimal SAD-value (α_m,β_m), the velocity magnitude and angle can be estimated:

$$V_n = \frac{\sqrt{(\alpha_m \Delta x)^2 + (\beta_m \Delta z)^2}}{nT}, \Theta_n = atan \frac{\alpha_m \Delta x}{\beta_m \Delta z}, \tag{8.4}$$

with Δx and Δz the lateral and axial sampling distances and T the time between subsequent acquisitions. The procedure was performed for individual lags (n=1) in a packet of speckle images and the median of these estimates was calculated in order to minimize the effect of spurious tracking errors. Since the velocity resolution in speckle tracking is at first determined by the image grid (see further), we interpolated the SAD matrix (parabolic fitting, [126]) to improve the accuracy. In order for this to work, we should have a starting image which is sufficiently sampled. Hence, we interpolated the image in both the axial (1x) and lateral (3x) directions.

Speckle tracking imposes restrictions on the maximal and minimal velocity which can be measured. Concerning the lateral tracking, the maximal trackable velocity $V_{max,x}$ scales with PRF according to:

$$V_{max,x} = \left\lfloor \frac{S_x - K_x}{2} \right\rfloor \cdot \Delta x \cdot PRF \tag{8.5}$$

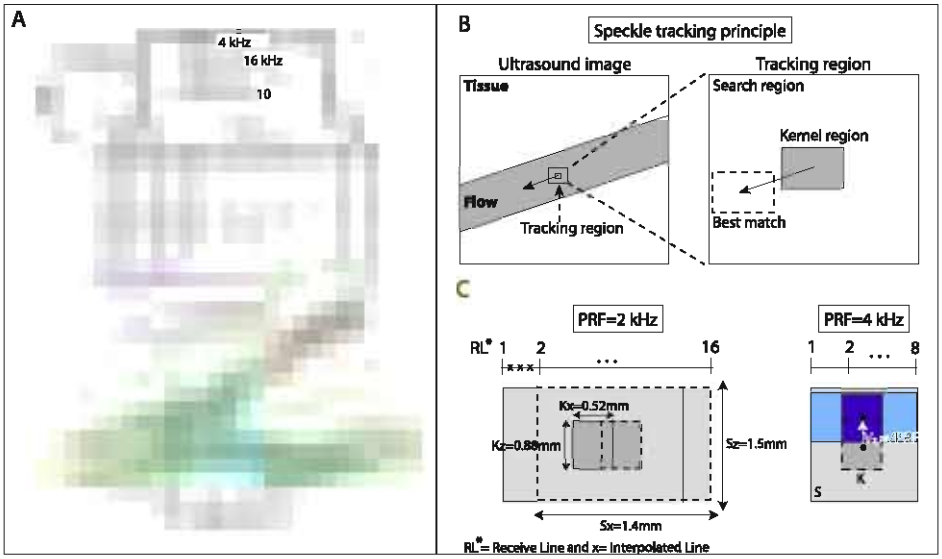

FIGURE 8.1: **Panel A**: Beam interleaved scansequencing of the patient specific CFD-based carotid phantom, illustrated for PRF=4kHz. **Panel B**: Speckle tracking principle: the region of interest is divided into kernels and the optimal match of a kernel in a surrounding search region is estimated over an ensemble of 10 speckle images using an SAD-algorithm. **Panel C**. The applied tracking setups for PRF=2 and 4kHz. Using a maximal trackable lateral velocity of 85 cm/s, 2 kernels fitted in the 2kHz region and 1 kernel in the 4 kHz region. The 2kHz region consisted of 16 receive lines and the power data were further interpolated to fit in 3 lines in between the original beams (indicated with x). The 4kHz region consisted of 8 lines and the same interpolation was applied. The 4kHz setup also shows the principle of 'simplified tracking': the auto-correlation estimate $v_{z,PE}$ is used to translate the kernel a distance Δz and only lateral motion (v_x) is estimated by ST.

S_x is the lateral search region size, K_x the lateral kernel size and Δx the lateral sampling distance after envelope interpolation. In case of beam interleaved acquisition, the maximum size of S_x is given by the interleave group width as determined by the image depth (PRF_{max}), the slow-time PRF, and the receive beam overlap. The interleave groupsize is the limiting factor for S_x since speckle decorrelation occurs across interleave groups, making it difficult to perform speckle tracking in a search region larger than the IGS. The minimal trackable lateral velocity or resolution velocity $V_{res,x}$ scales with PRF as follows:

$$V_{res,x} = \frac{\Delta x \cdot PRF}{n} \tag{8.6}$$

with n the lag between the acquisitions used for tracking (n>1 is referred to as multilag tracking). Without substantial interpolation, $V_{res,x}$

is coarse compared to the expected range of velocities in clinical applications. We illustrate this with a theoretical example. When tracking one kernel (width of 4 beams) in an interleave region given according to a PRF of 4 kHz, PRF_{max} of 16 kHz, Δx of 0.14 mm, and PRB of 2, the maximal lateral velocity V_{max} is 1.12 m/s and the minimal lateral velocity $V_{res,x}$ is 0.56 m/s. This can for instance be compared to the expected velocities in the common carotid, ranging from 0.1-1 m/s in healthy subjects. Concerning axial tracking, equation 8.6 is equally valid but using the axial resolution distance. However, the maximal axial velocity can be defined with more flexibility compared to the maximal lateral velocity restricted by equation 8.5, since the interleaving concept is only a restricting factor when tracking in the lateral dimension.

In order to reduce the variance of the tracking estimates, it is desirable to do spatial averaging. This however implies that the tracking estimates should lie in close vicinity of each other, in order to retain sufficient spatial resolution. When using a low PRF, this means several tracking estimates are needed for each interleave region. The number of tracking estimates that fit inside an interleave group is given by:

$$N_K = \left\lfloor \frac{IGS - 2 \cdot \left\lfloor \frac{V_{max,x}}{V_{res,x}} \right\rfloor - K_x + 2}{K_x - overlap} + 1 \right\rfloor \tag{8.7}$$

with N_K the number of kernels in the interleave group and $overlap$ the number of overlapping beams for each kernel (with $1 \leq overlap \leq K_x - 1$).

8.2.2.c *Combining ST and PE*

The same scanning procedure was applied for ST and PE, and two different imaging setups were investigated, using a PRF of 2 kHz and 4 kHz respectively. Further, a PRF_{max} of 16 kHz and a transducer centre frequency of 5 MHz was applied, two receive lines were acquired in parallel, and a packet size of 10 was acquired for clutter filtering and averaging the estimated flow velocities. Using this setup, the autocorrelation method resulted in a maximal measurable velocity of 15 cm/s and 31 cm/s for respectively 2 and 4 kHz. For speckle tracking, an interleave groupsize of 16 and 8 beams was obtained for respectively 2 and 4 kHz. The lateral beam density was close to the Rayleigh criterion for both setups, and resulted in 9 and 18 interleave groups for 2 and 4 kHz respectively, and an overall frame rate of 22 frames per second (fps).

A kernel size of 0.88 x 0.52 mm (lateral x axial) was chosen. For both setups, we chose a maximal trackable velocity of 85 cm/s and 65 cm/s in respectively the lateral and axial direction, a trade-off between the acquisition/averaging setup and the possible maximum velocity. This choice resulted in a search region of 1.36 x 1.53 mm for 2 kHz and 0.94 x 1.14 mm for 4 kHz (both smaller than IGS, cfr. fig. 1-C). According to equation 8.7, two kernels were fitted in the 2 kHz interleave region and one kernel in the 4 kHz interleave region. After envelope interpolation, the velocity resolution for ST was 7 cm/s and 14 cm/s laterally for respectively 2 and 4 kHz. In the axial direction, the resolution velocity was 3 cm/s (2 kHz) and 6 cm/s (4 kHz).

Three different possibilities of combining the lateral velocity v_x from ST ($v_{x,ST}$) and axial velocity v_z from PE ($v_{z,PE}$) were investigated:
(1) $v_{x,ST}$ from 2D speckle tracking and $v_{z,PE}$ are combined by replacing the axial estimate of ST by the phase-shift estimate, further labeled as *ST-PE*,
(2) $v_{x,ST}$ from 2D speckle tracking and $v_{z,PE}$ are combined but $v_{z,PE}$ is corrected for aliasing artifacts based on $v_{z,ST}$:

$$\angle \hat{R}(1)_{corrected} = \angle \hat{R}(1) + sign(v_{z,ST}) \cdot \left\lfloor |v_{z,ST}| / v_{Nyquist} \right\rfloor \cdot 2\pi \quad (8.8)$$

with $\angle \hat{R}(1)$ the angle of the estimated autocorrelation function at lag 1 and $v_{Nyquist}$ the Nyquist velocity limit. This method is further labeled as *ST-PE: unwrapped*,
(3) a simplified speckle tracking where the axial kernel displacement corresponds to $v_{z,PE}$ while the search region is confined to lateral tracking (1D-ST) only. This method is further labeled *ST-simplified* and is also illustrated in fig. 1-C for the 4 kHz setup.

The variance of the velocity estimates was reduced through spatial averaging: (1) PE-estimates were averaged in a region of 3 beams and 2 pulselengths, (2) estimates from ST and the combined ST-PE methods were median filtered in a 5x3 kernel region.

8.2.2.d Performance analysis

A linear regression analysis was performed, taking into account all spatial and temporal velocity measurements below the Nyquist limit and above the clutter filter cut-off velocity, further called the normal range of velocities. The accuracy of the estimated velocity vector field was

further quantified with a temporal analysis of the mean absolute deviation $|V_{US} - V_{CFD}|$ of each velocity component for each frame. To directly compare the performance of both imaging setups, the 2 kHz estimates (2 kernels per IG) were interpolated to the 4 kHz kernel positions (1 kernel per IG). Estimator performance was also investigated using two different signal-to-noise ratios (SNR) during postprocessing. A default SNR of 20 dB was applied for all simulations. The effect of high noise levels was investigated by applying an SNR of 5 dB. If no noise level is especially mentioned in the text or figures, the 20 dB SNR was applied.

8.2.3 CFD-based ultrasound simulations

8.2.3.a Ultrasound simulations

The backscattered ultrasound signals were simulated with the Field II software [17, 18], which is based on the spatial impulse response estimation as described by Tupholme [94] and Stephanishen [95]. In this approach, blood is modeled as a collection of random point scatterers with normally distributed amplitude. The density of the scatterers is related to the imaging system bandwidth, with approximately 10 scatterers per resolution cell assuring Gaussian distributed RF-signals. To mimic realistic scatterer displacement in complex blood flow conditions, numerically computed flow fields are necessary to propagate the scatterers correctly. In [110], we presented a method which couples the output of computational fluid dynamics (CFD) with the Field II software. For each emitted beam, the scatterer position is updated based on the CFD-velocity fields. In this approach, spatial interpolation is necessary to interpolate the CFD velocity vectors from the irregular CFD grid to the random scatterers. Further, temporal interpolation is performed to match the CFD and ultrasound timescales (5 ms versus $62.7\mu s$ for a PRF of 16 kHz). We refer to [110] for further details on the CFD-US coupling procedure.

2x4 cm scans were simulated with a 192 element linear array transducer of 5 MHz centre frequency. Each transducer element was divided into 4 mathematical elements which ensured that every scatterer was imaged in the far-field of each individual element. A fixed transmit focus of 2 cm in depth was chosen, with an F-number of 2.5 on transmit. Dynamic focusing and an expanding aperture were used to retain an F-number of 1.4 on receive. Rectangular and cosine tapered apodization were used on transmit and receive respectively. A sinusoidal excitation pulse of 2.5 pulse periods was applied. No frequency dependent

attenuation was included in the simulations. For further details on the imaging setup, we refer to the ST-setup mentioned in [132]. Although the tissue surrounding the blood vessel was not simulated, the effect of clutter filtering on the blood signal was included by assuming all clutter is attenuated by the filter. A second order polynomial regression filter was applied prior to PE (cut-off is 1.94 and 3.88 cm/s for respectively 2 and 4 kHz) and a fourth order FIR filter was used prior to ST (cut-off is 2.53 and 5.05 cm/s for respectively 2 and 4 kHz). The time-invariant FIR filter was used for ST to identically filter subsequently acquired speckle images.

8.2.3.b CFD

A carotid artery bifurcation was reconstructed from MRI-scans of a healthy volunteer (Mimics, Leuven, Belgium), in which we artificially added an eccentric plaque in the internal branch (cfr. fig. 8.1-A). The commercial CFD-software Fluent 6.2 was used to numerically solve the Navier-Stokes equations with a finite volume method. The applied boundary conditions were a velocity profile at the common carotid, measured with PW-Doppler in a healthy volunteer, and a 45-55% externa/interna flow division. Incompressible Newtonian blood behaviour was assumed with a viscosity of 3.5 mPas and a density of 1050 kg/m^3. For further details on the CFD-setup and according phantom construction, we refer to [110].

8.2.4 In-vivo data

Raw IQ-data were recorded during examination of the carotid artery of a healthy volunteer using a 7L probe for vascular imaging and a GE Vingmed Vivid 7 ultrasound system (GE Vingmed Ultrasound, Horten, Norway). Color flow images were recorded with an imaging setup equal to the simulations (both 2 and 4 kHz). Hence, the in-vivo ST and PE estimates were obtained with the same processing as the simulations. The 2D flow estimates were superimposed on color flow images, and the flow angle was investigated in segments of the carotid artery where flow is expected to be aligned with the geometry. For this purpose, the mean and standard deviation (std) of the flow angle was analyzed in the common carotid in-vivo (the first four lateral lines) and in the external carotid for the simulations (the last four lateral lines). The external carotid was chosen for the simulations since swirling flow was present in the common carotid for several frames.

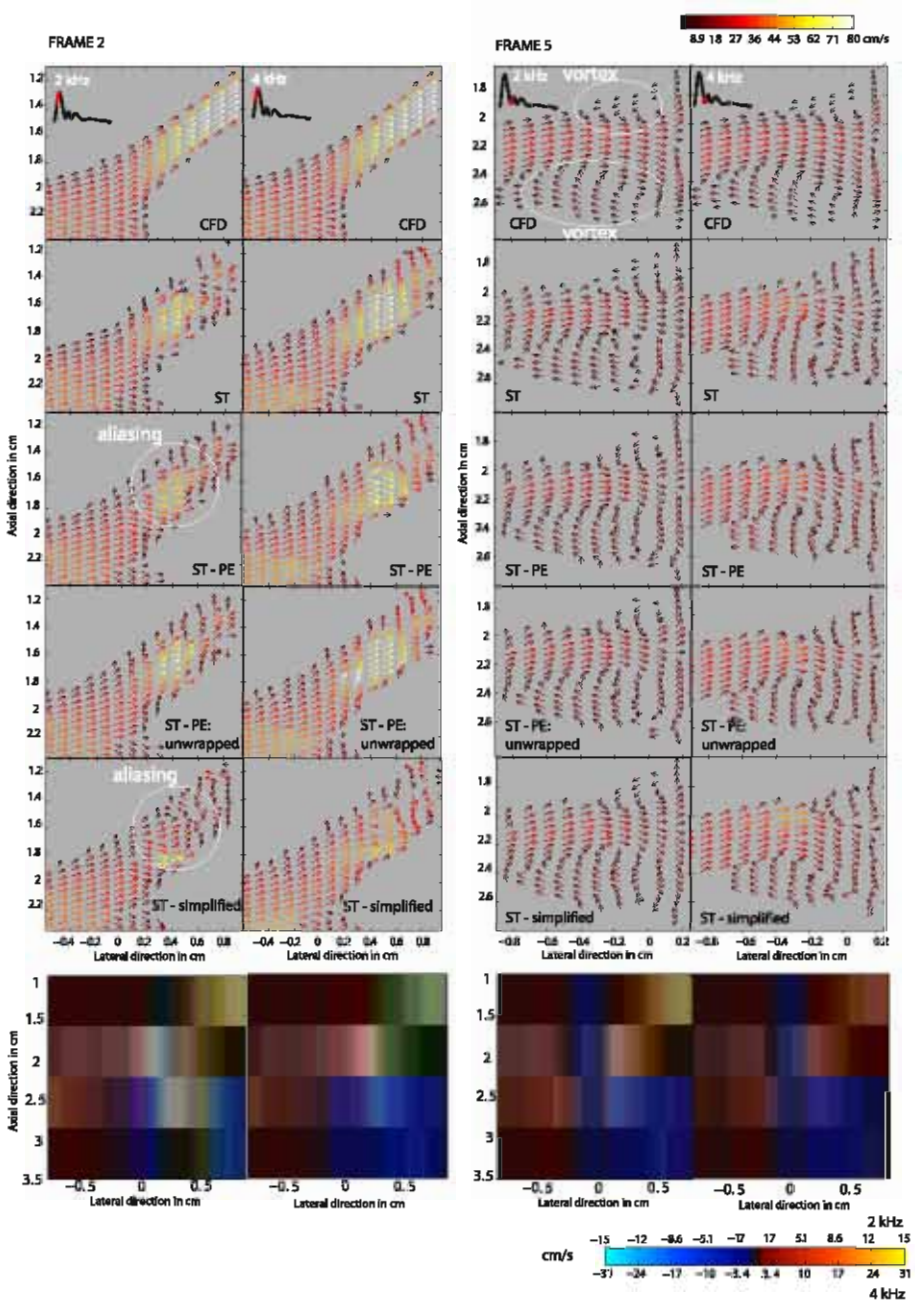

FIGURE 8.2: Comparison of the four 2D flow estimators and the reference CFD flow field for frame 2 (systole) and frame 5 (diastole). A setup with PRF of 2 and 4kHz is shown. The lower panels show the color flow images corresponding to the phase shift estimates (SNR of 20 dB).

8.3 RESULTS

8.3.1 CFD-based ultrasound simulations

The performance of ST and the three ST-PE combination techniques was compared to the reference CFD flow field with vector plots of the

complete cardiac cycle. Note that the comparison is based on dynamic CFD vector fields, taking into account the location and timing of the fired ultrasound beams in order to provide correct reference values [110]. Two important phases of the cardiac cycle are shown in fig. 8.2: systolic acceleration (frame 2) and the onset of diastole (frame 5), as indicated by the red part on the flow curve. Frame 2 shows zoomed-in plots of the external carotid artery, the location where the highest velocities of the complete cardiac cycle prevail. A higher PRF demonstrated reduced aliasing and improved ST performance. Both ST and the unwrapped version of ST-PE show a good qualitative agreement with the reference CFD flow field. Integrating the PE-estimate without unwrapping (*ST-PE* and *ST-simplified*) shows obvious aliasing artifacts for both PRF's. Frame 5 shows vector plots zoomed in on the common carotid during the onset of diastole, showing a large vortex in the internal bulb and a smaller one on the opposite side. Both the 2 and 4 kHz imaging setups are able to capture the large zone of swirling flow. Low velocities dominate during this stage and hence the influence of the clutter filter becomes important. The 4 kHz setup estimates

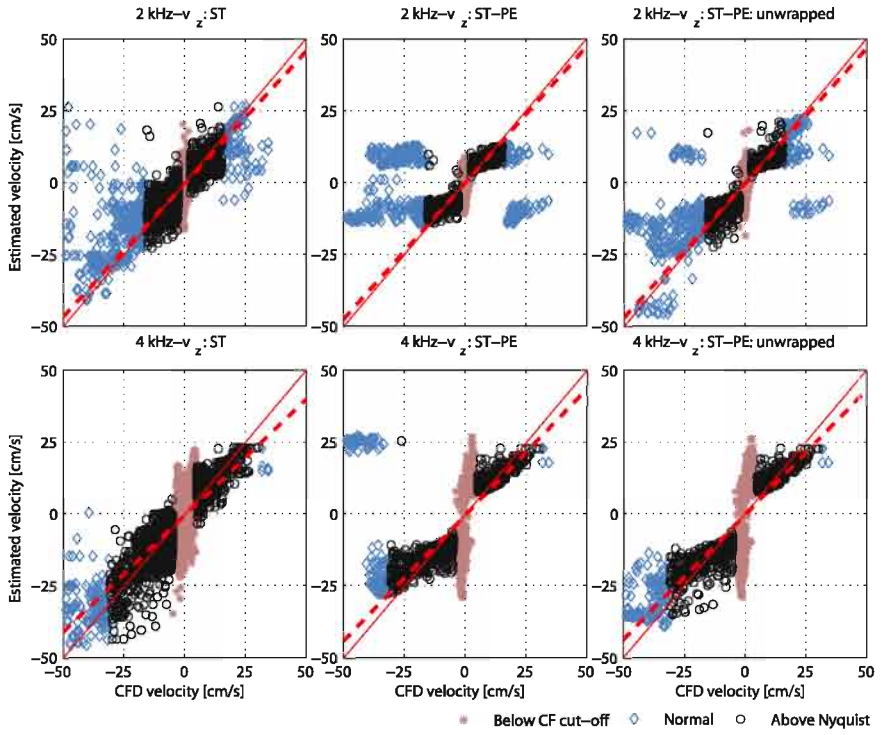

Figure 8.3: Scatterplots and associated linear regression analysis of the normal velocity range for the axial velocity component (PRF of 2 and 4 kHz), shown for the three different axial estimators: *ST*, *ST-PE* and *ST-PE: unwrapped* (SNR of 20 dB).

suffer most from clutter filtering, and all methods imaged with 4 kHz have difficulties capturing the smaller vortex near the external carotid, which is not the case for 2 kHz.

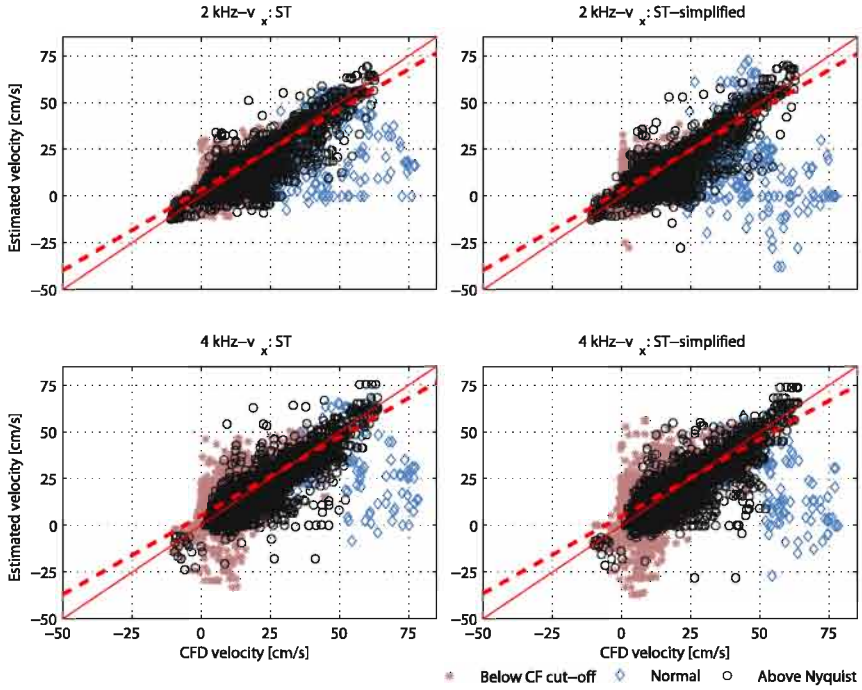

FIGURE 8.4: Scatterplots and associated linear regression analysis of the normal velocity range for the lateral velocity component (PRF of 2 and 4 kHz), shown for the two different lateral estimators: *ST* and *ST-simplified* (SNR of 20 dB).

The estimator performance is further compared to the CFD-reference for all velocity estimates in space and time, as shown in the scatterplots of fig. 8.3 and 8.4 (for SNR of 20 dB) for respectively the axial (v_z) and lateral velocity (v_x) component. Black circles indicate the normal range of velocities, blue squares the aliased range and red stars the clutter filtered range. Fig. 8.3 quantifies the improved ST performance for v_z when using 4 kHz. In the normal range of velocities, a lowered spread can be observed for PE estimates for all setups. A bias can also be observed for PE variants; overestimation in the vicinity of the clutter filter transition region, while underestimation close to the Nyquist limit. Aliasing errors are apparent for PE but are partly corrected for by the proposed unwrapping procedure, especially for 4 kHz. Fig. 8.4 demonstrates a larger spread in lateral estimates of the simplified ST-method when the axial estimates alias. A linear regression analysis was performed for the normal range of velocities, and Table 8.1 and 8.2

Table 8.1: Linear regression analysis for the complete cardiac cycle of v_x and v_z as estimated by speckle tracking (ST), phase-shift estimation (PE), corrected phase-shift estimation (ST-PE: unwrapped) and the simplified tracking method (ST-simplified), compared to the CFD reference. Analysis was based on those values within the normal range of velocities, i.e. not influenced by clutter filtering and within the Nyquist range. Data are reported for both imaging setups (PRF=2 and 4kHz).

		ST		ST-PE		ST-PE:unwrap		ST-simplified	
		2 kHz	4 kHz	2 kHz	4 kHz	2 kHz	4 kHz	2 kHz	4 kHz
$\overline{m}$ (cm/s)	v_x	2.05	2.69	2.09	2.75	2.09	2.72	1.90	2.28
	v_z	-0.36	0.36	-0.01	0.21	0.04	0.63	-0.02	0.10
σ (cm/s)	v_x	5.19	6.32	5.19	6.27	5.22	6.38	5.25	6.70
	v_z	2.83	4.67	2.07	3.48	2.07	5.46	2.17	3.55
β $(slope)$	v_x	0.86	0.84	0.86	0.84	0.86	0.84	0.86	0.83
	v_z	0.92	0.81	0.95	0.88	0.94	0.87	0.96	0.88
$R^2(gof)$	v_x	0.83	0.82	0.83	0.82	0.82	0.82	0.82	0.80
	v_z	0.86	0.86	0.92	0.92	0.92	0.91	0.92	0.92

Table 8.2: Linear regression analysis for the complete cardiac cycle of v_x and v_z as estimated by speckle tracking (ST), phase-shift estimation (PE), corrected phase-shift estimation (ST-PE: unwrapped) and the simplified tracking method (ST-simplified), compared to the CFD reference. Analysis was based on those values within the normal range of velocities, i.e. not influenced by clutter filtering and within the Nyquist range. Data are reported for PRF=2kHz and low SNR (5dB).

		ST		ST-PE		ST-PE:unwrap		ST-simplified	
		2 kHz	4 kHz	2 kHz	4 kHz	2 kHz	4 kHz	2 kHz	4 kHz
$\overline{m}$ (cm/s)	v_x	5.30	9.26	5.41	9.24	5.34	9.14	5.02	8.59
	v_z	-0.65	-1.36	0.21	0.71	0.31	0.88	0.01	0.19
σ (cm/s)	v_x	7.50	11.28	7.43	11.32	7.52	11.38	7.64	11.38
	v_z	4.77	7.42	2.70	5.49	3.33	5.77	2.97	5.00
β $(slope)$	v_x	0.70	0.58	0.70	0.57	0.69	0.49	0.69	0.51
	v_z	0.85	0.84	0.84	0.75	0.83	0.75	0.87	0.79
$R^2(gof)$	v_x	0.70	0.51	0.70	0.49	0.69	0.49	0.67	0.51
	v_z	0.63	0.65	0.90	0.89	0.90	0.89	0.88	0.88

provide the mean ($\bar{m}$) and standard deviation (std) on the differences between the ultrasound estimates and the reference flow, the slope (β) and the R^2 goodness-of-fit parameter of respectively v_z and v_x. For all imaging setups, the estimation of v_z improves for *ST-PE* compared

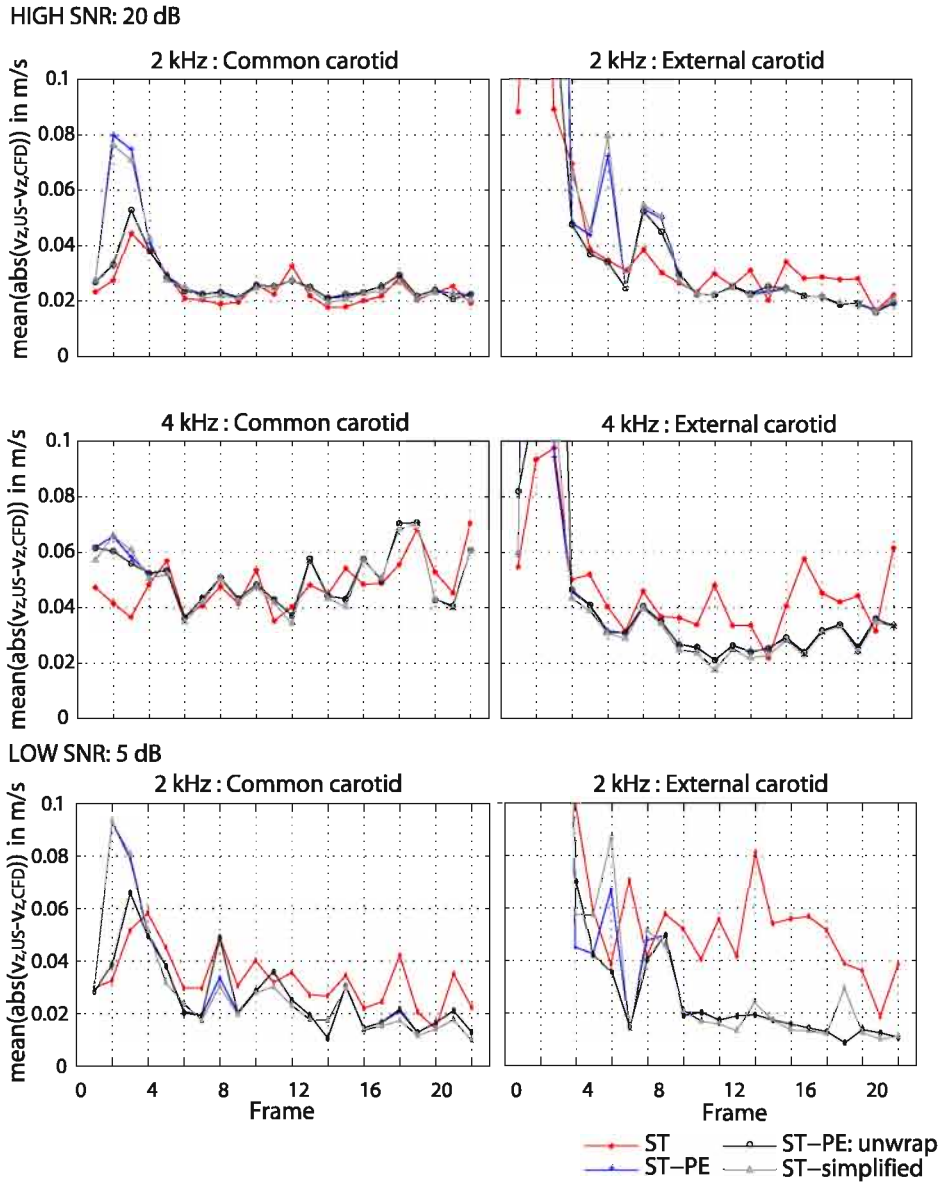

FIGURE 8.5: Temporal analysis of the mean absolute deviation of the axial velocity component with respect to the CFD reference flow field. The common and external carotid are investigated seperately, for ST and the three ST-PE combination techniques, and for both PRF's (2 and 4 kHz). A SNR of 20 dB was applied during post-processing of the simulations (four upper panels), and high noise levels were investigated with an SNR of 5 dB (two lower panels).

to ST, in terms of decreased standard deviation (std) and an increased goodness-of-fit (R^2). A decrease in std of 37% (2kHz) and 35% (4kHz) was observed for high SNR (20dB), and of 77% (2kHz) and 50% (4kHz) for low SNR (5dB). Table 8.1 also quantifies a slightly deteriorated performance for v_x of the simplified ST method.

Fig. 8.5 shows the temporal analysis of the mean absolute deviation of the estimated v_z with respect to the CFD-reference. The performance of all investigated estimators was analyzed for both imaging setups in the common and external carotid artery. As could be observed in the flow curve of the common carotid artery (cfr. fig. 8.2), low flow prevails throughout most of the cardiac cycle. Hence, fig. 8.5 is zoomed in on the deviations present during these frames in diastole. ST shows for both PRF's the largest deviation in the external carotid during the low flow frames (cfr. frame 12 - 22). For the common carotid artery, ST shows deviations similar to the PE approach for high SNR (20 dB), and higher deviations in case of low SNR (5 dB). During the aliased frames (especially frame 2 and 3), large deviations are present in the external carotid (0.15 m/s<deviation<0.35 m/s for 2 kHz and 0.1 m/s<deviation<0.5 m/s for 4 kHz). During systole (see frame 2 in fig. 8.2), the unwrapping method is the overall best performer and ST the worst performer for 2 kHz. For 4 kHz, both ST and the unwrapping method perform well during this frame, with a deviation close to each other.

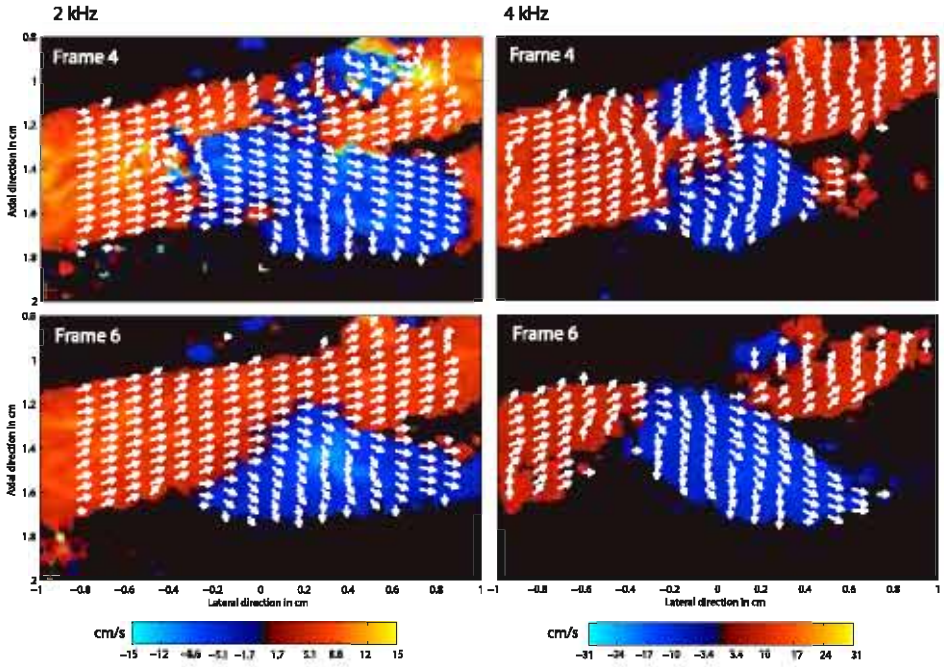

FIGURE 8.6: Demonstrating the potential of applying the *ST-PE* method in-vivo. 2D flow estimates from the *ST-PE* method are superimposed on the color flow images of a carotid artery of a healthy volunteer. Two frames (systole and diastole) and both imaging setups (2 and 4 kHz) are shown.

8.3.2 In-vivo data

Fig. 8.6 shows the *ST-PE* method superimposed on color flow images recorded in a healthy volunteer, for a frame in systole (frame 4) and diastole (frame 6) and for both imaging setups. The left panels of fig. 8.7 show a temporal analysis of the in-vivo mean flow angle in the common carotid artery and its associated standard deviation for the investigated 2D flow estimators. The cardiac cycle comprised 11 frames but the 1st frame was not taken into account due to signal loss in the common carotid artery. ST tracks best the reference angle that was determined from geometrical considerations (dashed black line), but shows the highest standard deviation during most of the cycle. The right panels show the same angle analysis but based on the simulations. One should note that the simulation results were derived from the external carotid in order to analyze flow conditions which were aligned with the axis of the vessel. During the second half of the cycle (frame 10 - 22), ST is closest to the reference flow angle derived from CFD (solid black line), as was the case in-vivo. The estimators perform quite similar during most of the cardiac cycle regarding standard deviation.

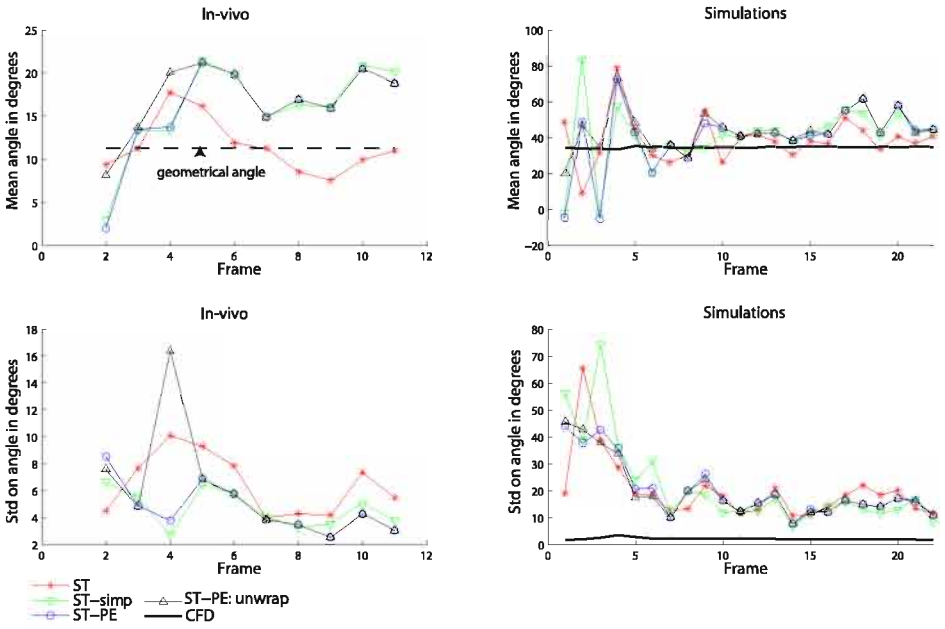

FIGURE 8.7: Analysis of the in-vivo flow angle (mean and standard deviation) is shown in the left panels. The right panels show a similar analysis but derived from the simulated flow estimates. All four 2D flow estimators are compared and the solid black line indicates the reference flow angle.

8.4 Discussion and Summary

In previous work, we compared the performance of speckle tracking and crossed-beam vector Doppler in a patient-specific carotid bifurcation model by integrating CFD and Field II ultrasound simulations [132]. In our examples, we demonstrated ST to be the superior lateral velocity estimator and VD the better axial velocity estimator. For a detailed discussion on the advantages and limitations of the simulation environment, we refer to [110]. With the aim to develop a clinically applicable and robust 2D flow estimator, we investigated the natural extension of our previous work, combining speckle tracking and phase-shift estimation to measure v_x and v_z respectively. To the best of our knowledge, such a combined approach has not previously been investigated in detail.

While the concept of combining ST and PE is straightforward, its practical implementation is not. Challenges arise from the fact that a common acquisition scheme does not reconcile the acquisition and processing requirements of the individual techniques. To achieve satisfactory results with the PE approach, the slow-time PRF needs to be adapted to the velocity range of interest. Further, for the combined approach to work properly, the maximum axial velocity should lie below the Nyquist limit, to avoid obscuring the combined estimate. This means that the PRF will vary for different clinical applications, and can in many cases be quite high (e.g. 4-10 kHz). Considering the interleaved acquisition mode used, this poses some challenges. The interleaved acquisition is necessary to obtain a high frame rate speckle acquisition (in the kHz range), making tracking of complex blood movement feasible. The number of receive lines in each interleave group is, as described by equation 8.1, dependent on the depth of the scan (PRF_{max}) and the slow-time PRF, such that high PRF's or deep scanning leads to few interleaved beams. In this case the possible kernel width may become very small. However, the choice of the kernel size depends on the imaging system resolution, with the lower limit of K_x related to the in-focus -3dB beam width ($K_x = \lambda F_{2-way}$, λ the wavelength and F_{2-way} the two-way F-number), as put forward by Wagner [57]. Further, the tracking performance becomes also highly dependent on the spatial interpolation for high PRF's, due to the coarse velocity resolution initially given for ST. In particular, the lateral beam sampling is typically low to adhere to frame rate requirements. In this

work, both linear interpolation of envelope-detected data as well as parabolic fitting around the SAD minimum was therefore needed to obtain a velocity resolution close to the clutter filter cut-off velocity.

Combining the requirements of both approaches and considering the carotid imaging setup described in this work, the optimal choice of slow-time PRF is difficult to find and consequently becomes a compromise in unifying the requirements of both approaches. In particular, adhering to a requirement of avoiding aliasing in a combined estimator might decrease performance when tracking high blood flow, compared to using ST alone at a lower PRF. An exception is the case where the speckle decorrelation is so rapid that extreme frame rates (high PRF's) are essentially needed to track any movement. In general, multi-lag tracking might increase performance for a broader range of velocities when using a high PRF. Decimation in time is then applied for ST and tracking is performed for every *nth* (n>1) speckle image within a packet of data. Such an approach is considered further work. On the other hand, unwrapping based on axial speckle tracking estimates may also help, as can be seen in the vector plots in fig. 8.2 and the scatter plots in fig. 8.3 and 8.4. However, due to the variance on the axial ST estimates, the direct approach used in this work may also lead to spurious errors when unwrapping. This explains why the standard deviation increases for the unwrapped combined estimator as seen in Table 8.1 and 8.2. Problems also emerge when axial velocities wrap around all the way into the clutter filter stop band for low PRF's, as can be observed for the 2 kHz setup in fig. 8.2, where the signal in the external carotid aliases substantially during systole. In any case, as aliasing artifacts may be difficult to avoid, they should be visible in the final display to notify the operator. This can for instance be achieved by visualizing arrows on top of a conventional color flow image as given for the in vivo examples in fig. 8.6.

An alternative approach that avoids interleaving issues would be to track only within the group of parallel receive beams, as previously reported in [133]. However, only a small number of PRB (2-4) can be utilized without reducing the transmit aperture and therefore the sensitivity. Further, artifacts due to the misalignment of transmit and receive beams should be corrected to ensure good performance [134], increasing complexity and cost. Another alternative would be to use unfocused (plane) transmit beams and a high number of parallel receive

beams as reported in [45]. However, it remains to be shown whether this approach provides sufficient sensitivity in clinical practice.

A different acquisition aspect concerns the pulse length requirements for ST and PE. ST is a wide-band technique, as the related crosscorrelation technique, benefiting from short ultrasound pulses and high spatial resolution. On the other hand, PE is a narrow-band technique benefiting from longer pulses (e.g. 4 to 8 periods). In our setup, a relatively short ultrasound pulse of 2.5 periods was used as a compromise. As can be observed in the in vivo example in fig. 8.6, the combined estimator works quite well for the given setup. In clinical practice, however, longer pulses will be necessary in many cases. A detailed investigation of ST or the combined estimator approach with regards to sensitivity and pulse length is considered future work. However, it is worth noting that with regards to sensitivity, the proposed acquisition setup using focused beams has an advantage. Using small apertures or unfocused transmit beams in conjunction with a high number of PRB, the transmitted pressure in depth quickly decreases and longer pulses are necessary.

Different lateral sampling requirements of ST and PE is also an issue. In conventional CFI, the image is often undersampled in order to yield a higher frame rate. Due to smoothing and the low dynamic range used in the color images, visible artifacts because of undersampling are limited. On the other hand, in order to produce high quality speckle and ensure a good tracking performance, undersampling should be avoided. In this work, marginal sampling of the RF signal variation was ensured by using (approximately) the Rayleigh criterion as the beam distance. This still infers undersampling by a factor of two for the envelope detected data, and performance might be suboptimal. Coherent interpolation of the RF-data within the interleave region or a group of parallel beams could be a solution to achieve sufficient sampling and frame rate. This imposes however the requirement that phase-cancellation between beams does not occur for the velocity range of interest. The practical limits of such complex interpolation with regards to arterial flow remain to be investigated. It is also worth noting that this approach would substantially increase computational demands.

Overall, the PE estimator showed decreased variance of the axial estimates, compared to using pure ST for the examples explored. This

can be observed in the scatter plots of fig. 8.3 and the regression results in Table 8.1 and 8.2. One should note that a bias was noticeable for PE in our examples for both low and high velocities. Overestimation on the lower range can be attributed to the clutter filter, as polynomial regression filters are known to produce a bias close to the clutter filter transition region [41, 113]. The underestimation for increased velocities can partly be attributed to averaging. When previously comparing ST and crossed-beam vector Doppler, we showed that ST was less robust towards added noise. Also, we showed ST performance decreased in out-of-focus areas and for increased out-of-plane blood movement [132]. As can be observed by comparing Table 8.1 and 8.2, the combined estimator approach has advantages for ensuring robust axial estimates in unfavorable signal-to-noise conditions.

The simplified tracking approach, fully combining ST and PE, is particularly interesting, as potential variance attributed to the 2D search regions can be avoided. In principle, this approach may therefore produce more stable lateral tracking estimates. However, we did not observe this in our examples due to the biased autocorrelation estimates. Interestingly, results showed that the simplified tracking approach marginally decreased lateral tracking performance in the normal range of velocities for both SNR conditions investigated, as given in Table 8.1 and 8.2. The simplified approach also has obvious computational advantages compared to full 2D tracking, and a high potential for real-time operation on modern scanner systems. In any case, utilizing special purpose multimedia instruction sets (MME/SIMD) on modern CPUs or going towards a graphical processor unit (GPU) implementation will make real-time performance of blood flow speckle tracking feasible for a high number of tracking kernels.

As the performance of the estimators is highly dependent on the flow field, we analyzed the deviation of the estimated v_z with respect to the CFD-reference for each frame (cfr. fig. 8.5). In the external carotid artery, ST showed the highest deviation from the reference during the low flow phases (both 2 and 4 kHz), and the combination approach proved advantageous. In the common carotid artery, the opposite occured and ST estimates resulted in the lowest deviation from the reference during these frames. It should be noted that in the common carotid artery, relatively low axial velocities were present since the flow direction was almost perpendicular to the beam. Hence, the axial ve-

locities were often close to the clutter filter cutoff, where the PE approach suffers from a bias due to the clutter filter. Improved results for PE may be obtained for velocities close to the clutter filter transition region by using a different clutter filter than the polynomial regression type used in this work.

To illustrate the feasibility of the estimators in vivo, we recorded data from a healthy volunteer using the exact same 2 and 4 kHz imaging setup as for the computer simulations. As can be observed in fig. 8.6, the ST-PE method provides reasonable velocity vector fields in line with what one would expect in a healthy carotid bifurcation. To quantify the in vivo results and compare it to the simulation results, we calculated the estimated angle of the velocity vectors in areas where the flow is expected to be well aligned with the axis of the vessel. For the in vivo data, the common carotid artery was chosen, while for simulations only the external carotid artery was used due to the swirling flow otherwise present. As can be seen in fig. 8.7, the mean angle estimated by ST was closest to the reference for the in vivo data, but with an overall higher standard deviation. This may be attributed to the low axial velocity component due to the near perpendicular angle in the in vivo data, and hence to clutter filtering artifacts as previously discussed. On the other hand, in the simulated data, a larger angle and larger axial velocities were present. Similar results for ST and the combined approaches can here be observed. This can partly be attributed to the higher SNR of 20 dB used for the example, and improved results when incorporating PE are expected for lower SNRs as observed globally. Overall, it can be concluded that the in vivo application of speckle tracking and a combined estimator was feasible for the given carotid artery of a healthy volunteer. Further work is needed to map the potential for patients with varying SNR conditions and for complex flow patterns due to pathology.

8.5 Conclusion

When designing a 2D blood velocity vector estimator based on speckle tracking, the added axial velocity information available using the autocorrelation approach may be used to increase overall robustness. However, a unified acquisition which ensures good tracking performance and at the same time avoids aliasing is not always possible. Unwrapping using the axial speckle tracking estimate can be used with success

to some extent, but may also introduce spurious unwrapping errors. A fully combined approach where only 1D lateral tracking is performed showed a marginal decrease in performance compared to 2D tracking, but has large computational advantages. Further work will focus on in vivo trials in patients with stenosed carotid arteries.

Four

Integrating fluid-structure interaction and ultrasound simulations

CHAPTER 9

A simulation environment for validating ultrasonic blood flow and vessel wall imaging based on FSI simulations: ultrasonic assessment of arterial distension and wall shear rate

In the final part of this dissertation, a simulation environment is presented integrating the Field II software and fluid-structure interaction (FSI) simulations, allowing construction of synthetic ultrasound images based on physiologically realistic behavior of both the blood flow and arterial wall. To demonstrate the potential of our model for vascular ultrasound research, we study clinically relevant imaging modalities of arterial function related to both vessel wall deformation and arterial hemodynamics: arterial distension and wall shear rate imaging.

Our model is applied to a 3D straight tube, representative of the common carotid artery, and different degrees of arterial distension are simulated. The RF-data from the FSI-Field II coupling are further processed for arterial wall and flow imaging. Using an available wall track-

ing algorithm, arterial distensibility is assessed. Using an autocorrelation estimator, blood velocity and shear rate are obtained along a scanline.

We obtain very good agreement between the flow and distension as obtained from the FSI-Field II model and the reference FSI values. The wall application shows a high sensitivity of distension measurements to the measurement location. Interestingly, the model indicates that strong reflections between tissue transitions can potentially cloud a correct measurement. The flow imaging application demonstrates that maximum shear rate is underestimated for the simulated setup. Moreover, given the difficulty of measuring near-wall velocities with ultrasound, maximal shear rate is obtained at a distance from the wall. However, ultrasound shear rates correlate well with the FSI ground truth for all distension degrees, suggesting correction of the severe underestimation by ultrasound might be feasible in certain flow conditions.

This chapter is based on "*A simulation environment for validating ultrasonic blood flow and vessel wall imaging based on fluid-structure interaction simulations: ultrasonic assessment of arterial distension and wall shear rate*", as submitted for publication.

9.1 Introduction

At present, ultrasonic echography is still the preferred method for clinical screening of atherosclerosis in large, superficial arteries. In particular, the carotid artery is often investigated in clinical protocols since the artery directly supplies blood to the brain and the location is prone to development of atherosclerosis. Moreover, as the carotid artery is a large elastic vessel, measuring its stiffness might indirectly provide information on aortic stiffening. Hence, its screening may identify subjects at risk of cardiovascular disease in general, and stroke in particular. However, current ultrasound modalities have their limitations in this setting. Most commonly used clinical blood flow imaging modalities are still limited to 1D measurements since only the velocity component in the direction of the ultrasound beam is visualized. This is particularly a disadvantage for complex velocity fields as may occur in the vicinity of the carotid bulb, where zones of blood recirculation and swirling flow patterns may arise [86]. Other imaging modalities

aim to assess arterial stiffness, but here the current methods are also hampered. A common application is measuring tissue velocities using Doppler based methods, which is limited to 1D visualization as well. Often, tissue velocities are further integrated to assess vessel distension [5]. However, vessel kinematics rather than vessel mechanics is hence assessed.

With the rapid evolution in ultrasound imaging technology and computer processing power, it has become feasible to design better imaging modalities. A practical problem is, however, the validation and optimization of these imaging modalities. Especially for complex settings as the carotid artery, which shows complex flow patterns and a highly deformable elastic wall, new and optimized ultrasound modalities (pulse firing sequences, beam-forming, processing of radio-frequency (RF) ultrasound data) aiming for improved visualization would require thorough validation.

In recent work [110], we developed a computer simulation tool which integrated computational fluid dynamics (CFD) with ultrasound simulation (US) software (Field II) [17, 18], providing a flexible tool for the validation and development of ultrasound blood flow modalities in the presence of complex flow. In the simulation environment, the ultrasonic echoes are simulated by modeling blood as a random point scatterer distribution on which the ultrasound waves reflect. The scatterer positions are updated using the CFD-velocity fields interpolated in space and time. We used this tool to construct a patient-specific 3D ultrasound phantom of the carotid artery and we assessed the performance of 1D flow imaging methods like pulsed wave Doppler and color flow imaging, demonstrating its inability to portray complex flow patterns [110]. We further compared the performance of two major research lines in 2D velocity estimators: crossed-beam vector Doppler and speckle tracking, demonstrating that speckle tracking would probably make most chance to be practically applicable [132].

An important limitation of our work, however, was the absence of the moving vessel wall in our model, which influences flow visualization through the motion of the boundaries of the fluid domain, as well as via ultrasound echoes generated by the vessel wall. Fluid-structure interaction (FSI) simulations allow for the coupled computation of blood flow and arterial wall mechanics. It is therefore a natural extension

of our work to seed scatterers also in the vessel wall, and to use FSI-simulations to calculate scatterer positions in both the blood flow and vessel wall. Although the basic principle behind this extension is logical and straightforward, the practical implementation is not. A first challenge is the grid formulation used in FSI-simulations, where both the fluid and structural part are described with nodal grid positions changing with time, which challenges the scatterer position assessment. Further, the creation of a vessel wall phantom also poses specific challenges. In contrast to blood scatterers which move in and out of the computational domain, tissue scatterers are fixed to the tissue. The complex composition and layering of the vessel wall also requires flexibility in adapting scattering properties in localized regions. Implementing the layered structure in the scatterer phantom imposes additional requirements on the mesh elements used to solve the structural problem. Furthermore, the transition between the vessel wall and surrounding tissue/blood creates strong specular reflections, which should be appropriately mimicked in the ultrasound software.

The aim of this paper is two-fold. In a first section, we elaborate on our methodology based on a 3D FSI-simulation of blood flow and wave propagation in a 3-layered tube, representative of the common carotid artery. Scatterer phantoms of both the blood flow and arterial wall are generated and hence a virtual echographic phantom of a straight arterial segment is obtained. In a second section, the potential of the model is illustrated via two applications on currently used ultrasound modalities in vascular research, one related to measuring distension of the arterial wall and one related to assessing the wall shear rate of the blood flow along the arterial wall.

As a first application, the ultrasonic measurement of vessel distension will be investigated, which is often used to measure arterial stiffness. We will use the RF-data resulting from scatterers in the arterial wall to assess the performance of a previously used [135] vessel wall-tracking algorithm based on a modified autocorrelation velocity estimation algorithm [5]. In particular, the sensitivity of these wall-tracking algorithms to the measuring position in the arterial wall will be demonstrated, where we anticipate a decrease in measured diameter distension from the blood-lumen interface towards the adventitia, as we have previously reported in vivo [135]. In a second application, we will study to what extent it is possible to measure velocity and shear rate profiles

using Doppler-based measurements along one scanline. The shear rate relates to the shear stress, the tangential force exerted by the blood on the endothelial cells, which line the lumen of the blood vessel. Low or oscillating shear stress has been shown to promote the development of atherosclerosis, and is hence a clinically relevant hemodynamic parameter when screening for patients at high cardiovascular risk [6]. Shear stress is obtained as shear rate multiplied with blood viscosity, but given the difficulty to know the exact value of viscosity in the (more plasma-like) boundary layer in the direct vicinity of the arterial wall, we will focus on shear rate for the remainder of this work. As earlier described by Brands et al. [7], shear rate profiles can be derived from flow velocity profiles measured with ultrasound. However, due to difficulties in measuring the low velocities in the vicinity of the moving wall, the maximal shear rate is measured at a certain distance from the wall, while the actual maximal shear rate might be differing from this position and in magnitude. To the best of our knowledge, the relationship between ground-truth and ultrasound-derived shear rate has never been studied in detail. As the magnitude of the wall motion might have an effect on this relation, we have performed three simulations with various degrees of arterial distension.

9.2 Methods

9.2.1 Simulating Fluid-Structure interaction (FSI)

FSI-simulations were performed in a partitioned way, computing the flow and structural equations with a separate flow and structural solver. An in-house code 'Tango' was used to couple the flow solver Fluent (Ansys, Canonsburg, PA, USA) and the structural solver Abaqus (Simulia,Inc., Providence, RI, USA). In particular, Dirichlet-Neumann partitioning was used, which means the flow problem is solved for a given displacement, and the structural problem is solved for a stress boundary condition applied on the wet side of the structure. For each timestep, coupling iterations were performed between the flow and structural solver, and the transfer of information was limited to the fluid-structure interface: a face stress transfer from fluid to structural domain and a displacement transfer from structural to fluid domain. However, vascular FSI-problems are often strongly coupled problems due to the compliant vessel walls and the similar fluid and structural densities. Hence, a weak coupling, i.e. directly transferring the stresses and displacements may lead to numerical instabilities [75, 136]. To enhance

convergence of the coupling iterations, an Interface Quasi-Newton method was used [63, 64]. This technique replaces the complex fluid or solid solver on the interface by approaching the Jacobian of the solver on the interface. Further, an Arbitrary Lagrangian Eulerian (ALE) method was used to match the different grid formulations for the fluid and structural domain. The fluid domain is often described in the Eulerian way, which considers motion from a fixed point. The Lagrangian formulation is the intuitive way of describing the structural domain, and considers motion from a point moving with the material. In the ALE method, the flow equations are written in an arbitrary Lagrangian-Eulerian formulation and are solved on a deforming mesh. The fluid grid deforms in an arbitrary way, independent from the flow velocity, and its boundaries follow the structural domain's deformation. The structural problem is formulated in the Lagrangian manner.

A straight elastic tube with inner radius 3 mm, outer radius 4 mm, and length 5 cm was simulated. The vessel wall was modeled using a linearized elastic material model with a Young modulus of 250 kPa, Poisson modulus of 0.49, and density 1200 kg/m^3. The linearization was performed with respect to a reference pressure and inner radius of respectively 10 mmHg and 3 mm. Circumferential and longitudinal movement of the tube was prevented. Blood was modeled as a Newtonian liquid with a viscosity of 3.5 mPas and a density of 1050 kg/m^3. A velocity profile was measured in the common carotid artery of a healthy volunteer using ultrasonic pulsed wave Doppler (12L linear array vascular probe, GE Medical Systems, Milwaukee, WI, USA) and was applied as a mass flow inlet condition to increase stability during the coupling iterations. The outlet boundary condition was a non-invasively measured pressure waveform, scaled with a pulse pressure of 40 mmHg, representative of a healthy hemodynamical condition. This pressure condition resulted in an arterial distension $\Delta D/D$ ($\Delta D=D_{max}-D_{min}$ and $D=D_{min}$) of 9%. To obtain additional datasets with lower degree of distension, we ran simulations using the same pressure waveform, but with an amplitude scaled to pulse pressures of 20 and 4 mmHg or arterial distensions of 4% and 1%. The fluid-structure interface was modeled as a no-slip boundary.

The flow solver Fluent uses a finite volume method, with PISO (Pressure-Implicit with Splitting of Operators) pressure-velocity coupling and first order time accuracy. First order pressure discretization and sec-

ond order upwind for momentum were applied. The fluid mesh consisted of 34400 triangular prisms and was adapted to the position of the fluid-structure interface with a spring analogy. Abaqus is a finite element structural solver which uses Hilber-Hughes-Taylor [137] implicit time integration and takes into account the geometric non-linearities due to large deformations. The structural domain was composed of 720 quadratic continuum hexahedrons (20 nodes) and numerical damping of high-frequency errors was increased (α=-0.3) to eliminate spurious oscillations due to the different time discretizations in Fluent and Abaqus. Hexahedral elements were used to allow layered modeling of the vessel wall. A non-matching mesh existed on the interface requiring appropriate interpolation of the transfer variables. The cardiac cycle of 1s was divided into timesteps of 5 ms and 2 cycles were computed to obtain results independent of transient effects. The Womersley number was 4.12; the peak Reynolds number was 845 (1 % distension-case). The coupling algorithm was executed on one core, the flow solver on six cores and the structural solver on six cores of a dedicated machine with two Intel Xeon 5355 quad-core processors (2.66GHz).

9.2.2 Simulating ultrasound

The RF-signals from the vessel wall and blood were simulated using the Field II software created by Jensen et al [17, 18]. This simulation software allows modeling arbitrary ultrasound transducers and realistic image scan sequencing. The approach is limited to linear wave propagation and is based on the spatial impulse response estimation as described by Tupholme [94] and Stepanishen [95]. Using linear system theory, the ultrasound field is determined based on the ultrasonic excitation pulse, the temporal impulse responses of the transmitting and receiving transducers, and the spatial impulse response at a given point. For further details on the software background, we refer to [17, 18]. Field II models tissue as a collection of random point scatterers. The required scatterer density is related to the imaging system resolution, with 10 scatterers per resolution cell assuring Gaussian distributed RF-signals [58]. The scattering strength is modeled using a normal distribution of scattering amplitudes with mean and standard deviation varying according to the tissue properties. To appropriately mimic specular reflections, scatterers with high mean amplitude are positioned in a regular fashion at the tissue transitions. Dynamic objects are achieved by moving the point scatterers during simulation.

Each ultrasound beam is simulated individually, and it is therefore possible to update the position of moving scatterers between beam acquisitions.

9.2.2.a *Integrating FSI and ultrasound: creating a fluid scatterer phantom*

In [110], we described a method to generate scatterers during Field II simulations based on CFD-calculations with rigid walls. 3D spatial interpolation was performed to transform the CFD velocity vectors to the random scatterer cloud, and temporal interpolation of the CFD velocities was required due to the large disparity in the ultrasound and CFD timescales (63 μs versus 5 ms for the simulated color flow imaging application).

For distensible fluid geometries, straightforward linear temporal interpolation of the velocity fields is however not possible. This is illustrated in fig. 9.1-A, if one considers the position of the red point at time point $T_{FSI,1}$ of the FSI-calculation and the same absolute position of this point at the next FSI timestep $T_{FSI,2}$. In case of a decreasing fluid volume, this point ends up outside the fluid volume at $T_{FSI,2}$ (white point in fig. 9.1-A) . In case of increasing fluid volume, the point ends up further from the vessel wall at $T_{FSI,2}$ compared to $T_{FSI,1}$ (yellow point in fig. 9.1-A). Hence, temporal interpolation between the same absolute positions at different FSI-timesteps is incorrect. Complex mathematical methods exist to derive velocity fields for changing fluid domains at timesteps intermediate to the chosen FSI-timesteps. This, however, would be an impractical approach due to high computational times [138, 139]. We therefore followed an approach outlined below, which allowed us assessing scatterer velocities as illustrated in the flowchart of fig. 9.1-B.

The scatterer displacement will be approximated by updating scatterer velocities for each FSI-timestep. A first problem arises from the fact that a backward Euler time discretization scheme is used for the flow simulations. As such, when deriving scatterer velocities using the current situation at FSI-frame $T_{FSI,1}$, the scatterer positions at subsequent ultrasound simulation timesteps will not follow the wall motion. This is illustrated for the red point in fig. 9.1-A, with corresponding velocity vector V at $T_{FSI,1}$. For increasing volumes, the red scatterer would be propagated in a horizontal manner according to the vector V, and

A

B

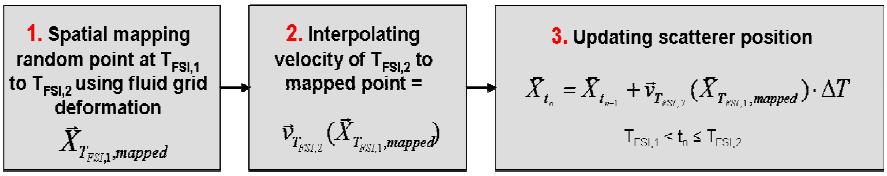

FIGURE 9.1: Panel A: Illustration of the principles behind the creation of the fluid scatterer phantom. In case of distensible fluid geometries, absolute positions can not be compared between two time steps and hence linear interpolation of the velocity fields is not straightforward. Instead, the velocity field at the future timestep $T_{FSI,2}$ is used to derive the scatterer displacement. Scatterers are mapped in space to the next timestep using the fluid grid displacement and hence the same relative position of the scatterer in the vessel is obtained. Once the future position of the concerned scatterer is determined, the velocity vector is extracted. Using these future velocity vectors, the scatterers will follow the vessel wall motion. This is illustrated in case of an increasing and decreasing fluid volume. In the latter case, the same absolute position of the red point at $T_{FSI,1}$ is a point outside the fluid volume. In the former case the red point ends up too far from the vessel wall, indicating the need for mapping scatterer positions conserving the relative position in the vessel wall. Panel B: A flowchart of the creation of the fluid phantom.

a void would arise near the wall. In case of decreasing volumes, the red scatterer would end up outside the fluid volume due to its horizontal propagation. In order to follow the wall motion, the situation

at the next FSI-timestep $T_{FSI,2}$ should be considered when updating the scatterer velocity at $T_{FSI,1}$. As illustrated in fig. 9.1-A, the red scatterer has a velocity vector V at $T_{FSI,2}$ which indicates the correct wall motion. The velocity vectors at $T_{FSI,2}$ will therefore be applied for the ultrasound simulation timesteps $\geq T_{FSI,1}$ and $<T_{FSI,2}$.

Now we know when to extract the scatterer velocities, the question remains where to extract the scatterer velocity vector from the velocity field at $T_{FSI,2}$. As was previously explained, absolute positions at different FSI-timesteps can not be compared. Consequently, one cannot extract the velocity vector at $T_{FSI,2}$ at the same location the scatterer finds oneself at $T_{FSI,1}$. A suitable location can be found, keeping in mind the scatterer displacement between FSI-timesteps is influenced by both the flow and structural movement. If a flow scatterer were solely displaced due to the structural movement, one can assume that its relative position in the blood vessel is conserved. To find the same relative location of a scatterer at $T_{FSI,2}$, the scatterer location at $T_{FSI,1}$ is mapped onto its new location at $T_{FSI,2}$ using the deformation of the fluid grid between $T_{FSI,1}$ and $T_{FSI,2}$. This is also illustrated in fig. 9.1-A. This is possible because of the ALE grid formulation and since remeshing is unnecessary due to the relatively small volume changes between FSI timesteps (typical for vascular FSI-applications). For this purpose, the fluid grid deformation known in the nodal grid points is interpolated to the random points using the same Matlab procedure as described in [110].

Once the mapped scatterer location at $T_{FSI,2}$ is known, the velocity vector of the scatterer can be obtained with 3D spatial interpolation [110]. Subsequently, the new scatterer position $\vec{x}_{t_n}$ at t_n ($T_{FSI,1} < t_n \leq T_{FSI,2}$) can be calculated as:

$$\vec{x}_{t_n} = \vec{x}_{t_{n-1}} + \vec{v}_{T_{FSI,2}}(\vec{x}_{T_{FSI,1},mapped}) \cdot \Delta T \tag{9.1}$$

With $\vec{x}_{t_{n-1}}$ the scatterer position at the previous timestep t_{n-1}, ΔT the timestep between t_{n-1} and t_n, and $\vec{v}_{T_{FSI,2}}(\vec{x}_{T_{FSI,1},mapped})$ the velocity vector at $T_{FSI,2}$ at the location found by mapping the scatterer position $\vec{x}_{T_{FSI,1}}$ on the next FSI-timestep $T_{FSI,2}$. A complete overview of the procedure can be found in fig. 9.1-B.

With this approach, the discrete motion of the fluid-structure interface and a scatterer which would be placed at the interface is exactly

the same, so that a scatterer can never leave or enter the blood domain, which is the aim. Inside the blood domain the velocity with which the scatterer is moved is taken at the new time level, but at a location which does not correspond to the location of the scatterer at the new time level. This can be seen in the fact that the proposed mapping of the scatterer position onto the next FSI-timestep does not take into account the motion of the scatterer due to the flow field. This would require an iterative approach, but the computational cost to perform this operation for the complete scatterer family would be excessively high. Neglecting the effect of the flow field on the mapping procedure entails a scatterer displacement error proportional to (i) the difference between the velocity vector at $T_{FSI,2}$ at its mapped location and at its actual position when taking into account the flow motion, and (ii) the elapsed time between two FSI timesteps.

9.2.2.b Integrating FSI and ultrasound: creating a structure phantom

The structure phantom generation is less complex because of the Lagrangian grid formulation. The grid displacement corresponds with the material displacement and hence also with the scatterer displacement. However, the vessel wall needs more refined scatterer generation due to its complex composition, with flexibility of defining different scattering properties in different vessel regions. Therefore, point scatterers are generated in each hexahedron of the structural mesh. This way, scattering characteristics can be changed at very localized regions of the wall. In particular, the mesh was divided into 3 layers of hexahedrons, with scatterer properties easily modifiable for each layer. This represents to some extent the intima, media and adventitia of an artery, although we assumed equal thickness of each layer, while this is not the case in vivo. For each hexahedron of the mesh, a surrounding box was used to randomly generate scatterers, with points outside the bounding box being deleted, as illustrated in fig. 9.2. Displacement vectors were obtained by subtracting the grid position of $T_{FSI,1}$ from $T_{FSI,2}$ and assigning them to the scatterers by weighted averaging. Besides these random scatterers, the vessel wall also causes specular reflections at the transition regions between different tissue types (i.e. tissue/vessel wall and vessel wall/blood). Specular reflections can not be simulated in Field II but can be mimicked by positioning scatterers in a regular fashion at the wet and dry boundary of the structure, as illustrated in fig. 9.2-A. More specifically, for each hexahedron in the intima or adventitia layer, the side adjacent to a different tissue type was determined and scatterers were placed at fixed distances. These mimicked

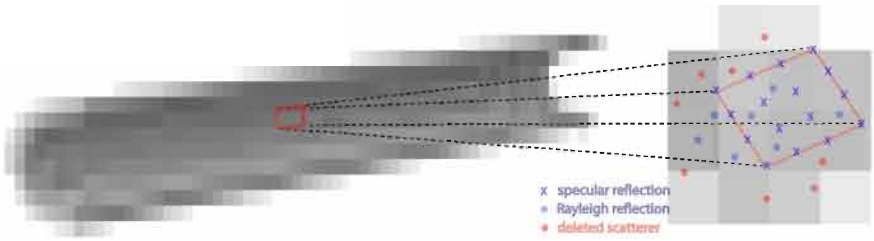

Figure 9.2: Illustration of the principles behind the creation of the structure scatterer phantom. The vessel wall is divided in several layers using hexahedral elements, allowing flexibility in changing scattering properties according to the concerned vessel layer. Due to the complex composition of the vessel wall (potentially including calcifications etc...), scatterers were created in the individual hexahedrons. A random uniform spatial distribution was obtained by creating them in a bounding box and deleting scatterers outside the considered hexahedron. Besides these random scatterers, specular reflections created by tissue transition regions were mimicked by placing scatterers at fixed distances at the wet and dry side of the structure.

specular reflections had a higher intensity than the scattering from the random tissue and blood scatterers. An overview of the different scattering properties attributed to the different tissues can be found in Table 9.1.

9.2.3 Ultrasonic imaging setup

Ultrasound applications for both flow and vessel wall imaging were investigated to validate and apply the new simulation tools. Wall shear rate imaging as described by [7, 8], and distension measurements [5] were chosen since distensible vessel phantoms are important for their analysis. For both applications, a linear array transducer with appropriate centre frequency and excitation was implemented. Each transducer element was divided into four smaller rectangular mathematical elements so that the backscattered signal from each point scatterer was simulated with sufficient accuracy. The focal depth position was set at 2 cm, and a dynamic focus and expanding aperture was used on receive to retain constant imaging properties throughout depth. To reduce beam sidelobes, apodization was applied (=amplitude weighting of the receiving transducer elements). A complete overview of the simulation parameters can be found in table 9.1. Both methods were based on ultrasonic velocity estimation of respectively blood and tissue as described below.

TABLE 9.1: Simulation setup for respectively the flow (F) and wall (W) application

Ultrasound set-up parameters for the shear rate and wall distension application		
	Blood flow	Wall distension
centre frequency f_0	5 MHz	8 MHz
# elements	192	192
Pitch	246 μm	203 μm
Height	6 mm	3.25 mm
Focus	2 cm	2 cm
Dynamic receive focusing	yes	yes
Expanding aperture	yes	yes
Pulseperiods	sinusoidal	sinusoidal
PRF_{max}	8000 Hz	8000 Hz
PRF	8000 Hz	1000 Hz
Packetsize	64	3

Assigned scatterer properties		
	Mean amplitude	STD
Inner wall (specular reflections)	0	1
Outer wall (specular reflections)	0	0.01
Wall	50	0.01
Blood	100	0.01

9.2.3.a *Vessel wall imaging application: measurement of vessel distension*

When measuring vessel distension, ultrasound signals are emitted perpendicular to the vessel wall. Vessel wall motion was tracked by integrating wall velocities: z[t+ Δt]=z[t]+v[t]Δt, with z[t] the position in the vessel wall, v[t] as estimated by ultrasound (modified autocorrelation approach [5]), and Δt the velocity resolution corresponding to the packet size times the pulse repetition period (3·1/1000). Only the RF-data of the arterial wall were processed for this application, hence neglecting a potential effect of the flow motion on the wall velocity estimator. Compared to the flow imaging application, an imaging setup with much higher resolution was required (i.e. shorter pulselength and higher frequency). The 12L linear array probe (GE Medical Systems, Milwaukee, WI, USA), as used in the applied distension software [5, 135], was modeled with a 1.5 period sinusoidal pulse excitation of 8 MHz centre frequency. Due to the lower velocity range of tissue

compared to blood, a lower PRF of 1 kHz was applied. Details of the ultrasound set-up are provided in Table 9.1.

9.2.3.b Flow imaging application: measurement of wall shear rate

For this application, the tube phantom was angled 70 degrees with respect to the ultrasound beam (=axial) direction, which is of the same order of magnitude as when measuring carotid blood flow in vivo. Velocity profiles in the axial direction were obtained using the autocorrelation algorithm described for ultrasound applications by Kasai et al [36], as most often used in color flow imaging. An ensemble of ultrasonic pulses is fired along the arterial cross-section and the phase-shift between the backscattered ultrasonic waves was estimated. The axial velocity v_z was calculated according to:

$$\frac{2\hat{v}_z f_0}{c} = \frac{PRF}{2\pi} \arctan\left(\frac{Im\left\{\widehat{R}(1)\right\}}{Re\left\{\widehat{R}(1)\right\}}\right) \tag{9.2}$$

with PRF (=pulse repetition frequency) the frequency of emitting ultrasound beams, f_0 the centre frequency of the ultrasound pulse and $\widehat{R}(1)$ the estimated autocorrelation function at lag 1. The Doppler signal from blood is completely defined by the autocorrelation function since it can be described by a complex Gaussian proces, and hence R(1) can be approximated with N-1 pairs of complex samples Z:

$$\widehat{R}(1) = \frac{1}{N-1} \sum_{i=1}^{N-1} Z(i-1)Z^*(i) \tag{9.3}$$

Note that only the RF-signal from the blood was used to estimate flow velocities. Hence, no clutter filter was applied to the data. A 4-period sinusoidal excitation pulse with 5 MHz centre frequency was chosen. Velocity profiles halfway the tube were obtained using a packet of 64 (=N) pulses emitted with a PRF of 8 kHz, resulting in 120 frames for the complete cardiac cycle and are first displayed as color M-mode images, presenting color-coded velocity information along the scanline as a function of time and depth. To obtain shear rate values, data are further processed by smoothing the two-dimensional distribution of angle-corrected velocities using a 2D median filter (2 pulselengths in depth and 3 cardiac frames) to remove occasional extreme velocity values. A sliding window averaging filter was used to remove further fluctuations. In the results, all displayed velocities are angle-corrected velocities and thus represent velocities along the axis of the tube. Finally, shear rate values are obtained by numerical differentiation of the velocity profiles.

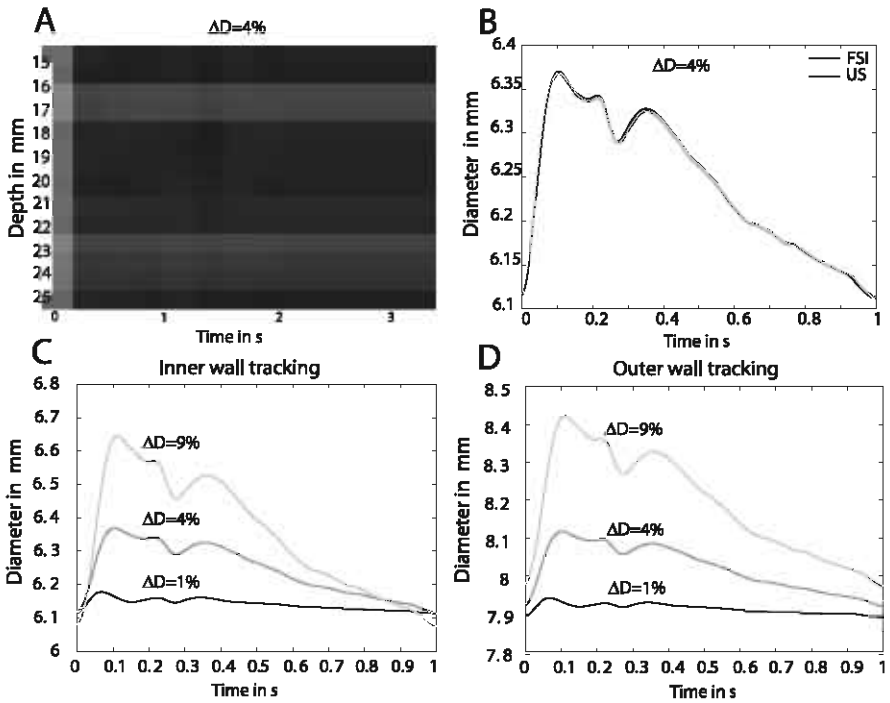

FIGURE 9.3: M-mode images were created based on RF-data obtained from the FSI-US coupling procedure, for the three simulated degrees of distension. These were further used for tracking the vessel wall motion using a modified autocorrelation approach [5]. Panel A shows an RF M-mode image for the 4 % distension case. Inner and outer wall tracking are shown for all cases in panels C and D. Panel B shows the comparison between the ultrasound wall tracking and the ground truth obtained from tracking Abaqus nodes.

9.3 RESULTS

For all three simulated cases, converged FSI simulations of two cardiac cycles were obtained within 12 hr. These FSI-datasets provided reference data on the deformation of the vessel wall and on the flow field and derived wall shear rate. RF-data of the complete cardiac cycle were obtained from the ultrasound simulations within 1.7 hr and 16 hr for respectively the fluid and structural part on 3.4 GHz Intel Pentium IV processors.

9.3.1 Vessel wall imaging application: measurement of vessel distension

RF ultrasound data for the wall were generated from the FSI-US coupling procedure, and are displayed as an M-Mode image in fig. 9.3-A. Using the distension software of Rabben et al [5], the motion of the

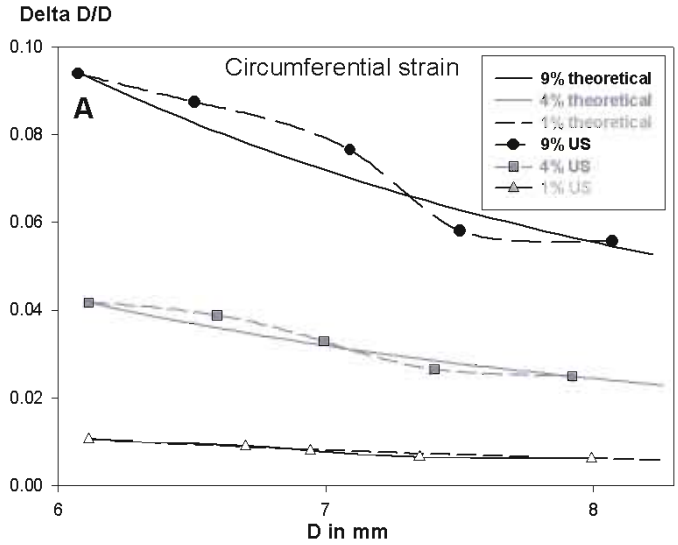

FIGURE 9.4: The circumferential strain ΔD/D for all distension degrees obtained with the FSI-US coupling procedure (dashed lines) and compared to the theoretical relationship (solid lines).

anterior and posterior intima-lumen transitions was tracked ('inner wall' tracking), as shown in fig. 9.3-A. Subtracting these tracking curves yielded the vessel diameter distension waveform, as displayed for the 4 % arterial distension in fig. 9.3-B (gray curve). An excellent match with the distension curve directly derived from the FSI simulations (black curve) was achieved (for all three cases). For the three simulated degrees of distension, the distension waveform obtained from the FSI-US coupling procedure is shown for the inner and outer wall tracking in Fig. 9.3-C & D.

In fig. 9.4, we further analyzed arterial distension using the circumferential strain ΔD/D, which is frequently used in clinical practice as a measure of arterial distensibility. Using the simulated RF-data, the circumferential strain ΔD/D was computed at several depths within the wall for all three distension degrees, as indicated by the dashed lines in fig. 9.4. Assuming an incompressible material and neglecting deformation along the vessel axis, the theoretical ΔD/D- curves were also computed and indicated by the solid lines. While the circumferential strain ΔD/D obtained from theoretical calculation as well as FSI computations resulted in a $1/D^2$ -relationship, this was not the case for the wall tracking based on the FSI-US coupling procedure. Interestingly, there was a very good match between theory and ultrasound wall

tracking based on the FSI-US data of the inner and outer wall tracking. However, tracking based on points within the vessel wall resulted in an S-shaped relationship between ΔD/D and depth in the arterial wall.

9.3.2 Flow imaging application: measurement of wall shear rate

Fig. 9.5 shows the color M-mode images as well as the two-dimensional velocity (angle-corrected values) and derived shear rate distribution in depth and time, obtained from the FSI-US coupling procedure for the three simulated cases. Since mass flow inlet boundary conditions were applied, smaller distensions resulted in higher velocities and shear rate profiles. For all cases, FSI-US shear rate reaches its maximum value at a certain distance from the wall. Fig. 9.6 shows in more detail the correspondence between the ground truth information (velocity profile and shear rate obtained from the FSI data) and the simulated ultrasound measurements, in case of the largest distension and for two different

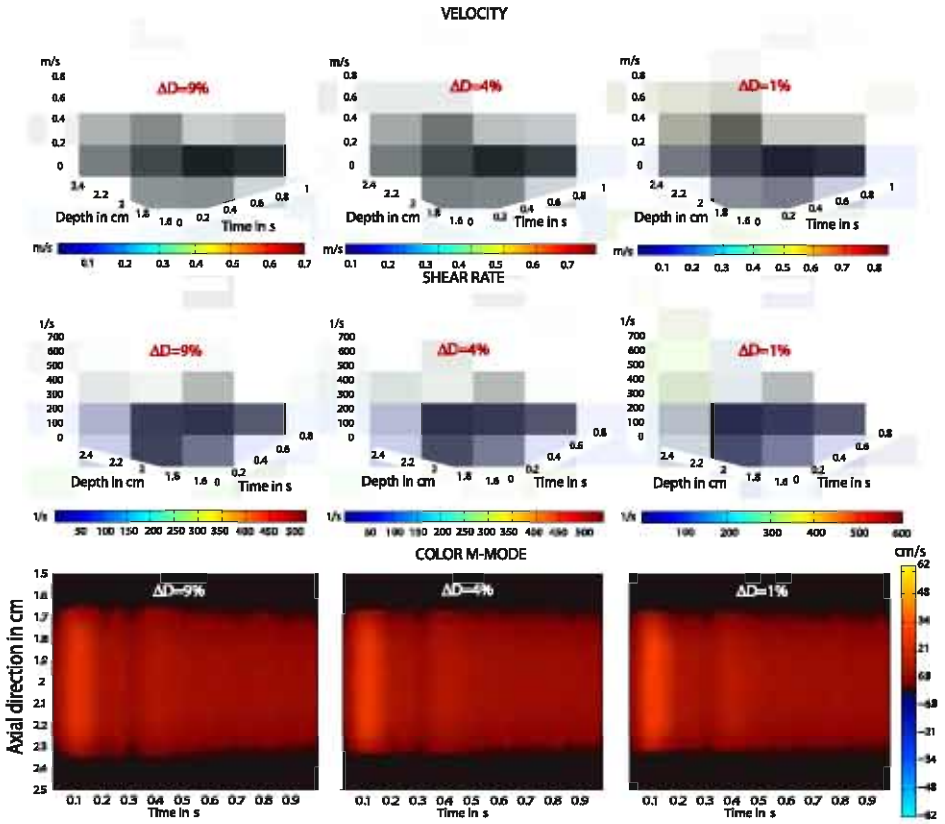

FIGURE 9.5: The two-dimensional velocity and shear rate distribution in depth and time for all degrees of distension. The lower row shows color M-mode images of the axial velocities (not angle corrected) corresponding to the shown 2D velocity distributions.

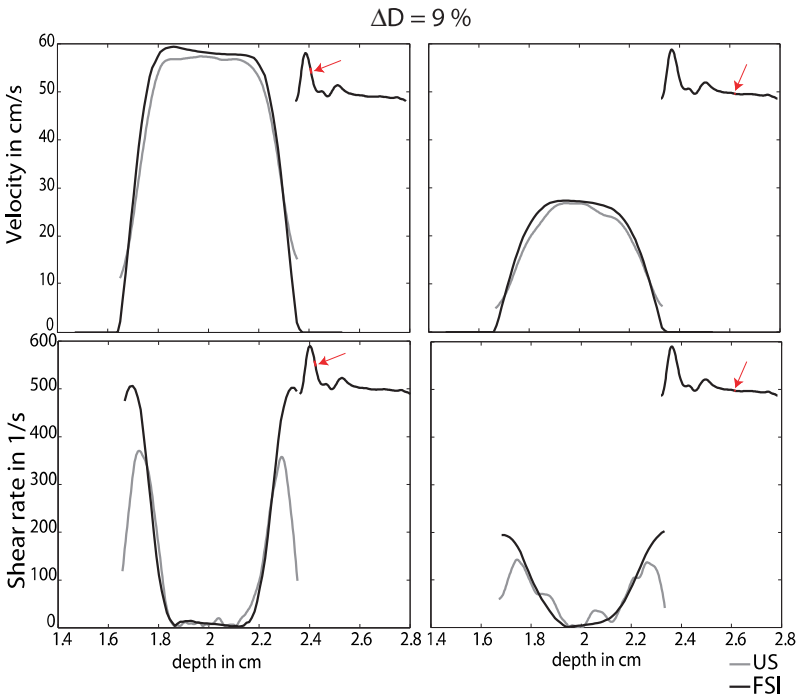

Figure 9.6: The velocity and shear rate profiles obtained from the FSI-US coupling procedure (gray) are compared to the FSI ground truth (black) at 2 cardiac frames, as indicated on the velocity curve imposed at the tube inlet. The ellipse indicates the posterior wall has a better agreement of FSI-US and FSI shear rates in space, compared to the anterior wall.

cardiac frames (as indicated on the velocity curve imposed at the tube inlet). FSI-US derived maximal shear rate is systematically lower than the reference value derived from the FSI simulations, with the largest discrepancy appearing near peak systole. This is also demonstrated in the upper panels of fig. 9.7 showing the maximal shear rate curve throughout the cardiac cycle for the three simulated cases. The lower panels of fig. 9.7 reveal the position of the maximal shear rate in the cardiac cycle as obtained from the FSI-US data, compared to the actual wall position. There was no clear relation between the location of maximal shear rate and the actual position of the arterial wall. However, one can notice that the position of the ultrasound-derived maximal shear rate shows an asymmetrical trend compared to the vessel centre: maximal shear rate is measured closer to the posterior wall than to the anterior wall for all distension degrees (see also fig. 9.7). For the anterior wall, the average distance between the position of maximal shear rate and the wall was 0.747±0.119, 0.815±0.185 and 0.810±0.138 mm for the 1%, 4% and 9% distension case, respectively. For the posterior wall,

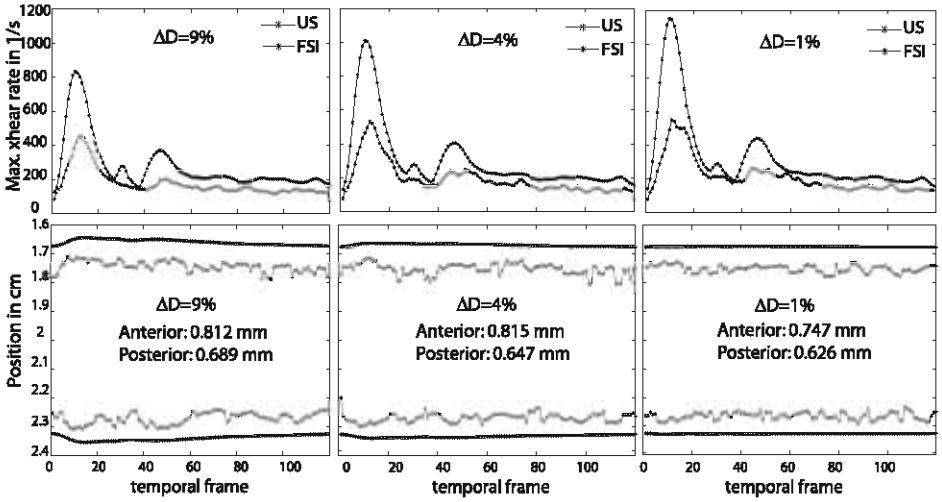

FIGURE 9.7: The upper panels show, for the 3 degrees of distension, the maximal shear rate throughout the cardiac cycle as derived from the FSI-data and from the FSI-US simulations. The lower panels show the position of the maximal shear rate compared to the actual wall position. The average distance of the maximal shear rate to the wall position is given for the anterior and posterior side.

values were 0.626±0.119, 0.647±0.138 and 0.689±0.155 mm. Despite the fact that the maximal shear rate obtained from FSI-US is lower than the maximal FSI values, it is clear from fig. 9.7 that both values show similar patterns throughout the cardiac cycle and that they are

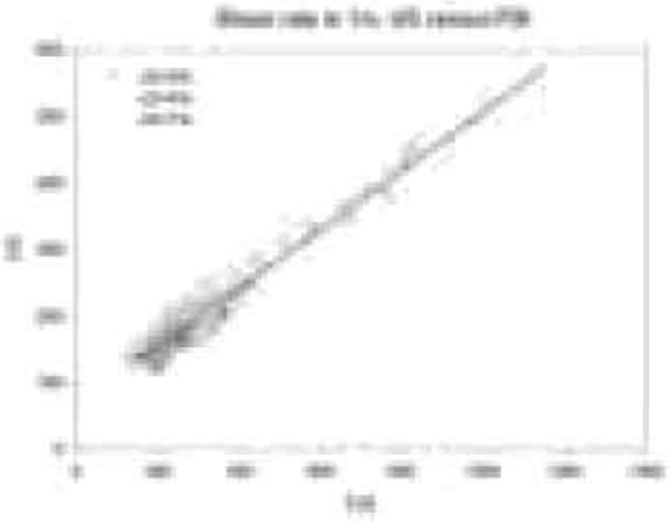

FIGURE 9.8: Correlation between the maximal shear rate as estimated by ultrasound and the FSI ground truth values for all distension degrees. For the three simulated cases, a similar linear trend is found ($y = 0.44\,x + 65$ 1/s).

correlated. To assess whether this correlation is the same for the three simulated cases, the shear rate values obtained from FSI-US simulations are plotted versus the FSI ground truth values in fig. 9.8. Both curves were aligned in time (using the peak as reference) to account for the temporal filtering effect resulting from the averaging and smoothing operations on the FSI-US velocity curves. Ultrasound significantly underestimated the actual wall shear rate for all three distension degrees but the same linear trend was observed for the different cases (y=0.44x+65 1/s). It is clear that the underestimation by ultrasound augments for increasing shear rate values. For an FSI reference value of 200 1/s, the underestimation is about 25 %, increasing to about 50 % for a reference value of 800 1/s.

9.4 Discussion

The work presented in this study is an extension of our previously described method of coupling CFD and Field II ultrasound simulations, allowing us retrieving RF-signals from complex flow fields with flexible control of flow and imaging parameters [110]. Using this tool, different uni- and multidimensional flow imaging methods were evaluated in the presence of complex flow [132]. However, this simulation tool was based on flow simulations assuming rigid walls, neither did it allow us to derive RF-data from the vessel wall itself. Therefore, we extended our approach and coupled the Field II ultrasound simulation software with flow and tissue data obtained from FSI-simulations, which take into account the complex interaction between fluid and arterial wall mechanics when solving the flow and structural equations. As for the CFD-US simulation environment, RF-signals were simulated with the Field II ultrasound software where tissue is represented by point scatterers. Scatterer positions were derived from the fluid velocity and structural displacement fields as computed by an in-house FSI-code ("Tango") which allows to couple Fluent with Abaqus. To validate the coupling procedure (in particular the computation of the fluid and structure scatterer phantom) and to demonstrate the potential of the multi-physics model, we simulated the flow in a deforming straight 3D tube with dimensions and fluid characteristics representative for blood flow in the common carotid artery. Three different degrees of arterial distension were modeled and the potential of the simulation tool was demonstrated with ultrasonic distension and wall shear rate measurements.

Integration of biomechanics and ultrasonic analysis is not novel, but in most studies either the biomechanical part has been simplified (using analytical equations or in-vivo measurements for the flow and/or mechanical behaviour [56, 59, 104]), either the ultrasound physics model has been compromised [61]. The work showing the closest agreement with ours was recently published by Balocco et al [140], who proposed a simulation model where the Field II simulation software is integrated with fluid-structure interaction as computed by COMSOL multiphysics. The simulated RF-lines were further processed to produce B-mode, M-mode images, and Doppler blood velocity estimations. Unfortunately, Balocco et al. provide limited detail on the creation of their scatterer phantom (and associated complexities) and on the imaging set-up used to create the B-mode, M-mode and flow images, making it difficult to directly compare the performance of both models. As for the fluid-structure interaction simulations, we used an in-house code (Tango) which allows to (strongly) couple any black-box CFD and structural solver (in our case Fluent with Abaqus). The described methodology is therefore generically applicable, and provides computational results equivalent to those obtained using a monolithical solver such as COMSOL. Major differences between studies may exist in the way the scatterer phantom is created. Unfortunately, Balocco et al. do not disclose any details in this respect and it is unclear how they dealt with the difficulties related to the interpolation in time and space of scatterer positions in a deforming geometry, a non-trivial problem. Both studies are, however, totally different at the level of the chosen ultrasound applications. We focused our simulations on applications where the motion of the arterial wall - and hence the FSI interaction - is particularly important, i.e. measurement of hemodynamic (wall shear rate) and mechanical (vessel distension) indices of arterial function. These techniques are commonly applied in pre-clinical vascular research, but there is still a lack of clarity concerning the accuracy (shear rate) and the link with intrinsic mechanical properties (vessel distension) hampering their use on a larger scale in clinical studies. We studied these problems in a tubular (but 3D) model for two main reasons: (i) as we study quite advanced applications based on data derived from the flow field (shear rate) and wall deformation (tissue velocities and wall distension), it is justified to start with a geometry where flow field and wall deformation are more comprehensible than in the complex case of a bifurcating vessel, where not only the flow field but also

the wall deformation is complex, with out-of-plane motion, swirling flow, etc... (ii) the applications studied are clinically applied to straight vessel segments such as the brachial or common carotid artery, which are tubular-like structures.

Although a validation of our model in a strict sense is not straightforward, our results clearly indicate that our approach provides RF-data leading to realistic ultrasound images (as we also previously demonstrated for the CFD-US simulations [131]). For the vessel wall imaging, the distension curve as obtained by tracking Abaqus nodes from the FSI-simulation was compared to the ultrasonic wall tracking result at a similar depth in the vessel wall (fig. 9.3). This was shown in fig. 9.3-B for the 4 %-distension case with a quasi perfect match between input and output of the FSI-US coupling procedure, and a similar level of agreement was obtained for the two other cases. The fluid phantom used for the FSI-US integration resulted in velocity profiles showing a clear resemblance with the Fluent solution (fig. 9.6), and demonstrating typical deviations from the actual velocity profile (especially near the wall) as can be expected from ultrasound measurements. Data are also in good quantitative as well as qualitative agreement with in vivo data reported by Hoeks et al. and Brands et al [7, 8].

We subsequently focused on two applications of clinically relevant vascular imaging methods, one involving the arterial wall and one involving the blood flow. A commonly applied measure for arterial distensibility is ΔD/D (= circumferential strain in case of planar deformation). Ultrasonic wall tracking algorithms have been developed to track vessel wall motion based on integrating estimated tissue velocities [5]. The RF wall tracking based on our FSI-simulations demonstrated that ΔD/D is very sensitive to measurement location (cfr. fig. 9.4), with a decreasing trend in ΔD/D from inner to outer wall , confirming results from previous in-vivo studies [135]. Although we expected a $1/D^2$ dependency on theoretical grounds, we rather obtained an S-curve of ΔD/D, which was flattened in the neighborhood of tissue transitions. This curve flattening can be explained by the strong (specular) reflections present near the vessel wall boundaries, which blur the velocity measurement in its immediate neighborhood. Indeed, when repeating the ultrasound simulations without specular reflections, the theoretical $1/D^2$ dependency was obtained (data not shown). Hence, deducing deformation trends and material properties of the studied vessel

wall tissue based solely on wall tracking measurements within the arterial wall may lead to flawed interpretations. This might particularly be the case in the presence of arterial calcifications, causing sharp echographic interfaces in the arterial wall.

Considering the flow field application, simulation of wall shear rate assessment prevailed excellent agreement with the findings of Brands et al [7, 8], who demonstrated that the maximum of ultrasound-derived wall shear rate was obtained at a certain distance from the wall. We could not observe a relation in the location of maximal shear rate and vessel distension, but maximal shear rate location was closer to the posterior than anterior wall, when calculating the average distance between the vessel wall and maximal shear rate location. The observed distances were in the same order as can be derived from the data shown in Brands et al [7] ($\pm$ 833 μm when deriving this from their reported figures). The (small) difference between FSI-US velocity measurements at the anterior and posterior wall is related to the ultrasound physics (e.g. point spread function of the ultrasound system is asymmetrical in the depth direction with higher intensities below than above the imaged point) and not to the numerical FSI calculations, which show axial symmetry in the results.

Brands et al tested their wall shear rate measurements in-vivo and in-vitro. For 30 in-vivo carotid examinations, they found a low variance on the reproducibility of the wall shear rate measurement (5%) [7]. The in-vitro study entailed validation with laser Doppler anemometry (LDA) in a flow model of a distensible tube. However, a larger discrepancy of 11 % was reported between both methods [7]. Note that LDA has a similar limitation as ultrasound in the sense that it does not allow measurement of flow velocities near a moving wall. Hence, this in-vitro validation can not be considered as a real reference value for the actual shear rate. It is here that our FSI-US model has an added value. In fig. 9.8, we have plotted the maximal shear rates as estimated by ultrasound versus the FSI ground truth values. Interestingly, a similar linear relation was revealed for all distension degrees, suggesting that the underestimation by ultrasound could be compensated for (at least for the simulated setting). Finally, it is worth mentioning that in pulsatile flow conditions, the maximal shear rate not necessarily occurs at the position of the wall itself even for the simple case of a straight tube (as illustrated by fig. 9.6).

Note, however, that further optimization of the simulation of shear rate imaging is necessary before drawing hard conclusions with respect to real-life in vivo applications. In particular, the ultrasound signal generated by the wall should be taken into account as well as an extensive study of the influence on the applied clutter filter, which was neglected in this study. Also, the settings applied during processing of the ultrasound data (e.g. temporal and spatial filtering) are crucial for the estimates of velocity and even more for the obtained values of the wall shear rate. As such, the simulations should be well matched with the settings used for the in-vivo imaging. Further, the simulated cases here represent blood flow in straight arterial segments, with a fully developed symmetrical inflow velocity profile. It can be anticipated that in bended arteries and in the vicinity of complex bifurcations (such as the carotid artery), the flow profile will be far more complex. In these conditions, the correspondence between ultrasound-based estimates of wall shear rate and their actual values will, without any doubt, be far more complex.

Although the multiphysics model as presented in this study represents a major improvement over our existing model, limitations are still present, both at the biomechanical and acoustical level. Concerning the FSI-simulations, different distension degrees could have been modeled by applying stiffer material properties. However, since we were only interested in wall movement and not wall stresses, we only scaled the pressure wave. More realistic material behavior including anisotropic and hyperelastic material properties could have been modeled (at the expense of higher computational times). The influence of the surrounding tissue on the vessel wall movement, residual stresses and effects of longitudinal pre-stretch of the structure could be taken into account in future work. Further, the boundary conditions to solve the fluid problem could be refined by applying a physiologically realistic vascular impedance as outlet boundary condition, inducing more realistic wave reflection and propagation phenomena in the tube.

The Field II method is also based on some assumptions: nonlinear propagation of ultrasound waves and multiple scattering are not included, with the latter one limiting the accuracy of distension measurements in-vivo. The Field II-approach also ignores the shape of the scatterers (disc shaped red blood cells). We did not include frequency

dependent scattering or noise in our simulations. Furthermore, the tissue echogenic properties are simulated as a combination of random scatters in the wall and mimicked specular reflections along the inner and outer boundary of the wall. Although this results in realistically looking RF spectra, further fine-tuning and optimization towards RF-spectra of actual tissue may be mandatory, especially when simulating more complex arterial tissues with the inclusion of vessel inhomogeneities and plaque. In particular, the fibrous structure of the vessel wall which leads to scattering correlation in the fiber direction could be included in the phantom modeling. It should also be stressed that the distension data are solely based on RF-signals from the wall, while the shear rate application relied only on RF-signals from the flow. The shown applications should therefore mainly be considered as a demonstration of the potential of the simulation tool in developing vascular imaging tools, rather than a thorough validation of each of these applications. It is, for that matter, most likely that the imaging and signal processing setups can be further optimized for each specific application.

In summary, we demonstrated a simulation environment to validate and develop ultrasonic vascular imaging applications. An elaborate technique to integrate fluid-structure interaction (FSI) and the Field II ultrasound simulation software was presented. This multiphysics ultrasound simulation environment was applied to two ultrasound imaging applications where distensible ultrasound phantoms are indispensable for their analysis: wall distension and wall shear rate measurement, applied to the case of a straight 3D tube subjected to three levels of distension. The RF wall tracking algorithm was able to quasi perfectly track the motion of the inner and outer vessel wall. As anticipated, distension measurements showed a high sensitivity to measurement location in the wall but the simulations also revealed that strong specular reflections from tissue transitions potentially cloud correct measurements within the media of the vascular wall. Further, the flow imaging application revealed that maximal shear rate was measured at a certain distance from the vessel wall as previously demonstrated in vivo by Brands et al [7, 8], and that the location where measured shear rate is maximal, is closer to the posterior than to anterior wall. For the three simulated cases, a similar linear trend between ultrasound estimated shear rate and the FSI-ground truth was found, suggesting that the underestimated ultrasound values could be corrected for. Based

on the above observations, we conclude that our method to couple fluid-structure interaction and ultrasound simulations provides realistic radio-frequent signals from both the tissue and the blood pool which can be processed into ultrasound-derived medical images and measurements. Further research will focus on applications for the ultrasonic investigation of the carotid bifurcation.

Five

Conclusions

CHAPTER 10

Conclusions

10.1 The future of vascular ultrasound

Due to its efficacy, low cost, non-invasive and patient-friendly nature, and proven clinical value, ultrasound has become and remains one of the world's leading medical imaging modalities. A wide range of applications has become available over the past decades, with its ability to image moving structures in real-time as a particular strength. In this manuscript, we focused on ultrasound imaging for vascular purposes, which has been shown to be as accurate as the more expensive imaging modalities (MRI, CT...) in the diagnosis of vascular disease [141]. As such, a bright future is still ahead for vascular ultrasound. However, to further improve diagnosis and to stay competitive with other imaging modalities, more sophisticated methods for blood flow and vessel wall visualization are indispensable.

We developed a multiphysics simulation environment to improve vascular imaging modalities, using an advanced model for the ultrasound imaging setup as well as for the vessel hemodynamics and mechanics. We demonstrated the reliability, accuracy and realism of the simulated ultrasound data, as well as its usefulness in validating and exploring new imaging modalities. Further, we believe that the key strength of this work lies in its multidisciplinary nature, unifying several domains

in the field of biomedical engineering. Due to the increased computational power of the past years, such an approach has not only become feasible but is also essential when striving for optimized ultrasound imaging.

10.2 Assessing the realism of the developed simulation environment

Creating a multiphysics simulation tool for ultrasonic image improvement sounds very appealing, especially since in-vitro and in-vivo testing may not provide sufficient validation. As such, we developed a simulation environment, combining the power of computational blood vessel modeling and ultrasound simulations. More particularly, the Field II ultrasound simulation software was first coupled with computational fluid dynamics (CFD), to provide a versatile tool in validating flow imaging modalities. In a next stage, ultrasonic images of both the blood flow and vessel wall were simulated by integrating fluid-structure interaction (FSI) simulations with the ultrasound simulation model. For both coupling methodologies, the performance of our simulation tool was demonstrated by relating the synthetic images with the ground truth as obtained from CFD or FSI.

Although the basic performance of the simulation environment was established this way, one should pay attention to the necessary realism and clinical relevance of the developed tool. For this purpose, the truthfulness of our simulator was assessed by comparing the simulated ultrasound data to real images. First, the degree of realism of the CFD-Field II coupling was judged, by matching the simulated imaging setup with an in-vitro flow model of a carotid artery. In this study, we directly linked the simulated and measured ultrasound images. Indeed, the flow field from the experiments was simulated with CFD, by scanning the in-vitro phantom and measuring the appropriate boundary conditions during the experiment. The CFD-results were subsequently used as an input to the Field II simulations. Good qualitative and quantitative agreement was obtained between simulated and experimental ultrasound flow images, although future research may improve the similarity between both, by refinements at the level of both the CFD and ultrasound simulations, as well as the experimental design.

The realism of our model was also considered when exploring 2D flow

estimation, more particularly in the study analyzing the performance of a combined "speckle tracking-phase shift estimation" approach. Following a comparative study based on synthetic data, the feasibility of both the combined flow estimator and speckle tracking was demonstrated with in-vivo data from a carotid artery of a healthy volunteer. It should be noted that we could not perform CFD-simulations based on the carotid artery of the studied volunteer. Hence, the in-vivo data were only indirectly compared to the simulated results, and performance of the imaging methods was judged based on expected flow patterns. Therefore, our future plans include improved in-vivo validation of the simulations, by performing CFD/FSI-simulations based on a vascular geometry and boundary conditions measured in a patient with a significantly stenosed carotid artery. These data can then be used to construct the computational scatterer phantom for the Field II simulations.

10.3 Improving blood flow visualization

Using our CFD-Field II simulation tool, we confirmed the inability of the traditional 1D flow estimators to visualize complex 3D flow patterns. This conclusion is based on comparison of the simulated color flow images with the true flow field as obtained from CFD. Hence, the logical continuation of our research was to investigate multidimensional flow estimation, and study the strengths and weaknesses of two techniques being explored by the medical ultrasound community: speckle tracking (ST) and vector Doppler (VD).

Both techniques are challenging to implement, and no clinically robust method has resulted yet. ST is complicated because it needs high frame rates to track the quickly moving blood. Further, speckle patterns may decorrelate in the presence of temporal and spatial flow gradients, deteriorating the performance of the method. VD is mainly hampered by aliasing, as is the case with 1D Doppler techniques. Furthermore, the angle between the transmission and receive scanline should be sufficient to obtain reliable lateral flow velocity estimates. However, the angle can not be chosen arbitrarily because of the limited transducer sizes. Both methods are also affected by the strong tissue signal in the vessel lumen. No vessel wall was present in our simulations, but the effect of clutter filtering on the flow estimates was taken into account. In our simulated imaging setups, VD suffered most (dramatically) from

this.

Overall, our results showed that the performance of both flow estimators is very dependent on when (in the cardiac phase) and where (in the carotid artery) the flow field is measured. We could conclude that ST was in general a better lateral (perpendicular to scanline) flow velocity estimator, and VD a better axial (parallel to scanline) flow velocity estimator. However, due to practical scanning limitations present for VD, and because ST achieves a higher dynamic range of accurately measured velocities, ST is considered as a more consistent and practical approach.

It should be noted that although different imaging setups were explored in this study, a thorough parameter study of both 2D flow estimators is required to fully establish their applicability. More particularly, the sensitivity of VD to different scanning angles, and the effect of different tracking setups on ST should be investigated. Furthermore, the performance of other imaging techniques like plane wave imaging and parallel receive beamforming, which both allow higher frame rates for speckle tracking, should be analyzed and compared to our presented study.

As ST is the better lateral velocity estimator and VD the superior axial velocity estimator, a combination of both methods can potentially result in a more robust method. As such, we defined a flow estimator based on ST to measure lateral flow and using phase-shift estimation (PE), as used in VD, to obtain the axial flow velocity component. This flow estimator requires a common acquisition scheme, which is quite challenging as the nature of both measurement techniques is quite different. Good speckle tracking results are desired, but at the same time, aliasing should be avoided for the Doppler-component. Therefore, we proposed an anti-aliasing approach based on the axial estimate from ST, which was successful to some extent, but also introduced spurious unwrapping errors. As was the case for the ST and VD study, the data were quite dependent on the position and timing of the flow measurement, but in general, both simulated and in-vivo data showed clinical potential.

Another flow related imaging method was studied using the coupled FSI-Field II simulation tool: wall shear rate imaging. This technique is

still in an experimental phase, but is highly clinically relevant as wall shear rate is an important biomechanical stimulus of endothelial function and a factor involved in the genesis of atherosclerosis. We investigated ultrasonic shear rate by measuring velocities along a scanline with a phase-shift estimation method. Maximal shear rate was underestimated compared to the true value, but results correlated well with the FSI ground truth. This suggests that correction of the severe underestimation by ultrasound is possible for the studied flow conditions. Further, shear rate was maximal at a certain distance from the wall, which was attributed to the difficulties in measuring near-wall velocities. The location of maximal shear rate was also closer to the posterior wall than the anterior wall, which can be explained by the spatially variant ultrasound system.

The presented investigation of wall shear rate was a pilot-study, which will be continued in the future. First of all, shear rate was obtained through a traditional 1D flow estimator, but it would be interesting to explore the potential of 2D flow estimators in this matter. Further, the feasibility of the method should be assessed in a 3D-geometry with complex flow patterns. Probably, the biggest challenge in assessing wall shear rate is clutter filtering, and improved filtering techniques are potentially necessary to make the method applicable in real-life conditions.

10.4 Improving vascular wall visualization

The integration of fluid-structure interaction simulations with Field II opened a new world of vascular imaging applications, namely those related to the vessel wall. Although no method has been developed yet to assess the true mechanical properties of the vessel wall, we investigated a parameter related to arterial stiffness, i.e. arterial distension.

Using an existing vessel distension algorithm, based on estimation of vascular tissue velocities [5], arterial distension measurements were investigated in straight vessel segments with different degrees of distensibility. We showed that this imaging application is highly sensitive to the measurement location, as previously reported in-vivo [135]. More interestingly, we found that the presence of strong echoes (like specular reflections) may cloud a correct measurement; a finding which might be of particular importance in calcified vessels.

Although the arterial distension measurement has shown its relevance in clinical trials, strain imaging methods assessing the complex 3D mechanical deformation are still desired, particularly in the context of plaque characterization and assessment of plaque vulnerability. Ultrasonic strain imaging methods have been developed to image cardiac motion and to detect cancerous tissue, but applying the same principles to the vessel wall is highly challenging due to the limited spatial resolution of ultrasound compared to the dimensions of vascular tissue. More advanced ultrasonic imaging techniques, like supersonic shear imaging [142], might be needed in this context.

10.5 What is beyond the horizon?

Until now, our simulation environment has been used to test human imaging applications. However, ultrasound is also a frequently applied imaging tool in small animal research. Mice models are commonly used to increase our knowledge on cardiovascular disease, and high frequency ultrasound examinations may play an important role in this respect. Especially the development of wall shear rate and strain imaging in mice might be useful to increase our understanding on the pathophysiology and genesis of atherosclerosis. In this context, a multidisciplinary project has taken off at our lab in 2010, with the ultimate aim to improve diagnosis and treatment of aneurysms and dissections. This project will include follow-up studies of genetically modified mice (aneurysms, plaques, Marfan-syndrome), and our simulation environment will support the exploration of new imaging modalities.

While this dissertation focused on imaging techniques relying on conventional linear array probes, the concept of our simulation environment could be expanded to more advanced techniques, like contrast-enhanced imaging, harmonic imaging, intravascular ultrasound,... This potentially requires the implementation of more specialized ultrasound simulation approaches. Further, we concentrated in this manuscript on vascular applications, and hence the cardiac field remains unexplored territory. Accurate modeling of cardiac imaging will however require advanced FSI-models, to capture the complex heart motion. Since 3D cardiac imaging modalities have recently become available, it would also be interesting to extend the 3D imaging concept to vascular applications with the help of our simulation tool.

Finally, we would like to mention that clinical validation of the investigated ultrasound imaging modalities is one of our future priorities. Improving early detection of cardiovascular disease has always been one of the major research lines of our research group. One of our most elaborate and ongoing research projects in this matter is the Asklepios population study, which follows up over 2500 seemingly healthy adults between 35 and 55 years at the onset of the study, to find preliminary indicators of cardiovascular disease. In this study, ultrasound is extensively used as an imaging tool, and as such, these data offer a large playground to clinically test our simulation results.

Bibliography

[1] A. Bonny, F. Lacombe, M. Yitemben, B. Discazeaux, J. Donetti, P. Fahri, R. Megbemado, and B. Estampes. *The 2007 ESH/ESC Guidelines for the management of arterial hypertension.* Journal of Hypertension, 26:825–825, 2008.

[2] J.S. Wright, J.K. Cruickshank, S. Kontis, C. Dore, and R.G. Gosling. *Aortic compliance measured by non-invasive Doppler ultrasound: description of a method and its reproducibility.* Clin. Sci., 78:463Ű468, 1990.

[3] M. De Melis, U. Morbiducci, L. Scalise, E.P. Tomasini, D. Delbeke, R. Baets, L. Van Bortel, and P. Segers. *A Noncontact Approach for the Evaluation of Large Artery Stiffness: A Preliminary Study.* American journal of hypertension, 21:1280–1283, 2008.

[4] J. Benyu, L. Baoming, K.L. McNeill, and P.J. Chowienczyk. *Measurement of pulse wave velocity using pulse wave Doppler ultrasound: comparison with arterial tonometry.* Ultrasound in Medicine & Biology, 34:509–512, 2008.

[5] S. I. Rabben, S. Bjaerum, V. Sorhus, and H. Torp. *Ultrasound based vessel wall tracking: an autocorrelation technique with RF center frequency estimation.* Ultrasound in Med. & Biol., 28:507–517, 2002.

[6] S. Glagov, C. Zarins, D. P. Giddens, and D. N. Ku. *Hemodynamics and atherosclerosis.* Arch. Pathol. Lab. Med., 112:1018–1031, 1988.

[7] P. J. Brands, A. P. G. Hoeks, L. Hofstra, and R. S. Reneman. *A non-invasive method to estimate wall shear rate using ultrasound.* Ultrasound in Med. & Biol., 21:171–185, 1994.

[8] A. P. G. Hoeks, S. K. Samijo, P. J. Brands, and R. S. Reneman. *Noninvasive Determination of Shear-Rate Distribution Across the Arterial Lumen.* Hypertension, 26, 1995.

[9] L.F. Richardson. *British patent no.12.* Filed May 10 1912, issued March 27 1913.

[10] B. Goldberg, R. Gramiak, and A. Freimanis. *Early history of diagnostic ultrasound: the role of american radiologists.* AJR. Am. J. Roentgenol., 160:189–194, 1993.

[11] G.D. Ludwig. *The velocity of sound through tissues and the acoustic impedance of tissues.* Journal Acoustic Society America, 22:862–866, 1950.

[12] J. Wild and J. Reid. *Application of echo-ranging techniques to the determination of structure of biological tissues.* Science, 115:226–230, 1952.

[13] D. Howry and W. Bliss. *Ultrasonic visualization of soft tissue structures of the body.* J. Lab. Clin. Med., 40:579Ű592, 1952.

[14] I. Edler and C. Hertz. *The use of ultrasonic reflectoscope for the continuous recording of the movements of heart walls.* Clin Physiol Funct Imaging, 24:118Ű136, 1954.

[15] S.Satomura. *Ultrasonic doppler method for the inspection of cardiac functions.* J. Acoust. Soc. Am., 29:1181Ű1185, 1957.

[16] C. Rumack, S. Wilson, and J. Charboneau. *Diagnostic ultrasound.* St. Louis: Elsevier Mosby, 2005.

[17] J. A. Jensen and N. B. Svendsen. *Calculation of pressure fields from arbitrarily shaped, apodized, and excited ultrasound transducers.* IEEE transactions on Ultrasonics, Ferroelectrics, and Frequency control, 39(2):262–267, 1992.

[18] J. A. Jensen. *Field: A program for simulating ultrasound systems.* Medical and Biological Engineering and Computing, 34:351–352, 1996.

[19] D. H. Evans and W. N. McDicken. *Doppler ultrasound: Physics, instrumentation and signal processing.* John Wiley & Sons Inc, 2000.

[20] R.S.C. Cobbold. *Foundations of biomedical ultrasound.* Oxford university press, 2007.

[21] K.K. Shung. *Diagnostic ultrasound.* CRC press, Taylor and Francis group, 2005.

[22] T.Szabo. *Diagnostic ultrasound imaging.* Elsevier academic press, 2004.

[23] J.A.Jensen. *Estimation of blood velocities using ultrasound.* Cambridge university press, 1996.

[24] B.Angelsen. *Ultrasound Imaging Waves, Signals, and Signal Processing.* Emantec AS, Trondheim, Norway, ISBN 82-995811-2-5.

[25] B. Angelsen. *A theoretical study of the scattering of ultrasound from blood.* IEEE Trans Biomed Eng, 27:61–67, 1980.

[26] L. Lovstakken. *Signal processing in diagnostic ultrasound: Algorithms for real-time estimation and visualization of blood flow velocity.* ISBN: 978-82-471-0525-2, Trondheim, Norway, 2007.

[27] H.F. Routh, Y.F. Law, L.Y.L. Moa, M. Ojha, and P.J. Vaitkus. *Role of models in understanding and interpreting clinical Doppler ultrasound.* Medical progress through technology, 15:155–169, 1989.

[28] J.G. Abbot and F.L. Thurstone. *Acoustic speckle: theory and experimental analysis.* Ultrasonic imaging, 1:303–324, 1979.

[29] J. Acoust. Soc. Am. *Modeling of nonlinear ultrasound propagation in tissue from array transducers.* Advances in echo imaging using contrast enhancement, 113:139–152, 2003.

[30] D.H. Simpson, P.N. Burns, and J.Souquet. *Techniques for perfusion imaging with microbubble contrast agents.* IEEE Trans. Ultrason. Ferroelect. Freq. Contr, 48:1483–1494, 2001.

[31] V.L.Newhouse, A.R. Ehrenwald, and G.F. Johnson. *The dpendence of ultrasound Doppler bandwidth on beam geometry.* IEEE. Trans. Son. Ultrason., 27:50–59, 1980.

[32] A.V. Oppenheim and P.W. Schafer. *Digital signal processing.* Prentice Hall, Englewood Cliffs, NJ, 1975.

[33] P.D. Welch. *The use of fast Fourier transform for the estimation of power spectra: a method based on time averaging over short, modified periodograms.* IEEE Trans Audio Electroacoust, AU-15:70–73, 1967.

[34] T.Loupas, J.T. Powers, and R.W.Gill. *An axial velocity estimator for ultrasound blood flow imaging, based on a full evaluation of the Doppler equation by means of a two-dimensional autocorrelation approach.* IEEE. Trans. Ultrason. Ferroelec. Freq. Contr., 42:672–688, 1995.

[35] H.Torp and K.Kristoffersen. *Velocity matched spectrum analysis: a new method for surpressing velocity ambiguity in pulsed-wave Doppler.* Ultrasound Med. Biol., 21:937–944, 1995.

[36] C. Kasai, K. Namekawa, A. Koyano, and R. Omoto. *Real-Time Two-Dimensional Blood Flow Imaging Using an Autocorrelation Technique.* IEEE Transactions on Sonics and Ultrasonics, 32(3):458–464, 1985.

[37] P.Z.Peebles. *Probability, random variables and random signal processing.* McGraw-Hill, NY, 1993.

[38] F.E. Barber, J.W. Eberhard, and S.G. Karr. *A new time domain technique for velocity measurements using Doppler ultrasound.* IEEE Trans. Biomed. Eng, 21:109–113, 1974.

[39] O.Bonnefous and P.Pesqué. *Time domain forumation of pulse-Doppler ultrasound and blood velocity estimation by cross correlation.* Ultrasonic imaging, 8:73–85, 1986.

[40] H.Torp, X.M. Lai, and K. Kristoffersen. *Comparison between cross-correlation and auto-correlation technique in color flow imaging.* Proceedings of the 1993 IEEE Ultrasonics Symposium, IEEE, Piscataway, NJ:1039–1042, 1993.

[41] S. Bjaerum, H. Torp, and K. Kristoffersen. *Clutter filter design for ultrasound color flow imaging.* IEEE Transactions on Ultrasonics, Ferroelectrics and Frequency Control, 49(2):204–216, 2002.

[42] L.N. Bohs and G.E. Trahey. *A novel method for angle independent ultrasonic imaging of blood flow and tissue motion.* IEEE Transactions on Biomedical Engineering, 38(3):280–286, 1991.

[43] L. N. Bohs, B. H. Friemel, and G. E. Trahey. *Experimental velocity profiles and volumetric flow via two-dimensional speckle tracking.* Ultrasound in medicine & biology, 21(7):885–898, 1995.

[44] L.N. Bohs, B.J. Geiman, M.E. Anderson, S.M. Breit, and G.E. Trahey. *Ensemble tracking for 2D vector velocity measurement: Experimental and initial clinical results.* IEEE Transactions on Ultrasonics, Ferroelectrics and Frequency Control, 45(4):912–924, 1998.

[45] Jesper Udesen, Michael Bachmann Nielsen, Kristina Rue Nielsen, and Jorgen Arendt Jensen. *Examples of In Vivo Blood Vector Velocity Estimation.* Ultrasound in Medicine & Biology, 33(4):541–548, April 2007.

[46] M.D. Fox. *Multiple Crossed-Beam Ultrasound Doppler Velocimetry.* IEEE Transactions on Sonics and Ultrasonics, 25(5):281–286, 1978.

[47] M. Scabia, M. Calzolai, L. Capineri, L. Masotti, and A. Fort. *A real-time two-dimensional pulsed-wave Doppler system.* Ultrasound in Medicine & Biology, 26(1):121–131, 2000.

[48] E.G.A. Aird and J.Conway. *CT simulation for radiotherapy treatment planning.* British Journal of Radiology, 75:937–949, 2002.

[49] J. Bittoun, J. Taquin, and M. Sauzade. *A computer algorithm for the simulation of any nuclear magnetic resonance (NMR) imaging method.* Magn. Reson. Imaging, 2:113–120, 1984.

[50] J.A. Jensen. *Linear description of ultrasound imaging systems.* Notes for the international summer school on advanced ultrasound imaging Technical University of Denmark, Release 1.01, 2001.

[51] A.D. Pierce. *Acoustics, An Introduction to Physical Principles and Applications.* Acoustical Society of America, New York, 1989.

[52] J.A. Jensen. *A new calculation procedure for spatial impulse responses in ultrasound.* Journal of the acoustical society of America, 105:3266–3274, 1999.

[53] H. Gao, H. F. Choi, P. Claus, S. Boonen, S. Jaecquesa, G. H. van Lenthe, G. Van der Perre, W. Lauriks, and Jan DŠhooge. *A Fast Convolution-Based Methodology to Simulate 2-D/3-D Cardiac Ultrasound Images.* IEEE TUFFC, 56(2):404–409, 2009.

[54] T.Hergum, S.Langeland, E.Remme, and H. Torp. *Fast Ultrasound Imaging Simulation in K-space.* IEEE TUFFC, 56(6):1159–1167, 2009.

[55] J.A. Jensen. *Users' guide for the Field II program.* Release 2.86, August 17:1–58, 2001.

[56] J.A.Jensen and P.Munk. *Computer phantoms for simulating ultrasound B-mode and CFM images.* Acoustical imaging, 23:75–80, 1997.

[57] R.F. Wagner, S.W. Smith, J.M. Sandrik, and H. Lopez. *Statistics of speckle in ultrasound B-scans.* IEEE Transactions on sonics and ultrasonics, 30(3):156–163, 1983.

[58] J.M.Thijssen. *Ultrasonic speckle formation, analysis and processing applied to tissue characterization.* Pattern Recog. Lett., 24:659Ű675, 2003.

[59] A.T.Kerr and J.W.Hunt. *A method for computer simulation of ultrasound doppler color flow imagesŮI. theory and numerical method.* Ultrasound in Med. and Biol., 18:861–872, 1992.

[60] H.Oung and F. Forsberg. *Doppler Ultrasound Simulation Model for Pulsatile Flow with Nonaxial Components.* Ultrasonic Imaging, 18:157–172, 1996.

[61] M.Khoshniat, M.Thorne, T.Poepping, S.Hirji, D.Holdsworth, and D.Steinman. *Real-time numerical simulation of Doppler ultrasound in the presence of nonaxial flow.* Ultrasound in Med. and Biol., 31(4):519–528, 2005.

[62] Simone Balocco, Olivier Basset, Jacques Azencot, Piero Tortoli, and Christian Cachard. *3D dynamic model of healthy and pathologic arteries for ultrasound technique evaluation.* Medical Physics, 35(12):5440–5450, December 2008.

[63] J. Degroote, K. J. Bathe, and J.Vierendeels. *Performance of a new partitioned procedure versus a monolithic procedure in fluid-structure interaction.* Computers & Structures, 87:793Ű801, 2009.

[64] J. Vierendeels, L. Lanoye, J. Degroote, and P. Verdonck. *Implicit coupling of partitioned fluid-structure interaction problems with reduced order models.* Computers and Structures, 85:970–976, 2007.

[65] Lieve Lanoye. *Fluid-structure interaction of blood vessels.* PhD, 2007.

[66] C. M. Rhie and W. L. Chow. *Numerical Study of the Turbulent Flow Past an Airfoil with Trailing Edge Separation.* AIAA Journal, 21:1525–1532, 1983.

[67] S.A.Vasquez and V.A.Ivanov. *A Phase Coupled Method for Solving Multiphase Problems on Unstructured Meshes.* Proceedings of ASME FEDSM'00: ASME 2000 Fluids Engineering Division Summer Meeting, 2000.

[68] G. De Santis, P. Mortier, M. De Beule, P. Segers, P. Verdonck, and B. Verhegghe. *Patient-specific computational fluid dynamics: structured mesh generation from coronary angiography.* Med Biol Eng Comput., Feb 17, 2010.

[69] M.S. Olufsen, C.S. Peskin CS, W.Y. Kim, E.M. Pedersen, A. Nadim, and J. Larsen. *Numerical simulation and experimental validation of blood flow in arteries with structured-tree outflow conditions.* Ann Biomed Eng., 28:1281–99, 2000.

[70] Y. Fung. *Biomechanics: motion, flow, stress, and growth.* Springer, 1990.

[71] L. R. Scott S. C. Brenner. *The mathematical theory of finite element methods.* Springer, 2002.

[72] R. W. Ogden. *Non-linear elastic deformations.* Dover Publications, N.Y., 1997.

[73] Joris Degroote. *Development of algorithms for the partitioned simulation of strongly coupled fluid-structure interaction problems.* PhD, 2010.

[74] M.D. Buhmann. *Radial Basis Functions: Theory and Implementations.* Cambridge University Press, 2003.

[75] P. Causin, J.-F. Gerbeau, and F. Nobile. *Added-mass effect in the design of partitioned algorithms for fluid-structure problems.* Computer Methods in Applied Mechanics and Engineering, 194:4506–4527, 2005.

[76] C. Forster, W.A. Wall, and E. Ramm. *Artificial added mass instabilities in sequential staggered coupling of nonlinear structures and incompressible viscous flows.* Computer Methods in Applied Mechanics and Engineering, 196:1278–1293, 2007.

[77] J. Degroote, S. Annerel, and J. Vierendeels. *Stability analysis of Gauss-Seidel iterations in a partitioned simulation of fluid-structure interaction.* Computers & Structures, in press:DOI: 10.1016/j.compstruc.2009.09.003, 2009.

[78] J. Degroote, A. Swillens, P. Bruggeman, R. Haelterman, P. Segers, and J. Vierendeels. *Simulation of fluid-structure interaction with the interface artificial compressibility method.* Communications in Numerical Methods in Engineering, in press:DOI: 10.1002/cnm.1276, 2009.

[79] G.H. Golub and C.F. Van Loan. *Matrix computations.* Johns Hopkins University Press, Baltimore, MD, USA, 3rd edition, 1996.

[80] R.M.Nerem. *Vascular fluid mechanics, the arterial wall, and atherosclerosis.* Transactions of the ASME, 114:274–282, 1988.

[81] S.Izumo A.M.Malek, S.L.Alper. *Hemodynamic shear stress and its role in atherosclerosis.* JAMA, 282:2035–2041, 1999.

[82] L.N.Bohs, B.H.Friemel, B.A.McDermott, and G.E.Trahey. *A real time system for quantifying and displaying two-dimensional velocities using ultrasound.* Ultrasound Med. Biol., 19:751–761, 1993.

[83] L. N. Bohs, B. J. Geiman, M. E. Anderson, S. C. Gebhart, and G. E. Trahey. *Speckle tracking for multi-dimensional flow estimation.* Ultrasonics, 38(1-8):369–375, 2000.

[84] B. Dunmire, K. W. Beach, K-H Labs, M. Plett, and D. E. Strandness. *Cross-beam vector Doppler ultrasound for angle-independent velocity measurements.* Ultrasound in Medicine & Biology, 26(8):1213–1235, October 2000.

[85] Q.Long, X.Y.Xu, B.Ariff, S.A.Thom, A.D.Hughes, and A.V.Stanton. *Reconstruction of blood flow patterns in a human carotid bifurcation: a ccombined CFD and MRI study.* Journal of magnetic resonance imaging, 11:299–311, 2000.

[86] D.A.Steinman, J.B.Thomas, H.M.Ladak, J.S.Milner, and J.D.Spence B.K.Rutt. *Reconstruction of carotid bifurcation hemodynamics and wall thickness using computational fluid dynamics and MRI.* Magnetic Resonance in Medicine, 47:149–159, 2002.

[87] I.Marshall, S.Zhao, P.Papathanasopoulou, P.Hoskins, and X.Y.Xu. *MRI and CFD studies of pulsatile flow in healthy and stenosed carotid bifurcation models.* Journal of Biomechanics, 37:679–687, 2004.

[88] D.A.Steinman, T.L.Poepping, M.Tambasco, R.N.Rankin, and D.W.Holdsworth. *Flow patterns at the stenosed carotid bifurcation: effect of concentric versus eccentric stenosis.* Annals of Biomedical Engineering, 28:415–423, 2000.

[89] E.A.Finol and C.H.Amon. *Blood flow in abdominal aortic aneurysms: pulsatile flow hemodynamics.* Journal of Biomechanical Engineering, 123:474–483, 2001.

[90] Simone Balocco, Olivier Basset, Jacques Azencot, Piero Tortoli, and Christian Cachard. *3D dynamic model of healthy and pathologic arteries for ultrasound technique evaluation.* Medical Physics, 35(12):5440–5450, December 2008. PMID: 19175104.

[91] K.R.Moyle, L.Antiga, and D.A.Steinman. *Inlet conditions for image-based CFD models of the carotid bifurcation: is it reasonable to assume fully developed flow?* J.Biomech.Eng., 28:371–379, 2006.

[92] J.S.Milner, J.A. Moore, C.R.Ethier, B.K.Rutt, and D.A.Steinman. *Computed hemodynamics of normal human carotid artery bifurcations derived from magnetic resonance imaging,.* J.Vasc.Surg., 28:143–156, 1998.

[93] F.P.Glor, B.Ariff, A.D.Hughes, P.R. Verdonck, D.C.Barratt, A.D.Augst, S.A.Thom, and X.Y.Xu. *Influence of head position on carotid hemodynamics in young adults,*. Am J Physiol Heart Circ Physiol., 287:H1670–1681, 2004.

[94] G. E. Tupholme. *Generation of acoustic pulses by baffled plane pistons.* Mathematika, 16(209-224), 1969.

[95] P. R. Stepanishen. *Transient radiation from pistons in an infinite planar baffle.* The Journal of the Acoustical Society of America, 49:1629, 1971.

[96] H.Torp, K.Kristoffersen, and B.A.J.Angelsen. *Autocorrelation techniques in color flow imaging: signal model and statistical properties of the autocorrelation estimates.* IEEE transactions on ultrasonics, ferroelectrics, and frequency control, 41:604–612, 1994.

[97] J.A.Jensen. *Speed-accuracy trade-offs in computing spatial impulse responses for simulating medical ultrasound imaging.* Journal of computational acoustics, 9:731–744, 2001.

[98] D.S.Zrnic. *Estimation of spectral moments for weather echoes.* IEEE Trans. Geosci. Electron., GE-17:113Ű128, 1979.

[99] H.Torp, K.Kristoffersen, and B.Angelsen. *On the Joint Probability Density Function for the Autocorrelation Estimates in Ultrasound Color Flow Imaging.* IEEE Trans. Ultrason., Ferroelec., Freq. Contr., 42:899–906, 1995.

[100] R. H. Chesarek. *Ultrasound imaging system for relatively low-velocity blood flow at relatively high frame rates.* US patent 4888694, 1989.

[101] J.Udesen, M.B.Nielsen, K.R.Nielsen, and J.A.Jensen. *Examples of in-vivo blood vector velocity estimation.* Ultrasound in Med. and Biol., 33:541–548, 2007.

[102] M.M.Dupin, I.Halliday, and C.M.Care. *A multi-component lattice Boltzmann scheme: towards the mesoscale simulation of blood flow.* Med Eng Phys., 28:13–18, 2006.

[103] G.R.Cokelet. *Rheology and hemodynamics.* Annu Rev Physiol., 42:311–24, 1980.

[104] M.Schlaikjer, S.Torp-Pedersen, and J.A.Jensen. *Simulation of RF data with tissue motion for optimizing stationary echo canceling filters.* Ultrasonics, 41:415–419, 2003.

[105] R.W.Gill. *Measurement of blood flow by ultrasound.* Ultrasound in Med. and Biol., 11:625–641, 1985.

[106] D. Shattuck, M. Weinshenker, S. Smith, and O. Von Ramm. *A parallel processing technique for high speed ultrasound imaging with linear phased arrays.* The Journal of the Acoustical Society of America, 75(1273-1282), 1984.

[107] P.R.Hoskins. *Simulation and validation of arterial ultrasound imaging and blood flow.* Ultrasound in Med. and Biol., 34(5):693–717, 2008.

[108] N.Stergiopulos, D.F.Young, and T.R.Rogge. *Computer simulation of arterial flow with applications to arterial and aortic stenoses.* Journal of Biomechanics, 25:1477–1488, 1992.

[109] M.Nakamura, S.Wada, and T.Mikami. *Effect of flow disturbances remaining at the beginning of diastole on intraventricular diastolic flow and colour M-mode Doppler echocardiograms.* Medical and biological engineering and computing, 42:509–515, 2004.

[110] A. Swillens, L. Lovstakken, J. Kips, H. Torp, and P. Segers. *Ultrasound simulation of complex flow velocity fields based on computational fluid dynamics.* IEEE Transactions on Ultrasonics, Ferroelectrics and Frequency Control, 56(3):546–556, 2009.

[111] K.V.Ramnarine, D.K.Nassiri, P.R. Hoskins, and J.Lubbers. *Validation of a new blood-mimicking fluid for use in Doppler flow test objects.* Ultrasound Med Biol., 24:451–9, 1998.

[112] J.S.Milner, J.A.Moore, C.R.Ethier, B.K.Rutt, and D.A.Steinman. *Computed hemodynamics of normal human carotid artery bifurcations derived from magnetic resonance imaging.* J.Vasc.Surg., 38:143–156, 1998.

[113] H.Torp. *Clutter rejection filters in color flow imaging: a theoretical approach.* IEEE Trans. Ultrason. Ferroelectr. Freq. Control, 44:417–424, 1997.

[114] K.Funamoto, T.Hayase, and Y.Saijo. *Numerical Experiment of Transient and Steady Characteristics of Ultrasonic-Measurement-Integrated Simulation in Three-Dimensional Blood Flow Analysis.* Annals of biomedical engineering, 37:34–49, 2009.

[115] Gregg E. Trahey, John W. Allison, and Olaf T. von Ramm. *Angle Independent Ultrasonic Detection of Blood Flow.* IEEE Transactions on Biomedical Engineering, BME-34(12):965–967, 1987.

[116] I.A. Hein and W.D. O'Brien. *Current time-domain methods for assessing tissue motion by analysis from reflected ultrasound echoes-a review.* IEEE Transactions on Ultrasonics, Ferroelectrics and Frequency Control, 40(2):84–102, 1993.

[117] J R Overbeck, K W Beach, and D E Strandness. *Vector Doppler: accurate measurement of blood velocity in two dimensions.* Ultrasound in Medicine & Biology, 18(1):19–31, 1992. PMID: 1566522.

[118] P. J. Philipps, A. P. Kadi, and O. T. Von Ramm. *Feasibility study for a two-dimensional diagnostic ultrasound velocity mapping system.* Ultrasound in medicine & biology, 21(2):217–229, 1995.

[119] P. R. Hoskins. *Peak velocity estimation in arterial stenosis models using colour vector Doppler.* Ultrasound in medicine & biology, 23(6):889, 1997.

[120] Oliver D. Kripfgans, Jonathan M. Rubin, Anne L. Hall, and J. Brian Fowlkes. *Vector Doppler imaging of a spinning disc ultrasound Doppler phantom.* Ultrasound in Medicine & Biology, 32(7):1037–1046, July 2006.

[121] A. Pastorelli, G. Torricelli, M. Scabia, E. Biagi, and L. Masotti. *A Real-Time 2-D Vector Doppler System for Clinical Experimentation.* IEEE Transactions on Medical Imaging, 27(10):1515–1524, 2008.

[122] L.N. Bohs, S.C. Gebhart, M.E. Anderson, B.J. Geiman, and G.E. Trahey. *2-D motion estimation using two parallel receive beams.* IEEE Transactions on Ultrasonics, Ferroelectrics and Frequency Control, 48(2):392–408, 2001.

[123] R. Steel, K. V. Ramnarine, A. Criton, F. Davidson, P. L. Allan, N. Humphries, H. F. Routh, P. J. Fish, and P. R. Hoskins. *Angle-dependence and reproducibility of dual-beam vector doppler ultrasound in the common carotid arteries of normal volunteers.* Ultrasound in medicine & biology, 30(2):271–276, 2004.

[124] S. Ricci, S. Diciotti, L. Francalanci, and P. Tortoli. *Accuracy and Reproducibility of a Novel Dual-Beam Vector Doppler Method.* Ultrasound in Medicine & Biology, 2008.

[125] W. R. Milnor. *Hemodynamics.* Williams & Wilkins Baltimore, 1982.

[126] I Cespedes, Y Huang, J Ophir, and S Spratt. *Methods for estimation of subsample time delays of digitized echo signals.* Ultrasonic Imaging, 17(2):142–171, April 1995.

[127] J. Udesen, F. Gran, K. Hansen, J.A. Jensen, C. Thomsen, and M.B. Nielsen. *High frame-rate blood vector velocity imaging using plane waves: Simulations and preliminary experiments.* IEEE Transactions on Ultrasonics, Ferroelectrics and Frequency Control, 55(8):1729–1743, 2008.

[128] K. Hansen, J. Udesen, C. Thomsen, J.A. Jensen, and M. Nielsen. *In vivo validation of a blood vector velocity estimator with MR angiography.* IEEE Transactions on Ultrasonics, Ferroelectrics and Frequency Control, 56(1):91–100, 2009.

[129] B. H. Friemel, L. N. Bohs, K. R. Nightingale, and G. E. Trahey. *Speckle decorrelation due to two-dimensional flow gradients.* IEEE Transactions on Ultrasonics, Ferroelectrics and Frequency Control, 45(2):317–327, 1998.

[130] Torbjorn Hergum, Tore Bjastad, Kjell Kristoffersen, and Hans Torp. *Parallel beamforming using synthetic transmit beams.* IEEE Transactions on Ultrasonics, Ferroelectrics, and Frequency Control, 54(2):271–280, February 2007.

[131] A. Swillens, T. De Schryver, L. Løvstakken, H. Torp, and P. Segers. *Assessment of Numerical Simulation Strategies for Ultrasonic Color Blood Flow Imaging, Based on a Computer and Experimental Model of the Carotid Artery.* Annals of Biomedical Engineering, 37(11):2188–2199, 2009.

[132] A. Swillens, P. Segers, H. Torp, and L. Lovstakken. *Two-dimensional blood velocity estimation with ultrasound: speckle tracking versus crossed-beam vector Doppler based on flow simulations in a carotid bifurcation model.* IEEE Transactions on Ultrasonics, Ferroelectrics and Frequency Control, 2:327–339, 2010.

[133] L.N. Bohs, S.C. Gebhart, M.E. Anderson, B.J. Geiman, and G.E. Trahey. *2-D motion estimation using two parallel receive beams.* IEEE Transactions on Ultrasonics, Ferroelectrics and Frequency Control, 48(2):392–408, 2001.

[134] A. Hergum, T. Bjastad, K.Kristoffersen, and H. Torp. *Parallel beamforming using synthetic transmit beams.* IEEE Transactions on Ultrasonics, Ferroelectrics and Frequency Control, 54(2):271–280, 2009.

[135] P. Segers, S. I. Rabben, J. De Backer, J. De Sutter, T. Gillebert, L. Van Bortel, and P. Verdonck. *Functional analysis of the common carotid artery: relative distension differences over the vessel wall measured in vivo.* J Hypertension, 22:973–981, 2004.

[136] J. Degroote, P. Bruggeman, R. Haelterman, and J. Vierendeels. *Stability of a coupling technique for partitioned solvers in FSI applications.* Computers & Structures, 86:2224Ű2234, 2008.

[137] H. M. Hilber, T. J. R. Hughes, and R. L. Taylor. *Improved numerical dissipation for time integration algorithmsin structural dynamics.* Earthquake Eng. and Struct. Dynamics, 5:283Ű292, 1977.

[138] P. Le Tallec and J. Mouro. *Fluid structure interaction with large structural displacements.* Comput. Methods Applied Mech Engineering, 190:3039–3067, 2001.

[139] M. A. Fernandez and P. Le Tallec. *Linear stability analysis in fluidŰstructure interaction with transpiration. Part I: Formulation and mathematical analysis.* Comput. Methods Applied Mech Engineering, 192:4805Ű4835, 2003.

[140] S Balocco, O Basset, G Courbebaisse, P Delachartre, P Tortoli, and C Cachard. *3D dynamical ultrasonic model of pulsating vessel walls.* Ultrasonics, 44 Suppl 1:e179–183, December 2006. PMID: 16857232.

[141] S. Bierig and A. Jones. *Accuracy and cost comparison of ultrasound versus alternative imaging modalities, including CT, MR, PET, and angiography*. Journal of Diagnostic Medical Sonography, 25:138–144, 2009.

[142] J.Bercoff, M.Tanter, and M.Fink. *Supersonic shear imaging: a new technique for soft tissue elasticity mapping*. IEEE TUFFC, 51:396–409, 2004.